Bernhard Thaler, MSc

Ultrafast Photoinduced Dynamics of Atoms and Dimer Molecules inside Helium Nanodroplets

DOCTORAL THESIS

to achieve the university degree of

Doktor der technischen Wissenschaften

submitted to

Graz University of Technology

Supervisor

Assoc. Prof. Dipl.-Ing. Dr.techn. Markus Koch

Institute of Experimental Physics

Graz, January 2020

AFFIDAVIT

I declare that I have authored this thesis independently, that I have not used other than the declared sources/resources, and that I have explicitly indicated all material which has been quoted either literally or by content from the sources used. The text document uploaded to TUGRAZonline is identical to the present doctoral thesis.

Date

Signature

Contents

Abstract

The study of ultrafast photochemical reactions on the femtosecond time scale of nuclear and vibrational motions, termed femtochemistry, has enabled fundamental insights into various fields of science such as photochemistry, photobiology or photoinduced processes in semiconductors (photovoltaics). Studies on molecular systems have up to now been performed either in the isolated (gaseous) or in the condensed (solution) phase. Within this thesis, the opportunities provided by helium nanodroplets to serve as a new solvent for femtochemistry experiments in an intermediate regime are investigated, which might allow the investigation of a wide range of systems that were previously inaccessible.

The droplets provide a cold (0.37 K), superfluid and low perturbing quantum fluid environment, and are routinely used to synthesize and investigate tailor-made and weakly bound systems. The ability to load the droplets with multiple, also heterogeneous species enables the formation of complex aggregates or even microsolvation environments, which consist of a single chromophore and a number of solvent molecules, bridging from gas phase to solution. Here, the helium droplet's potentials and limitations for ultrafast studies are tested, and dynamics on the most simple chromophores possible, namely single atoms and diatomic molecules, are investigated.

By combining pump-probe photoelectron and photoion spectroscopy with time-dependent density functional theory simulations, the dynamic solvent response on photoexcitation of fully solvated indium atoms is characterized. Photoexcitation results in the expansion of the atom's valence orbital, causing the He solvation layer (bubble) around the atom to expand within a few hundred femtoseconds due to repulsive Pauli interactions. Following the expansion, the atom is ejected from the droplet within several ten picoseconds, superimposed by a breathing oscillation of the expanded bubble. Those different dynamical processes can be precisely distinguished by distinctive signatures in the time resolved photoelectron spectra, proofing the ability of this method to trace ultrafast processes in the droplet interior.

The described processes are superimposed on the intrinsic dynamics of more complex structures, which is successfully demonstrated by time resolved experiments on indium dimers. Following photoexcitation, a twofold response of the molecule-droplet-system is found: First, the same dynamics also present for the atom are measured, namely bubble expansion, oscillation and molecule ejection. Second, superimposed on these droplet-related dynamics, a coherent vibrational motion (wave packet) is launched in the excited molecular state, representing intramolecular dynamics. Surprisingly, the wave packet coherence of the solvated molecule is conserved for several ten picoseconds, exceeding the decoherence times of conventional solvents by at least a factor of ten. The results clearly prove the potential of helium nanodroplets to act as nanoscale reactors for ultrafast chemistry, opening the door for future experiments on many molecular systems.

Kurzfassung

Die Untersuchung ultraschneller, photochemischer Reaktionen auf der Femtosekunden-Zeitskala von Kern- und Schwingungsbewegungen, kurz Femtochemie, hat grundlegende Einblicke in verschiedenste Bereiche der Naturwissenschaften, wie Photochemie, Photobiologie oder photoinduzierte Prozesse in Halbleitern (Photovoltaik) ermöglicht. Bisher wurden Untersuchungen an molekularen Systemen entweder in der isolierten (gasförmigen) oder in der kondensierten (flüssigen) Phase durchgeführt. Im Rahmen dieser Dissertation werden die Möglichkeiten von Helium-Nanotröpfchen untersucht, als neues Lösungsmittel für femtochemische Experimente in einem Zwischen-Regime zu dienen, was die Untersuchung einer Vielzahl von bisher nicht zugreifbaren Systemen ermöglichen könnte.
Die Tröpfchen bieten eine kalte (0,37 K), supraflüssige und störungsarme Quantenfluid-Umgebung und werden routinemäßig zur Erzeugung und Untersuchung maßgeschneiderter und schwach gebundener Systeme verwendet. Die Fähigkeit, die Tröpfchen mit merhreren, auch verschiedenen Spezies zu beladen ermöglicht die Bildung komplexer Aggregate oder sogar Mikro-Lösungsumgebungen. Diese bestehen aus einem einzelnen Chromophor und einer Reihe von Lösungsmittelmolekülen und ermöglichen damit eine Überbrückung von der Gasphase zur Lösung. In dieser Arbeit werden die Potenziale und Grenzen von Heliumtröpfchen für ultraschnelle Studien getestet und die Dynamik der einfachsten möglichen Chromophore, nämlich einzelner Atome und zweiatomiger Moleküle, untersucht.
Mit einer Kombination von Pump-Probe-Photoelektronen- und Photoionenspektroskopie mit Simulationen der zeitabhängigen Dichtefunktionaltheorie wird das dynamische Lösungsmittelverhalten bei Photoanregung von vollständig gelösten Indiumatomen charakterisiert. Die Photoanregung führt zur Ausdehnung des Valenzorbitals des Atoms, wodurch sich die Helium-Solvatisierungs-Hülle (Blase) um das Atom aufgrund abstoßender Pauli-Wechselwirkungen innerhalb weniger hundert Femtosekunden ausdehnt. Nach der Expansion wird das Atom innerhalb von einigen zehn Pikosekunden aus dem Tröpfchen ausgestoßen, überlagert von einer Atmungsschwingung der expandierten Blase. Die unterschiedlichen dynamischen Prozesse können durch spezifische Merkmale in den zeitaufgelösten Photoelektronenspektren genau unterschieden werden, was die Fähigkeit dieser Methode belegt, ultraschnelle Prozesse im Inneren der Tröpfchen zu verfolgen.
Die beschriebenen Prozesse überlagern die intrinsische Dynamik komplexerer Strukturen, was erfolgreich mit zeitaufgelösten Experimenten an Indium Dimeren demonstriert wird. Nach der Photoanregung ist eine zweifache Reaktion des Molekül-Tröpfchen-Systems zu beobachten: Zunächst wird die gleiche Dynamik gemessen, die auch für das Atom vorliegt, nämlich Blasenexpansion, Oszillation und Molekülausstoß. Zweitens wird, überlagert mit dieser tröpfchenbezogenen Dynamik, eine kohärente Schwingungsbewegung (Wellenpaket) im angeregten molekularen Zustand gestartet, was eine intramolekulare Dynamik darstellt. Überraschenderweise bleibt die Wellenpaket-Kohärenz des gelösten Moleküls für einige zehn Pikosekunden erhalten und übertrifft damit die Dekohärenzzeiten in herkömmlichen Lö-

sungsmitteln um mindestens einen Faktor zehn. Die Ergebnisse belegen eindeutig das Potenzial von Helium-Nanotröpfchen, als nanoskalige Reaktoren für ultraschnelle Chemie zu dienen, und öffnen die Tür für zukünftige Experimente an vielen molekularen Systemen.

Research output

The following publications are subject to the current PhD thesis. Full texts are found in chapter 4, including detailed descriptions of the respective author contributions and supplementary informations.

Peer-reviewed publications:

1. B. Thaler, S. Ranftl, P. Heim, S. Cesnik, L. Treiber, R. Meyer, A.W. Hauser, W. E. Ernst, and M. Koch
   Femtosecond photoexcitation dynamics inside a quantum solvent.
   Nat. Comm. **9**, 4006, 2018

2. B. Thaler, R. Meyer, P. Heim, S. Ranftl, J. V. Pototschnig, A. W. Hauser, M. Koch, and W. E. Ernst
   Conservation of Hot Thermal Spin-Orbit Population of ^{2}P Atoms in a Cold Quantum Fluid Environment
   J. Phys. Chem. A **123**, 3977-3984, 2019

3. B. Thaler, M. Meyer, P. Heim, and M. Koch
   Long-lived nuclear coherences inside helium nanodroplets.
   submitted to Phys. Rev. Lett., 2019

4. B. Thaler, P. Heim, L. Treiber, and M. Koch
   Ultrafast photoinduced dynamics of single atoms solvated inside helium nanodroplets.
   J. Chem. Phys. **152**, 014307, 2020

5. B. Thaler, P. Heim, L. Treiber, and M. Koch
   Photoinduced fragmentation dynamics of indium dimers in helium nanodroplets (working title).
   in preparation, 2020

Non peer-reviewed publications:

1. M. Meyer, B. Thaler, P. Heim, and M. Koch
   Femtosecond solvation dynamics of indium dimers inside superfluid helium nanodroplets
   EPJ Web Conf. **205**, 06005, 2019

The following publications are not subject to this thesis, but contain contributions by the author that were achieved during the time of his PhD.

Peer-reviewed publications:

1. M. Koch, B. Thaler, P. Heim, and W. E. Ernst
   The Role of Rydberg–Valence Coupling in the Ultrafast Relaxation Dynamics of Acetone
   J. Phys. Chem. A **34**, 6398–6404, 2017

2. M. Rumetshofer, P. Heim, B. Thaler,W. E. Ernst, M. Koch, W. von der Linden
   Analysis of femtosecond pump-probe photoelectron-photoion coincidence measurements applying Bayesian probability theory
   Phys. Rev. A **6**, 062503, 2018

3. P. Heim, M. Rumetshofer, S. Ranftl, B. Thaler, W.E. Ernst, M. Koch, and W. von der Linden
   Bayesian Analysis of Femtosecond Pump-Probe Photoelectron-Photoion Coincidence Spectra with Fluctuating Laser Intensities.
   Entropy **1**, 93, 2019

4. P. Heim, S. Mai, B. Thaler, S. Cesnik, D. Avagliano, W. E. Ernst, L. González, and M. Koch
   Revealing ultrafast population transfer between nearly degenerated electronic states.
   accepted by J. Phys. Chem. Lett., 2020

5. L. Treiber, B. Thaler, P. Heim, M. Kitzler, and M. Koch
   Laser assisted electron scattering inside a quantum solvent (working title).
   in preparation, 2020

Non peer-reviewed publications:

1. B. Thaler, M. Meyer, P. Heim, L. Treiber, W. E. Ernst, and M. Koch,
   Femtosecond dopant-to-solvent energy transfer inside helium nanodroplets.
   EPJ Web Conf. **205**, 05023, 2019

2. P. Heim, M. Rumetshofer, B. Thaler, W. E. Ernst, W. von der Linden, and M. Koch
   Bayesian probability theory to identify false coincidences in coincidence experiments.
   EPJ Web Conf. **205**, 09025, 2019

List of Figures

List of Tables

Abbreviations

Ak	alkali metal
BBO	beta barium borate
BO	Born-Oppenheimer
BS	beam splitter
DPS	differential pumping stage
EL	Euler Lagrange
FEL	free electron laser
FWHM	full width at half maximum
GSB	ground state bleach
HeDFT	helium density functional theory
He_N	helium nanodroplets
LBO	lithium triborate
LIF	laser induced fluorescence
MCP	microchannel plate
MUV	middle ultraviolet
NUV	near ultraviolet
OPA	optical parametric amplifier
PE	photoelectron
PES	potential energy surface
PEPICO	photoelectron photoion coincidence
PI	photoion
REMPI	resonance enhanced multiphoton ionization
SHG	second harmonic generation
SO	spin-orbit
TDDFT	time dependent density functional theory
TD-HeDFT	time dependent helium density functional theory
TOF	time-of-flight
TRPES	time resolved photoelectron spectroscopy
TRPIS	time resolved photoion spectroscopy
UHV	ultra high vacuum
VUV	vacuum ultraviolet
WP	wave packet

CHAPTER 1

Introduction

Since the beginng of research in the field of spectroscopy, one key drive has been the motivation to investigate dynamical processes of matter, including chemical reactions. The study of photoinduced kinetics, where the absorption of light allows to overcome large transition barriers, has developed into the wide field of photochemistry [1]. With the advent of ultrashort laser pulses, also the direct temporal observation of photoinduced processes and reaction intermediates became possible, ultimately leading to the field of femtochemistry, and the Nobel Prize in Chemistry for A. Zewail [2]. Since then, nearly all fields of science have used ultrafast experiments to gain insight into light-matter interactions. Investigations on such excited systems have been conducted in the condensed phase, where however strong interactions of the chromophore (photoexcited molecule) with the solvent often complicate interpretations and hinder the comparison with theoretical calculations. To overcome these limitations, isolated systems have been successfully investigated in the gas phase and in seeded molecular beams [3], or cryogenic matrices [4]. Both methods are combined in the use of helium nanodroplets (He_N), which allow controlled experiments within the cold matrix of low perturbing superfluid helium.
During the past few decades, He_N have emerged as a powerful tool for (so far mainly non time-resolved) spectroscopic studies [5–9]. Their outstanding properties in the cooling of most energetic degrees of freedom, including translational, vibrational and rotational motion, has enabled for example the investigation of weakly bound molecular networks [10], high spin systems [11], or highly reactive species [12]. Further beneficial properties of He_N include optical transparency up to 20 eV, and the ability to easily use sequential pickup techniques, enabling the formation and stabilization of multi-species systems, like core-shell nanoparticles [13] or microsolvation environments [14, 15].

Why perform femtochemistry experiments in He_N?
The investigation of ultrafast processes in He_N has so far been mainly focused on alkali metal atoms and molecules on the droplet surface [16–28], simulations of solvated species [29–31], pure droplets [32–37], rotational dynamics [38–44] and strong-field cluster dynamics [45–48]. Within this thesis, the potentials and limitations of He_N to act as nanoscale containers for time-resolved studies of fully solvated chromophores will be studied. If applicable, He_N could then act as a missing link between time-resolved studies in solution and in isolated systems, as they provide several advantages compared to both methods, which

are shortly summarized in the following:

1. Compared to the condensed phase, He_N allow the investigation of isolated systems without the strong perturbation of an external environment, enabling easier comparisons with simulations.

2. The low temperature of the droplets (0.37 K), which is well below the superfluid phase transition of He, provides a low perturbing environment. Dopants and clusters are cooled to their energetic ground states, simplifying high resolution spectroscopy experiments [5], and enabling the preparation and stabilization of weakly bound systems [11].

3. Conventional solvents can be directly excited by the laser pulses, if not in direct resonance, then at least by Raman scattering, which complicates solute specific interpretations. He_N, on the other hand, are optically transparent up to about 20 eV, and not Raman active.

4. As the droplets are probed under high vacuum conditions, the detection of charged species is possible, including ion charge-to-mass ratios [49], photoelectron kinetic energies [50], their angular distributions via imaging techniques [51, 52], as well as coincidence detection [53]. Time resolved photoelectron spectroscopy (TRPES) is not limited by dark states, and photochemical reactions can be followed on the entire reaction pathway [50].

5. Dopant pickup techniques for He_N allow an easy preparation of tailor made systems, for example fragile and metastable molecular clusters [54, 55], or metal clusters and nanowires with multi-shell structures [13, 56]. Compared to seeded beams, a much lower vapour density for pickup is needed, allowing the gentle isolation of also very large molecules without fragmentation, examples include proteins [57] or fullerenes [58].

6. The ability to control the average number of picked up molecules allows to precisely follow the transition from isolated molecules to a microsolvation regime by successively adding solvent molecules [14, 15], thereby directly bridging from the isolated to the condensed phase.

1.1 Key research questions

To test the potential of He_N for ultrafast studies, several specific research questions were formulated, which cover different aspects that are important for studies on isolated systems:

(1) **Are photoelectrons good observables for the study of ultrafast processes of chromophores inside He_N?**
Photoions, which have so far been routinely used for time-resolved experiments on the droplet's surface, exhibit strong attractive interactions with the helium solvent. Therefore, their applicability as observable for dynamics in the droplet interior is strongly hindered. Photoelectron (PE) spectroscopy, on the other hand, has been used in several studies in He_N, however mostly within non time-resolved experiments [59–61] or for time-resolved dynamics in pure droplets [32, 37, 62]. It remains to be answered, how the usually present fast dynamical response of a chromophore after photoexcitation affects the ability to resolve ultrafast dynamics (e.g. dynamical shifts) in He_N with PE spectroscopy.

(2) **What is the response of the solvent on chromophore photoexcitation?**
Whereas it is known that the helium solvent is only slightly influenced for rotational-vibrational

excitation of dopants [5], the stronger interaction upon electronic photoexcitation can lead to strong repulsive interactions, leading to a significant solvent rearrangement. In the extreme case of solvated metal atoms or small metal clusters, strong blue-shifts in the excitation spectra are measured, as consequence of a strong repulsive excited state interaction [60, 63–67]. On the other hand, some fully solvated organic molecules have been found to experience hardly any excitation energy shift when measuring the zero phonon lines of the $S_1 \leftarrow S_0$ transition [5]. The question arises, to what extent the interaction of excited electronic states drives solvent-induced dynamics, which may blur the studied system's internal dynamics.

(3) **What is the available time scale for studies inside the droplet?**
In the case of repulsive excited state interactions, it has been known that most chromophores are ejected from the droplet upon photoexcitation [29, 65, 66, 68–72]. If this should be the case for the studied system of interest, the question arises, how fast the ejection proceeds, and therefore after which time span the helium environment is lost.

(4) **What are the time scales of intrinsic electronic chromophore relaxation?**
The He_N influence may lead to modified excited state geometries of photoexcited molecules, possibly leading to curve crossings and relaxation dynamics, which transfer excess vibrational energy to the He solvent. There exist several examples in literature where electronic relaxation upon high state excitation was observed, however never with sufficient temporal resolution [63, 65, 67, 69, 73]. The question of how the droplet's intrinsic excitations affect the relaxation dynamics is thereby not only of importance for photochemical reactions in molecules, but also for the understanding of the quantum fluid properties.

(5) **What is the droplet's influence on intrinsic molecular dynamics?**
The ultimate criterion for He_N to act as solvent for femtochemistry experiments will be a detailed knowledge of their influence on excited molecular dynamics. Especially it must be clarified, weather wave packet dynamics in the vibrational manifold are exposed to strong decoherent or dissipative interactions. Such interactions are usually present in conventional solvents, and would hinder system specific time-resolved studies within He_N. In comparison, sufficently long wave packet coherence times have been observed in cryogenic rare gas matrices [74, 75] and for alkali molecules on the droplet surface [19, 21–23], motivating for systematic studies also in the droplet's interior.

(6) **How strong does the coupling of the droplet's internal modes with the chromophore depend on the excited mode?**
Lastly, the degree of an excited molecule's interaction with the solvent will most likely depend on the nature of the photoexcited molecular mode: Interesting aspects include the influence of the vibrational energy and therefore the energy mismatch to the internal droplet modes, the vibrational symmetry, modes with permanent dipole moments, large amplitude modes, or modes in electronic states with ionic character.

Within this thesis, experiments and simulations have been performed to answer questions (1)-(5), and satisfactory results could be obtained at least for questions (1)-(3) and (5). Experiments regarding

question (4) are somewhat ambiguous and are still under interpretation. All these results are presented in chapter 4 and wrapped up in chapter 5. Experiments regarding question (6) are at the status of preparation during the writing of this thesis, and will be shortly previewed in chapter 5.

CHAPTER 2

Scientific background

In the following, the scientific background of the thesis is presented and summarized. First, necessary basic informations on femtosecond spectroscopy and helium nanodroplets are presented, followed by a summary of the current status of research on ultrafast dynamics in the quantum solvent.

2.1 Femtochemistry

Since the first spectroscopic experiments by Joseph von Fraunhofer at the beginning of the 19th century, spectroscopy has, up to this day, enabled the investigation of matter in probably every scientific direction possible. Light-specific interactions allow to study the atomic, molecular or electronic structure of matter in various phases and length scales. Especially physical and chemical processes that are initiated by the interaction with photons take place on very fast time scales, and most historic investigations gave only a static picture via indirect measurements, or indirect insight on dynamics via linewidth analysis. With the advent of femtosecond lasers during the last few decades of the 20th century, it became possible to directly visualize the dynamics of molecules on their intrinsic time scales, leading to vast applications in various fields such as physics, chemistry, biology or material science.
The direct study of atomic motions within chemical bonds on their intrinsic time scale was pioneered by Ahmed Zewail, who was awarded the Nobel Prize of Chemistry in 1999 and formed this field of research, which was termed 'femtochemistry' [2]. The following sections give an overview on photoinduced femtosecond processes and experimental methods, which are important for this thesis. Detailed descriptions can be found in Refs. [50, 76], out of which the main points are extracted.

Basis concepts:
The key objective of time-resolved molecular studies has ever been to understand and control the conversion of photon energy after photoexcitation into other forms of energy. In polyatomic molecules, the initiated processes comprise a complex interplay of nuclear and electronic degrees of freedom, and the coupling of those leads to a variety of possible dynamics, like dissociation, internal conversion, isomerization or proton and electron transfer. Such primary steps in photochemistry generally take place on ultrafast time scales, and are the basis for processes like vision [77] or photosynthesis [78]. To get access

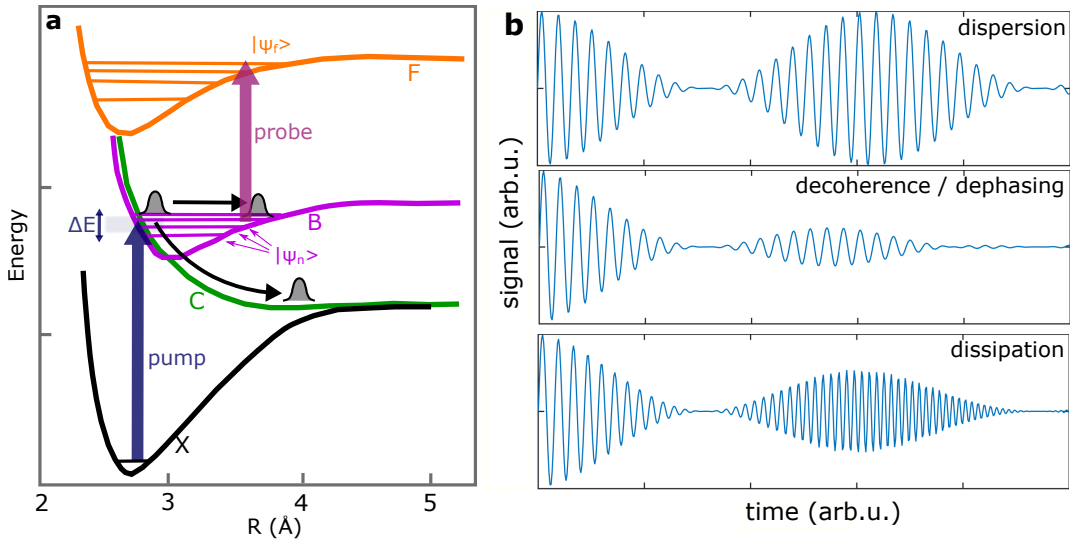

Figure 2.1: Schematic representation of possible wave packet dynamics for a diatomic molecule. Panel **a** shows the typical sequence of a pump-probe experiment. A pump pulse transfers population from a ground state X and generates a coherent superposition of vibrational levels (wave packet) in an excited electronic state B. This wave packet (WP) then evolves on the excited PES and is interrogated at a specific time delay by a second pulse (probe pulse), which projects the wave packet on a final state F. Electronic transition to a different state C leads to dissociation of the molecule. Panel **b** shows a typical oscillating signal obtained from this experiment. Three transient signal changes on the WP dynamics can be distinguished: dispersion due to excited state anharmonicity, decoherence due to elastic interactions with a solvent, and dissipation due to inelastic interactions.

to these time scales, the typical experimental approach is a pump-probe scheme [50]: A short and spectrally broad pump pulse initiates a reaction by the creation of a so called wave packet (WP), which then evolves on an excited state potential energy surface. Time delayed interrogation of this motion with a second laser pulse, the probe pulse, then enables to 'take snapshots' and visualize the ultrafast process. Fig. 2.1 shows these three steps of a general pump-probe experiment in an isolated diatomic molecule: A femtosecond pump pulse of energy E_{pump} excites the molecule from its ground state X to some excited state B, with initial wave function $\Psi_i(\Delta t = 0)$. Because of the large spectral bandwidth ΔE_{pump}, several vibrational levels are coherently populated simultaneously. Interferences between the molecular (nuclear) eigenstates $|\Psi_n\rangle$ with energies E_{n} lead to a spatial focusing of the population (wave packet, WP), which then evolves within the electronic potential according to

$$|\Psi_i(\Delta t)\rangle = \sum_n \widetilde{a_{\mathrm{n}}} e^{-iE_{\mathrm{n}}\Delta t/\hbar} |\Psi_{\mathrm{n}}\rangle \,. \tag{2.1}$$

The exact form of the WP is determined by the shape and form (spectrum, phase) of the pump pulse and the transition moment between ground and excited state, both of which are included in the complex coefficient $\widetilde{a_{\mathrm{n}}}$ for each state. After a certain waiting time Δt, the probe pulse transfers the excited state population to a certain final state $|\Psi_{\mathrm{f}}\rangle$, and the final signal to be measured can be written as

$$S_i(\Delta t) = |\langle \Psi_{\mathrm{f}}| \vec{\mu}(\vec{r}) \vec{E}_{\mathrm{probe}} |\Psi_i(\Delta t)\rangle|^2 = \left| \sum_n \widetilde{b_{\mathrm{n}}} e^{-iE_{\mathrm{n}}\Delta t/\hbar} \right|^2 \tag{2.2}$$

with $\vec{\mu}(\vec{r})$, the transition dipole moment of the probe transition and $\vec{E}_{\mathrm{probe}}$, the electric field of the probe

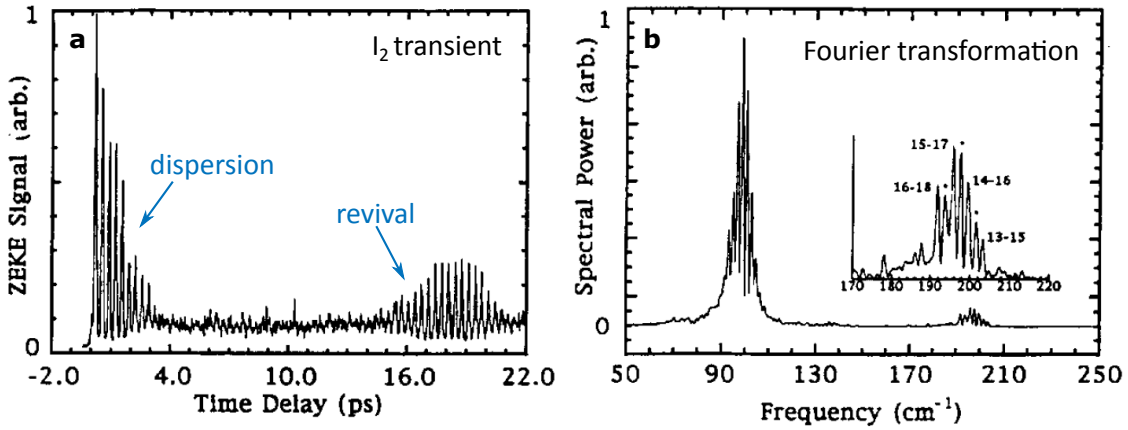

Figure 2.2: WP signals of photoexcited I_2, measured with time-resolved Zero Electron Kinetic Energy (ZEKE) spectroscopy after 345 nm excitation. Panel **a** shows the transient signal, exhibiting vibrational WP dynamics that disperse and again form revivals at 17 ps. Panel **b** shows the transient signal's Fourier transformation. The adjacent vibrational beat frequencies of the anharmonic I_2 potential can be nicely resolved for the nearest-neighbour levels ($\sim$100 cm^{-1}), and also the larger beat frequencies around 200 cm^{-1} can be partly explained with next nearest neighbour coherences. Figure adapted from Ref. [79].

pulse. The coefficients

$$\widetilde{b_{\mathrm{n}}} = \widetilde{a_{\mathrm{n}}} \langle \Psi_{\mathrm{f}} | \vec{\mu}(\vec{r}) \vec{E}_{\mathrm{probe}} | \Psi_{\mathrm{n}} \rangle = \widetilde{a_{\mathrm{n}}} d_{\mathrm{n}\to\mathrm{f}} \tag{2.3}$$

include the transition moments $d_{\mathrm{n}\to\mathrm{f}}$ to the final state as well as state amplitudes $\widetilde{a_{\mathrm{n}}}$. Equation 2.2 can be rewritten to

$$S_i(\Delta t) = \sum_n \sum_{m \le n} |\widetilde{b_{\mathrm{n}}}||\widetilde{b_{\mathrm{m}}}| cos\{(E_{\mathrm{n}} - E_{\mathrm{m}})\Delta t/\hbar + \Phi_{\mathrm{mn}}\}, \tag{2.4}$$

where all initial phase differences between different eigenstates, as well as from the probe transition to the final state, are collected in the phase factor Φ_{mn} (note that the $\widetilde{b_{\mathrm{n}}}$ factors are now within absolute values). Equation 2.4 shows that the measured signal is a sum over two-photon transition amplitudes covered by the pulse bandwidths and contains therefore coherences between degenerate two-photon transitions. Signals originate from transitions from a single ground state to at least two different excited states, $|\Psi_{\mathrm{m}}\rangle$ and $|\Psi_{\mathrm{n}}\rangle$, which are probed to a single final state $|\Psi_{\mathrm{f}}\rangle$. The different terms in the sum have periodic time dependencies with frequencies $(E_{\mathrm{n}} - E_{\mathrm{m}})/\hbar$, which depend on the energetic spacing between pairs of energy levels. The measured signal can therefore be thought of as coherent superposition of single quantum beats (see as example the I_2 transient in Fig. 2.2), showing a temporal behaviour that depends on the exact overlap between initial and excited, but also between excited and final states. As will be explained below, the choice of $|\Psi_{\mathrm{f}}\rangle$, determined by the experimental technique, crucially influences the measured transients.

WP signals and decoherence:
Especially for a diatomic molecule, WP motion can be seen as quantum mechanical analogue to a classical, vibrating molecule. If the transition probability to the final state thereby somehow changes with internuclear distance (e.g. due to different Franck-Condon factors, see below), the measured signal will show an oscillating behaviour (Figs. 2.1b and 2.2a), resulting from periodic movements of the WP into regions with high transition probability. In an anharmonic potential (e.g. Morse shape), this oscillation contrast will decay with time, as the interfering quantum beats have different frequencies due to different energetic spacings. This dispersion leads to a spreading of the WP, which reduces the focused character that is responsible for the alternating transition probability. However, as no phase information is lost, the WP will

refocus at some later time and the original oscillation contrast is restored (WP revivals, Fig. 2.1b, upper panel, and Fig.2.2a). This situation changes, if the molecule is subject to some external perturbation, for example when embedded in a solution or a matrix environment. Collisions of the molecule with other species then might destroy the constant phase relations between the quantum beats, and will generally lead to both vibrational relaxation (dissipation), as well as losses in phase relations between the modes. Within this thesis, the irreversible loss in oscillation contrast will be termed 'decoherence'. Decoherence times in typical solvents range between only a few hundred femtoseconds up to of a few ps in special cases [80]. If only elastic interactions without relaxation are present (here termed 'pure decoherence', in literature sometimes also 'pure dephasing') the populated vibrational levels stay the same, which solely leads to an oscillation contrast decay (Fig. 2.1b, middle panel). Purely inelastic interactions, on the other hand, could also conserve coherence, and thereby cause phase-conserving vibrational relaxation, leading to an increase in vibrational frequency due to larger energetic spacings in lower energy regions of the potential energy surface (Fig. 2.1b, lower panel). Such an interaction has been described for example for WP dynamics in solid rare gas matrices [81], and will be called 'phase conserving dissipation' within this thesis.

Born-Oppenheimer approximation:
The physical picture behind the concept of WP dynamics in potential energy surfaces is a somewhat simplified one, describing the complex coupling of nuclear and electronic degrees of freedom. The so called Born-Oppenheimer (BO) approximation decouples the fast, light electron dynamics from the slow, heavy nuclear dynamics by assuming that the full molecular wave function can be viewed as a simple product of a vibrational (Ψ_{ν_α}) and an electronic (Φ_α) part:

$$\Psi(r, R) = \Phi_\alpha(r, R) \cdot \Psi_{\nu_\alpha}(R) \tag{2.5}$$

with r the electron coordinates and R the nuclear positions, α thereby indexes the electronic states and ν_α vibrational states within. The BO principle now enables the concept of potential energy surfaces by solving the Schrödinger equation for the electrons in fixed nuclear geometries:

$$H_{\mathrm{el}}\Phi_\alpha(r, R) = E_\alpha(R)\Phi_\alpha(r, R). \tag{2.6}$$

The nuclei are thought to move within the electronic potential, and the electrons quickly adapt to the nuclear geometries. WP dynamics in so obtained potentials represent then simple adiabatic dynamics, as long as only a single electronic state is involved. In the case when different potential energy surfaces intersect, the BO approximation breaks down and strong coupling between nuclear and different electronic degrees can occur (see Fig. 2.3). Such couplings are generally referred to as non-adiabatic or non-BO dynamics, and are especially suited to be studied with photoelectron spectroscopy.

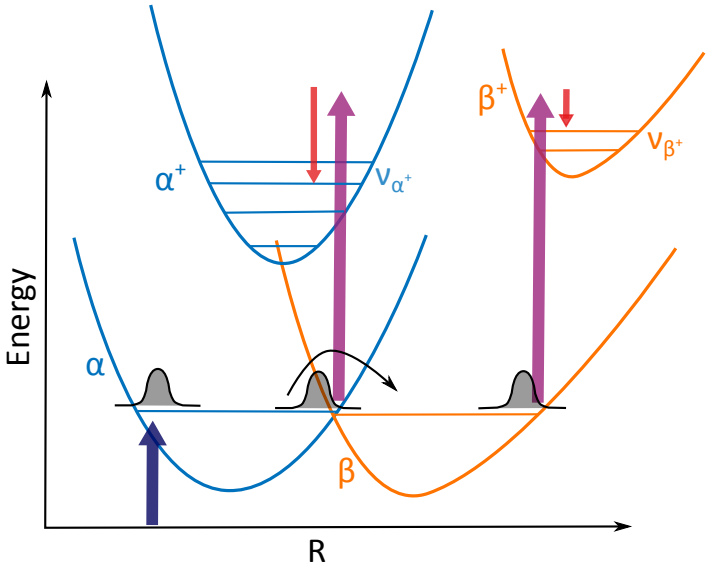

Figure 2.3: Non-adiabatic coupling between two different electronic states, leading to ionization into different ionic states due to Koopmans' theorem, depending on the Franck-Condon overlap of the vibrational levels. Due to different binding energies in the two geometries, different photoelectron kinetic energies are measured (indicated as downwards arrows).

2.2 Photoionization spectroscopy

As mentioned above, the nature of the final state $|\Psi_f\rangle$ crucially influences the degree of information that can be obtained from pump-probe studies. Several probe schemes have been developed, including non-linear wave mixing or transient absorption for condensed phase experiments, or laser induced fluorescence and photoionization in the gas phase, and in recent years also X-ray or electron diffraction. Measurements within this thesis applied photoionization, in particular time-resolved photoion spectroscopy and time-resolved photoelectron spectroscopy (TRPES), the theoretical concepts and advantages of which are in the following shortly summarized.

Both photoions and photoelectrons can be measured as integrated yield (which can be thought of as summation over multiple final states $|\Psi_f\rangle$), however with a low degree of differentiation. More sophisticated approaches apply mass- or angle-resolved photoions, and energy- or angle-resolved photoelectrons, or a simultaneous detection applying photoelectron-photoion-coincidence spectroscopy, which in its full extent allows to study the full molecular structure in a reaction microscope (COLTRIMS) [82].

Whereas time-resolved mass spectroscopy is rather simple, interpretations are limited. Especially well suited to study non-adiabatic processes like the one depicted in Fig. 2.3 is TRPES, as it allows to be sensitive to both the nuclear and the electronic degrees of freedom. Another advantage is the reduced constraint due to selection rules, as the outgoing electron has a large range of allowed symmetries and any molecular state can be ionized, allowing to trace molecular reactions along the entire reaction pathway.

The general form of a TRPES experiment that measures the kinetic energy E_{kin} of the PE with a 1+1 pump-probe scheme is the following:

$$E_0(\nu) + h\nu_{\text{pump}} + h\nu_{\text{probe}} = E_{\text{I.E.}} + E_{\text{ion}}(\nu) + E_{\text{kin}}. \tag{2.7}$$

where $E_{\text{I.E.}}$ is the ionization energy and $E_{\text{ion}}(\nu)$ the vibrational energy of the ion. The initial energy E_0 can mostly be ignored for seeded beam experiments. After excitation, the pump photon energy

($h\nu_{\mathrm{pump}}$) is redistributed through possible adiabatic and non-adiabatic WP propagations, leading to time dependent E_{kin}, as the ionization energy $E_{\mathrm{I.E.}}$ and the populated $E_{\mathrm{ion}}(\nu)$ may change.
In TRPES, the transition moment of equation 2.3 takes the form

$$d_{\mathrm{n}\to\mathrm{f}} = \langle \Psi_{\mathrm{f}}(R,r); \Psi_{\mathrm{e}}(\mathbf{k},R,r) | \, \vec{\mu}(\vec{r})\vec{E}_{\mathrm{probe}} \, | \Psi_{\mathrm{n}} \rangle \tag{2.8}$$

and therefore includes both the wave function of the electron (with wave-vector $\mathbf{k}$) and the ionic system. Using the above introduced BO-approximation one can write

$$d_{\mathrm{n}\to\mathrm{f}} = \langle \Phi_{\alpha^+}\Psi_{\nu_{\alpha^+}}; \Psi_e | \, \vec{\mu}\vec{E}_{\mathrm{probe}} \, | \Phi_\alpha \Psi_{\nu_\alpha} \rangle \tag{2.9}$$

with α^+ the ionic state (final state f) populated when ionizing the neutral state α (initial state n). This expression can be further simplified by using the Franck-Condon principle, which states that the nuclear geometry and momentum will not change during the instantaneous absorption of a photon. The transition moment can then be decoupled,

$$d_{\mathrm{n}\to\mathrm{f}} = \langle \Psi_{\nu_{\alpha^+}} | \Psi_{\nu_\alpha} \rangle \, \langle \Phi_{\alpha^+}; \Psi_e | \, \vec{\mu}\vec{E}_{\mathrm{probe}} \, | \Phi_\alpha \rangle \tag{2.10}$$

where the first factor is the Franck-Condon factor, that describes the vibrational overlap between the excited and the ionic state. In the case of WP motion, this overlap defines the region of increased transition probability (see Fig. 2.3); for the simple case of diatomic molecules, periodic motion into this so called Franck-Condon window is responsible for the signal oscillation. It is therefore clear, that oscillating signals will only be observed when the ionic geometry differs from the neutral one and hence large changes of vibrational numbers ν are present.
Whereas the Franck-Condon factor describes the nuclear, adiabatic dynamics, the second term in equation 2.10 becomes important in the case of non-adiabatic dynamics, e.g. the crossing of the WP to a different electronic state (Fig. 2.3). At the crossing point (degeneracy) of states α and β (e.g. an avoided crossings in diatomic molecules, or a conical intersection in the case of polyatomic molecules), the WP may split between the states, or completely transfer from α to β. The photoionization process is then crucially influenced by the electronic transition moment and the nature of the ionic states. Using a Hatree-Fock like picture of independent electron orbitals, the so called Koopmans' theorem states that the ionization energy of a specific state is always the negative energy of the removed electron's orbital. Therefore, different excited states with different orbital structure might correspond to different ionic states, as sketched in Fig. 2.3. As the potential energy surface of the involved ionic states can greatly differ, the ionization energy during a non-adiabatic transition will change, and in the TRPES spectra a second PE energy band might be measured, according to equation 2.7. In the case that ionization from states α and β proceeds to the same ionic state, TRPES spectra may still provide the necessary information as the Franck-Condon factors might also change, although not as pronounced as for ionic state changes. More differentiation, also upon ionization to the same ionic state can be retrieved from photoelectron angular distributions (PAD). Such measurements make use of the fact that the symmetry of the ionized state will also reflect on the symmetry of the photoelectron distribution (vector $\mathbf{k}$). As such techniques have not been used within this thesis, the reader is referred to Refs. [52, 76] for more details.
Both photoelectrons and photoions may also be detected in coincidence (PEPICO), allowing the retrieval of mass selective PE spectra. Such measurements allow the identification of ionic states with different fragmentation channels [83], cluster selective PE detection [53], or the interpretation of different intramolecular relaxation and dissociation pathways [84–86].

2.3 Helium nanodroplet isolation

Spectroscopic studies of isolated species at low temperature have, historically seen, mostly been performed either in seeded supersonic beams or in cryogenic solid matrices. Helium nanodroplet (He_N) isolation represents a combination of those two techniques, combining their advantages and thereby enabling the study and synthesis of a wide variety of systems that were previously hard to access due to the limited formation ability of multi-species systems. Within this section, important properties of He_N that are essential for spectroscopy are briefly reviewed. As spectroscopic studies inside He_N have been performed now for over two decades, there exist a variety of review articles with detailed descriptions of the technique and spectroscopic applications [5–9, 87].
The Institute of Experimental Physics at TU Graz, where this thesis was written, has a long history on the application of He_N, with a number of PhD theses, which also provide a detailed introduction into the technique [88–92]. As the focus within this work lies on the application of He_N to serve as reaction containers for time resolved studies, the following section will focus on droplet properties that have possible implications on such femtochemistry studies. In the then following section, ultrafast studies that have been performed up to now in He_N will be reviewed.

2.3.1 Generation, properties and doping of He_N

More details on contents of this section are found in the review article of Toennies and Vilesov [5], 'the' standard work on the helium nanodroplet isolation technique.

Generation of He_N:
He_N for spectroscopy are usually produced by applying free jet expansions of pre-cooled (10-20 K range), high pressurized (10-100 bar) He gas through few-μm nozzles, implemented in a molecular beam apparatus (see Fig. 2.4a&b). For the experiments conducted within this thesis, He_N were retrieved by working within the subcritical expansion regime, meaning to start at a point in the He phase diagram with He in the gaseous phase, which is expanded into high vacuum, causing condensation (Fig. 2.4a). Followed by the expansion, the droplets condensate in the immediate region after the nozzle and finally reach pressure regions where no interaction among different droplets is present, as the final velocity distribution is very narrow and strictly in forward direction. The droplets then further cool down due to evaporative cooling, finally reaching temperatures of around 0.37 K (Fig. 2.4b).

Properties of He_N:
With the experimental parameters used during the work of this thesis (40 bar stagnation pressure, 5 μm nozzle diameter), typical droplet sizes lie in the range of a few thousand He atoms, depending on the nozzle temperature. Droplet size distributions have been measured by scattering experiments [94], and can be calculated by applying the Knuth Model scaling laws for clusters formed in free jet-expansion, which is described in the PhD thesis of F. Lackner [91]. Mean droplet sizes as a function of nozzle temperature obtained from such a calculation are shown in Fig. 2.4e, together with the expected radii when assuming spherical droplets and bulk helium densities. Cluster size distributions are fairly broad and follow a log-normal distribution, with FWHMs that are on the order of the mean cluster size.
The density profile of pure droplets is fairly flat, with particle densities in the center similar to the bulk value of 0.022 atoms/Å^3, and quickly dropping to zero at the droplet edge (Fig. 2.4c), for which reason it is often safe to assume a spherical form. Mean He atom binding energies for droplets larger than about 1000 atoms also lie at the bulk value of 5 cm^{-1}, which is an important quantity for the estimation of size

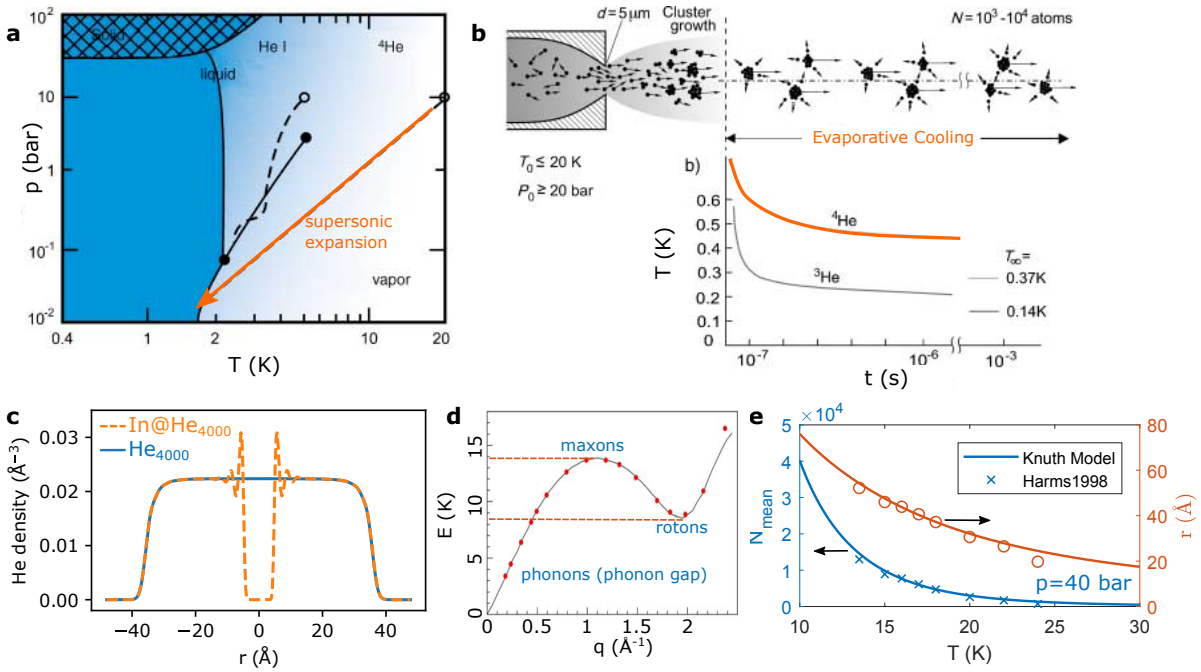

Figure 2.4: Formation process and physical properties of He_N. Panel **a** shows the phase diagram of He, the orange arrow follows the typical trajectory of a supersonic expansion into the superfluid phase. Panel **b** shows the typical expansion process of a free gaseous jet through a 5 μm nozzle. Following the expansion, the He atoms condensate to form droplets, which further cool down to the intrinsic temperature of 0.37 K via evaporation. Panel **c** shows He_{4000} density profiles, obtained by HeDFT, for a pure droplet and for an In atom placed at the droplet center. Panel **d** shows the dispersion relation of bulk liquid He, the characteristic excitation regions are indicated. Panel **e** shows the droplet size dependence on nozzle temperature, for the typical source parameters of 40 bar expansion pressure and a nozzle diameter of 5 μm, which were used for the experiments within this thesis. Panels **a** and **b** were adapted from Ref. [5], panel **d** from Ref. [93].

changes upon the input of external energy (collision with dopants, photoexcitation).

An important aspect of He_N, especially for dynamics, are the droplet's intrinsic excitations, which have been mostly studied theoretically, and are explained in great detail in Ref. [95]. Those excitations are responsible for the cooling of foreign molecules down to the droplet's temperature. The coupling of the different excitations to molecular degrees of freedom defines the dissipative dynamics on molecular excitations and will therefore benchmark the ability to study and also control photochemical reactions. Excitations are generally grouped in surface (ripplons) and bulk modes (phonons). Whereas ripplons exhibit rather low energies in the range below 1 K, phonon energies lie in the few-K range and are therefore more important for the coupling to ro-vibrational modes of molecules. The phonon dispersion curve is assumed to be similar to the bulk-excitation curve (shown in Fig. 2.4d), which density of states consists of two specific maxima, with excitations called maxons and rotons. The specific form of the roton minimum dispersion curve of liquid He is then responsible for the onset of superfluidity below a certain critical velocity (Landau velocity) due to the then lacking possibility to generate phonon excitations, which generate friction. However, other excitation like ripplons or also quantum vortices may still cause dissipative effects below the critical velocity. The special form of the dispersion curve is also thought to be responsible for the observation of long rotational and vibrational lifetimes of molecules in He_N. The density of states of liquid He is very low below the roton minimum (<8.5 K, phonon gap) and above the maxon maximum (14 K), causing a very low coupling of the excitations to low energetic rotational [7]

and high energetic vibrational modes [55], resulting in long lifetimes.

Doping of He_N:
Droplets are loaded with foreign atoms or molecules by letting them pass through pickup cells that contain the desired species in the gaseous phase at a sufficient vapour pressure ($>10^{-5}$ mbar). A dopant collides with the droplet, causing the generation of multiple droplet excitations, which cool down the dopant to the droplet temperature. This thermal equalisation is thought to proceed for all available molecular degrees of freedom, with certain exceptions: Stable excited states have been found when the vibrational or electronic energies are significantly larger than the available droplet excitation energies, and no intermediate energies are available for a cascade-like relaxation [55, 96]. Further, excited states with different spin angular momenta were found to not relax, for species on the droplet surface [88, 97], and in the droplet interior [98].
During relaxation, the dissipated energy is thought to be released from the system with the evaporation of He atoms, leading to a shrinking of He_N size. When assuming a constant pickup cross section, the pickup probability of n particles follows a Poisson distribution

$$P_n(z) = \frac{z^n}{n!} e^{-z}, \tag{2.11}$$

with z the mean number of particles picked up. After immersion into the droplet, the dopants are expected to move freely within the interior, due to the flat density and the superfluid character of the He. This unhindered movement results in the fast coagulation of different dopants into clusters and complexes, which are often only very weakly bound through van der Waals interaction, but are nevertheless stable due to the low temperatures.
Due to the Pauli repulsion of the dopant's valence electrons with the closed shell He surrounding, atoms and molecules reside in regions of zero helium density, called solvation shell bubbles, shown in Fig. 2.4d for an In atom in the droplet's center. As van der Waals forces are still present, the nearby He is still shaped around the dopant into several shells of increased He density. Due to the favourable energetic configuration, most atoms and molecules are thought to occupy equilibrium locations fully enclosed in the droplet's interior. Depending on the strength difference of the dopant-He and He-He binding potentials [99], some species like alkali metals and their small clusters have however also been found to reside in "dimples" at the droplet surface.

2.3.2 Spectroscopy in He_N and experimental observables

Since the first spectroscopic experiments on molecules inside He_N, conducted on SF_6 [100], multiple classes of molecules and molecular networks have been investigated. Already for SF_6, the sharp rotational lines suggested a very weak coupling of rotational motion to the bath and therefore long lifetimes. Ground state ro-vibrational spectroscopy experiments on the same molecule later confirmed the theoretically predicted internal droplet temperature of around 0.37 K [101]. Although only directly valid for rotational motion, this result indicated that all energetic degrees of freedom might be cooled down to this temperature inside He_N. These experiments were also the first ones to suggest the emergence of superfluidity in He_N on a microscopic level: Comparisons of linewidths in ^{4}He droplets with ^{3}He droplets revealed that rotational motion in the non-superfluid ^{3}He is indeed highly quenched [102]. Owing to the consequentially weak interaction in the ground state, exotic structures can be stabilized and investigated in He_N [11, 54, 55]. The comparably simple pickup technique of helium droplets, in combination with low temperature and high mobility inside, further allows the tailor made synthesis of heterogeneous complexes, examples

include microsolvation environments [14] or bimetallic nanoparticles [13].
For spectroscopic applications [8], the optical density in the droplet beam is too low to apply absorption techniques and methods are therefore mostly laser based, with differences in sensitivity and possible observables. In the following, different approaches are briefly described, details on vibrational spectroscopy, mostly applying depletion methods, are found in Refs. [7, 103], and details on electronic spectroscopy, mostly appling laser induced fluorescence (LIF) or photoionization, are found in Ref. [6].

Infrared spectroscopy:
Investigations for molecular structure or electronic ground state dynamics mostly use the cooling of excited ro-vibrational bands by the droplets. A laser is tuned through a specific wavelength region and excites the dopant at its specific resonant frequencies. The excited energy is then dissipated by the coupling to the droplet's intrinsic modes and eventually leads to the evaporation of He atoms and hence the reduction of mean droplet size, which can be detected downstream of the droplet beam. One applied method uses the coaxial interaction of the droplet beam with a counter-propagating laser, and the beam depletion (signal drop of e.g. the He_2 signal) is measured with a quadrupole mass spectrometer. Another often applied method uses a laser that crosses the droplet beam at nearly right angles, and is then reflected back and forth in a multipass cell to interact several times with the He_N. In this case, a bolometric detector can be used at the end of the droplet beam, which measures its kinetic energy via heat generation after absorption.
As infrared spectroscopy is not suitable for direct time-resolved studies, relevance for this thesis mostly comes from indirect linewidth analysis, for example via claims about vibrational and rotational relaxation time scales [7, 55].

Electronic spectroscopy:
For the case of high resolution electronic spectroscopy, the mostly applied method has long been laser induced fluorescence (LIF), either for variable excitation energies while monitoring the total fluorescence yield (recording excitation spectra), or by single energy excitation with dispersed fluorescence of the emitted light (recording emission spectra).
As complementary approach, photoionization finds increased usage, as it also allows to monitor for example mass channels in photoion (PI) spectroscopy, or the direct monitoring of electronic binding energies by using photoelectron (PE) spectroscopy (see section 2.2). As disadvantage for photoions, they may be subject to strong attractive forces, causing the immersion into the droplets, preventing their detection. Photoelectrons, on the other hand, have been found to be fully ejected from the droplet in various studies, with only weak distortion [32, 59, 60], thereby opening the possibility to use all advantages of TRPES (see section 2.2) also for He_N spectroscopy. Both PE and PI may be measured by time-of-flight detection, or with imaging techniques (velocity map imaging), which additionally provide insights into the ionized molecular orbital in case of PE, or kinetic energy releases upon fragmentation in case of PI. Also photoelectron-photoion coincidence (PEPICO) spectroscopy has been used recently with He_N [104], but has however the same limitation as photoions, which might be only detectable when previously ejected, or for the investigation of surface located species.
Recently, the group of F. Stienkemeier has also succeeded in applying two-dimensional electronic spectroscopy in He_N, a method widely applied in the condensed phase, which is rather challenging for isolated systems due to insufficient sensitivity [27]. The method allows to achieve a unique spectro-temporal resolution and directly gives insights into coupling effects and different broadening mechanisms.
As photochemical and especially femtochemical reactions mainly proceed in excited electronic states, the mentioned methods should all be applicable for the study of ultrafast processes in He_N. This thesis

deals with femtosecond studies on fully immersed atoms and dimer molecules using photoionization, in particular TRPES.

2.3.3 Simulation of dynamic processes in He_N

As parts of this thesis deal with the simulation of dynamics inside He_N, a basic description of the applied formalism, namely He density functional theory (HeDFT), is presented in the following. Simulations are performed with the publicly available BCN-TLS-4HeDFT package [105], derivations and explanations on how the formalism is implemented can be found in review articles [93, 106] and in the DFT-manual found in the online repository [105]. Here only details on how to simulate photoinduced dynamics are presented. Ref. [106] also deals with general recent improvements regarding the He functional used, as well as the implementation of HeDFT to describe vorticity in He_N.
Starting point for the description of HeDFT is a Kohn-Sham approach considering only a single Slater determinant due to the bosonic nature of helium. This approach defines the total energy of a system solely as a functional dependent on the effective one-particle density $\rho(\mathbf{r})$ of helium. The total energy of a pure droplet is then written as

$$E[\rho] = T[\rho] + \int \mathrm{d}\mathbf{r}\mathcal{E}_c[\rho], \tag{2.12}$$

with $T[\rho]$ the kinetic energy of the helium atoms, and the functional $\mathcal{E}_c[\rho]$, which accounts for He-He interactions and non-local effects. The most used functional for this term is the Orsay-Trento functional [107], which was parametrized to fit the dispersion relation of liquid He (Fig. 2.4d), but is in its full form however seldom applied to inhomogeneous systems due to computational limitations.
When introducing an impurity like a foreign atom into the droplet, equation 2.12 has to be adapted by adding the impurity-helium interaction potential $E_{\mathrm{I-He}}$, which has to be known separately, and must be obtained from ab-initio calculations. For simplicity, we here include only a description for heavy (classical) impurities, like the within this thesis described indium (In). For light impurities, their full wave function has to be considered, yielding quantum-mechanical solutions also for the impurity [106]. The total energy for a He-droplet system with a classical impurity can be obtained by simple adding a term to equation 2.12 that account for the kinetic energy of the impurity and a term that integrates the helium density over the diatomic potential,

$$\begin{aligned} E[\rho, \mathbf{r_I}] = T[\rho] + \frac{p_I^2}{2m_I} + \int d\mathbf{r}\mathcal{E}_c(\rho) \\ + \int d\mathbf{r}\rho(\mathbf{r})E_{\mathrm{I-He}}(|\mathbf{r} - \mathbf{r_I}|). \end{aligned} \tag{2.13}$$

Defining an order parameter (effective wave function) $\Psi(\mathbf{r}, t)$ with

$$|\Psi(\mathbf{r}, t)|^2 = \rho(r, t), \tag{2.14}$$

and variation with respect to Ψ gives the time-dependent Euler-Lagrange (EL) equation

$$i\hbar\frac{\partial}{\partial t}\Psi(\mathbf{r}, t) = \left[-\frac{\hbar^2}{2m_{He}}\nabla^2 + \frac{\delta\mathcal{E}_c}{\delta\rho} + E_{I-He}(|\mathbf{r} - \mathbf{r_I}|)\right]\Psi(\mathbf{r}, t). \tag{2.15}$$

Assuming a stationary wave function, one obtains the time-independent EL equation:

$$\left[-\frac{\hbar^2}{2m_{He}}\nabla^2 + \frac{\delta\mathcal{E}_c}{\delta\rho} + E_{I-He}(|\mathbf{r} - \mathbf{r_I}|)\right]\Psi_0(\mathbf{r}) = \mu\Psi_0(\mathbf{r}), \tag{2.16}$$

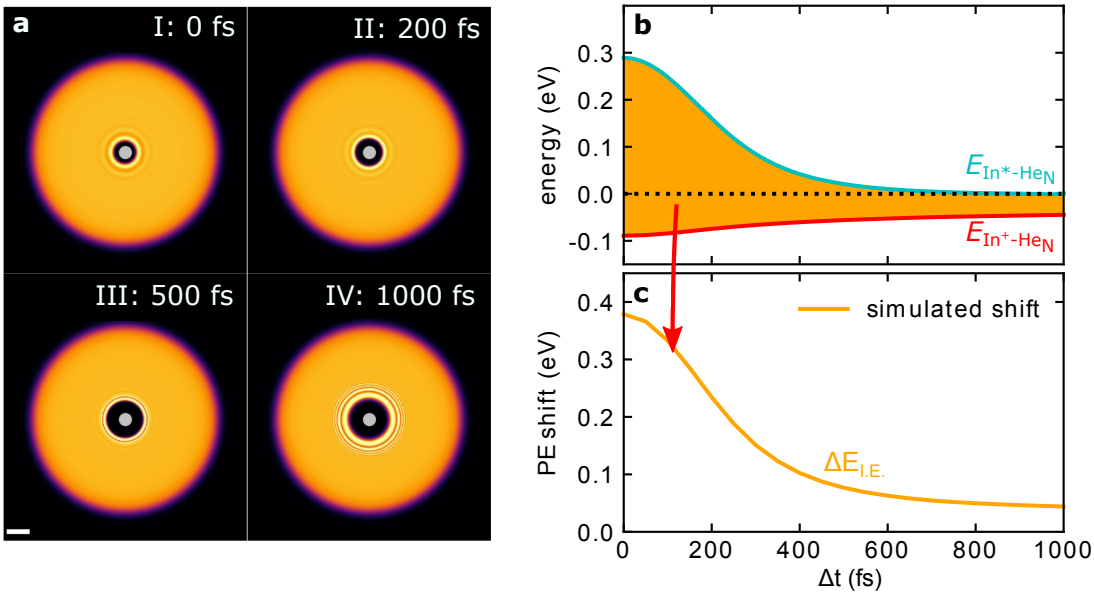

Figure 2.5: Application of TD-HeDFT to obtain time resolved PE spectra for the case of In photoexcitation. Panel **a** shows He densities with an In atom located in the droplet's center, with In in its electronic ground state ($5^2P_{1/2}$, I) and during consecutive time steps after switching to the excited state ($6^2S_{1/2}$, II-IV). Panel **b** shows the transient interaction energy of the atom with the droplet, both for the excited and the ionic state, and panel **c** the difference of the two, which can be directly translated into the PE energy with equation 2.18. Figure adapted from Ref. [108].

with the chemical potential μ. An iterative solution of equation 2.16 yields the total system's energy as well as the droplet density, for example as function of impurity position within the droplet, for which the specific location has to be however additionally constrained. Such static densities are for example used for the calculation of absorption or emission spectra, as well as starting densities for time-dependent simulations (e.g. photoexcitation or photoionisation).
For time-dependent HeDFT (TD-HeDFT) simulations, the full EL equation for the helium and Newton's equation of motion for the impurity have to be solved:

$$\begin{aligned} i\hbar\frac{\partial}{\partial t}\Psi &= \left[-\frac{\hbar^2}{2m_{He}}\nabla^2 + \frac{\delta\mathcal{E}_c}{\delta\rho} + E_{I-He}(|\mathbf{r}-\mathbf{r_I}|)\right]\Psi, \\ m_I\ddot{\mathbf{r}}_\mathbf{I} &= -\nabla_{r_I}\left[\int d\mathbf{r}\rho(\mathbf{r})E_{I-He}(|\mathbf{r}-\mathbf{r_I}|)\right], \end{aligned} \tag{2.17}$$

As result, the time-dependent helium density of the droplet and impurity trajectories are retrieved.

Application of TD-HeDFT for photoexcitation dynamics:
In the case of photoexcitaion dynamics, the following procedure is applied to obtain time-resolved photoelectron spectra:

1. The helium density around the impurity in its ground state is computed by solving the static HeDFT equations.

2. The temporal evolution of the system is retrieved by performing a time-dependent HeDFT calculation with the ground state He density as initial configuration but with the excited state pair potential; this approach is sometimes referred to as frozen droplet approximation.

3. Third, for various times during the temporal evolution, the pair potential energies E_{I-He} are summed up for the whole droplet for both the excited state and for the ionic state. The difference between the interaction energies directly compares to the difference in ionization energy ($\Delta E_{\mathrm{I.E.}}$) of the immersed impurity and therefore, with knowledge of the bare atomic binding energy E_{bind}, to the photoelectron energy:

$$\begin{aligned} E_{\mathrm{PE}}(t) &= h\nu - E_{\mathrm{bind}} + \Delta E_{\mathrm{I.E.}} \\ &= h\nu - E_{\mathrm{bind}} + \Big[\int \rho_{\mathrm{He}}(\mathrm{r},\mathrm{t}) E_{\mathrm{I}^*-\mathrm{He}}(\mathrm{r} - \mathrm{r}_{\mathrm{In}}(\mathrm{t})) d^3 r \\ &\qquad - \int \rho_{\mathrm{He}}(\mathrm{r},\mathrm{t}) E_{\mathrm{I}^+-\mathrm{He}}(\mathrm{r} - \mathrm{r}_{\mathrm{In}}(\mathrm{t})) d^3 r \Big] \end{aligned} \tag{2.18}$$

   This last step is shown in Fig. 2.5 for the case of In photoexcitation in the droplet center.

The described procedure is however only applicable in the case of single states with isotropic symmetry (e.g. S), in the case of anisotropic, and also multiple, states, the additional degrees of freedom have to be taken explicitly into account to allow coupling effects [29, 106].

Details on implemented programs and processing steps to use the BCN-TLS-4HeDFT package, as applied within this thesis, are given in appendix D.

2.4 Status of Research: Ultrafast dynamics inside He_N

In the following, recent progresses on the description of ultrafast (picoseconds and faster) processes proceeding inside He_N are reviewed, with focus on ultrafast experiments and discussion of historically important "static" studies. Dynamical processes in general proceed when systems are somehow driven out of equilibrium, and are thereby undergoing some rearrangement or relaxation on specific reaction coordinates. Here, ultrafast dynamics in He_N are therefore grouped with respect to the most participating degree of freedom, i.e., translation, vibration, rotation, spin or orbital angular momentum, electronic excitation. However, the described processes might involve the coupling of several degrees of freedom, making this assignment somewhat ambiguous, and the categories may show some overlap. The last two sections further review photochemical reactions in He_N, and only mention recent dynamics involving charged particles. Where the reviewed results overlap with results obtained within this PhD thesis, references to the corresponding sections in chapter 4 are given.

2.4.1 Translational and solvation dynamics

Owing to the superfluid character of the low temperature helium, as well as the constant He density inside the droplet, it is believed that foreign species move unhindered inside the quantum fluid [5]. However, based on pure superfluidity arguments this is true only for velocities lower than the critical Landau velocity (approx. 58 m/s), which connects the onset of friction in a superfluid to the ability to generate collective excitations (e.g. phonons) at sufficiently high kinetic energy [109]. The topic of translational dynamics is therefore closely related to the question of the exact dynamical processes that might be responsible for superfluid behaviour inside the droplets. Besides the classical excitations (see Sec. 2.3.1) of bulk liqudid helium (rotons), which are responsible for superfluidity as they require a minimum velocity in order to be excited, other sources of friction inside He_N might be present, like surface excitations (ripplons), quantum evaporation [95], quantized vortices, or cavitation [110], all of which may contribute to friction also below the Landau velocity.
Strong translational interactions of dopants with He_N are present during the doping process, where the inelastic collision causes dopants to cool down and loose kinetic energy, which is transferred to the helium. However, the ultrafast dynamics underlying this process are hard to access experimentally, and insights must be gained through simulations. Recent studies applying TD-HeDFT investigated the pickup process of heliophobic [111] and heliophilic dopants [31, 112]. It was found that after collision, fast dissipative effects decelerate the dopant within at maximum a few ten ps, and excess energy is thereby released by the ejection of fast He atoms from the droplet. As those dynamics are not related to photoinduced effects, no more details are given here.
Tranlational motion of dopants can however also be initiated after photoexcitation, making it ideally suitable to study this dynamics in pump-probe experiments. There exist two prominent examples in which the photon energy is (at least partly) transferred to kinetic energy of dopants: First, the kinetic energy release by photodissociation and second, dopant ejection following excitation to a He-repulsive state.
Stronge accelerations of dopants inside the superfluid can be achieved by photodissociation of molecules. Such photoinduced reactions have been investigated experimentally in the group of M. Drabbels in non-time resolved ion imaging experiments on alkyl iodides [113–116] and recently also theoretically in the group of M. Gonzáles with hybrid DFT simulations [30, 117, 118]. The large kinetic energy release during dissociation (or predissociation) causes velocities on the order of several hundred meters per second, which are considerably larger than the critical Landau velocity. The fragment motion therefore results

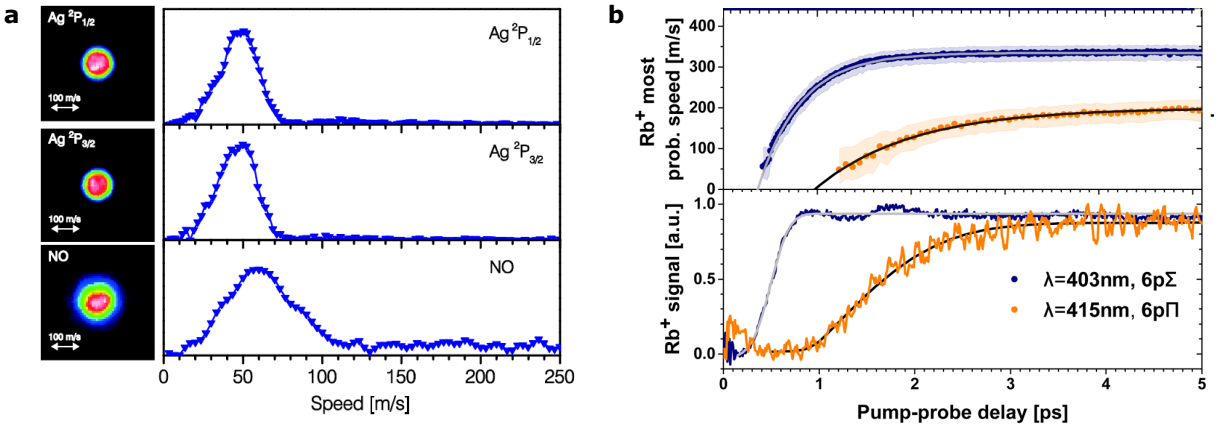

Figure 2.6: Examples for measured ejection dynamcis of dopants from He_N. Panel **a** shows velocity distributions obtained after photoinduced ejection of Ag atoms and NO molecules (Figure obtained from Ref. [71]). Panel **b** shows the most probable velocity (upper) and total photoion yield (lower) as function of pump-probe delay, after Rb 6p←5s excitation (Figure obtained from Ref. [120]).

in strong dissipative dynamics in the droplet, and ultimately leads to ejection. Despite strong deceleration compared to gas phase fragmentation, the dissociation products were not found to be caged inside the droplets (with the exception of CF_3I [116], see below) which was attributed to the quantum, more specifically, superfluid nature of the He_N. In contrast to these results on alkyl iodides, experiments on Cr_2 dissociation showed no signs of ejected fragments, but rather the trapping of one ground state Cr atom in the droplet's interior, and one excited state Cr atom on the droplet's surface, despite a kinetic energy release of about 3200 cm^{-1} [119].

In contrast to dissociation, also pure photoexcitaoin of solvated species, especially for the case of Rydberg state excitation of atoms or molecules, has been found to lead to the ejection of the dopant from the droplet [29, 65, 66, 68–72]. The ejection is a consequence of strong repulsive interactions due to the extended electron density of excited states, which is also responsible for the pronounced blue-shift of in-droplet excitation. As this excess energy is not completely transferred to the dopants (see also results in Sec. 4.4), the acceleration proceeds somehow "softer", thereby enabling studies also in the transition regime of superfluid behavior around the cricital velocity. Photoexcitation dynamics of silver (Ag) atoms excited to the ^2P manifold have been thoroughly investigated in a combined experimental and theoretical study by the groups of M. Drabbels and M. Barranco, respectively [29, 71]. By applying velocity map imaging methods and TD-HeDFT simulations they found that silver, and experimentally also other molecules excited to Rydberg states, exhibit final velocities upon dopant ejection, which are very close to the value of the critical Landau velocity of 58 m/s (see Fig.2.6a). Detailed analysis of the simulations further gave indications that this limiting velocity is nearly independent of the dopant starting location, an indication for efficient deceleration above the Landau limit. At small velocities, no significant friction, similar to a "free particle" that adiabatically follows the excited state potential could be retrieved, as expected for superfluid behaviour.

The first translational motion that was studied directly in time-resolved experiments was the photoexcitation dynamics of alkali metals (Ak). Owing to their symmetric and extended electron density already in the electronic ground state, Ak atoms do not solvate into the droplet interior, but rather occupy locations directly at the droplet surface in dimple-like structuers. Very similar to the case of fully solvated atoms, Ak atoms are known to desorb from the droplet surface due to repulsive excited state interactions [73, 121–125], often accompanied by the formation of X*He molecules, termed exciplexes,

which are discussed in more detail in Sec. 2.4.5. Those experiments were conducted by F. Stienkemeier, M. Mudrich and coworkers in Freiburg, and employed time-resolved photoion spectroscopy. Based on the strong attractive interaction of cations with helium, the detection of photoions is however not only dependent on the neutral, but also the ionic species [25]. After pump excitation, the dopant might be ejected from the droplet, however, following probe ionization, it might be recaptured (also outside) by the attractive He environment, which hinders detection. The transient ion yield therefore shows a gradual increase, depending on the moment and the location of ionization (see Fig. 2.6b). For the case of Rb photoexcitation, also the transient velocities of the ionized species were recorded with imaging techniques, providing additional insight into the ejection process [25]. Depending on the blue shift of the in-droplet excitation band, the desorption process was distinguished between thermal (5p←5s, slow) and impulsive (6p←5s, fast) desorption. For the impulsive case, the surface location and the large blue-shift of the Rb 6p←5s transition results in a fast dynamic repulsion of the He surrounding, which was also sensed with TRPES [26].

Besides the surface bound Ak atoms, time-resolved ejection processes have also been measured for pure droplets, with observed ejection of not only He atoms [33, 35, 37, 126], but also He_2 molecules and larger clusters [34]. These experiments were carried out by the group of O. Gessner and D. Neumark in Berkeley, performing 3p/4p←1s excitation with high-harmonics, and in experiments at the free electron laser (FEL) FERMI in Trieste (Italy), applying direct 2p/2s←1s excitation [37]. Ejection in both experiments was found to proceed within a few hundred femtoseconds, and therefore considerably faster than for the surface-bound Ak atoms, probably due to the much lower masses of ejected He atoms (see also discussion in Sec. 4.4).

Within this thesis, time resolved experiments and simulations on the ejection dynamics of fully immersed In atoms have been performed, thereby filling the gap between static experiments on fully immersed species and time-resolved experiments on surface-located atoms. These investigations can be found in Secs. 4.3 and 4.4.

For the dynamics prior to ejection, the following facts were available at the start of this thesis: Before leading to propagation to the droplet surface, photoexcitations of dopants is believed to cause the expansion and oscillation of the so called He solvation bubble. Such bubbles are thought to enclose all atomic and molecular species in liquid He, even in their electronic ground state (see detailed descriptions e.g in the review article of A. Weis and P. Moroshkin [127]). The bubble formation is influenced by an interplay between the repulsive interactions of the valence electrons and the helium's surface tension. The dynamics of electron bubble formation has been investigated both experimentally by electron injection [128] and theoretically [129], and was found to proceed on picosecond time scales. Bubble formation dynamics after He_2^* photoexcitation could be measured in bulk liquid helium also in pump-probe experiments [130] employing LIF detection. By closely analysing not only the expansion, but also the following oscillation dynamics, the hydrodynamic models of superfluidity were tested and succesfullly applied also on microscopic scales. In synchrotron experiments, the formation and propagation of bubbles could be observed in He_N by analysing widths and shifts of fluorescence emission bands from He molecules [131]. Recently the formation of a bubble around He, either excited directly or through relaxation to the ^2S state, could be directly measured by applying TRPES after FEL excitation [37].

Within this thesis, the time-resolved bubble dynamics was measured for fully immersed atoms and molecules. By applying TRPES, the bubble was found to expand within a few hundred fs, and a bubble oscillation could be observed, superimposed to the ejection dynamics. These results are presented in Secs. 4.3, 4.4 and 4.7.

2.4.2 Electronic dynamics

The interaction of dopants with the surrounding He can lead, already in the case of atoms via the formation of atom*-He exciplexes, to the intersection and crossings of different electronic states, which can cause fast relaxation dynamics. The thereby liberated potential energy is dissipated to the helium, eventually leading to the detachment of He atoms from the droplet. There exist a variety of non-time resolved experiments that describe droplet-induced relaxation after dopant excitation, both for fully solvated species [59, 63, 65, 67, 69, 70, 72], and on the droplet surface [24, 125]. Relaxation was identified either via PE spectroscopy [24, 59, 69], or with resonance multiphoton ionization spectroscopy [65, 67, 70, 72]. For Al, time-resolved single photon counting experiments of the fluorescene yield gave an upper limit for the relaxation time scale of approximately 50 ps, based on the experimental resolution [63].
Direct electronic relaxation of photoexcited states has been observed for the case of pure droplet excitation [33]. In TRPES experiments of O. Gessner and co-workers, relaxation of excited He after in-droplet 3p/4p←1s excitation down to the 3d state has been found to proceed within about 200 fs, possibly enabled by the symmetry breaking during the atom's propagation through the asymmetric surface region. In a different experiment with changed probe-sensitivity (3 eV instead of 1.6 eV probe energy), further relaxation channels down to the 2^1P states could be identified [126]. Even this 2^1P signal however further decayed, which lead the authors to conclude that ultimately the 2^1S state of He is populated. This relaxation channel could indeed recently be confirmed in FEL experiments by direct 2^1P excitation [37], where the radiationless 2p→2s transition was found to proceed faster than the experimental resolution of a few fs. In this thesis, time-resolved experiments on highly excited electronic states of Al and In were performed, the results of which are presented in Sec. 4.5.
Electronic relaxation may also proceed between spin-orbit (SO) split states, which distinguish by the orientation of the electron's spin with respect to the orbital angular momentum. Combined electronic and SO relaxation has been found for fully solvated Cr atoms [70, 72], with additional relaxation also to the electronic ground state [72]. Isolated SO relaxation in an excited electronic state, on the other hand, has been found to proceed in fully solvated Ag atoms [69] and for Rb atoms on the droplet's surface [73]. For the case of Rb, the desorption of RbHe exciplexes within the normally bound $^2\Pi_{1/2}$ could be rationalized with the energy release through droplet-induced SO realxation following $^2\Pi_{3/2}$ excitation by applying TD-HeDFT simulations [28]. Surface located species in their electronic ground state, like Ak atoms [88, 97], or highly excited states, like Al atoms in quarted states [132], have been found to show no SO relaxation. During the work on this thesis it was surprisingly found that also for fully solvated In atoms the thermal population in the SO-split ground state does not decay on the time scale of the experiment, detailed descriptions are found in Sec. 4.2.

2.4.3 Vibrational dynamics

Vibrational and rotational relaxation dynamics of molecules in He_N have been extensively studied with infrared spectroscopy based on linewidth analysis [7]. The fact that narrow rovibrational lines can be measured in He_N, compared to significant broadenings in other solvents, were among the first hints that He_N can behave as a special spectroscopic matrix [5]. Both vibrational and rotational relaxation time scales are thereby thought to be strongly dependent on the involved energy scales of excited modes and their relative energy compared to the intrinsic droplet excitation spectrum. This spectrum was found to roughly follow the bulk superfluid density of states (compare with the dispersion relation of liquid He shown in Fig. 2.4d), with the so called phonon gap below 5 cm^{-1} and a high density of states up to approximately 10 cm^{-1} [101]. Homogeneously broadended rotational linewidths are therefore strongly dependent on the energy of the rotational mode [7]. Energies below 5 cm^{-1} can only couple to lower

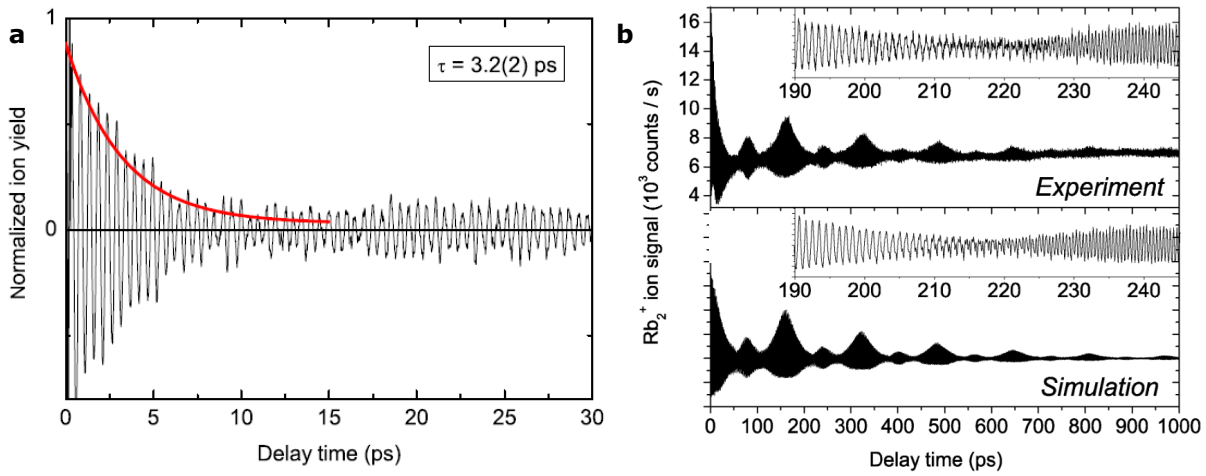

Figure 2.7: Vibrational WP dynamics of alkali metal dimers on the surface of He_N. Panel **a** (adapted from Ref. [19]) shows the WP dynamics of K_2 molecules, which were excited to the $A^1\Sigma_u^+$. Panel **b** (adapted from Ref. [23]) shows WP dynamics of Rb_2, excited to the $1^3\Sigma_g^+$

.

energetic surface modes (ripplons), therefore showing long lifetimes up to several ns, whereas rotational modes of higher energies can have lifetimes of only a few ps [133]. Detailed discussion on rotational dynamics and recent attempts to directly visualize those in pump-probe experiments are described in the next section.

Vibrational energies are an order of magnitude larger and their lifetimes have also been found to show great variation. As infrared spectroscopy experiments depend on the vibrational relaxation, causing a He depletion signal when being resonant (see Sec. 2.3.2), relaxation times are in most cases at least on the order of the experimental time scale (μs to ms). However, as the vibrational spacing increases, longer lifetimes might be present, again based on the strong mismatch to the He droplet modes, resulting in weak coupling. An extreme case was the observation that excited HF (with $\Delta\nu$ around 4000 cm^{-1}) does not relax at all on the flight time in the apparatus (0.5 ms) [55]. This situation however changes for the case of polyatomic molecules. The then present intermediate vibrational levels in other degrees of freedom cause vibrational relaxation to proceed in a cascading process, where the individual steps couple more strongly to the droplet modes [96].

Frequency-domain measurements have, despite high spectroscopic resolution, the disadvantage that claims about vibrational lifetimes or dynamic processes depend on the interpretation of homogeneous linewidths, which are often overshadowed by inhomogeneous broadenings resulting form droplet size effects [7]. Furthermore, lifetime statements only allow to make claims about vibrational relaxation times (comparable to the longitudinal relaxation time T_1 in NMR), and not about decoherent (elastic) interactions of vibrational states without relaxation ("transversal" relaxation time T_2). Both processes can be studied with the use of vibrational wave packets. For their basic concepts, the reader is referred to Sec. 2.1, to also recall the different sources of oscillation signal decays when observing WP motion in solvents, namely dispersion, decoherence, pure (elastic) decoherence, and dissipation. The first direct vibrational studies in time resolved experiments have been performed by F. Stienkemeier, M. Mudrich and coworkers on alkali molecules [19–23, 27] and on alkali-He exciplexes [134, 135] with photoion spectroscopy.

Vibrational wave packet dynamics were studied on Na_2 in its excited and ground triplet states, the latter being populated through coherent anti-stokes Raman scattering [20]. For both cases, the influence of the

He_N was found to be negligible, which was attributed to fast ejection in the excited state, and a weak ground state interaction of the surface bound molecule. Contrastingly, wave packet dynamics of K_2 in the excited $A^1\Sigma_u^+$ state were found to be subject to rather strong decoherence (see Fig. 2.7a), whereas ground state dynamics again revealed only a minor influence [19]. The wave packet oscillation within the excited $^1\Sigma_u^+$ state was found to be damped with a time scale of only 3.2 ps, which was later successfully simulated by applying a model that accounted for dissipative quantum dynamics in combination with desorption arguments [22]. Surprisingly, the dissipative effects could be incorporated based on a simple model that accounts for vibrational damping only above a certain vibrating velocity close to the critical Landau value. The authors claim that this result may be a direct visualization of superfluidity on the microscopic scale of single molecular motion. However it remains unclear, how this viewpoint of classical motion is connected to the picture from infrared spectroscopy, where relaxation depends on the molecule's mode-coupling to the elementary excitations of He. The vibrational spacing of around 70 cm^{-1} ($\sim$0.5 ps) would indeed lie in a region close to the elementary excitation spectrum, where fast relaxation could be expected.

Detailed studies have also been performed on the triplet state of Rb_2 [21], where only a very weak interaction was found, with damping rates on the order of 0.5 ns^{-1} and the observation of several wave packet revivals (see Fig. 2.7b). With a compared to K_2 different (dissipative) quantum mechanical approach, the damping could be rationalized to be mainly influenced by decoherent effects through vibrational relaxation [23]. Relaxation was found to proceed via a cascading-like process through the well resolved vibrational beats. Faster relaxation for higher levels was found, which was rationalized with the strong generation of heat at higher energies that cannot be dissipated away by the droplet, resulting in the breakdown of superfluidity due to a probable phase transition. It however remains unclear, why exactly dissipative effects on K_2 are that much stronger than on Rb_2, especially as the vibrational spacing for Rb_2 lies with around 35 cm^{-1} ($\sim$1 ps) even closer to the excitation spectrum for He_N. However, additional differences, like the different spin multiplicity, atomic mass, vibrational energy or solvation behaviour might also affect the decoherent properties. One explanation might involve different couplings of the molecules to the surrounding He dimple structure at the surface: Different solvation strengths would result in different dimple radii and oscillation frequencies of the Ak_2-He_n system (in analogy to the bubble oscillation of the fully immersed species). If the vibrational frequency of K_2-He_n would lie more closely to the K_2 vibrational energy, stronger dissipation should be expected.

Besides the vibrational studies on alkali dimers, also WP dynamics of homo- and heteronuclear trimers in quartet states were investigated [27, 136]. Transient photoion spectra were strongly influenced by fragmentation dynamics into both, trimer molecules, as well their subsequent fragmentation to dimers and monomers. However, superimposed vibrational dynamics could be extracted, enabling the assignment of the complex vibronic structure and giving decay times on the order of a few to several ten ps, and therefore identifying rather strong coupling to the He_N.

Apart from alkali molecules on the droplet surface, attempts have also been made to study vibrational dynamics of the fully immersed molecule LiI [137]. Whereas it was not surprising that the transient photoion yield showed no oscillation contrast due to the limiting detection probability from the droplet's interior, also photoelectrons gave no apparent signal. This disappointing result led the authors to conclude that coherent WP motion inside the droplets is dissipated very quickly, hindering femtosecond studies inside He_N for most molecular species.

Within this thesis, vibrational WP dynamics were studied for fully immersed In_2 molecules, showing rather pronounced oscillations and decoherence times of about 4 ps. These results, presented in Sec. 4.7, open up the important question, which parameters influence vibrational WP motion inside He_N.

Besides the experimental results, simulations on vibrational relaxation inside He_N have been performed

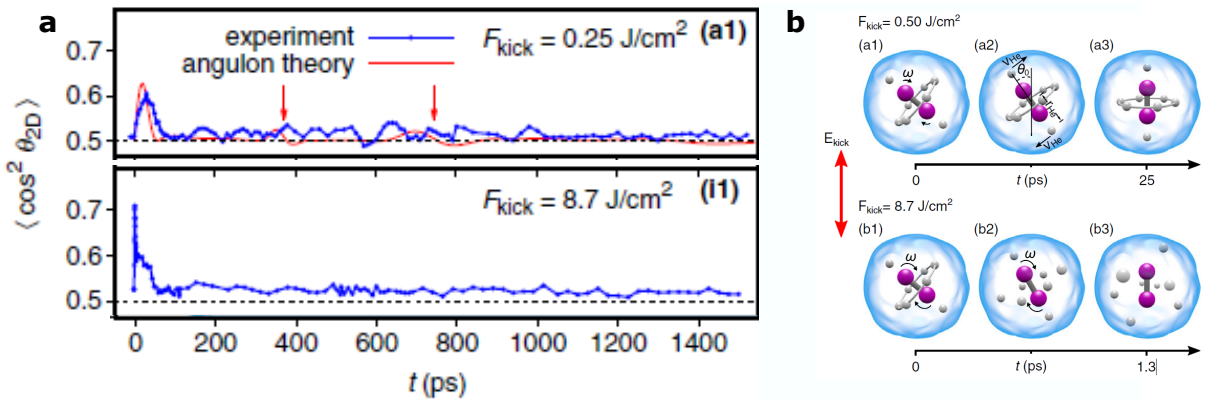

Figure 2.8: Rotational dynamics after impulsive alignment of I_2. Panel **a** shows the appearance of revivals when aligning with moderate laser intensity (upper plot) and the absence of revivals for larger intensities (lower plot). Panel **b** shows the I_2 molecule with the adiabatically following solvation layer for low intensities (upper images) and the temporary decoupling from the layer at larger intensities (lower images).

only recently by the group of M. Gonzàles for ground state vibrational excitation in I_2 [138] by applying a hybrid density functional approach. It was found that relaxation proceeds on a cascading like process on nanosecond time scales, with larger relaxation rates for higher vibrational levels, in agreement to the results obtained for Rb_2 [23].

2.4.4 Rotational dynamics

The observation of sharp rotational lines of molecules inside He_N shows that they can rotate with very little perturbation [5]. Futhermore it has been shown, that in the case of ^{3}He droplets, the rotational motion is significantly quenched, assigning the low influence on rotation in ^{4}He droplets to their superfluid nature [102]. Generally, different rotational behaviour is found for light and heavy molecules. At this point the rotational energies for a linear molecule are recalled:

$$E_{\mathrm{rot}} = Bj(j+1), \quad \text{with} \quad B = h^2/8\pi^2 I, \tag{2.19}$$

where B is the rotational constant, j the rotational quantum number and I the moment of inertia. Light molecules inside He_N have been found to exhibit rotational constants very similar to their free counterpart, which was interpreted as unperturbed rotation within the droplet, decoupled from the He bath. Heavy molecules, on the other hand, were found to exhibit significantly reduced rotational constants, owing to much larger moments of inertia compared to the gas phase. The correspondingly increased mass of the rotor is explained with the first He solvation shell, which is thought to be dragged along the rotating molecule (adiabatic following), and is decoupled from the rest of the superfluid droplet.
Recently, the group of H. Stapelfeldt in Arrhus has started to investigate rotational dynamics also in the temporal regime [38–40, 42–44, 139–142]. By using moderately intense laser pulses, molecules could be sharply aligned in the laboratory frame, set by the laser pulse polarization. Coulomb explosion of the molecules with a second, intense laser pulse combined with coincidence imaging of the ionized fragments then allows to analyse the degree of alignment with respect to the laser polarization axis. Alignment could be reached via impulsive stimulation through short laser pulses (450 fs) [38], as well as in the adiabatic and the near-adiabatic regime, with ns and ps pulse durations, respectively [39, 40]. By applying correction algorithms that incorporate possible He_N influences on the ion trajectories, it was shown that for the case

of near-adiabatic alignment, the degree of alignment is improved compared to seeded beam experiments, which was attributed to the lower rotational temperature of 0.4 K inside the droplet [40]. By using elliptically polarized light, even 3D-alignment inside He_N could be achieved, again with higher degrees of alignment than in the gas phase [42]. Recently, the same group has also succeeded in aligning molecules inside He_N under field-free conditions [44]. By truncating the linearly chirped alignment pulse in time with a high quality longpass filter, the alignment pulse could be switched off within about 10 ps, and high degrees of alignment were retained for several 10 ps. This temporal window should be sufficiently long to be able to study photoinduced processes on aligned molecules under field-free conditions, with the possibility to directly observe not only structural, but also bimolecular reactions. The effect of long lasting alignment could however neither be explained with the reduced temperature of He_N, nor with increased moments of inertia, and was therefore rationalised with an additional impeding effect of the helium surrounding on the molecular rotation. Closely related to this effect is also the question how coherent rotational dynamics in general is influenced inside He_N, which was also recently investigated by analysing the transient degree of alignment.

In free molecules, which are exposed to moderately intense laser pulses that are shorter than the rotational periods (several ps), so called rotational wave packets are generated, in close analogy to the vibrational wave packets discussed in Sec. 2.1. Owing to strong dispersive effects, the rotational signal then decreases shortly after laser interaction, but is periodically retained at later times in WP revivals. Due to the known sharp rotational linewidths inside He_N, it was expected that such coherent signals might also be measureable in the quantum solvent. First attempts to observe rotational WPs with CH_3I and other molecules were however only partly successful [38]. The measurements showed that maximum alignments were reached several ten ps after the kick-pulse, which is significantly later than what would be expected solely from increased moments of inertia. However, no hints on revival structures could be found. Whereas this effect might be explainable with strong pure (elastic) decoherence, leading to irreversible losses of phase information, the slow rotational dynamics after the alignment pulse is harder to explain. The authors speculated that He_N related influences (transfer of angular momentum, collective He modes) during the alignment process of the kick pulse may play a role. Subsequent experiments on I_2 inside He_N showed the same slow alignment process, and at low enough laser fluences indeed also rotational revivals could be identified (see Fig. 2.8), which occurrence could also be explained theoretically by applying a quasiparticle model [139]. At higher laser intensities the initial alignment was reached much faster, and the rotational revivals disappeared (Fig. 2.8). This effect was explained with a decoupling of the molecular motion from its co-rotating solvation shell due to the large angular velocity. Despite a following re-arrangement of the solvation structure, all coherent properties of the rotational degrees of freedom were lost, explaining the absence of revivals. Similar rotational recurrences could also be found in the case of near-adiabatic alignment with a much longer laser pulse, which was explained by the truncating form of the pulse, leading to very similar initial conditions as for the (impulsive) short pulse alignment [43].

A recent theoretical study by the group of M. Gonzáles on rotational relaxation of H_2 isotopes inside He_N revealed relaxation times on the nanosecond time scale [143]. Surprisingly, lifetimes were found to increase for lighter molecules (increased rotational energies due to lower moments of inertia). This result seems to be at odds with the general consensus in frequency domain spectroscopy, that reduced linewidths are found for lower rotational energies [7], rationalised with the phonon gap in the excitation spectrum of liquid He.

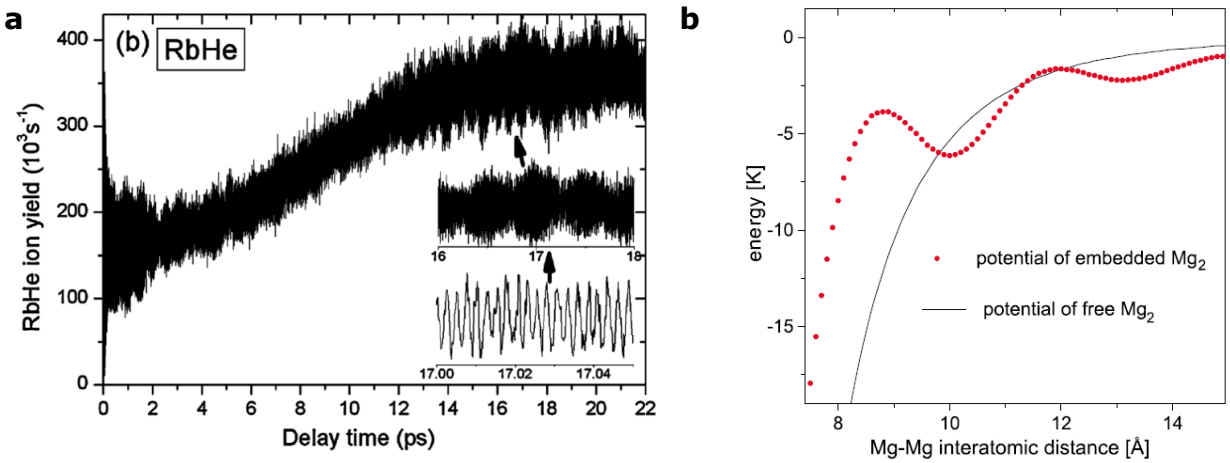

Figure 2.9: Examples for photoinduced molecular reactions inside He_N. Panel **a** shows WP signals of Rb^*He, which are modulated not only by the electronic (fast modulatin), but also vibrational coherence (slow modulation), the figure was adapted from Ref. [135]. Panel **b** shows the Mg-Mg interaction potential, compared for the free Mg_2 and for Mg_2 immersed in the droplet. The latter potential exhibits local minima, that may be overcome after Mg photoexcitation, resulting in the formation of Mg molecules (figure taken from Ref. [64].)

2.4.5 Chemical reactions

A strong motivation for ultrafast studies inside He_N comes from the prospect to study and directly control photochemical reactions by making use of the special confinement character of the quantum fluid. Envisaged photochemical reactions, meaning excited state dynamics affecting chemical bonds, include e.g. photoassociation (which is difficult in gas phase), photoisomerizaion, radiationless decay, electron or proton transfer processes, or photodissociation. Inside He_N, there exist only a few examples that have been studied, mostly including either photoassociation or photodissocation.

One of the first demonstrations of photoinduced molecule formation was the observation of excited alkali metal atom (Ak)-helium complexes (exciplexes). The formation process is triggered by photoexcitation of the Ak atom to an, in general, repulsive excited state, leading to a fast rearrangement of the solvation layer. However, owing to weak attractive interactions to He, the formation of a Ak*He complex may be triggered simultaneously. First time-resolved experiments based on time-correlated single photon couting revealed formation times on the order of a few ten ps for the case of K*He and Na*He [121, 144]. In the group of F. Stienkemeier, also several pump-probe studies on exciplex formation were performed, applying photoion spectroscopy [17, 18, 134, 135], and recently also TRPES in combination with TD-HeDFT simulations by the Barranco group [28]. For the case of Rb^*He excited to the $^2\Pi_{3/2}$ state, formation times of around 8 ps could be measured [18]. Surprisingly, not only electronic, but also vibrational coherences (see Sec. 2.4.3) were measured in Rb^*He with high contrast [134, 135] (see Fig. 2.9a), and could be assigned to vibrational levels in the middle of the Rb^*He excited state potential. Apparently, vibrational coherence is initiated during the molecule formation process, opening the prospect to not only initiate a photochemical association inside He_N, but also coherently control it. Vibrational relaxation was found to proceed for rather long time scales (>1 ns), suggesting that a significant fraction of exciplexes remains bound to the droplet [134]. This result contrasts with previous assumptions, which indicated a faster desorption [135], only recently combined experimental and theoretical studies could show that spin-orbit relaxation, and the thereby released energy, may play a role to the desorption process [28].

Apart from the exciplex dynamics, no time-resolved studies on direct molecule formation have been

performed up to now, especially not between heteronuclear species. However, there exist examples where such reactions have been described in the frequency domain: An intriguing property of He_N, up to now however not fully understood, is the ability to spatially separate different dopants. The most prominent example for such a system discussed in literature is the case of several Mg atoms inside the droplet [64, 145]. Multiple Mg are believed to not coagulate into clusters, but rather form metastable, foam-like structures, with He density in between that acts as a separating barrier (see Fig. 2.9b). The first indication for this special behaviour of Mg was drawn from a shifted excitation band at the low energy side of the $MgHe_N$ resonance, which is present up to high doping rates. Photoexcitation at this presumed Mg-foam resonance then results in the previously mentioned rearrangement of the solvation shell structure, driving the foam to collapse and form a Mg cluster [64]. This reaction could also be triggered and temporally resolved after non-resonant ionization [46], and was recently identified and characterized with PE spectroscopy [61].
Apart from forming a metastable network well inside the droplets, different atoms might also occupy configurations where one (heliophilic) dopant immerses into the droplet center, and another (heliophobic) dopant resides at the surface. Such a system was suggested to exist for different alkali species [146], and was recently also demonstrated for the case of Rb and Sr bound to He_N [147]. Following Sr excitation, not only Sr^+, but also $SrRb^+$ and Rb^+ mass signals could be detected, hinting at photoinduced bond formation, and also Sr excited state energy transfer to a potentially separated Rb atom. The proposed model is that Sr resides in the droplet interior, and moves to the droplet surface upon photoexcitation, a process that has been suggested also in the context of bubble formation and propagation [131], and eventually reacts with the surface-residing Rb atom. A similar process has been proposed to proceed following Cr_2 excitation, where spectral signatures indicated dissociation into a surface bound and a fully immersed Cr atom, which recombine again after subsequent photoexcitation [119].
Besides bond formation, also photoinduced dissociation has been investigated within He_N, however, experimentally never with time resolution, and focusing mostly on the translational dynamics of the photofragments [113] (see Sec. 2.4.1). It was shown that following fragmentation of CH_3I, the products of I and CH_3 can recombine, completely dissipating their translational energy and resulting in full He droplet evaporation, which ultimately enables ion detection [116]. As such an effect couldn't be measured with the heavier dissociating CF_3I molecules, the mass difference of the two photofragments was attributed to be the determining factor for recombination. This picture could recently be also confirmed in time-resolved hybrid DFT simulations, where it was found that lighter species tend to recombine with much higher probability [118].
Within this thesis, a fragmentation reaction of In_2^+ could be identified, which is assumed to be initiated after a subsequent excitation of the ionized dimer with an additional probe photon. The liberated dissociation energy enables the ion product to escape from the droplet, despite the strong attractive ion interaction. These results are presented in Sec. 4.8.

2.4.6 Ultrafast dynamics involving charged particles

Up to here, only dynamics within neutral droplets or on neutral dopants have been discussed, as the aim of this thesis was to characterize the He_N's ability to serve as cold container for femtochemistry studies, which involve mainly neutral state dynamics. However, there exist various examples for dynamics inside He_N involving charged dopants, e.g. electrons, ions or ionized clusters. The main difference involving such species is the much more pronounced influence on the He solvent. Whereas neutral ground state dopants are hardly influenced at all, exemplified by the sharp rotational and vibrational linewidths, the influence is stronger in the excited state (see above), and very significant in the ionic state. The dipole

dominated interactions of the neutral are then overcome by stronger interactions with ionic contributions, leading for example to the solidification of He atoms around cations (snowball formation) [148–150]. Investigated processes on charged systems involve the ignition of nanoplasmas on doped droplets after intense laser pulse interaction [47, 48, 151, 152], Penning ionization of dopants after droplet excitation [153, 154], interatomic Coulombic decay [104, 155, 156], or collective autoionization dynamics [157, 158]. As ultrafast processes involving such charged systems are beyond the scope of this review section, the reader is referred to the cited literature and corresponding review articles [6, 36, 159].

CHAPTER 3

Experimental setup

Experiments within this thesis were all conducted in FemtoLab I at the Institute of Experimental Physics, TU Graz. The setup consists of three main parts: the optical setup, the photoelectron/photoion/PEPICO spectrometer and the helium droplet machine with the He_N source and the pickup chamber. In the following, all three components are shortly described, more informations regarding the spectrometer can be found in the master's thesis of Markus Bainschab [160], the droplet apparatus is described in more detail in the PhD thesis of Markus Koch [89] and in the master's thesis of Sascha Ranftl [161].

3.1 Optical setup

The complete optical setup as arranged in the laboratory is shown in Fig. 3.1. Femtosecond laser pulses are retrieved from a commercial, amplified Ti:sapphire laser system, consisting of a Coherent Vitara Oscillator and a Legend Elite Duo Amplifier. Laser pulses with a center wavelength of 800 nm and approximately 25 fs pulse length are delivered with 3000 Hz at an average pulse energy of 4-4.5 mJ. Right after the laser exit, the pulses are split in a pump- and probe path with beam splitter 1 (BS1) at a ratio of 80:20, respectively.
Pump pulses (80% reflected at BS1) are guided into an Optical Parametric Amplifier (OPA, Light Conversion OPerA Solo) and are frequency tuned to the desired wavelength, which within this thesis lay mostly in the range between 250 and 400 nm. A detailed discussion of the OPA's different modes of operation is found in the respective manual and in the masters's thesis of Stefan Cesnik [162]. After the OPA, pump pulses are guided into a prism compressor with variable prism positions in order to adjust possible frequency chirps. The compressor can be bypassed when more pulse energy is needed (and time resolution is not critical), as approximately 50% of pulse energy is lost due to multiple reflections. Pulse energies can be further reduced in a continuous way by an ultra broadband wire grid polarizer (Thorlabs WP25M-UB).
Probe pulses (20% transmitted at BS1) are guided over the whole optical table in order to compensate for the long pump beam path inside the OPA, a delay stage (Delay Stage 1) is used for rough time delay compensation. Probe pulse energies can be adjusted with a $\lambda/2$ plate (Thorlabs AHWP10M-980) in combination with a 2-stage thin film polarizer (Laser Components TFPK-800 RW50-27-3UV). An optional

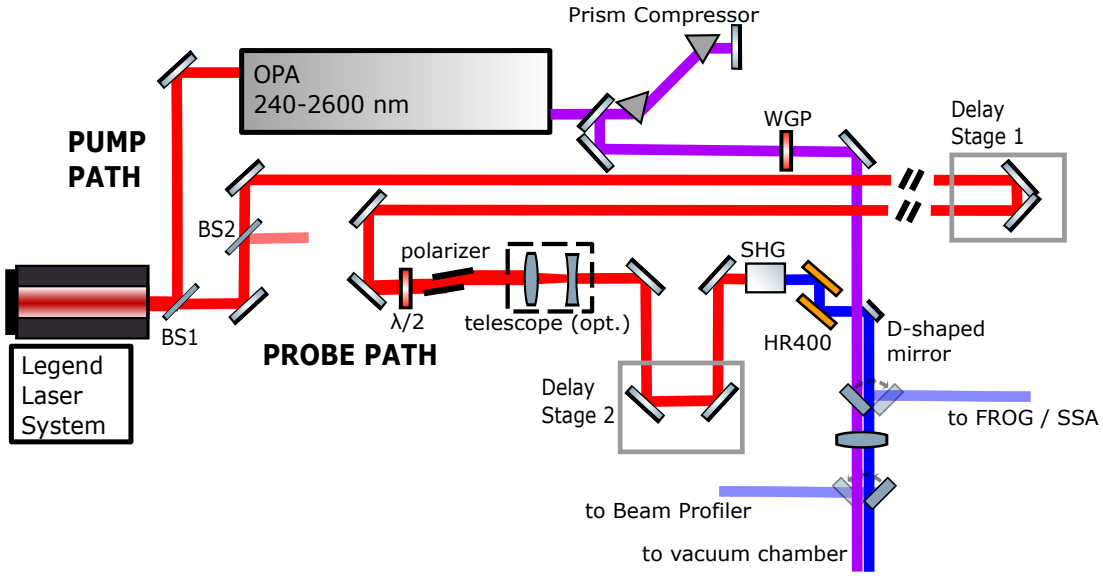

Figure 3.1: Schematic of the optical setup used for experiments within this thesis. Laser pulses are split in a pump and a probe-path with variable delay. Pump pulses are frequency tuned in an Optical Parametric Amplifier (OPA), probe pulses are frequency doubled (Second Harmonic Generation, SHG). Both pulses are focused into the measurement chamber and are spatially and temporally overlapped in the focal region. BS...beam splitter, OPA...optical parametric amplifier, WGP...wire grid polarizer, SHG...second harmonic generation, HR...high reflective, SSA...single shot autocorrelator, FROG...frequency resolved optical gating.

lens telescope can be used to reduce the pulse beam diameters for higher conversion efficiency and to change the probe beam divergence to cover larger photoionization volumes. After passing a motorized delay stage (Newport M-443-4), the probe beam is frequency doubled, separated from the fundamental with low GDD mirrors (Altechna 1-OS-2-0254-5) and overlaid with the pump beam with a D-shaped aluminium mirror (Thorlabs PFD10-03-F01).

3.2 Molecular beam setup

A complete overview of the vacuum apparatus can be seen in Fig. 3.2. It consists of three separated ultra-high vacuum (UHV) parts, which are connected with UHV valves and can therefore be vented separately: The helium droplet source chamber, the pickup chamber together with the differential pumping stage (DPS), and the main chamber with the time-of-flight (TOF) spectrometer.

3.2.1 Helium droplet beam generation and dopant pickup

The droplet source consists of a high vacuum chamber, which is pumped by a turbopump (Pfeiffer, ATM 2900M) at 2800 l/min. The chamber is connected to a cold head, which operates at a 2-stage-compression procedure (Gifford-McMahon process) and cools down to approximately 10 K. For precise temperature control, a resistive heater in combination with a diode enables temperature regulation between 10 and 35 K (PID feedback control). High purity (99.9999 %) He gas is cooled to the cold head temperature and is expanded through a 5 μm nozzle under high pressure (typically 40 bar). Upon this supersonic expansion, the helium liquefies and droplets are formed. After passing a 300 μm skimmer, the He_N enter the pickup chamber, where metal atoms are picked up by resistively heated ovens, whereas molecules are pickup up by crossing an effusive beam at right angles (see Sec. 3.2.3). In the pickup chamber, two

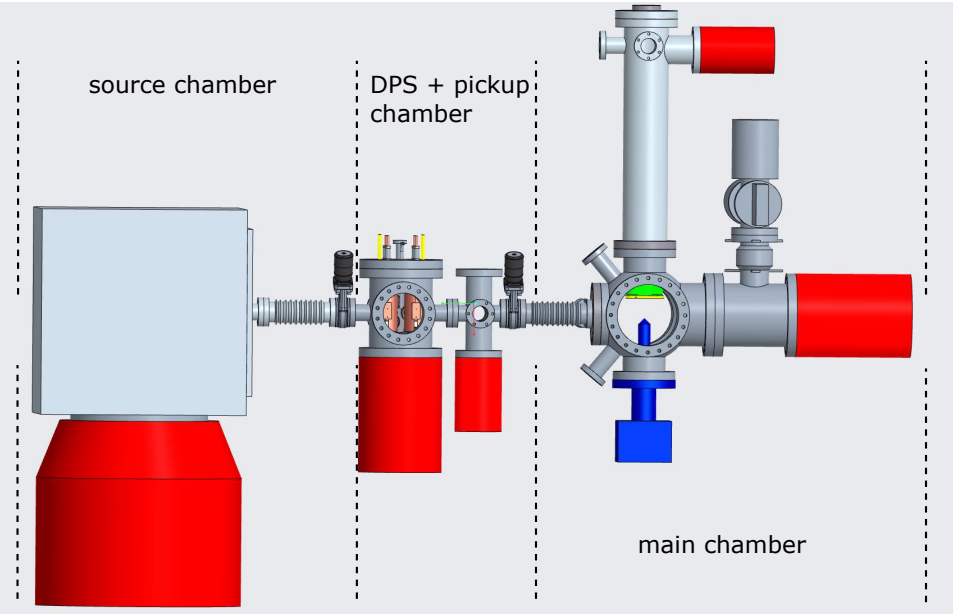

Figure 3.2: Schematic overview of the droplet beam apparatus, which can be grouped into three main components: the source chamber, where the He_N are generated, the pickup chamber together with the differential pumping stage (DPS), and the main chamber.

separate metal ovens can be used, both of which are surrounded by cooling shields (see Fig. 3.3). Before entering the main chamber, the droplets pass a differential pumping stage (DPS), which is separated from the neighbouring chambers by 5 mm diameter holes.

3.2.2 Time of Flight Spectrometer

Doped droplets enter the main chamber, where two spectrometers are located. Downstream of the droplet beam, a quadrupole mass spectrometer (Balzers Instruments, QMG 422 Quadstar 422) is used to analyze doping concentrations and to align the He source. At right angles to the droplet beam, a linear time of flight (TOF) spectrometer is used for the detection of photoelectron (PE) and photoions (PI) after laser ionization. For the detection of PE kinetic energies, the TOF is operated in a magnetic bottle type configuration, consisting of a strong permanent magnet below the ionization region, and a magentic field induced by a coil around the flight tube. Due to the magnetic gradients, a collection efficiency of nearly 100 % for the PE can be reached. A small repeller voltage (on top of the magnet) can be applied to optimize the kinetic energy resolution. PI are pushed into the flight tube with a strong positive voltage (typically 2 kV) on the repeller. Charged particles hit a Micro-Channel Plate (MCP) detector (Chevron type, Photonis), hits are decoupled behind the MCP-back on a phosphor scree, which has an additional positive potential of 500 V. Voltage pulses are amplified and analysed either with a counter (Stanford SR400) or with a fast digitizer card (Cobra Gage CBE-022-000). The flight times are then evaluated on the computer and translated into kinetic energies in the case of PE and into charge-to-mass ratios in the case of PI.

3.2.3 Gas pickup cell

For the study of room temperature gaseous species, which cannot be picked up like metals in tungsten ovens, a more sophisticated pickup cell is needed. The main requirement, especially for femtosecond

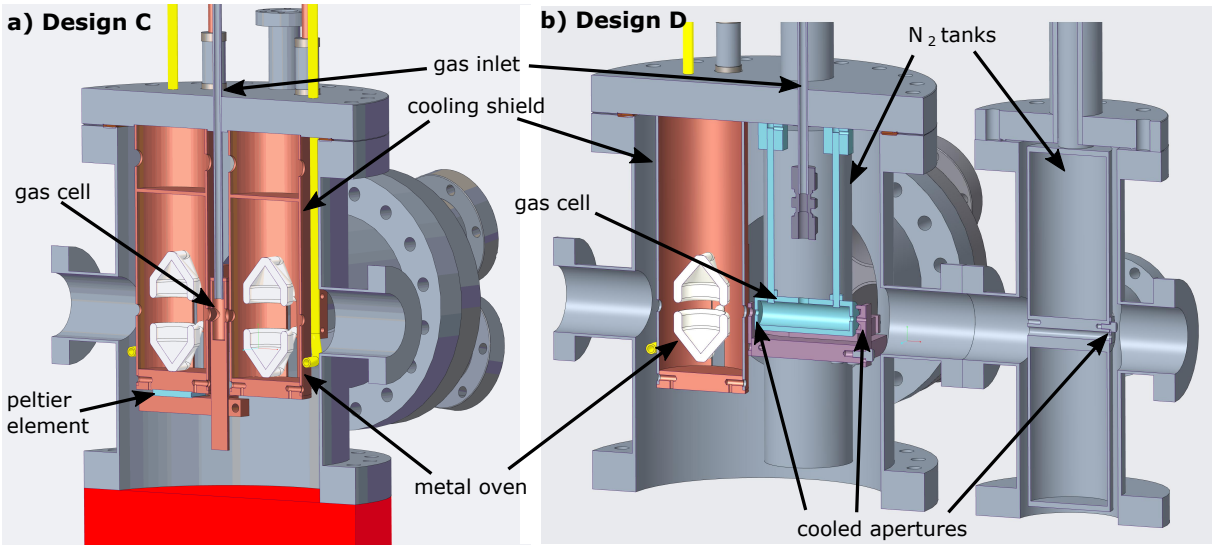

Figure 3.3: Drawing of the two tested variants of a gas pickup cell, implemented in the existing pickup chamber of the He_N apparatus. Panel **a** shows the version with a small pickup cell that is cooled by Peltier cooling. Panel **b** shows the version with apertures before and after the pickup cell (see close-up view in Fig. 3.4), as well as in the DPS, which are cooled with liquid nitrogen.

studies, is to achieve a low background stemming from effusive species that drift into the measurement region. For metals like In, this effect poses no problem because In rapidly condensates at the cool parts inside the cell and the vapour pressure in the chamber is therefore low. Further, the excitation bands of metals are often significantly shifted inside He_N, reducing the background from bare atom pump pulse excitation. These conditions change for gaseous molecules. Higher vapour pressures at room temperature as well as inherently broadened molecular bands with lesser shifts in He_N may contribute to a significant effusive background. Several designs of a gas pickup cell were constructed and tested during the work on this thesis, which are briefly described in the following. Designs A-C were tested to be implemented in the existing pickup chamber. The motivation was that by keeping the geometry simple and working with the existing pickup design, time can be saved and full flexibility while switching between experiments is obtained.

Design A: Slit cell with peltier cooling

In a first design, a configuration very similar to the metal ovens (however with steel crucibles) was tested, with a slit-formed opening parallel to the He_N beam to achieve maximum pickup. Both the lower and the upper container were cooled with Peltier elements down to a few °C. The hot side of the Peltier elements was attached to the cooling shield. Unfortunately with this design, no significant pickup signals could be achieved, as only high vapour pressure gases were tried, which vaporized too quickly through the slit opening. In future the cell might still be useful when working with low vapour pressure gases, which have to be heated similarly to the metals in the tungsten ovens.

Design B: Cross beam pickup

To better control the pickup conditions, an external gas supply via a dosing valve is used for all other designs, which enables the controlled introduction also of high vapour pressure gases. In a first try, direct cross beam pickup was implemented, meaning that the gas is "blown" directly onto the He_N beam from above, by guiding it through an inlet pipe with 4 mm inner diameter. The non picked-up gas

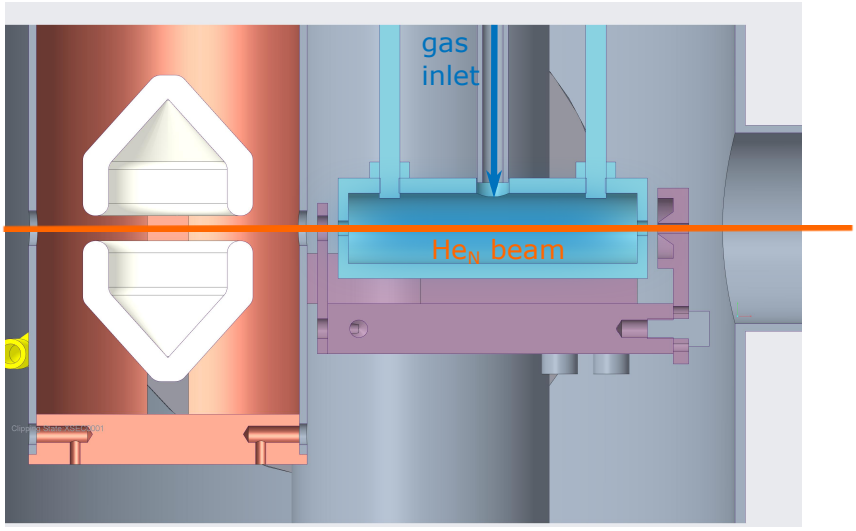

Figure 3.4: Close up of the gas cell geometry of Design D, with nitrogen cooled apertures in front and behind.

was thought to directly flow into the turbomolecular pump at the bottom, possibly reducing effusive backgrounds stemming from a full gas redistribution in the chamber. Unfortunately this was not the case. When testing the pickup contrast with the QMS downstream of the beam with the molecule dithiane, approximate ratios of 50% (meaning the ratio of picked up to the sum of picked up plus effusive molecules) could be measured. However, such a contrast could never be achieved with laser ionization for various molecules (argon, acetone, methanol or dithiane), contrasts here lay only in the range of 10-15%. The exact cause of this difference to the QMS contrast is not known, one factor might be broadened or shifted excitation bands within the droplet, out of which only a small fraction is excited/ionized with the laser bandwidth. As during a pump-probe measurement, not only the effusive contribution has to be subtracted, but also the pump-only and probe-only contributions from the picked up signal, these low contrast values gave spectra with very low signal/noise ratios. Also automatized long term measurements by using an electronically driven valve between source and pickup chamber (see Appendix B) gave not the desired stability, possibly due to unavoidable long-term drifts in the measurements.

Design C: Stylus cell with peltier cooling

As next design, the setup shown in Fig. 3.3a was tried, which includes a pickup cell in between the two cooling shields. The gas from the inlet pipe is guided into a small gas cell drilled inside a copper stylus, with 8 mm holes in direction of the He_N beam and a connection to a peltier element on the bottom. This cell is then cooled down to a few °C in order to prevent gas diffusion from the cell into the whole PU chamber. Also with this setup, the achieved contrasts lay in the range of only 50% (measured with QMS), comparable to Design B. For these designs we therefore concluded that the pickup chamber might be completely flooded with the gas and sufficient contrast is impossible. That this is not unlikely can also be estimated when assuming that the mean number of picked up molecules $\bar{k}$ can be estimated with

$$\bar{k} = \sigma \rho L \tag{3.1}$$

where σ is the capture cross section that can be approximated with $0.15 \cdot N^{2/3}\text{nm}^2$ [9], N is the droplet size (8000 assumed), ρ the number density of molecules (at $1{\cdot}10^{-5}$ mbar for dithiane) and L is the length of the pickup region (approx. 0.4 m in our case, assuming full distribution of molecules in the pickup

chamber). The retrieved value of $\bar{k} = 6$ is reasonable, as the measured pressure might be offset due to a wrong (Penning) gauge calibration. We therefore omitted the possibility of a gas cell inside the existing setup and started the construction of a completely new design.

Design D: Gas cell with liquid nitrogen-cooled traps

The newest design is shown in Fig. 3.3b. It consists of a new top flange for the pickup chamber, which has one standard metal oven pickup cell, with the addition of a longer gas cell downstream of the droplet beam, with 56 mm length, 14 mm inner diameter and 3 mm holes (see detailed drawing in Fig. 3.4). Gas is introduced through the same tubes as for the other designs, however a flexible tube is connected to the cell to facilitate beam alignment. Next to the cell, a liquid nitrogen tank is contained inside the chamber, which cools 2 mm apertures in front and behind the gas cell in order to immediately capture and freeze effusive gas diffusing out of the cell. The exit aperture is constructed in a conical geometry for optimal effusive capture (Fig. 3.4). A second tank with a 2 mm diameter trapping aperture is contained inside the DPS chamber. Both tanks will be filled from the outside with liquid nitrogen by using a funnel and a long tube, in order to fill the tank from the bottom upwards, while still being able to let vaporizing nitrogen escape. This cell setup is currently being built during the writing of this thesis, and its full characterization and implementation will be the topic of following master or PhD students.

CHAPTER 4

Results

4.1 Outline

The following chapter groups the results obtained during the work of this thesis in sections arranged according to their thematic results. Sections 4.2, 4.3, 4.4, 4.6 and 4.7 consist of already published or submitted publications, sections 4.5 and 4.8 contain results currently under discussion, of which the latest status is summarized. As the different publications also always tell a story on their own, this outline is thought to draw connections between them. The following chapter (Ch. 5) then gives an overall outlook, mentions open questions and relates the presented results to the formulated key research questions of chapter 1.

To probe the potentials and limitations of He_N for ultrafast studies on fully solvated species, we chose a bottom-up approach: By investigating the simplest systems possible, namely single atoms and diatomic molecules, the dynamics induced in the droplet upon photoexcitation can be isolated and investigated. As element of choice we chose the metal indium (In), as it represents a single valence electron system and exhibits several beneficial properties, summarized in table 4.1, that make it the ideal test system for ultrafast studies.

4.1.1 Ultrafast photoinduced dynamics of atoms in helium nanodroplets

In-He_N excitation spectrum and spin-orbit relaxation dynamics

As first experiments, we recorded the in-droplet excitation spectra of In and In_2; detailed descriptions of these measuremens are also found in the master's thesis of Sascha Ranftl [161]. Because dopant pickup in He_N resembles a statistical process, also In_2 and larger oligomers are formed. When recording the excitation spectrum, we were able to detect In and In_2, as both excitation bands lie within the same spectral region. However, no signatures for In_3 or larger clusters could be found. Fig. 4.1 shows the recorded spectra, together with indicated blue-shifts to the assigned bare atom/molecule transitions. For the In atom, a broad excitation band was found around 27,000 cm^{-1}, resembling the in-droplet $^2S_{1/2} \leftarrow {}^2P_{1/2}$ transition. However, also a second, much weaker band was found around 25,500 cm^{-1}, the assignment of which was quite puzzling at the beginning and could eventually be achieved by comparing

Table 4.1: Important phyiscal properties of indium, atomic data were taken from Ref. [163]

property	**value**		**important attributes for studies in HeN**
mass	114.81	u	
density	7.31	g/cm^3	
melting point	430	K	
vapour pressure (1000 K)	$1.27{\cdot}10^{-4}$	mbar	only moderate heating necessary
ionization potential	5.786	eV	2-photon ionization with visible / NUV light
electronic states	$5^2P_{1/2}$		ground state
	$5^2P_{3/2}$		2,213 cm^{-1} / 0.274 eV
	$6^2S_{1/2}$		24,373 cm^{-1} / 3.022 eV
			(symmetry simplifies simulations, accessible with NUV)
	$6^2P_{1/2}$		31,816 cm^{-1} / 3.945 eV
	$6^2P_{3/2}$		32,115 cm^{-1} / 3.982 eV
	$5^2D_{3/2}$		32,892 cm^{-1} / 4.078 eV
	$5^2D_{5/2}$		32,916 cm^{-1} / 4.081 eV
			(all accessible with NUV / MUV)

the experiments with theory calculations performed by R. Meyer from the in-house theory group of A. W. Hauser. This band resembles unrelaxed population in the spin-orbit split $^2P_{3/2}$ state, which lies approximately 2,200 cm^{-1} above the $^2P_{1/2}$ ground state, and is weakly populated at the chosen pickup temperatures of around 900 K, assuming Boltzmann distribution. This observation that spin-orbit split states seem to not relax after pickup, but rather stay populated inside He$_N$, was published as Ref. [98], which is included in this thesis as section 4.2. Photoexcitation bands of In$_2$ are discussed in Sec. 4.1.2.

Femtosecond photoexcitation dynamics of single atoms

For further experiments on In-He$_N$, excitation at the $^2S_{1/2} \leftarrow {}^2P_{1/2}$ band was chosen. Atoms and molecules in He$_N$ reside in enclosed bubbles inside the droplet (see Fig. 4.2a, ground state minimum). Photoexcitation to a repulsive excited state results in the expansion of this bubble, causing a fast relaxation of the excited state within a few hundred femtoseconds, which is measured as transient PE peak shift to lower energies (Fig. 4.2b). During this dynamics, most of the excess energy introduced through the blue-shifted in-droplet excitation is consumed by the droplet and converted into He kinetic energy of density waves. Following the fast dynamics, residual repulsive interactions cause the dopant to be ejected from the droplet. This ejection is measured as ongoing PE energy decrease within about 60 ps down to the bare atom value (Fig. 4.2d), as the ionization potential inside the droplets is lowered. The

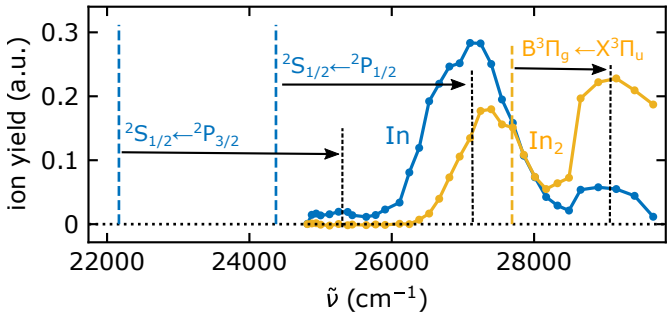

Figure 4.1: Excitation spectra of In monomers (blue) and In$_2$ molecules (yellow) within He$_N$ and their respective spectral shifts to the assigned bare atom / molecule transitions, respectively.

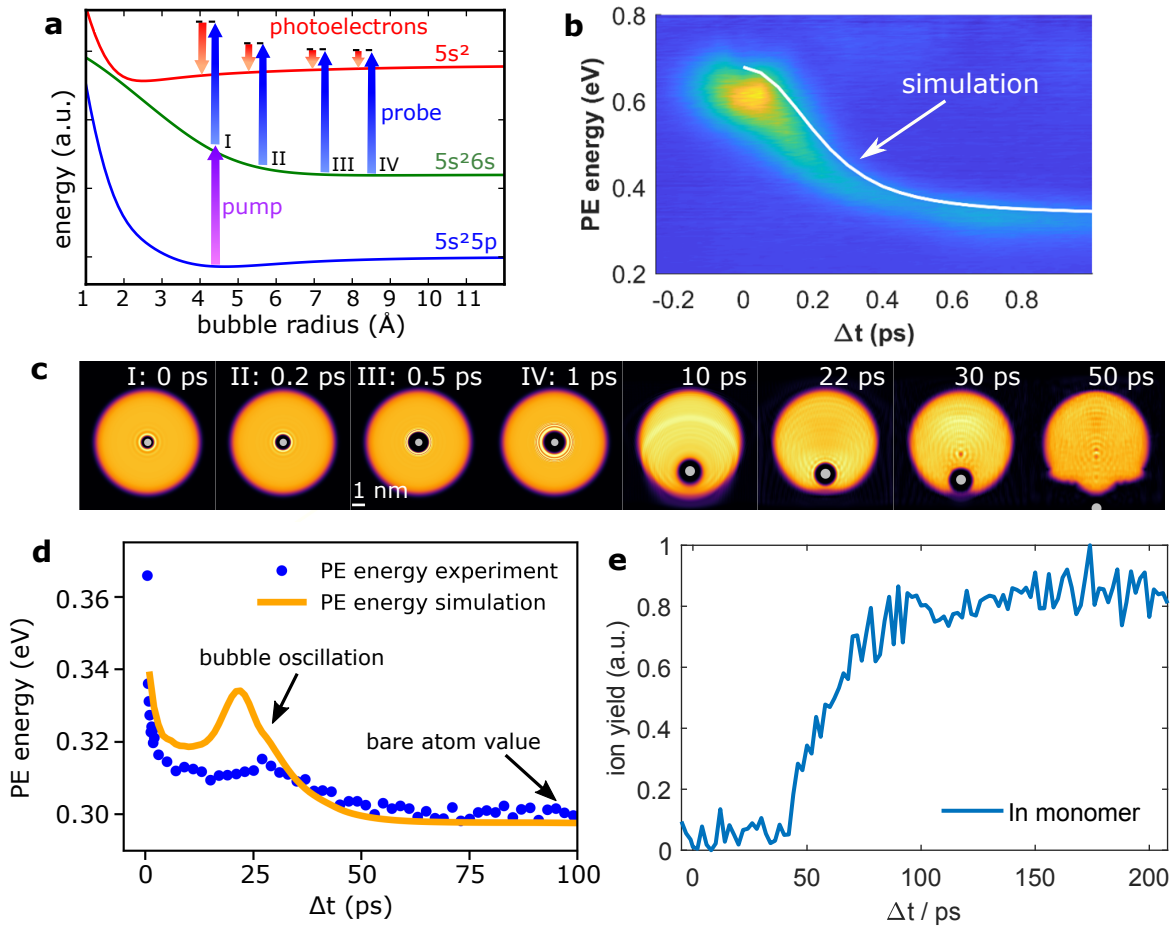

Figure 4.2: Overview of In $6^2S_{1/2} \leftarrow 5^2P_{1/2}$ excitation dynamics in He_N. Panel **a** shows a schematic of the In-He_N potential energy surfaces, pump and probe photon energies as well as PE energies are depicted with arrows for various steps during the bubble expansion. Panel **b** shows the transient PE energy shift, as consequence of the bubble expansion; the simulated shift, obtained with TD-HeDFT, is indicated as white line. He density plots of In-He_N for several time delays, obtained from the simulations, are shown in panel **c**. Panel **d** shows the transient PE energy for higher time delays, with the temporary energy increase around 30 ps as consequence of the bubble oscillation. Panel **e** shows the transient In^+ yield.

PE energy decrease is accompanied by a slight temporary increase around 30 ps, caused by a bubble contraction/oscillation (Fig. 4.2d). These experimental results prove that TRPES is able to fully resolve ultrafast dynamics of systems in the droplet interior. As complementary observable to the ejection, photoions show a transient increase (Fig. 4.2e), as ionization inside or in the vicinity of the droplets leads to the trapping of the cation, preventing detection. Because always an ensemble of spatially distributed ground state atoms is measured, the ion yield increase has a gradual form. The In-He_N dynamics could further be successfully simulated by the author of this thesis by applying time dependent helium density functional theory (TD-HeDFT) with the publicly available quantum chemistry package of the BCN-TLS-He-DFT group [105, 106] (see simulated peak shift in Fig. 4.2b&d). The good agreement between experiment and theory proves that ultrafast dynamics can be succesfully simulated in the droplet interior by quantum chemistry methods. Results on In-He_N excitation dynamics provide answers to the formulated research questions 1-4 and were published as Ref. [108], which is included in this thesis as section 4.3.

Full characterization of the photoinduced dynamics on atoms in He_N:
To fully characterize the photoinduced processes after In-He_N excitation, further experimental studies were performed, in which different experimental parameters like excitation energy or droplet size were varied, and more detailed simulations were performed. As main result, the bubble dynamics (expansion and contraction) were found to be purely local processes, independent on dopant location. Furthermore, claims about the atom's location in it's electronic ground state could be made, and In, though still fully solvated, was found to reside in a narrow region under the droplet's surface, independent of droplet size. These results on a detailed characterization of the In-He_N dynamics were published as Ref. [164], which is included as section 4.4.

Ultrafast relaxation dynamics following highly excited state excitation of atoms:
Following the photoexcitation studies on the first excited ($6^2S_{1/2}$) state, experiments were conducted that excite higher lying electronic states of In, namely the 5^2D (and possibly also 6^2P states) (see Tab. 4.1). The question to be answered was (research question 4), on which time scale possible electronic relaxation dynamics within He_N proceed, and how these dynamics are influenced by experimental parameters like droplet size or excitation energy. An in-droplet excitation band, centered around 36,000 cm^{-1} could be measured, which was assigned to stem from the above mentioned states. Unfortunately, in the time resolved measurements neither a clear relaxation to the $6^2S_{1/2}$ nor a relaxation to the ground state could be observed. We concluded that for In, no He-induced electronic relaxation is present. We changed to aluminium, as it has a very similar electronic structure to In, and electronic relaxation from the 3^2D to the 4^2S has previously been identified and was found to proceed below a 50 ps time scale in low temporal resolution studies [63]. After photoexcitation of Al, we could indeed observe a rapid signal decay of the 3^2D peak, however no PE signal at the 4^2S energy could be found, indicating full relaxation to the electronic ground state. The experimetnal results on highly excited states (In and Al) are still under discussion, and more detailed measurements have to be performed; the current status is summarized in section 4.5.

4.1.2 Ultrafast photoinduced dynamics of dimer molecules in helium nanodroplets

Femtosecond photoexcitation dynamics on In_2 in He_N:
After the complete characterization of solvent-induced dynamics following monomer photoexcitation, we started to investigate systems with a single internal degree of freedom, namely diatomic molecules. We chose In_2 molecules, as they can be simply obtained by increasing the heating power of the pickup oven, and the in-droplet excitation spectrum was alreday measured together with the one from the monomer. As is seen in Fig. 4.1, In_2 in He_N exhibits two large excitation bands in the investigated region. All results described within this thesis were conducted at the band around $29{,}000^{-1}$, which could be assigned to the in-droplet $B^3\Pi_g(II) \leftarrow X^3\Pi_u$ transition [165]. The band around $27{,}500^{-1}$ could so far not be assigned, detailed discussions and characterization measurements on both bands are found in the master's thesis of Miriam Meyer [166]. In the first time resolved experiments, the same solvent induced dynamics were characterized, which are also present for the monomer: We found that repulsive interactions of In_2 with He_N also cause the solvation bubble to expand after photoexcitation (see Fig. 4.3a&b), followed by ejection from the droplet. These experiments, together with a comparison to the monomer dynamics, were published as a conference proceeding (Ref. [167]), which is included as section 4.6.

Wave packet dynamics of fully solvated In_2 molecules:
As described in section 2.1, molecule photoexcitation with a spectrally broad pump pulse leads to the

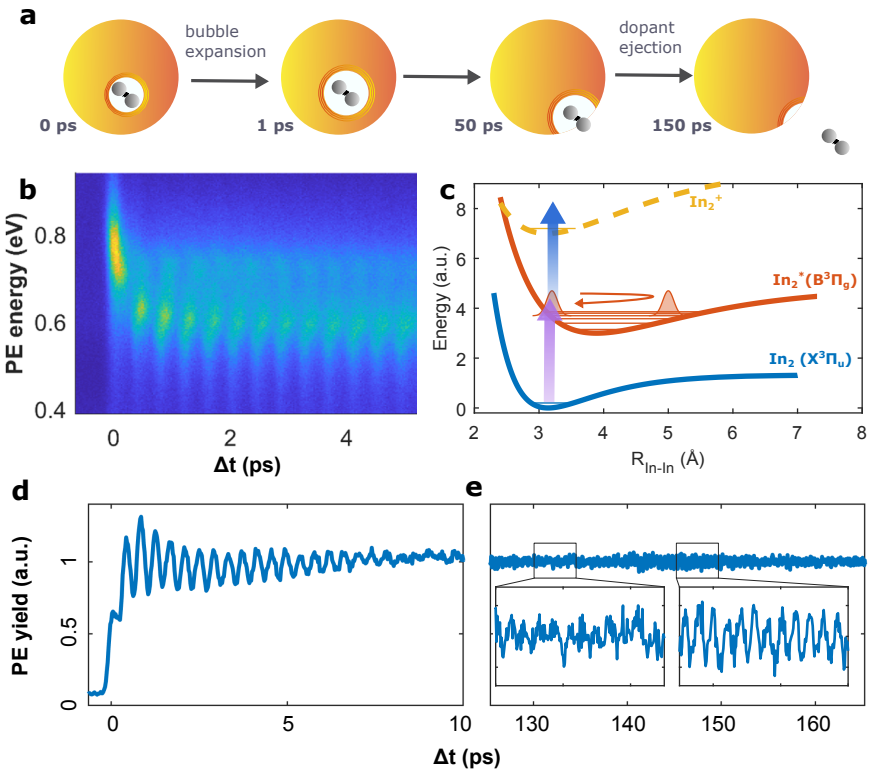

Figure 4.3: Overview of In_2 $B^3\Pi_g \leftarrow X^3\Pi_u$ excitation dynamics in He_N. Panel **a** schematically shows the droplet-related dynamics with respective time scales. Panel **b** shows the short time-scale (bubble expansion and WP) dynamics as measured with TRPES. Panel **c** schematically draws the In_2 potentials, with the WP motion in the excited state. Pump and probe pulses are indicated as arrows. Panels **c** and **d** show the integrated PE yield with oscillating signals for the initial WP and for the first half revival, respectively.

formation and propagation of vibrational wave packets (WP). Such a WP motion leads to oscillations in the transient signals, which we could observe in the transient In_2 PE spectra after $B^3\Pi_g(II) \leftarrow X^3\Pi_u$ photoexcitation: As depicted in Fig. 4.3b, the WP dynamics is superimposed on the bubble expansion dynamics. By closely analysing the WP transients with sliding window Fourier analysis we could show that the coherent WP motion of In_2 inside He_N lasts for a few 10 ps, and can even be measured after dopant ejection in the form of partial and full WP revivals (see Fig. 4.3e). This observation led us to conclude that the influence of the superfluid droplet on coherent WP motion is significantly lowered compared to conventional solvents, where complete decoherence of molecules is usually reached within at maximum a few ps. The results obtained with the investigation of In_2 WP dynamics inside He_N, which provide an answer to reserach question 5, were published in Ref. [168], which is found in section 4.7.

Fragmentation dynamics of ionized In_2 molecules in He_N

Upon close inspection of ion signals at short time delays after In_2 photoexcitation, a fragmentation channel in the ionized molecule was discovered. This observation was deduced from the observation of strong coherent photoion signals, but not at the In_2^+ charge-to-mass ratio, but rather at $InHe_n^+$ masses, with n reaching beyond 20. This result could be rationalized with a fragmentation channel in In_2^+, where the subsequent absorption of an additional probe photon excites a repulsive state. The kinetic energy release of the dissociation provides the translational energy, eventually leading to the ejection of In^+, which take along additional He atoms due to the strong attractive ion-He interaction. Because these $InHe_n^+$ signals

stem from the same probe window as the ones measured with PE, both signals are in phase, and no interpretations based solely on PE are affected by the fragmentation process. At the moment of writing this thesis, the results on In_2^+ fragmentation are being prepared for publication, the current status is presented in section 4.8.

4.2 Conservation of Hot Thermal Spin–Orbit Population of ^{2}P Atoms in a Cold Quantum Fluid Environment

This section consists of the following published publication:

Conservation of Hot Thermal Spin–Orbit Population of ^{2}P Atoms in a Cold Quantum Fluid Environment

B. Thaler, R. Meyer, P. Heim, S. Ranftl, J. V. Pototschnig, A. W. Hauser, M. Koch, and W. E. Ernst*
The Journal of Physical Chemistry A **123**, 3977-3984, 2019
https://doi.org/10.1021/acs.jpca.9b02920

* corresponding author

contributions

funding	M. Koch, W.E. Ernst
experimental design	M. Koch
preparation / setup	P. Heim, B. Thaler, S. Ranftl, M. Koch
data acquisition	B. Thaler, S. Ranftl
HeDFT simulations	R. Meyer, J. V. Pototschnig, B. Thaler
data analysis	B. Thaler, R. Meyer
interpretation	all authors
publication writing	R. Meyer, A. W. Hauser: Results and Discussion - HeDFT part, Appendix A B. Thaler, M. Koch, W. E. Ernst: Rest of publication, Appendix B

Abstract

The 0.4 K internal temperature of superfluid helium nanodroplets is believed to guarantee a corresponding ground state population of dopant atoms and molecules inside this cryogenic matrix. We have recorded 6s←5p excitation spectra of indium atoms in helium droplets and found two absorption bands separated by about 2000 cm^{-1}, a value close to the spin-orbit splitting of the In ^2P ground state. The intensities of the bands agree with a thermal population of the $^2P_{1/2}$ and $^2P_{3/2}$ states at 870 K, the temperature of the In pick-up cell. Applying femtosecond pump-probe spectroscopy, we found the same dynamical response of the helium solvation shell after the photoexcitation of the two bands. He-density functional theory simulations of the excitation spectra are in agreement with the bimodal structure. Our findings show that the population of spin-orbit levels of hot dopants is conserved after pick-up inside the superfluid droplet. Implications for the interpretation of experiments on molecular aggregates are discussed.

Introduction

The ability of helium nanodroplets (He_N) to isolate guest atoms, molecules or clusters in a nearly ideal cryogenic matrix has been widely exploited in the past decades [5, 7, 8]. For example, the rapid cooling of most degrees of freedom, including translational, vibrational and rotational motion enabled the study of novel and exotic systems such as weakly-bound molecular complexes [11, 54]. While many studies focused on energy transfer to the droplet, the influence of the helium environment to reorient atomic angular momenta (orbital and spin), has been investigated to a much lesser extent. Energy levels of atoms with partially filled, non-zero angular momentum orbitals (e.g. *P*- or *D*-states) are energetically split due to the interaction of the electron's spin with its orbital angular momentum. The magnetic moment of an atom depends on the total angular momentum resulting from spin-orbit (SO) coupling. Up to now, very little is known about the relaxation between these SO states inside He_N, especially in the ground state of the dopant species without additional perturbations by external fields. Here we present an investigation of the $^2P_{3/2} \rightarrow {}^2P_{1/2}$ population relaxation of indium (In) atoms inside the He_N. In is chosen because the SO splitting of 2212.6 cm^{-1} (274 meV) [163] gives two separable peaks in the excitation spectrum, while the higher $^2P_{3/2}$ state is, according to the Boltzmann factor, still sufficiently populated at the applied pickup temperature.

For $^2P_{3/2} \rightarrow {}^2P_{1/2}$ relaxation both energy and angular momentum have to be transferred to the He_N. Energetic relaxation inside droplets proceeds via the generation of elementary excitations such as phonons or surface excitations, eventually leading to the detachment of helium atoms due to evaporative cooling. Relaxation rates strongly depend on the coupling efficiency of the dopant to the droplet modes, leading to time constants ranging from picoseconds [63] to milliseconds [55]. Photoexcitation of atoms in He_N is often followed by population transfer to lower states, as was observed for surface-located alkali-metal atoms [73] and for fully immersed metal atoms [63, 65, 67, 69]. Electronic relaxation can be accompanied by reorientation of angular momenta, leading to spin-relaxations within the SO manifold and transitions to different spin multiplicities. The large amount of excess energy introduced into the system at photoexcitation in combination with an increased density of states for higher electronic states presumably leads to couplings between dopant–He-atom potential energy surfaces at close distances, which might induce transitions to lower dopant states [65, 69]. Without photoexcitation and on the weakly-interacting droplet surface, spin reorientation seems to be low, resulting in long spin-lifetimes of alkali-metal atoms in the electronic ground state [97, 169] and metastable quartet states of aluminum atoms that are picked up in excited states [132].

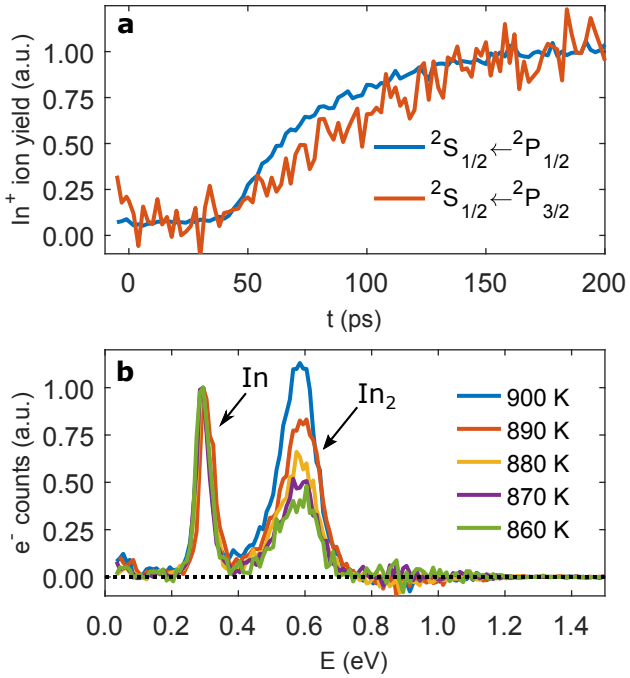

Figure 4.4: Panel (a) shows transient ion yields for the In monomer mass, recorded for excitation at 26600 cm^{-1} and 25200 cm^{-1}, corresponding to the excitation bands of $^2S_{1/2} \leftarrow {}^2P_{1/2}$ and $^2S_{1/2} \leftarrow {}^2P_{3/2}$ excitation, respectively. Panel (b) depicts photoelectron spectra measured at 200 ps time delay and 27000 cm^{-1} excitation photon energy, recorded for various pickup-oven temperatures and corrected by subtraction of single pulse, as well as effusive indium signals. PE peaks assigned to the In monomer and dimer are indicated, each spectrum is normalized with respect to the In atom peak at 0.3 eV.

Based on this previous work, it was not clear if atoms solvated in the droplet interior, where the interaction is much stronger compared to the surface, undergo SO relaxation due to interactions with the surrounding He. For In atoms inside the droplets we find two absorption bands in the 6s←5p excitation spectrum, which lead us to the interpretation that both SO components of the 5p state are populated and that SO relaxation from the energetically higher $^2P_{3/2}$ to the lower $^2P_{1/2}$ state is negligible on the time scale of the experiment. As the assignment of the two bands is essential for our interpretation, we simulate the excitation spectrum with helium density-functional theory (He-DFT). While the simulated spectrum agrees with the experiment, the ground state holding potentials are predicted to have a second minimum close to the droplet surface in addition to the minimum in the center. To avoid possible ambiguities in the peak assignment associated to the $^2P_{1/2}$ and $^2P_{3/2}$ states, we perform femtosecond time-resolved ionization measurements. We find that both bands yield the same solvation shell dynamics, proving that the In atoms are fully solvated [108] and that excitation proceeds from different initial states.

Experimental Methods

He_N with a mean droplet size of $\overline{N} = 4800$ are generated via supersonic expansion of high purity (99.9999%) helium gas through a cooled nozzle (18 K nozzle temperature, 40 bar stagnation pressure, 5 μm diameter). The droplets are doped with In atoms inside a resistively heated pickup cell and the pickup conditions are monitored by a quadrupole mass spectrometer (Balzers QMG 422) at the end of the droplet beam. Temperatures, as stated within this work, are measured with a thermocouple attached to the heating elements of the pickup source, which might be slightly offset to the actual metal temperature.

After pickup and a differential pumping section, the droplet beam is crossed by a laser beam inside the extraction region of a 0.5 m linear time-of-flight spectrometer, which is operated in a magnetic bottle configuration for the measurement of photoelectrons, whereas photoions are extracted with a positive repeller voltage of 2 kV. Femtosecond laser pulses are obtained from a commercial Ti:sapphire laser system (Coherent Vitara oscillator and Legend Elite Duo amplifier, 25 fs pulse duration, 800 nm center wavelength, 3 kHz repetition rate). The laser output is split into pump and probe pulses with variable delay. An optical parametric amplifier (Coherent OPerA Solo) is used in the pump path in order to cover the desired wavelength region (330 to 405 nm), while the probe pulses are frequency doubled with a BBO crystal. The spectral widths of the pump and probe pulses are 550 cm^{-1} and 120 cm^{-1} (FWHM), respectively. The two beams are focused and spatially overlapped inside the extraction region of the spectrometer.
Photoexcitation of the In–He_N system at the 6s←5p atom transition results in the ejection of the excited In atom from the droplet within ∼50 ps [108], which can be deduced from a transient rise in ion yield as a function of pump probe delay (see Fig. 4.4a). Ionization within or in the vicinity of the droplet leads to recapture and no detection, which explains the absent signal for the first few 10 ps and the following signal rise. The excitation spectrum (Fig. 4.5a) is therefore recorded with a femtosecond two-photon ionization scheme, where the photon energy of the first pulse is scanned across the excitation band, and the second pulse ionizes the atoms outside of the droplets after 200 ps. We obtain the excitation spectrum by recording the photoelectron (PE) peak area assigned to the In monomer: Because the pickup process is of statistical nature, a fraction of droplets is loaded with more than one atom, making an assignment of photoelectron peaks to the specific species necessary. In the investigated spectral region, photoion charge-to-mass ratios of the indium monomer (In) and dimer (In_2) were detected; however, no mass signals of larger complexes (e.g. In_3) could be found. Fig. 4.4b shows PE spectra recorded at 200 ps time delay for various pickup conditions. The spectra show two characteristic features around 0.30 eV and 0.55 eV, which are allocated to In and In_2, respectively. The assignment follows directly from a variation of the pickup oven temperature: Higher temperatures result in higher vapor pressures, increasing the pickup probability of more than one atom and therefore enhancing the formation of dimer molecules. This is observed as a relative increase of the In_2 peak in Fig. 4.4b with temperature. We record the excitation spectrum for a pickup cell temperature of around 870 K.

Results and Discussion

As can be seen in Figure 4.5a, two bands showing significant blue-shifts to the free atomic transitions are retrieved. The more pronounced band around 27000 cm^{-1} is easily identified to in-droplet $^2S_{1/2} \leftarrow ^2P_{1/2}$ excitation, the strong blue-shift of 2600 cm^{-1} being an indication of full solvation inside the droplet and the strong repulsive interactions. The second, significantly less distinct band around 25200 cm^{-1} can be assigned to the in-droplet $^2S_{1/2} \leftarrow ^2P_{3/2}$ transition, showing a slightly larger blue-shift of 3000 cm^{-1}.
Before we give additional experimental proves for the assigned spectral features based on time-resolved measurements, we discuss the simulation of the excitation spectrum by means of He-DFT (for a detailed description see Appendix A). Simulation of the in-droplet $^2S_{1/2} \leftarrow ^2P_{1/2}$ and $^2S_{1/2} \leftarrow ^2P_{3/2}$ excitation bands (Fig. 4.5b) is based on the SO coupled In–He-atom pair potentials: $X^2\Pi_{1/2}$ corresponding to the $5^2P_{1/2}$ In atom ground state, $1^2\Pi_{3/2}$ and $1^2\Sigma_{1/2}$ both corresponding to the $5^2P_{3/2}$ In atom state, as well as $2^2\Sigma_{1/2}$ corresponding to the electronically excited $6^2S_{1/2}$ state (Figure 4.8, Appendix A). In a first step, He density distributions and corresponding solvation energies of the In–He_N system as a function of the dopant location are calculated. Fig. 4.6c shows the pseudo-diatomic potential energy

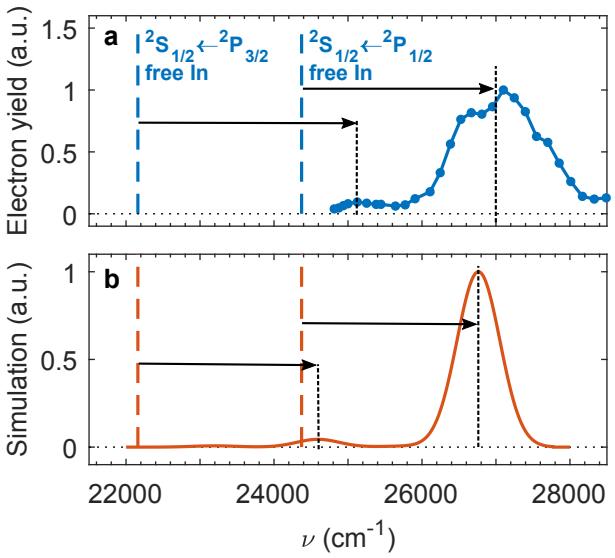

Figure 4.5: Excitation spectra of In inside He_N, measured with photoelectron spectroscopy (a) and simulated using He-DFT (b). The bare atom transitions are indicated as dashed lines, arrows show blue-shifts connected to the solvation inside the helium droplet.

surfaces (holding potentials) for the three lowest SO states. As can be seen, all of them exhibit negative solvation energies, indicating attractive interactions with the helium. We find that the exact form of these potentials crucially depends on the choice of In-He pair potentials due to the similarity of the He-He and the In(^{2}P)-He interaction (see Appendix B). This is also the reason why a structure with minima both in the center and at the edge of the droplet is retrieved. The excited $2^2\Sigma_{1/2}$ potential curve (Fig. 4.6b) reveals a positive solvation energy in the droplet interior, in agreement with the experimental observation of ejection from the droplet [108]. As next step, the location-dependent increase of photoexcitation energy $\Delta E(r)$ (Fig. 4.6a) is simulated under the so-called frozen droplet approximation: Assuming unchanged He density distributions in the lower In–He states during excitation, $\Delta E(r)$ is calculated by summation of the excited state $2^2\Sigma_{1/2}$ pair potential for the three lower state He density distributions. The simulated excitation spectra are obtained by weighting $\Delta E(r)$ with the radial probability density of the In atoms in the respective holding potential of the lower state (Fig. 4.6c), assuming Boltzmann weighted states with the droplet's temperature of 0.37 K and convoluting with Gaussian functions to account for broadening effects. Finally, to obtain the simulated excitation spectrum as shown in Fig. 4.5b, the areas of the two bands are scaled to the Boltzmann population ratio for the pickup oven temperature of 870 K (see below). Comparison to the experimental spectrum (Fig. 4.5a) reveals that the extraordinary large blue-shift is qualitatively reproduced, although slightly underestimated by the simulation, which we ascribe to inaccurate binding strengths of the (^{2}P) In-He pair potentials.

To support the assignment we compare the transient responses of the In-He_N complex to photoexcitation at both bands, which are represented by the time-resolved photoelectron spectra in Figs. 4.7a and b. The solvation shell expansion triggered by photoexcitation inside the droplet yields a transient PE peak shift within a few hundred femtoseconds [108]. This signature is observed for both excitation wavelengths in a very similar manner, as highlighted by dashed lines in Figs. 4.7a and b, indicating that both excitations occur in the droplet interior but from different initial states. The PE peak shift following $^2P_{3/2}$ excitation (Fig. 4.7b) yields a peak shift of 400 meV, which is slightly larger compared to 380 meV of the $^2P_{1/2}$ state, indicating a slightly stronger interaction with the surrounding He, which is expected as the $^2P_{3/2}$

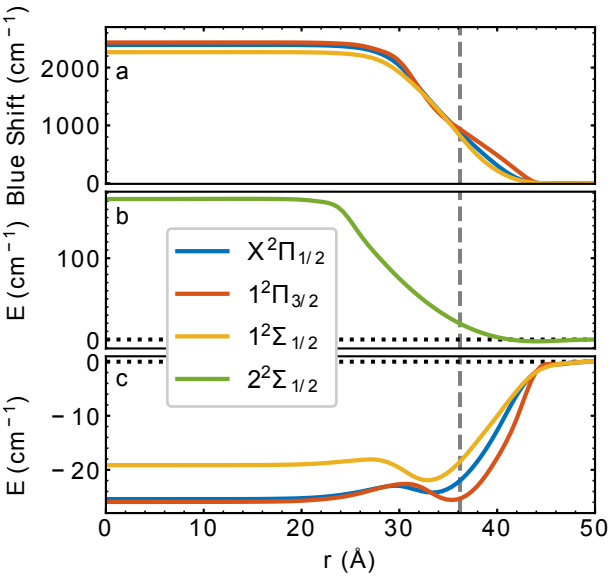

Figure 4.6: Panels (b) and (c) show the position dependent solvation energies of the In-He_{4000} system for In in the $^2P_{1/2}$ and $^2P_{3/2}$ states (corresponding to $1^2\Pi_{1/2}$ and $1^2\Pi_{3/2}$, $1^2\Sigma_{1/2}$, respectively) and in the first excited $^2S_{1/2}$ state (corresponding to $2^2\Sigma_{1/2}$). Panel (a) shows the position dependent extra energy curve one obtains when summing up the excited state $2^2\Sigma_{1/2}$ pair potentials in a He density configuration obtained in the ground states (frozen droplet approximation). The distance after which the pure droplet's density has dropped by a factor of 1/e compared to the bulk density is indicated by a dashed grey line.

state has a stronger blue-shift in the excitation spectrum. After one picosecond, both transient spectra converge to values slightly above the bare atom energies that would appear at approximately 0.30 eV. The remaining shift proceeds in the following 100 ps (not shown) as consequence of the dopant ejection. Detachment from the droplets is additionally confirmed by a transient rise in photoion yield, which shows similar forms for both excitation energies (see Fig. 4.4a). The $^2P_{3/2}$ PE spectrum at zero pump-probe delay (Fig. 4.7d) exhibits a double peak structure, which is a consequence of a second ionization pathway available at this wavelength. As indicated in Fig. 4.7e, non-resonant pump-probe ionization from $^2P_{1/2}$ leads to a second peak at lower energy, which is only present during the temporal overlap of the pump and probe pulse. The peak separation of (260±25) meV is in agreement with the tabulated bare atom value of 274 meV (2212 cm^{-1}) [163].

The assignment of the 25200 cm^{-1} band in the excitation spectrum to the $^2P_{3/2}$ SO component clearly shows that population in this state has not decayed within 1.2 ms after pickup, given by the flight time in our apparatus (430 ms^{-1} droplet velocity [170, 171], 0.53 m distance). We take this as direct experimental proof that SO relaxation is a very inefficient process for atoms immersed inside He_N unless it is accompanied by a previous laser excitation that triggers a strong interaction of the excited state orbital with the surrounding helium. Based on the Boltzmann distribution for a pickup temperature of 870 K, we estimate the higher state to be populated with about 5 % (Fig. 4.5b). The ratio of the corresponding excitation band areas ($^2P_{3/2}$ to $^2P_{1/2}$ in Fig. 4.5a) is approximately 6%. Considering uncertainties in the spectrum and the pickup temperature measurement (see Experimental Section), we therefore concluFde that no SO relaxation is induced by the He_N within 1.2 ms. In contrast to the cooling of translational, vibrational and rotational degrees of freedom that couple more strongly to the droplet's elementary excitations, the necessary energy and angular momentum transfer to induce a spin-flip seems not to be achievable without electronic excitation.

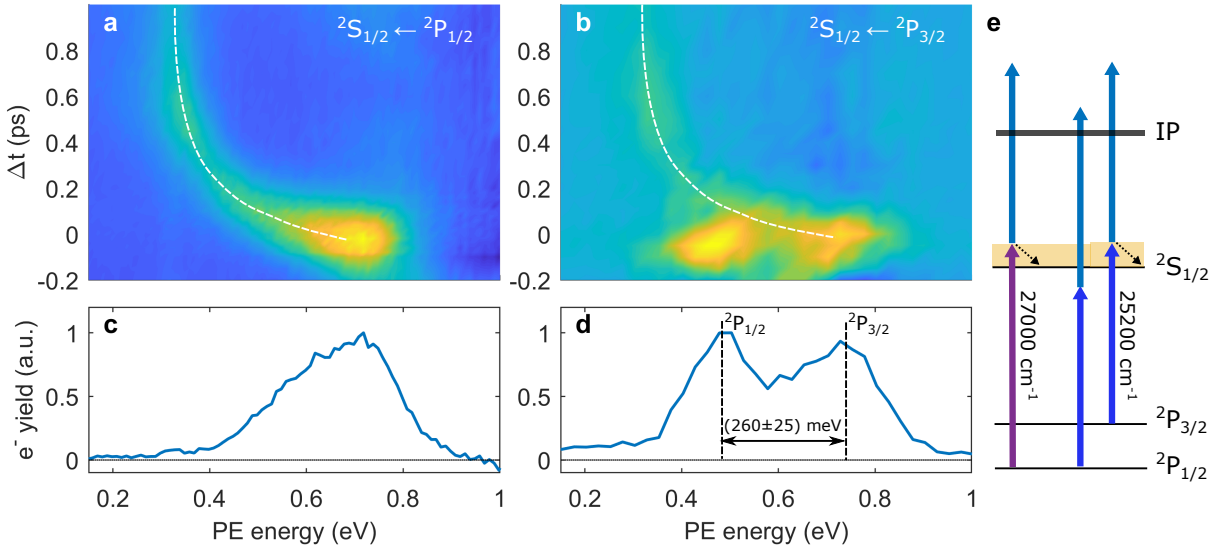

Figure 4.7: Transient photoelectron spectra for the $^2S_{1/2} \leftarrow {}^2P_{1/2}$ [panel (a)] and $^2S_{1/2} \leftarrow {}^2P_{3/2}$ [panel (b)] excitation of the In-He$_N$ complex, measured at 27000 cm^{-1} and 25200 cm^{-1}, respectively. The transient photoelectron energy shift is indicated with dashed white lines to guide the eye. Panels (c) and (d) show photoelectron spectra at zero time-delay between pump and probe (cross correlation). Panel (e) shows the energy level diagram for both excitation schemes, with the bubble expansion indicated by dotted arrows.

Conclusion

We have shown that populations in the ^2P SO sub-levels of In atoms inside helium nanodroplets are frozen after pickup. Although absence of SO relaxation has been found before for metastable aluminum atoms on the weakly interacting droplet surface [132], the lack of relaxation for species fully immersed in the droplet is rather surprising. In our case, the strong perturbation imposed on atoms in the droplet's interior is evidenced by blue-shifts of several thousand wavenumbers, in striking contrast to only a few wavenumbers for atoms on the surface.

Since the formation of complexes inside the droplets is based on the subsequent doping of multiple, often different species, our findings show that the involvement of higher states during the growth process cannot be neglected. Higher SO states with larger total angular momenta have to be included in the modeling of cluster aggregation, in particular because dipole-dipole interaction strongly depends on the magnetic moment. These results also affect the perspective of He$_N$ as nanoscale environments for cold controlled chemistry, where it is essential to prepare molecules in well-defined initial states [172]. Population in excited SO states has to be considered in future experiments investigating, for example, time-resolved dynamics regarding molecule formation [147], isomerization [173] or dissociation and recombination [119, 174, 175].

Appendices

Appendix A: Simulation of In–He$_N$ excitation spectra with HeDFT

In the following we give a detailed description of how the theoretical excitation spectrum of the In-He$_N$ system (Fig. 4.5b) is retrieved.

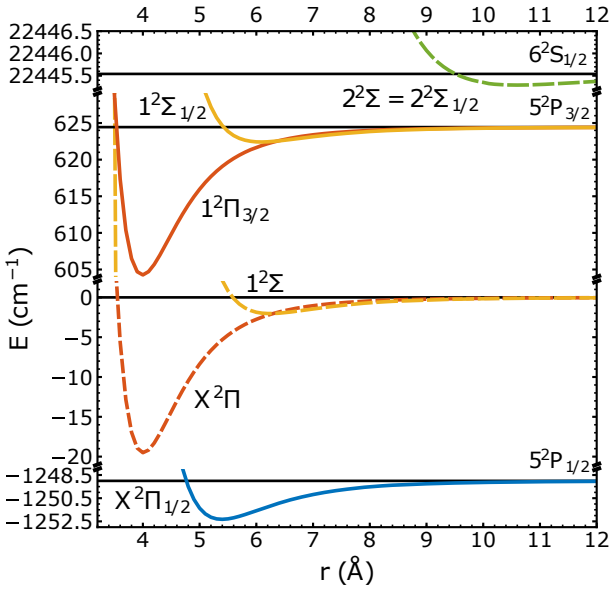

Figure 4.8: Spin-averaged (dashed) and spin-orbit coupled (solid) ab initio potential curves for the In-He molecule.

In-He diatomic interaction potentials: The potential energy surface of the In-He molecule, a necessary ingredient for the He density simulations discussed below, is calculated for the $X^2\Pi_{1/2}$, $1^2\Pi_{3/2}$ and $1^2\Sigma_{1/2}$ ground states and the $2^2\Sigma_{1/2}$ electronically excited state. We use the aug-cc-pV5Z [176] family of basis sets in combination with the ECP28MDF effective core potential of the Stuttgart/Köln group[177]. All ab initio calculations are performed with the MOLPRO software package [178]. A combination of multiconfigurational self consistent field calculations (MCSCF [179, 180]) and multireference configuration interaction (MRCI [181, 182]) is applied to the diatomic system in order to capture the very weak van der Waals type binding between He and In. In the MRCI approach, three valence electrons are included in the active space. The core orbitals are optimized in the preceding MCSCF treatment, but are kept doubly occupied. The In–He curves are corrected for basis superposition errors due to their significance for the extremely weak attractive interaction in both states. For interactions involving rare gas atoms, the usage of midbond basis functions has been suggested [183–185], but a standard counterpoise correction [186] is preferred due to the very different electronic structure of both fragments in the given case. In addition, the curves are basis set-extrapolated using additional calculations with the aug-cc-pVQZ, aug-cc-pVTZ and Def2-TZ basis sets and the three-point exponential extrapolation formula as suggested by Feller [187] or Wilson and Dunning [188] and the two point formula by Gdanitz [189], respectively. The spin-orbit splitting is calculated using the aug-cc-pV5Z basis set and the Breit-Pauli operator as implemented in MOLPRO.
As result, four potential energy curves $X^2\Pi_{1/2}$, $1^2\Pi_{3/2}$, $1^2\Sigma_{1/2}$, and $2^2\Sigma_{1/2}$ are obtained, which are shown in Fig. 4.8. The calculated excitation energy of about 23695 cm^{-1} (the $6^2S_{1/2} \leftarrow 5^2P_{1/2}$ asymptote) is reasonably close to the tabulated experimental value of 24373 cm^{-1} (Ref. [163]). For the spin-orbit splitting, about 85 percent (1873 cm^{-1}) of the experimental value (2213 cm^{-1}) are retrieved within the chosen computational approach[163].

Potential energy surfaces of the In-He_N system: The experimentally relevant ab initio potential energy curves are used to calculate the helium density distribution and the energy of the In-He_N system. Our approach is based on the application of the Orsay-Trento-density functional [107]. The density

functional code we use was written by F. Dalfovo, with modifications by K. Lehmann and R. Schmied [87, 95]. The free energy F[ρ] is written as a functional of the helium density ρ,

$$F[\rho] = E[\rho] + U_{\text{ext}}[\rho] - \mu N[\rho] - \mathbf{F} \cdot \mathbf{R}[\rho], \tag{4.1}$$

with E[ρ] denoting the Orsay-Trento-density functional and $U_{\text{ext}}[\rho]$ representing the external interaction potential describing the interaction between the droplet and the In atom in a specific electronic state via pairwise summations over the pair potentials shown in Fig. 4.8. The remaining terms of Equation 4.1 reflect two constraints put on the minimization procedure: the conservation of N, the particle number, and $\mathbf{R}$, the He_N mass center, together with their corresponding Lagrange multipliers, the chemical potential μ and the retraining force $\mathbf{F}$. One-dimensional potential energy scans of the In-He_N system can be obtained by a minimization of the free energy as a function of the distance of the In atom from the He_N center of mass. Defining the solvation energy of a single, fully immersed In atom inside a He_N as

$$E_{\text{sol}}(\text{In}) = E(\text{In@He}_N) - E(\text{He}_N), \tag{4.2}$$

we obtain the pseudo-diatomic potential energy surfaces shown in Figs. 4.6b and 4.6c.

Simulation of the In-He_N excitation spectrum: The theoretical excitation energies are obtained by assuming a $6^2S_{1/2} \leftarrow 5^2P_{1/2}$ vertical excitation of the In atom while taking into consideration that the energy needed will depend on the actual position of the atom inside the droplet. Taking account for the surrounding helium, excitation comes at the cost of a higher energy due to the confinement of the 6s orbital in the ground state helium bubble right after excitation. Computationally, such an energy correction is obtained by the inversion of the pair-potential technique used to obtain U_{ext} in Equation 4.1: Assuming no He relaxation at all during electronic excitation of the In atom, we can calculate this extra energy by the summation of pairwise interactions between He and In in the $^2S_{1/2}$ excited state for the initial helium density distribution corresponding to the electronic ground states of the In atom. Repeating this for all distances between the In atom and the droplet center of mass, we obtain the extra energy $\Delta E(r)$ needed for electronic excitation as a function of distance (see Fig. 4.9c).
We use this curve of extra energy cost to estimate the position and the width of the perturbed electronic excitation for a direct comparison to the experiment. First, we determine the radial probability density of an In atom in the calculated holding potentials. We use a finite difference approach ($\Delta r = 0.05$ Å) to solve the Schrödinger equation in the radial symmetric potentials for different values of angular momentum l. The lowest energy solutions for the $X^2\Pi_{1/2}$-potential (l = 0) are shown in Fig. 4.9a. In the next step, the states are populated using a Boltzmann distribution at 0.37 K, corresponding to the droplet's temperature. The Boltzmann weighted summation of the states yields the summed radial probability density plotted in Fig. 4.9b. The distance-dependent extra energy $\Delta E(r)$ is used to calculate the expected shift for the different populations (Fig. 4.9d). Hernando et al. [145] give a detailed discussion of the effects of deformations of the helium bubble on the shape of the calculated spectrum. We estimate the broadening due to breathing mode oscillations using the formalism of Hernando et al. to about 400 cm^{-1} (FWHM). In a final step, the theoretical spectra are convoluted with Gaussian distributions for the calculated bubble oscillations and the spectral width of the pump laser (500 cm^{-1} FWHM). As result, three excitation spectra corresponding to the the three ground state PESs ($X^2\Pi_{1/2}$, $1^2\Pi_{3/2}$ and $1^2\Sigma_{1/2}$) are retrieved. We omit the spectrum connected to the $1^2\Sigma_{1/2}$ because its ground state solvation energy is clearly higher than for the $1^2\Pi_{3/2}$ (Fig. 4.6c), making it unlikely to be populated by atoms in the originally degenerate $P_{3/2}$ state. Finally, the areas of the spectra corresponding to $^2S_{1/2} \leftarrow {}^2P_{1/2}$

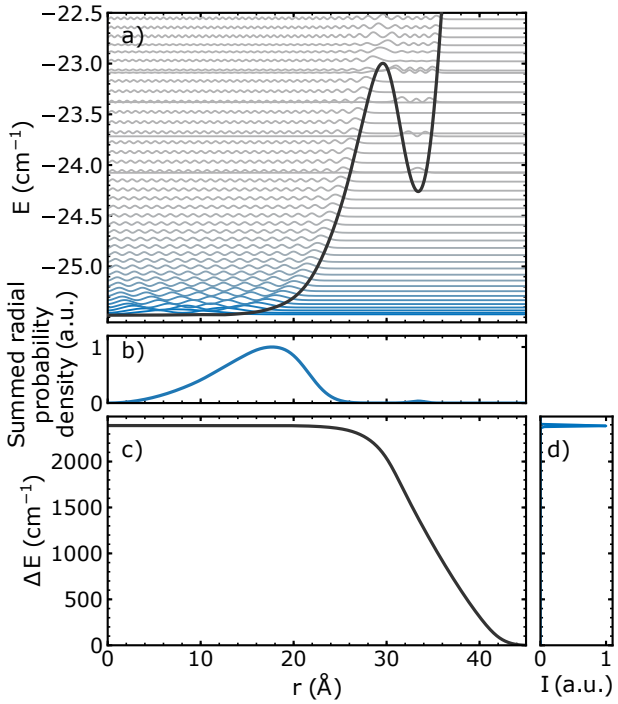

Figure 4.9: Construction of the simulated spectrum by the example of $2^2\Sigma_{1/2} \leftarrow X^2\Pi_{1/2}$ excitation. Panel (a) shows the holding potential for l = 0 and the normalized radial probabilities of vibrational wavefunctions for the In atom, colored corresponding to their relative occupation at 0.37 K. Panel (b) contains the (unnormalized) weighted sum of the radial probability (summed over all possible values of l) and (c) shows the extra energy $\Delta E(r)$ needed in the excitation process. Finally, panel d depicts the calculated shift in the excitation spectrum.

and $^2S_{1/2} \leftarrow {}^2P_{3/2}$ excitation are scaled to the expected Boltzmann populations at the chosen pickup temperature (870 K), eventually leading to the spectra shown in Fig. 4.5b.

Appendix B: Uncertainties in the solvation energy calculations

As is seen in Fig. 4.9a, a special situation of two minima on the potential energy surface for the ground state holding potential of the In-He_N system is found. We ascribe this finding with the qualitatively similar binding energies of He-He and In-He in their electronic ground states. The He functional approach therefore solely cannot answer the important question if In in its ground state resides in the droplet interior (droplet center) or at the droplet edge. Additionally, the exact form of the In-He potential energy surface (Fig. 4.8) has a high influence on the form of the solvation energy curve. To illustrate this, we compute the $X^2\Pi_{1/2}$ diatomic potential with a different basis set (Def2), which yields a sightly different binding energy of 2.9 cm^{-1}, compared to 3.3 cm^{-1} for the above-used aug-cc-pV basis. Fig. 4.10 shows the ground state and excited state solvation energies, computed with both the aug-cc-pV and the Def2 basis. Whereas the excited state potential energy surface is only slightly affected, the different pair potentials predict opposing trends in the solvation behaviour of the ground state: the holding potential for the aug-cc-pV basis yields a central minimum, whereas the Def2 potential yields a global minimum near the droplet edge.

To check for possible influences of the He-DFT method used, we further compare the ground state holding potential obtained with our calculations with a similar computation performed with the publicly-available BCN-TLS-He-DFT computation package [105, 106]. Fig. 4.10 (lower panel) also shows the ground state

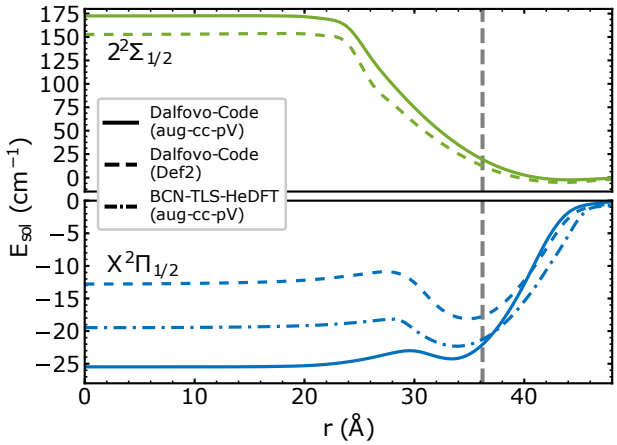

Figure 4.10: In-He_{4000} potential energy surface as function of distance r of the In atom to the He center of mass for different In-He pair potentials. For comparison, the ground state potential obtained with the BCN-TLS-He-DFT computation package using the aug-cc-pV basis set is shown as dash-dotted line. The approximate droplet radius where the He-density of a pure droplet has dropped to 1/e of the bulk value is indicated by the dashed grey line.

holding potential (computed with the aug-cc-pV basis) for this calculation, which again clearly suggests a double-minimum structure, with solvation energies in between the two obtained with our own code. The delicate differences of our results obtained with different methods and diatomic pair interaction potentials prove the extensive uncertainty one gets for quantitative results of such a floppy system. Strong dependencies of theoretical solvation properties on the pair-potentials have also been described for alkaline-earth metals inside He_N [190, 191], whose interaction energies also lie in this sensitive range. As the experimental results for In clearly prove full solvation, we expect the aug-cc-pV pair potential to provide a description closest to the real situation. However, as the simulated excitation spectrum exhibits less blue-shift than the experimental one, the (negative) solvation energy might still be overestimated.

4.3 Femtosecond photoexcitation dynamics inside a quantum solvent

This section consists of the following published publication:

Femtosecond photoexcitation dynamics inside a quantum solvent

B. Thaler, S. Ranftl, P. Heim, S. Cesnik, L. Treiber, R. Meyer, A. W. Hauser, Wolfgang E. Ernst, and M. Koch*

Nature Communications **9**, 4006, 2018
https://doi.org/10.1038/s41467-018-06413-9

* corresponding author

contributions

funding	M. Koch, W.E. Ernst
experimental design	M. Koch
preparation / setup	P. Heim, B. Thaler, S. Ranftl, M. Koch
data acquisition	B. Thaler, S. Ranftl, S. Cesnik, L. Treiber
TD HeDFT simulation	B. Thaler
diatomic pair potentials	R. Meyer, A. W. Hauser
data analysis	B. Thaler, P. Heim
interpretation	all authors
publication writing	B. Thaler, W. E. Ernst, M. Koch

Abstract

The observation of chemical reactions on the time scale of the motion of electrons and nuclei has been made possible by lasers with ever shortened pulse lengths. Superfluid helium represents a special solvent that permits the synthesis of novel classes of molecules that have eluded dynamical studies so far. However, photoexcitation inside this quantum solvent triggers a pronounced response of the solvation shell, which is not well understood. Here we present a mechanistic description of the solvent response to photoexcitation of indium (In) dopant atoms inside helium nanodroplets (He_N), obtained from femtosecond pump-probe spectroscopy and time-dependent density functional theory simulations. For the In-He_N system, part of the excited state electronic energy leads to expansion of the solvation shell within 600 fs, initiating a collective shell oscillation with a period of about 30 ps. These coupled electronic and nuclear dynamics will be superimposed on intrinsic photoinduced processes of molecular systems inside helium droplets.

Introduction

Since the award of the 1999 Nobel Prize for Chemistry [192], various fundamental molecular processes have been investigated on their natural time scales, e.g. fragmentation via different pathways on the molecular potential energy surface [193], non-adiabatic electron-nuclear coupling [194], or electron dynamics initiated by ultrashort laser pulses [195]. Superfluid helium nanodroplets (He_N) have been used as nanocryostats to isolate atoms or molecules at 0.4 K temperature, or to form new weakly bound aggregates [5, 8]. Their gentle influence on guest particles is demonstrated, for example, by electron spin resonance [97] or molecular rotation and alignment experiments [41, 42]. He droplets are an appealing spectrosopic tool because of their transparency for electromagnetic radiation up to the extreme ultraviolet energy regime [8]. However, photoexcitation inside the droplet leads to dissipation of significant excess energy via coupling to collective modes of the surrounding helium, which is expected to be a fast process. Femtochemistry inside He_N will allow real time tracking of photochemical reactions in novel systems, such as fragile agglomerates [10, 11, 55], or molecules in a microsolvation environment [14]. This will, however, require a detailed knowledge about the response of the quantum fluid to the photoexcitation of a dopant atom or molecule. So far, only the ultrafast dynamics in pure helium droplets have been studied [36], and femtosecond measurements on doped helium droplets were restricted to the surface bound alkali metals [6, 120] that can hardly couple to helium bubble modes. Since most foreign atoms and molecules reside inside the droplets and couple more strongly, we have concentrated on the electronic excitation of single atoms well inside the droplets. In this way, no other degrees of freedom such as rotation or vibration would interact and only the coupling of the electronic excitation with the modes of the surrounding helium should be detected. Previous spectroscopic studies in the frequency domain have shown blue-shifted excitation bands of dopants inside droplets compared to gas phase indicating that an excess energy is required to create a correspondingly larger helium bubble to accommodate the excited electron orbital [8]. This excess energy must be released to the helium in form of a damped helium excitation mode.

In our work, we follow the expansion of the helium bubble after electronic excitation of single indium (In) dopants in real time. After an expansion from 4.5 Å to 8.0 Å radius in 600 fs, we observe a contraction of the surrounding He at (28 ± 1) ps, as well as an ejection of the dopant atom from the droplet about 60 ps after the electronic excitation. As observable in our fs pump-probe measurements, we chose the photoelectrons released because they have been shown to exit the droplet rather ballistically without being significantly influenced by the helium environment [6, 36, 60]. In spite of its importance for photochemical

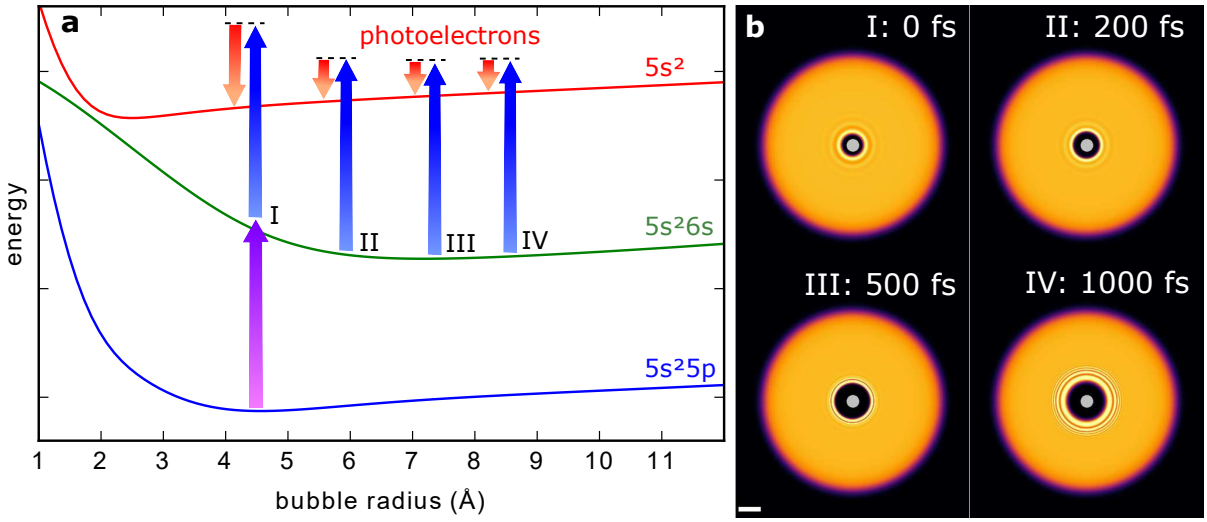

Figure 4.11: Temporal evolution of the In-He$_N$ system after photoexcitation. (a) Sketch of the In-He$_N$ potential energy surfaces as function of the bubble radius for In in its ground [$5s^2 5p$ ($^2P_{1/2}$), blue], lowest excited [$5s^2 6s$ ($^2S_{1/2}$), green] and ionic ground state [$5s^2$ ($^1S_0$), red]. The purple arrow indicates pump excitation at 376 nm, blue arrows indicate probe ionization at 405 nm for characteristic delay times and red arrows correspond to the PE kinetic energy, as measured by TRPES. (b) Helium density distributions of a He$_{4000}$ droplet with an In atom located in the centre for selected times after photoexcitation, as calculated with TDDFT. Scale bars, 10 Å.

studies in superfluid helium droplets, this sequence of events has not previously been observed.

Results

We investigate photoexcitation dynamics of the In-He$_N$ system with a combination of time-resolved photoelectron spectroscopy (TRPES) and time-dependent density functional theory (TDDFT) simulation, as described in the following. A mechanistic description of the processes deduced from experiment and theory will be discussed in the final paragraph.

Time-resolved photoelectron spectroscopy

The feasibility of ultrafast experiments inside He$_N$ ultimately depends on the availability of an experimental observable that is available with sufficiently low distortion by the intermediate helium. Ion detection, as used on the droplet surface, is not possible because ions are captured inside the droplet due to their attractive potential [6]. Photoelectron (PE) detection, in contrast, has been successfully used for pure and doped He$_N$ [6, 36, 60]. TRPES is a well established method for ultrafast gas-phase studies and is primarily sensitive to the electronic structure of a system [50, 196]. As depicted in figure 4.11a, after photoexcitation by a pump pulse the evolution of the excited state is probed by time-delayed photoionization and the PE kinetic energy (red arrows) is measured. When applied inside a He$_N$, photoexcitation induces an abrupt disturbance of the quantum fluid solvation shell due to expansion of the valence electron wave function. Because the energies of the electronic states depend on the structure of the He environment, the transient response of the quantum solvent can be sensed with TRPES (see figure 4.11a).

Figure 4.12 shows the time-dependent evolution of the PE signal within the first picosecond after photoexcitation (a), together with PE spectra at selected pump-probe times (b). Within about 600 fs the PE peak energy is shifted from 0.61 eV to 0.34 eV, followed by a slower decrease to 0.32 eV at 1000 fs,

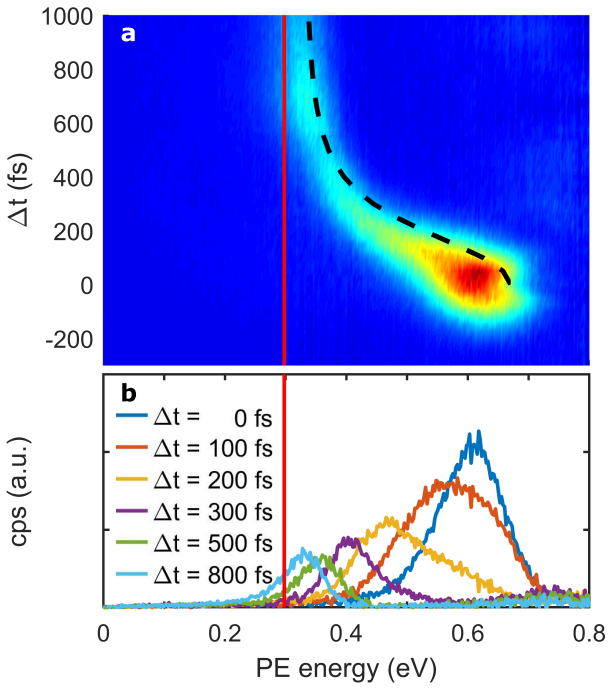

Figure 4.12: Time-resolved photoelectron (PE) spectra of single In atoms solvated inside He_N. The average droplet size is 4000 He atoms. (a) PE kinetic energy spectrum as function of the pump-probe time delay Δt, together with the simulated dynamics (dashed line) and the gas-phase PE energy (solid line). Around time-zero the PE signal is increased due to temporal overlap of the pump and probe pulses. Additionally, the total PE signal decreases during the expansion, which might be due to a decreased ionization probability for larger bubbles and/or lower escape probability of slow electrons from larger bubbles at long delays compared to fast electrons from small bubbles at short delays [60]. (b) Selected spectra for different pump-probe time delays, which resemble horizontal cuts through the 2D plot in (a).

which is about 0.02 eV above the gas-phase peak that appears at around 0.30 eV (solid line in figure 4.12). The remaining shift represents the reduced ionization potential of In atoms in the He environment due to polarization effects [60]. The linewidth of the PE spectra is significantly increased and changes within the first picosecond (figure 4.12b), which we ascribe to the following four reasons: First, during pump-probe cross correlation of 150 fs, saturation effects and the spectral width of the pump pulse are expected to contribute to the PE linewidth. Second, within the first 500 fs, a peak shift with a maximum slope of about 1 meV/fs in combination with the 150 fs pump-probe cross correlation leads to an expected contribution of about 150 meV. Third, ionization inside the droplet increases the linewidth, given by the Franck-Condon overlap of the excited and the ionic state (c.f., figure 4.11), which seems to be the dominant contribution to the linewidth after 500 fs. Fourth, relaxation of the photoelectrons due to binary collisions with individual He atoms on the way out of the droplet leads to an asymmetric shape of the PE peaks [60]. These decelerated electrons can be seen as wing extending to PE energies below the gas phase value (red line in figure 4.12b and Supplementary Fig. 7b).
In figure 4.13 the PE kinetic energy up to 100 ps is shown (blue dots). After a steep decrease representing the tail of the initial peak shift shown in figure 4.12, the peak position slowly decreases to reach a constant value at about 60 ps with a temporary increase at (28 ± 1) ps. The PE peak width shows a very similar trend (figure 4.13, red diamonds) with a steady decrease over time to about 35 meV at long time delays and a temporary increase. Detailed scans of PE peaks at short and long time delays are shown in Supplementary Fig. 7b. We note that except for very short time delays right after the pump-probe

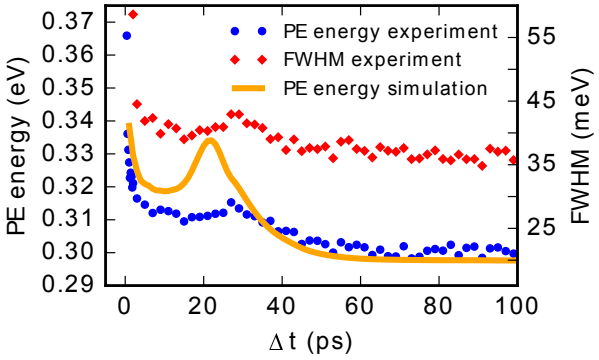

Figure 4.13: Photoelectron (PE) peak position and linewidth as function of time delay Δt. The transient peak position (blue dots) and full width at half maximum (FWHM, red diamonds) are shown within 100 ps after photoexcitation, as measured with TRPES and simulated with TDDFT (orange line). The experimental peak position and FWHM are obtained by Gaussian fits to the corresponding PE energy spectra. The start position for the TDDFT simulation was 20 Å from the droplet center in order to obtain a similar ejection behavior as the experiment.

overlap (cross-correlation), the total PE yield stays constant over the whole investigated temporal region.

Time-dependent helium density functional theory

To obtain further insight into the ultrafast dynamics, photoexcitation of the In-He_N system is simulated with TDDFT using the BCN-TLS-He-DFT computing package [105], which has been successfully applied to reproduce the dynamics of He_N loaded with various different atomic species [106]. In the present case, an extraordinary amount of excess energy of several hundred meV is coupled into the system in the photoexcitation process. We therefore carefully tested the simulations for convergence by variation of the simulation parameters (see Supplementary Note 3 and Supplementary Figs. 4 and 5).
figure 4.11b shows He density distributions for selected times after photoexcitation and the corresponding bubble expansion over time is plotted in figure 4.14a. Inside the droplet the energies of the In excited state ($5s^2 6s$) and its ionic state ($5s^2$) deviate from the bare atom values by the interaction energies $E_{He_N\text{-}In^*}$ and $E_{He_N\text{-}In^+}$, respectively. These interaction energies, plotted in figure 4.14b, are calculated by integrating the respective In-He pair potentials over the He density. While $E_{He_N\text{-}In^*}$ (green curve) is positive and decreases with time (for larger bubbles), $E_{He_N\text{-}In^+}$ (red curve) is negative and increases. This behavior can be expected from the repulsive and attractive character of the excited and ionic state pair potentials, respectively (Supplementary Fig. 3). The simulated PE peak shift with respect to the free atom, as plotted in figure 4.14c, is calculated as the difference of the two interaction energies ($E_{He_N\text{-}In^*}$ - $E_{He_N\text{-}In^+}$) and compared to the measured transient peak shift in figures 4.12a and 4.14c, revealing good agreement. Note that within 1000 fs $E_{He_N\text{-}In^*}$ decreases to zero, whereas $E_{He_N\text{-}In^+}$ is negative and reaches zero only at higher time delays. This results in a further peak shift between 1000 fs and 60 ps (see figure 4.13), as the dopant is ejected from the droplet. As can be seen in figure 4.14c, below 200 fs the experimental peak shifts are slightly lower than the simulated ones, which we ascribe to a distortion of the PE peaks due to a cross correlation signal caused by overlap of pump and probe pulses in this temporal region (c.f., figure 4.12b).
Next, we compare the steady decrease of the excited state electronic energy (cyan curve in figure 4.14b) to the kinetic energy of the helium atoms (dashed line in figure 4.14b), and find that the two curves show almost exactly complementary trends.

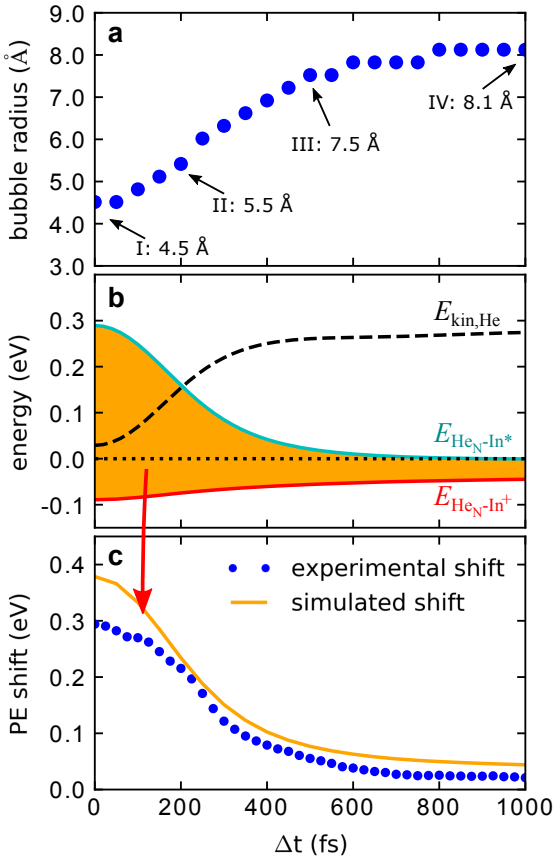

Figure 4.14: Photoexcitation dynamics of the In-He_{4000} system simulated with TDDFT. (a) Bubble radius as a function of time delay Δt, determined as position of the corresponding He distribution at which the density has dropped to 50% of the bulk value. Times for which the calculated He density is shown in figure 4.11b are indicated. (b) Interaction energy $E_{He_N-In^*}$ of the $5s^2 6s$ excited state (cyan curve) and interaction energy $E_{He_N-In^+}$ of the $5s^2$ ionic state (red curve). Additionally, the kinetic energy of the He atoms, $E_{kin,\,He}$, is plotted as dashed line. (c) Simulated PE peak shift induced by the He environment (orange line), obtained as $E_{He_N-In^*}$ - $E_{He_N-In^+}$ (indicated by the shaded area in (b)), which is also shown in figure 4.12a. For comparison to the measured shift of the PE peak position over time, the recorded electron spectra at all time delays (c.f., figure 4.12b) are fitted with Gaussian functions and the line positions are indicated here by blue dots.

Finally, the simulated PE peak position for an In atom, that is photoexcited at a distance of 20 Å from the droplet center, is shown in figure 4.13 (orange line). The choice of this position is justified by comparing simulated PE peak transients with different starting positions (see Supplementary Note 4 and Supplementary Fig. 6). The simulated curve shows the same overall decrease as the experimental values (blue dots), although with a more pronounced temporal increase at 22 ps.

Discussion

The transient shift in the pump-probe PE spectrum of the In-He_N system within the first ps (figure 4.12) has to be related to solvation shell dynamics, as no internal degrees of freedom are available for relaxation of the In atom in its lowest electronically excited state. The energy of the excited valence electron in the In*-He_N system is a very sensitive probe for the temporal evolution of the He environment because of strong Pauli repulsion with the surrounding helium [197]. TRPES measures the transient PE kinetic

energy, which additionally depends on a temporal shift of the ionic state energy ($E_{\mathrm{He_N\text{-}In^+}}$, figure 4.14b). Therefore, we use TDDFT modeling of the photoexcitation process in order to distinguish these two contributions. Previously, TDDFT simulations could only be compared to time-dependent experiments at the weakly-interacting droplet surface [120]. In the interior, the dopant-He interaction is much stronger, with the consequence that significantly more excess energy (270 meV $\approx$ 2200 cm^{-1} in our case) is coupled into the system during photoexcitation, challenging the accuracy of the TDDFT approach. The reproduction of the observed transient PE peakshift by TDDFT (figures 4.12a and 4.14c), without using any experimental input for the simulation, demonstrates that a simulation of photoexcitation dynamics is possible even in the case of significant excess energy.

By combining experiment and theory we obtain the following mechanistic picture of the coupled, ultrafast electronic and nuclear relaxation process: Photoexcitation increases the radial expansion of the valence electron wave function, as is suggested by the strong repulsive part of the In-He pair potential at short distances in the excited state (Supplementary Fig. 3). Pauli repulsion between the extended electron density and the closed-shell He thereby pushes the surrounding solvation shell away (see Supplementary Movie 1). The spherical He bubble containing the excited In atom almost doubles its radius from 4.5 Å to 8.0 Å within 600 fs after excitation (figures 4.11b and 4.14a). This process can also be explained with the corresponding potential energy surfaces (figure 4.11a): Because the equilibrium bubble radius of the excited electronic state is larger than that of the ground state, photoexcitation causes enlargement of the solvation shell. This nuclear relaxation can be followed as transient PE peak shift because the potential energies of the excited state and the ionic state depend on the distance of neighboring He atoms to the In dopant. From an energetic viewpoint, the bubble expansion is accompanied by the conversion of electronic energy into kinetic energy of the He atoms, as illustrated by the mirror-imaged progression of the two corresponding curves (excited state interaction energy $E_{\mathrm{He_N\text{-}In^*}}$ and kinetic energy of the He atoms $E_{\mathrm{kin,\ He}}$) in figure 4.14b. The minute decrease of the sum of $E_{\mathrm{He_N\text{-}In^*}}$ and $E_{\mathrm{kin,\ He}}$ over time represents energy transferred to He-He interactions (correlation energies).

The impulsive stimulation of the He solvation layer initiates a collective oscillation of the He bubble, the first contraction of which is observed as increase of the PE kinetic energy and linewidth in figure 4.13 at (28 ± 1) ps, induced by the temporally increased He density in the vicinity of the In atom. The repulsive character of the excited state In-He pair potential (see Supplementary Note 2 and Supplementary Fig. 3) leads to ejection of the In atom from the droplet on a time scale of about 60 ps (see Supplementary Movie 2). Consequently, the PE kinetic energy decreases to the free-atom value within this time span (see figure 4.13) and only one bubble oscillation can be observed. Dopant ejection is further confirmed by observing a rise in photoion yield on the same time scale (Supplementary Fig. 7a) and a transient change of the linewidth of the PE peak (see figure 4.13 and Supplementary Fig. 7b). While the TDDFT simulation assumes a fixed starting location of the In atom, the experimentally observed ensemble comprises a distribution of In atoms within the droplet. As a consequence, the timing of the first bubble contraction will appear smeared out in the experimental data, because the PE energy peak shift due to dopant ejection is superimposed on the pure bubble oscillation. Photoexcitation of the In dopant in the centre of the droplet induces multiple oscillations and no ejection within the simulated time span (see Supplementary Movie 3 and Supplementary Note 4). We therefore conclude, that the collective solvation shell oscillation has a period of about 30 ps, the observation of which provides insight into the hydrodynamics of the bubble in real time [127].

In conclusion, our experiments prove that ultrafast, coupled electronic and nuclear dynamics of particles located inside superfluid He nanodroplets can be observed and simulated. The expansion of the dopant solvation shell will be superimposed on any molecular relaxation dynamics on femtosecond time scales inside the droplet. When applying photoelectron detection, which seems to be a promising observable for

intrinsic molecular dynamics inside helium droplets, the photoelectron transients induced by solvation shell dynamics have to be known. The duration of dopant ejection, on the other hand, limits the time frame for which ultrafast reactions inside the quantum fluid can be observed. As a proof of concept, our results pave the way to use helium droplets as a novel sample preparation technique for ultrafast studies on previously inaccessible tailor-made or fragile molecular systems.

Methods

Helium droplet generation and In atom pickup

Helium droplets with an average size of about 4000 atoms are generated by supersonic expansion of high purity (99.9999 %) helium gas through a cooled nozzle (5 μm diameter, 18 K temperature, 40 bar stagnation pressure) into high vacuum. The expansion in combination with evaporative cooling results in droplet temperatures of about 0.4 K, which is well below the superfluid phase transition of helium. The He_N are doped with In atoms inside a pickup region, where indium is resistively heated. Pickup conditions are optimized for single atom pickup and for an acceptable signal-to-noise ratio. Indium was chosen as dopant because of its simple electronic structure with one valence electron and because its excited state is symmetric, simplifying the TDDFT simulations, as well as the interpretation. After passing a differential pumping stage to increase the vacuum quality, the doped droplets enter the measurement chamber, where the He_N beam is crossed at right angle by the femtosecond laser pulses inside the extraction region of a time-of-flight spectrometer.

Time-resolved photoelectron spectroscopy

A commercial Ti:sapphire femtosecond laser system (Coherent Vitara oscillator, Legend Elite Duo amplifier) delivers 25 fs laser pulses with 800 nm central wavelength and 4 mJ pulse energy at a repetition rate of 3 kHz. The pulses are split into a pump and a probe path with variable time delay. Pump pulses are frequency up-converted by an optical parametric amplifier (Coherent OPerA Solo) that tunes the wavelength to 376 nm (3.30 eV, 6 nm $\approx$ 60 meV full width at half maximum, FWHM). Probe pulses are frequency doubled to 405 nm (3.06 eV) with a 1 mm thick BBO crystal (3 nm $\approx$ 25 meV, FWHM) for short delays and with a 5 mm thick LBO crystal (1.5 nm $\approx$ 10 meV, FWHM) for long delays and guided over a delay stage. Dichroic mirrors are used in both beam paths to remove undesired wavelengths from the upconversion process. Pump and probe pulses are focused into the extraction region of the linear time-of-flight spectrometer, where they overlap in space and time at the intersection region with the He_N beam. A magnetic bottle configuration [198] ensures high electron detection efficiency and a small positive repeller voltage of a few hundred mV increases the electron kinetic energy resolution. At these parameters we estimate the relative energy resolution of the spectrometer to be about 10%, based on reference measurements. PE energies are calibrated with the free atom line, which position is retrieved by subtraction of the excited state binding energy [163] from the probe photon energy. The measurement chamber is operated at a base pressure of 10^{-10} mbar.
The intensities of the pump and probe pulses are optimized to obtain a maximum pump-probe signal with respect to pump-only and probe-only backgrounds. The pump wavelength for In excitation to the lowest excited state ($5s^2 6s$) is chosen to be 376 nm in order to optimize the monomer to dimer ratio (see Supplementary Note 1 and Supplementary Fig. 2), which is blue-shifted by 270 meV with respect to the gas-phase excitation wavelength at 410 nm [199]. This amount of excess energy is coupled into the In-He_N system at photoexcitation. The pump-probe cross correlation is estimated with 150 fs.

Time-dependent helium density functional theory

In the last years the approach of TDDFT for the bosonic system of helium has been successfully applied to describe the dynamical interaction of surface- and centre-located species with the helium quantum fluid, providing important insight into effects like superfluidity on the microscopic level [71], desorption dynamics [120], or collision processes [111, 112].

Details on the application and formalism of static and dynamic HeDFT are given elsewhere [106] and the computing package of the BCN-TLS group is available to the public as open source [105]. Here only the basic concepts and the terms that affect the presented results are given: Both static and dynamic computations are based on the Orsay-Trento functional [107], which attributes for He-He interactions, and the diatomic In-He potential energy surfaces. These pair potentials were calculated with high level ab initio methods for the ground, excited and ionic state (see Supplementary Note 2 and Supplementary Fig. 3). The simulations are performed for a He_{4000} droplet with the In impurity located in the centre by using a He-functional that includes the solid term [200]. We use a three dimensional Cartesian box of 96 Å length with a discrete grid size of 320 pt (0.3 Å spacing) and time steps of 0.1 fs to simulate the bubble expansion dynamics within the first ps and a grid size of 256 pt (0.375 Å spacing) and time steps of 1 fs for the bubble oscillation dynamics up to 100 ps. For the bubble oscillation dynamics the starting position was chosen to be at 20 Å distance to the centre, which is, based on the In-He_N ground state holding potential, a representative dopant location, and leads to a similar ejection behavior as in the experiment. Both the bubble expansion and the oscillation period are local effects and are found to be very similar for dopant locations in the droplet centre. With the statically optimized ground state He density, a dynamical evolution is triggered by replacing the ground state pair potential with the excited state pair potential. This instantaneous perturbation drives the system and TDDFT allows to follow the resulting dynamics in real time [106], by solving the TDDFT equations for the helium and Newton's equations of motion for the impurity. Photoelectron spectra are simulated by integrating the pair potential energies $E_{\text{He-In}}$ over the whole droplet density ρ_{He} for both the excited and the ionic state for various timesteps in the simulation. The difference between the interaction energies directly compares to the difference in ionization energy of the immersed impurity and therefore to the shift in PE energy:

$$\text{PE shift (t)} = \int \rho_{\text{He}}(\mathbf{r}, \text{t}) E_{\text{In}^*-\text{He}}(\mathbf{r} - \mathbf{r}_{\text{In}^*}(\text{t}))\ \text{d}\mathbf{r} - \int \rho_{\text{He}}(\mathbf{r}, \text{t}) E_{\text{In}^+-\text{He}}(\mathbf{r} - \mathbf{r}_{\text{In}^+}(\text{t}))\ \text{d}\mathbf{r}$$

Since a huge amount of energy is deposited into the system in the excitation process, the simulations were tested for numerical uncertainties by variation of different parameters (grid size, time step and cutoff energy), as presented in Supplementary Note 3 and Supplementary Figs. 4-5.

Supplements to: Femtosecond photoexcitation dynamics inside a quantum solvent

The following sections accompany the publication from *Nat. Comm.* **9**, 4006, 2018 as online supplementary material.
https://doi.org/10.1038/s41467-018-06413-9.

Supplementary Online Information

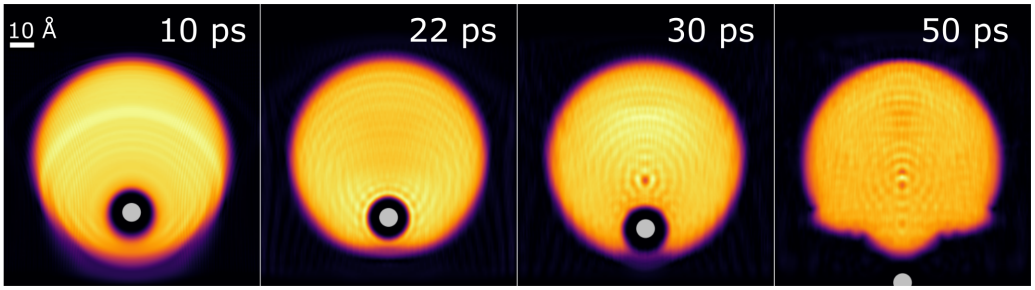

Figure 4.15: Snapshots from Supplementary Movie 2. Helium density distributions of a He_{4000} droplet with an indium atom, originally located at 20 Å distance to the centre, as obtained with TDDFT for characteristic time delays. The dopant is ejected from the droplet after 60 ps, accompanied by a contraction of the solvation shell (bubble) around 22 ps.

Supplementary Note 1: The In-He_N excitation spectrum

The In-He_N excitation spectrum in the region of the In $5s^2 6s \leftarrow 5s^2 5p$ transition was previously recorded and is shown in Supplementary Fig. 4.16. In addition to the monomer signal (blue line) an In dimer band (red line) appears with strong overlap to the monomer. The monomer signal shows a maximum at 368 nm, which is blue-shifted by 2800 cm^{-1} with respect to the free atom line (green, solid line) [199]. The excitation wavelength was chosen at 376 nm (black, dashed line) to obtain a good monomer-to-dimer ratio. Additionally, a reduced pickup temperature was used to minimize the dimer influence.

Supplementary Note 2: The In-He pair potentials

The most important inputs for both the static and time-dependent DFT simulations are the dopant-helium diatomic potential energy surfaces for all electronic states that are populated in the experiment. The spin-orbit coupling corrected energy curve of the ground state ($X^2\Pi_{1/2}$), the first excited state ($2^2\Sigma_{1/2}$) and the ionic state of the In-He molecule are shown in Supplementary Fig. 4.17. All three states are spherically symmetric and the spin-orbit splitting of the ground state to the $^2P_{3/2}$ ($1^2\Pi_{3/2}$ and $1^2\Sigma_{1/2}$, not shown in Supplementary Fig. 4.17) has a value of about 2000 cm^{-1}, for which reason the latter is not taken into account in the simulation.
For completeness, we give a short summary of the ab initio strategy: In the calculation, the aug-cc-pV5Z family of basis sets [176, 201] in combination with the ECP28MDF effective core potential of the Stuttgart/Köln group [177] is used. The ab initio calculations are performed with the MOLPRO software package [178]. To account for the weak van der Waals-type binding between the He and In, a combination of multiconfigurational self consistent field calculations (MCSCF) [179, 182] and multireference

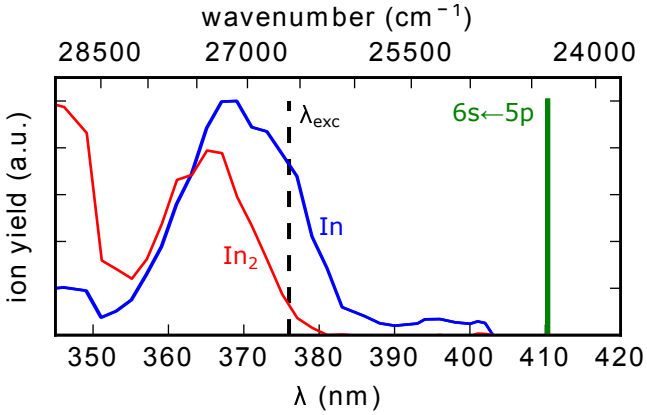

Figure 4.16: Excitation spectrum of the indium monomer (In) and the indium dimer (In_2), both solvated inside He_N. The spectra are measured in a pump-probe experiment with 200 ps time delay and photoion detection at the In monomer mass (115 amu) and the In dimer mass (230 amu), respectively. The pump-probe delay time is sufficiently long that both monomers and dimers are ejected from the droplet and ionized in the gas phase. The spectra were recorded at a higher In pickup temperature as the presented experiments in order to obtain a stronger dimer signal. Additionally, the gas phase In transition (green, solid line) and the applied excitation wavelength (black, dashed line) are indicated.

configuration interaction (MRCI) [181, 186] is applied. The active space of the MRCI approach consists of three valence electrons, the core orbitals are optimized in the MCSCF calculation and kept doubly occupied. The curves are basis set-extrapolated by applying additional calculations with the aug-cc-pVQZ and aug-cc-pVTZ basis set families and the three-point extrapolation formula by Wilson and Dunning [188]. By using the Breit-Pauli operator, the spin-orbit splitting is calculated.

Supplementary Note 3: Numerical error tests for the simulation

The large amount of 270 meV excess energy coupled to the system in the photoexcitation process, which is represented as high blueshift of the in-droplet excitation wavelength with respect to the free atom line (see supporting figure 4.16), is connected to an equally high amount of excited state interaction energy $E_{\mathrm{He_N\text{-}In^*}}$ (figure 3b). This situation requires a careful choice of the simulation parameters in order to avoid numerical errors. For example, the He repulsion by the excited state electronic wave function of the In atom causes a strong increase in the kinetic energy of the He. A correct description of the He movement requires a fine grid size and small time steps, especially within the first few fs, where the acceleration is high. We test for numerical errors by calculating the transient change of $E_{\mathrm{He_N\text{-}In^*}}$ for different grid sizes and different time steps, as shown in Supplementary Figs. 4.18 and 4.19. The grid sizes used for the simulations presented in the paper are 320 pt for simulation of the bubble expansion dynamics (0 to 1 ps) and 256 pt to simulate the bubble oscillation (0 to 100 ps). Supplementary Fig. 4.18c shows that for the short dynamics an increase to 384 pt does not change the interaction energy significantly, while a decrease to 256 pt would introduce errors on the order of about 1%. A similar behavior is observed for the higher timescales (see figure 4.18d), where a grid size of 192 pt introduces numerical errors that are on the order of the simulated energies, whereas nearly no deviation to the grid size of 320 pt is found.
The influence of the time step parameter turned out to be less pronounced, as shown in Supplementary Fig. 4.19c. An increase from 0.10 fs, as used for the shorter bubble expansion simulations, to 0.50 fs gives a slightly stronger change of $E_{\mathrm{He_N\text{-}In^*}}$, as compared to a decrease to 0.05 fs, both of which are, however, in the 10^{-10} eV range. The influence on the simulation for the longer bubble oscillation (simulated with 1 fs steps) is an order of magnitude higher (see Supplementary Fig. 4.19d), but still remains in the 10^{-9} eV

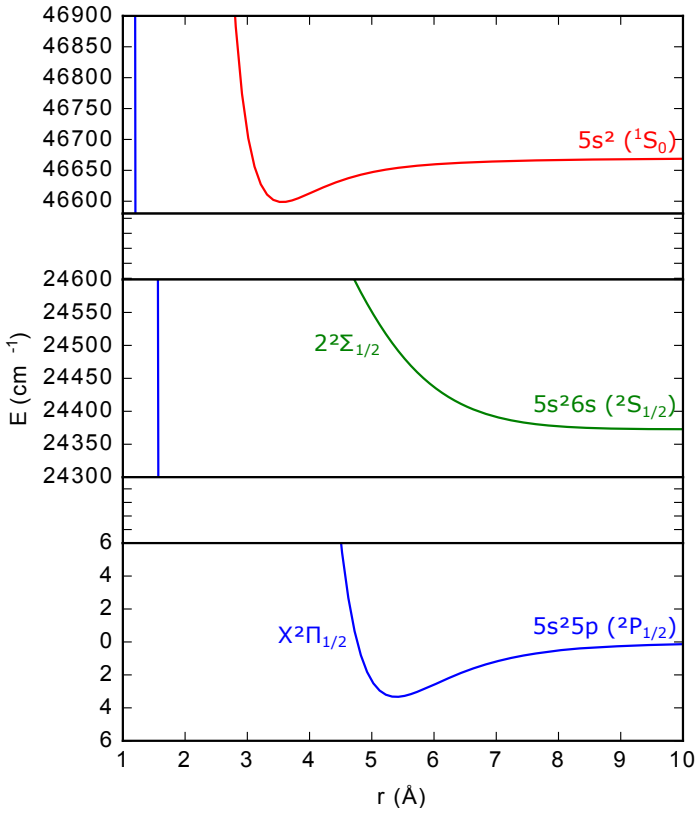

Figure 4.17: Indium-Helium interaction pair potentials used for the DFT and TDDFT simulations. Ground state (blue), first excited state (green) and ionic state (red).

range.

Another important parameter is the cutoff-energy for the different pair potentials, that has to be chosen high enough in order to avoid unphysical He density cumulations and energetic instabilities. The cutoff-energies for the ground state, the excited state and the ionic state potential are chosen with 2150 cm^{-1}, 1008 cm^{-1} and 5560 cm^{-1}, respectively. As the excited state cutoff-energy has the lowest value, different energies around 1008 cm^{-1} were tested with the result that the influence on the excited state interaction energy was below 10^{-10} eV (not shown).

Supplementary Note 4: Bubble dynamics for different locations inside the droplet

Whereas the simulated bubble expansion dynamics at short time delays (<1 ps) show no dependence on the position within the droplet where the dopant is photoexcited, the ejection process and the accompanied bubble oscillation observed at longer time delays are strongly dependent on the photoexcitation position. In Supplementary Figure 4.20a the bubble radius over time for a starting location in the centre of the droplet is shown, revealing a continued oscillation of the solvation shell with a period of about 30 ps and no ejection. This is in contrast to the 20 Å off-centre excitation position, which shows only one contraction, superimposed to an overall increase of the radius due to the ejection. Supplementary Figure 4.20b shows calculated PE peak energies as function of delay time for photoexcitation at various distances to the droplet centre. The counter-propagating trends of bubble radius and PE energy for both the centre and the 20 Å position clearly show that a contracted bubble coincides with an increased PE energy, which is a consequence of the increased In-He interaction energy of smaller bubbles (see figure 1 in

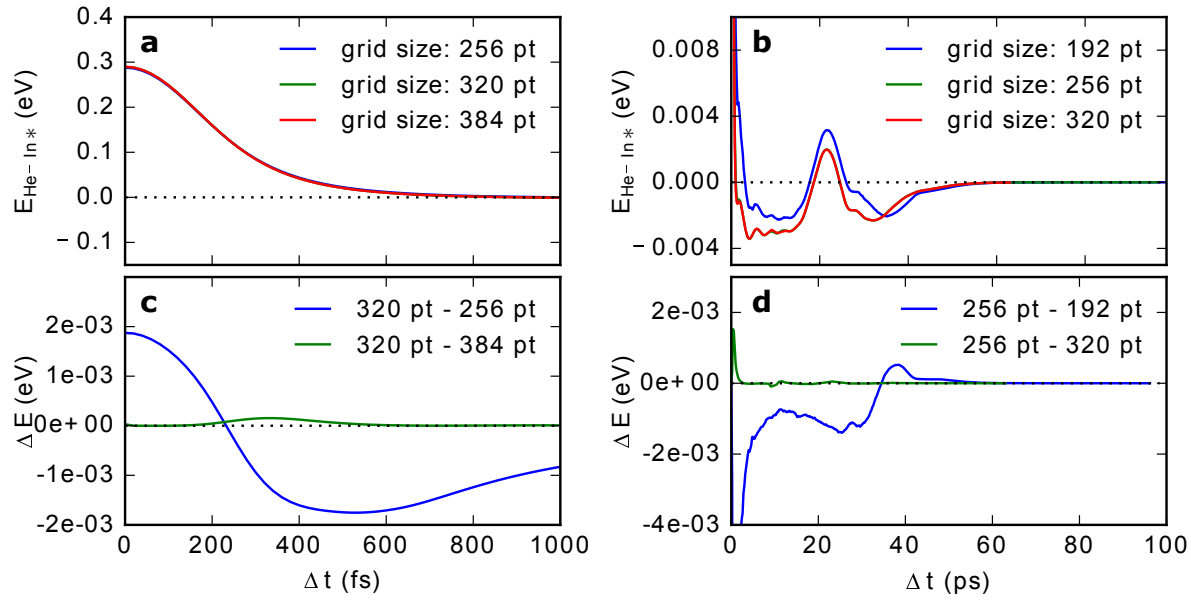

Figure 4.18: Dependence of the excited state interaction energy $E_{\text{He-In}^*}$ on the grid size parameters. (a) $E_{\text{He}_N\text{-In}^*}$ as function of time within the first picosecond for three different grid sizes of 256, 320 and 384 pts, calculated with 0.10 fs time steps. (b) $E_{\text{He}_N\text{-In}^*}$ for higher time delays for grid sizes of 192, 256 and 320 pt, calculated with 1 fs time steps. (c) Difference of interaction energy obtained with 320 pt grid size to that obtained with 256 and 384 pt, respectively. (d) Difference of interaction energy obtained with 256 pt grid size to that obtained with 192 and 320 pt, respectively.

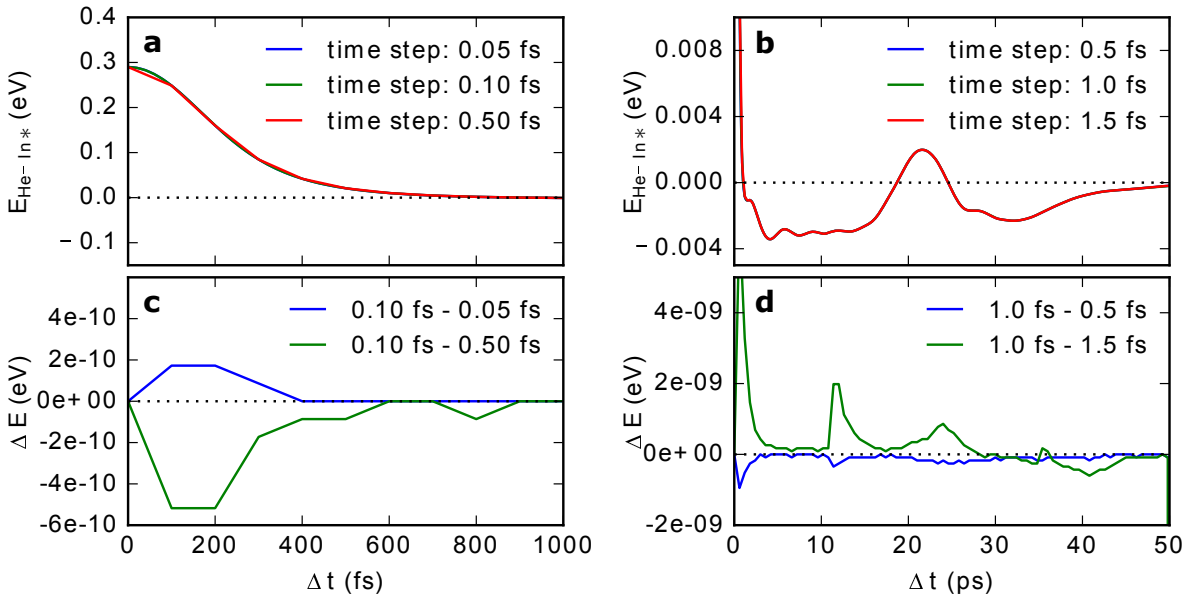

Figure 4.19: Dependence of the excited state interaction energy $E_{\text{He-In}^*}$ on the time step parameter. (a) $E_{\text{He}_N\text{-In}^*}$ within the first picosecond as function of time for three different time steps of 0.50, 0.10 and 0.05 fs, calculated with a grid size of 320 pt. (b) $E_{\text{He}_N\text{-In}^*}$ for higher timedelays for the time steps of 1.5, 1.0 and 0.5 fs, calculated with a grid size of 256 pt. (c) Difference of interaction energy obtained with 0.10 fs to that obtained with 0.50 fs and 0.05 fs, respectively. (d) Difference of interaction energy obtained with 1.0 fs to that obtained with 1.5 fs and 0.5 fs, respectively.

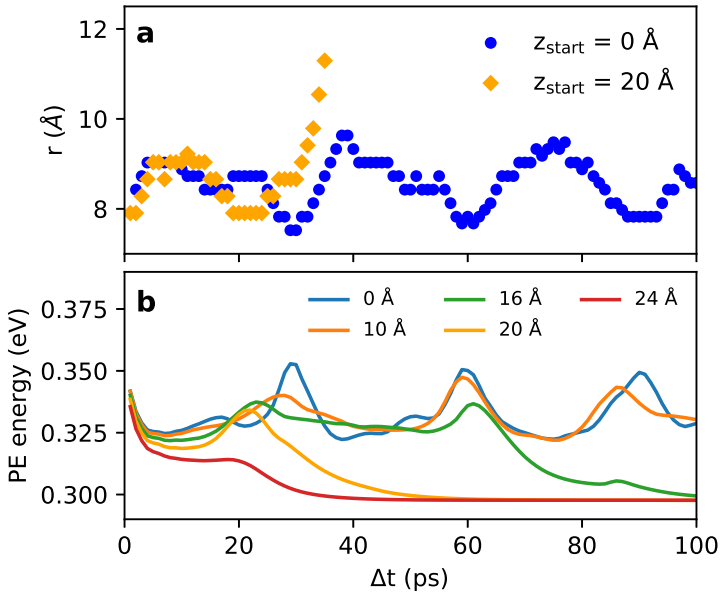

Figure 4.20: Comparison of the simulated In-He_N dynamics for photoexcitation at different positions. The bubble radius as function of time is shown in (a) and the corresponding transient change in photoelectron energy is shown in (b).

the main manuscript). Different appearance times of the first contraction for different starting locations can be explained with the superimposed PE energy decrease due to ejection, as well as effects caused by helium shock-waves that propagate through the droplet following the initial bubble expansion (see Supplementary Movies 2 and 3).
We choose the simulation of the 20 Å starting position for comparison with the measured transient PE peak shift (figure 3 of the main text) because for other locations either multiple or no bubble oscillations are predicted.

Supplementary Note 5: Transient ion yield and PE spectra at long time-delays

Ejection of the indium atoms can further be confirmed by a transient rise of ion yield. Because the ionic In^+-He potential is strongly attractive, the atoms deeply solvate into the droplets when being ionized within or even in the vicinity of the droplets, in which case they are not detected. Only when escaped from the long-range, attractive potential of the droplet they are truly free and are measured [120]. This is seen in the transient ion yield (Supplementary Figure 4.21a), where there is absent signal for the first 40 ps, followed by a signal rise within about 30 ps (to 67% of the maximum). The steady rise is connected to a position (and velocity) distribution of dopants inside the droplets before photoexcitation, resulting in an ensemble that gets ejected, which blurs the ion and electron transients. The same timescale of PE peak shift (figure 3 in main manuscript) and photoion yield rise confirms the correct interpretation of dopant ejection.
Further insight into the ejection process can be obtained from the line shapes of the PE lines. Supplementary Figure 4.21b shows PE spectra obtained from In–He_N at time delays of 0.8 ps (blue line) and 200 ps (red line), as well as for bare In atoms (yellow line). Ionization inside the droplet at 0.8 ps leads to a shift of the PE peak to higher energies with respect to the bare atom due to the reduced ionization potential inside the droplet [60]. The PE spectrum is significantly broader [(62 ± 2) meV, FWHM] compared to that of the bare atom [(35 ± 1) meV, FWHM] (see also figure 3 of the main text), which we ascribe to

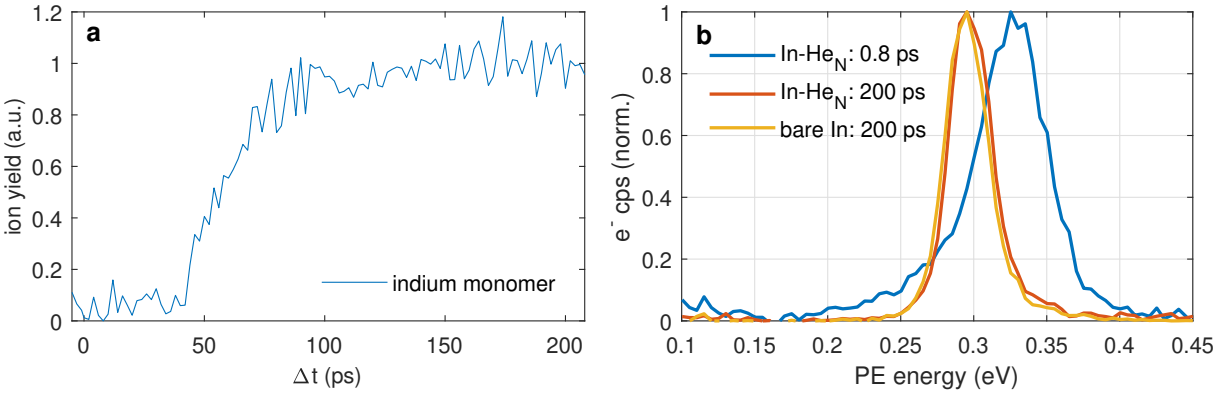

Figure 4.21: Transient photoion yield (a) and comparison of PE spectra at short and long time delays, as well as a PE spectrum of bare In atoms (b). The bare atom spectrum was recorded by deactivating the droplet source and exploiting the effusive In atom beam from the pickup source. The excitation wavelength for the bare indium spectrum was chosen with 410 nm (see Supplementary Figure 4.16).

the Franck–Condon overlap of the excited and ionic potential energy surface inside the droplet. Additionally, the 0.8 ps spectrum shows a wing extending below the bare atom line, representing decelerated electrons [60], as discussed in the results section of the main text. Ionization of the In–He_N system at 200 ps gives exactly the same line shape as the bare atoms, proving that all In atoms are ejected from the droplets.

4.4 Ultrafast photoinduced dynamics of single atoms solvated inside helium nanodroplets

This section consists of the following published publication:

Ultrafast photoinduced dynamics of single atoms solvated inside helium nanodroplets
B. Thaler, P. Heim, L. Treiber, M. Koch*
The Journal of Chemical Physics **152**, 014307, 2020
https://doi.org/10.1063/1.5130145

* corresponding author

contributions	
funding	M. Koch
experimental design	M. Koch
preparation / setup	P. Heim, B. Thaler, M. Koch
data acquisition	B. Thaler, L. Treiber
HeDFT simulations	B. Thaler
data analysis	B. Thaler
interpretation	all authors
publication writing	B. Thaler, M. Koch

Abstract

Helium nanodroplets can serve as reaction containers for photoinduced time-resolved studies of cold, isolated molecular systems that are otherwise inaccessible. Recently, three different dynamical processes, triggered by photoexcitation of a single atom inside a droplet, were observed on their natural time scale: Expansion of the He solvation shell (He bubble) within 600 fs initiates a collective bubble oscillation with ~ 30 ps oscillation period, followed by dopant ejection after ~ 60 ps. Here we present a systematic investigation of these processes by combining time-resolved photoelectron and photoion spectroscopy with time-dependent He density functional theory simulations. By variation of the photoexcitation energy we find that the full excess excitation energy, represented by the blue-shifted in-droplet excitation band, is completely transferred to the He environment during the bubble expansion. Surprisingly, we find that variation of the droplet size has only a minor influence on the ejection time, providing insight into the spatial distribution of the ground-state atoms before photoexcitation. Simulated particle trajectories after photoexcitation are in agreement with experimental observations and suggest that the majority of ground-state atoms are located at around 16 Å below the droplet surface. Bubble expansion and oscillation are purely local effects, depending only on the ultimate dopant environment. These solvation-induced dynamics will be superimposed on intramolecular dynamics of molecular systems and a mechanistic description is fundamental for the interpretation of future experiments.

Introduction

During the past few decades, superfluid helium nanodroplets (He_N) have emerged as a powerful tool in spectroscopy, serving as nanoscale containers for molecules, clusters and fragile complexes [5, 7–9, 103]. The ability of He_N to cool foreign species to the droplet temperature of 0.4 K enables, for example, the formation and investigation of weakly bound metastable complexes [54, 202], the stabilization of radicals [203], or the formation of complex structures via sequential pickup techniques [13, 204]. Additionally, He_N enable the generation of a controlled microsolvation environment [14, 15] by successively adding solvent molecules, bridging from gas phase to solution while observing changes of molecular properties.
While most studies in He_N have applied frequency resolved "static" spectroscopy, in recent years also femtosecond time-resolved studies have become an emerging research branch [6, 25–27, 36, 41, 44, 108, 205], motivated by the prospect to directly study dynamics in the mentioned tailor-made systems. Time-resolved photoelectron spectroscopy, a powerful technique to investigate coupled electronic and nuclear processes in gas phase molecules [50, 196], has recently proven its suitability to trace ultrafast dynamics in the droplet's interior [32, 37, 98, 108]. A mechanistic description of the primary processes triggered by photoexcitation can be obtained by combining time-resolved photoelectron and photoion spectroscopy with time-dependent density functional theory (TDDFT) simulations, as exemplified for fully solvated indium (In) atoms [108]. In their electronic ground state, dopants inside He_N reside in a solvation bubble, as consequence of repulsive Pauli interactions between the valence electrons and the helium. Photoexcitation causes a radial expansion of its valence orbital, which increases the repulsive interactions and initiates three main processes:
(I) Bubble expansion: The extra energy, which is needed for in-droplet excitation due to the repulsive excited state interactions, is converted into kinetic energy of the solvation-bubble expansion within a few hundred femtoseconds. During this relaxation the excited state energy decreases, resulting in a transient PE peak shift of a few hundred meV.
(II) Bubble oscillation: After the expansion, a breathing oscillation of the bubble is initiated, leading to

a temporary PE energy increase around 30 ps.
(III) Ejection: Within about 60 ps, the dopant is ejected from the droplet, which is measured as ongoing PE energy shift to lower energies, as the ionization potential inside He_N is lowered compared to the bare atom. As complementary observable, photoions show a transient increase in ion yield, with absent signals during the first 50 ps. Because of strong attractive interactions of the cation with helium, ionization at early time-delays leads to ion recapture, suppressing the detection. At higher time-delays the ion yield increases gradually, representing the initial atom distribution inside the droplet, which leads to the gradual ion yield increase and PE energy decrease.
As the described processes will be superimposed on intrinsic dynamics of molecules and aggregates in He_N, it is important to have a detailed understanding of the solvent induced dynamics. Subsequent to photoexcitation of dopants inside He_N, large amounts of excess energy are converted from electronic, potential energy into nuclear, kinetic energy. It remains to be answered, how the amount of excitation energy influences processes I-III. Additionally it is still unclear, if the described processes only depend on the local environment. At different locations within the droplet, the dopant might experience different amounts of He interaction, influencing the observed dynamics. To answer these questions, we extend our previous work on the In–He_N system and perform time-resolved PE and photoion spectroscopy under variation of droplet size and excitation energy, and support our experiments with TDDFT simulations.

Methods

Experimental setup: Helium nanodroplets are generated via continuous supersonic expansion of high purity (99.9999%) helium gas through a 5 μm diameter nozzle at different nozzle temperatures (T_{nozzle}) between 10 and 20 K, and 40 bar stagnation pressure. Mean numbers of He atoms for the chosen temperatures range from 2600 to 40000 [94], for 20 and 10 K respectively, and lie therefore mostly within the subcritical and slightly in the supercritical regime of He droplet generation [5]. In combination with evaporative cooling, the expansion process leads to the formation of liquid droplets at temperatures of about 0.4 K, well below the superfluid phase transition of helium. After the source chamber, the droplets pass through a pickup-cell, where In metal is vaporized in resistively heated crucibles and picked up by the droplets. The oven temperatures are optimized for single-atom pickup. After passing a differential pumping section, the doped droplets enter the measurement chamber, where they are crossed at right angles by femtosecond laser pulses inside the extraction region of a linear time-of-flight spectrometer (0.5 m).
The laser system consists of a commercial Ti:sapphire oscillator (Coherent Vitara) and dual stage amplifier (Coherent Legend Elite Duo) that delivers pulses of 25 fs duration at a repetition rate of 3000 Hz with a center wavelength of 800 nm and a pulse energy of 4 mJ. Pulses are split into a pump and a probe path and probe pulses are guided over a motorized delay line to obtain variable time delays between the two paths. Pump pulses are frequency-upconverted to wavelengths between 360 and 380 nm (3.44 and 3.26 eV, respectively) via a combination of optical parametric amplification and subsequent frequency quadrupling (Coherent OPerA Solo). Probe pulses are frequency doubled to 405 nm (3.06 eV) in nonlinear optical crystals. A 1 mm BBO crystal is used for the measurements of short time scale dynamics (yielding 25 meV FWHM). For measurements at longer time scales, which need a better energy resolution, a 5 mm LBO-crystal (10 meV FWHM) is used. Pump and probe paths are spatially overlapped and focused into the measurement chamber with a 1000 mm fused silica lens.

Data acquisition and analysis: By measuring the flight times, ion charge-to-mass ratios and PE

kinetic energies are retrieved. For electron detection, the spectrometer is operated in a magnetic bottle type configuration to ensure a high collection efficiency; a small positive repeller voltage is applied for slight electron deceleration to achieve a sufficient energy resolution. Ions are pushed into the flight tube via a high voltage of 2 kV.
Because the recorded PE spectra consist of only a single peak (ionization from the $6^2S_{1/2}$ state), we fit each spectrum with a single Gaussian function.

TDDFT simulations: The He density functional approach has been widely used to describe static and dynamic interactions of impurities with the superfluid, detailed descriptions are given elsewhere [29, 93, 106]. All simulations are performed with the BCN-TLS-He-DFT computation package [105]. In short, as basic ingredients for the simulation serve the In-He pair interaction potentials for In in its ground ($^2P_{1/2}$), first excited ($^2S_{1/2}$, $E_{\mathrm{In}^*-\mathrm{He}}$) and ionic state ($^1S_0$, $E_{\mathrm{In}^+-\mathrm{He}}$), which are taken from Ref. [108]. Starting point for the time-dependent computations are converged He densities from static calculations with In in its electronic ground state located at a fixed position inside the droplet. With this starting configuration, the TDDFT simulations are started by instantaneous switching to the excited state pair potential, justified by our experimental situation of ultrashort laser pulse excitation. During the computation, the coupled TDDFT equations for the superfluid (with the helium density ρ_{He} as parameter) and the classical equations of motion for the impurity are solved. He-He interactions are accounted for with the parametrized Orsay-Trento He-functional [107], including the solid term [200] to consider the strong impurity interaction. During consecutive time-steps, we record the He density weighted interaction energies between In and the whole droplet for the excited and the ionic state. The difference of the two is a measure for the droplet-induced shift in ionization energy ($\Delta E_{\mathrm{I.E.}}$) and therefore the shift one expects in the PE energy after ionization. For a given probe photon energy $h\nu$ and a bare atom binding energy $E_{\mathrm{bind,6S}}$ of the $6^2S_{1/2}$, one can calculate the simulated PE energy (E_{PE}) with:

$$\begin{aligned} E_{\mathrm{PE}}(t) &= h\nu - E_{\mathrm{bind,6S}} + \Delta E_{\mathrm{I.E.}} \\ &= h\nu - E_{\mathrm{bind,6S}} + \Big[\int \rho_{\mathrm{He}}(\mathrm{r},\mathrm{t}) E_{\mathrm{In}^*-\mathrm{He}}(\mathrm{r}-\mathrm{r}_{\mathrm{In}}(\mathrm{t})) d^3r \\ &\quad - \int \rho_{\mathrm{He}}(\mathrm{r},\mathrm{t}) E_{\mathrm{In}^+-\mathrm{He}}(\mathrm{r}-\mathrm{r}_{\mathrm{In}}(\mathrm{t})) d^3r \Big] \end{aligned} \tag{4.3}$$

For the dynamics ranging up to 1 ps we use discretized boxes ranging from 80 Å length to 116 Å with grid sizes from 320 points to 384 points, for droplet sizes between 1000 and 8000 He atoms, respectively. For the sake of computational cost only a droplet size up to about 8000 atoms is simulated, which is however far lower than the largest droplets experimentally accessible within this work (approx. 40000 atoms, for 10 K nozzle temperature). Time steps are chosen with 0.1 fs. For dynamics at higher time delays, smaller grids of 256 points and time steps of 1 fs are used.

Results

In the following we first present the dependence of In–$\mathrm{He_N}$ dynamics on the photoexcitation energy and on the droplet size, in both cases separately for short time scales ($0-1$ ps, bubble expansion) and long time scales ($0-200$ ps, bubble oscillation and dopant ejection). These experimental results are followed by simulated PE energy transients for different starting locations within the droplet, which are obtained from TDDFT calculations.

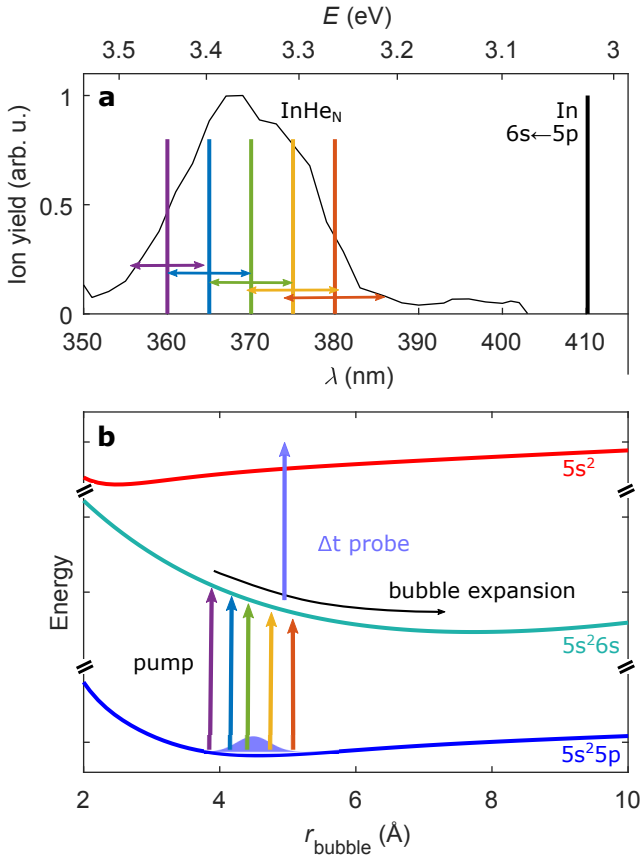

Figure 4.22: Pump-probe photoionization of the In–He_N system. Panel (a) shows the excitation band of the In 6s←5p transition inside He_N around 370 nm (3.35 eV), which is blue-shifted by about 0.3 eV with respect to the bare-atom transition at 410 nm (3.02 eV) [98]. Vertical colored lines mark the chosen excitation wavelengths, horizontal arrows indicate the spectral FWHMs; the black line indicates the bare atom transition. Panel (b) schematically shows the potential energy of the In–He_N system as function of the bubble radius r_{bubble}. 6s←5p excitation proceeds to a highly repulsive region, causing the bubble to expand.

Photoexcitation energy variation

Fig. 4.22a shows the excitation band of the In 6s←5p transition inside He_N. The strong blue-shift with respect to the bare atom transition is a consequence of repulsive interaction between the extended electron density of the excited In atom and the surrounding helium. Fig. 4.22b shows the In–He_N pseudo-diatomic potential energy as function of the bubble radius. The ground state equilibrium lies around 4.5 Å [108], a bubble size where the excited state potential is highly repulsive. The width of the excitation band can be explained with excitations at different initial radii, according to the probability distribution in the ground state. We perform pump-probe measurements with five pump wavelengths, equally distributed over the excitation band, to study the excitation energy dependence of the In–He_N dynamics.
Time-resolved PE spectra representing the bubble expansion within the first picosecond after photoexcitation for the different excitation wavelengths are shown in Fig. 4.23. Each spectrum exhibits a strong signal around time zero, the root cause of which is unknown. We speculate that nonlinear multiphoton ionization and/or increased ionization probabilities at small bubble radii may contribute to this signal enhancement. The cross correlation is followed by a transient shift of the PE energy to lower energies

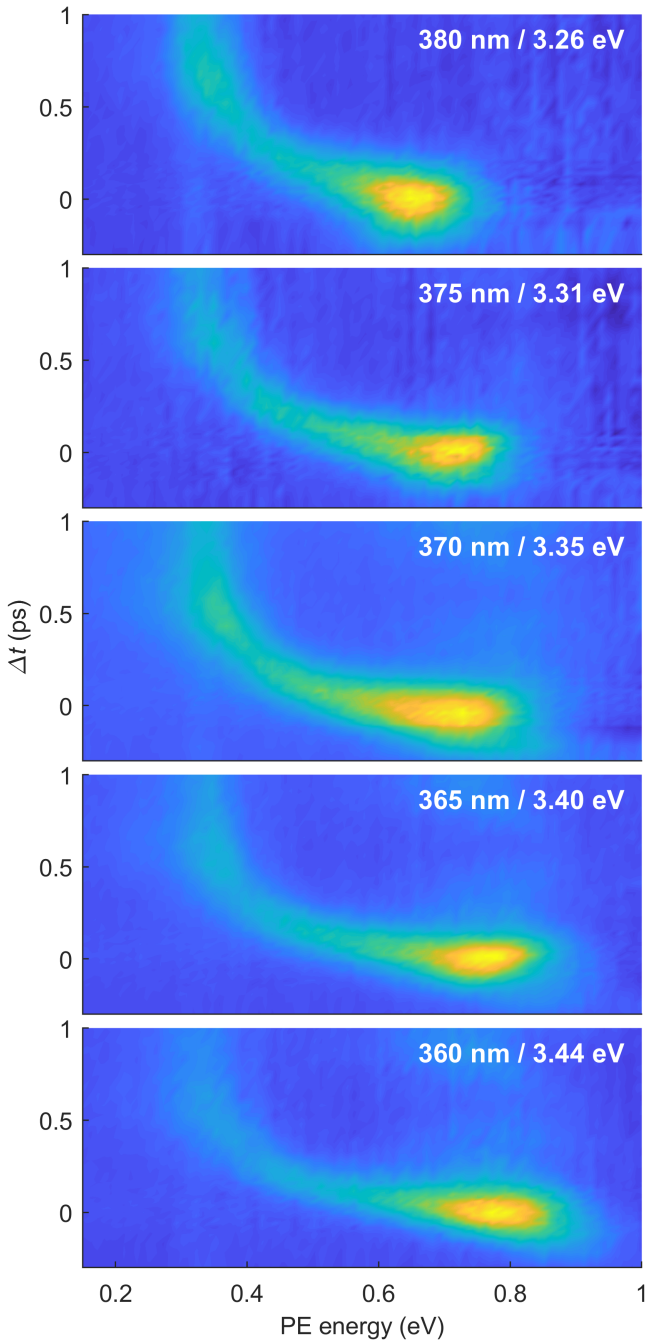

Figure 4.23: Excitation energy dependence of the short time scale dynamics. Time-resolved PE transients up to a time delay of $\Delta t = 1$ ps are shown for various excitation wavelengths, obtained with $T_{\mathrm{nozzle}} = 18$ K.

within a few hundred fs, as consequence of the bubble expansion. With increasing photoexcitation energy, the PE energy maximum at time zero shifts, as expected, to higher values ranging from (0.79 ± 0.02) to (0.65 ± 0.02) eV, for 360 and 380 nm, respectively. The energy difference of the time-zero energy peak of ~ 0.15 eV is slightly lower than the expected photon energy difference of ~ 0.20 eV. This small discrepancy might be explained with the spectral width of the pump pulses, causing excitation preferably within spectral regions with higher oscillator strengths closer to the center of the band, especially for the

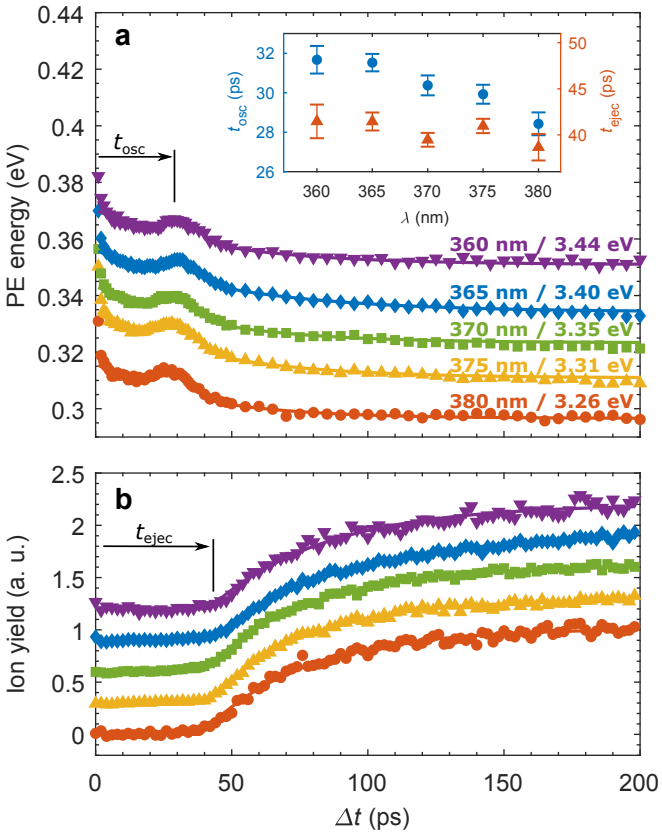

Figure 4.24: Excitation energy dependence of the long time scale dynamics (T_{nozzle} = 18 K). Panel (a) shows transient PE peak positions for time delays up to 200 ps, Panel (b) shows corresponding In ion yields. The inset in (a) shows the values for the oscillation maximum, t_{osc}, and the ion yield rise onset, t_{ejec}, as determined by fitting Eqs. 4.4 and 4.5 to the transients in panel (a) and (b), respectively. Error bars indicate the 95% confidence intervals. Note that data points in both panels for each wavelength are offset to each other for better visualization.

two measurements at the band edges (Fig. 4.22).

Up to 1 ps time delay, the PE energies for all excitation energies shift to 0.32 eV, which is approximately 0.03 eV above the gas phase transition, representing the remaining solvation energy differences of the excited and ionic state inside the droplet. The excess energy connected to the droplet-induced blue-shift is apparently fully transferred to the He surrounding during the bubble expansion within the first $\sim$ 600 fs. A comparison of the time duration for the PE peak shift reveals a faster energy decrease for smaller excitation wavelengths (higher excitation energies). This trend becomes evident by comparison of the initial slopes ($\Delta E/\Delta t$) of the shift curves in Fig. 4.23; e.g. the 360 nm slope is about twice as large as the one at 380 nm. The time spans for about 50% of the total PE shift are 130 and 180 fs, for 360 and 380 nm, respectively. This observation is in agreement with an increasing steepness of the excited state potential energy, corresponding to faster accelerations of the excited state wave packet obtained with higher excitation energies.

We now turn to the discussion of long time scale dynamics, namely the dependence of bubble oscillation and dopant ejection on the excitation energy. Fig. 4.24a shows the transient PE peak positions up to 200 ps, exhibiting a gradual decrease to the bare atom energy, as consequence of dopant ejection. At around 30 ps a temporary increase of PE energy is measured, representing the first bubble contraction

of the initiated breathing mode oscillation [108]. To quantitatively compare the contraction time for the different transient curves, we fit the time-resolved PE peak positions $E(t)$ with the sum of an exponential decrease with the time constant τ_e and a temporary Gaussian function centered around the oscillation maximum at t_{osc}:

$$E(t) = E_\infty + E_0 e^{-t/\tau_e} + A e^{-(t-t_{osc})^2/(2\sigma^2)}. \tag{4.4}$$

For the fit, the time interval between 3 and 120 ps is used. The inset in Fig. 4.24 shows the resulting values of t_{osc} for the different excitation wavelengths. As can be seen, t_{osc} slightly decreases by 10% from (31.7 ± 0.7) to (28.4 ± 0.6) ps for wavelengths from 360 to 380 nm, respectively. Apparently, a higher energy deposition into the initiation of the collective bubble oscillation causes a longer oscillation period. For a quantitative analysis of the excitation wavelength on the ejection process, we measure the ion yield, an observable with higher sensitivity to the dopant ejection process. The ion yield transients (Fig. 4.24b) are fitted to an exponential increase multiplied by a Heaviside step function Θ, to retain the characteristic ejection time t_{ejec}:

$$\text{Ion yield}(t) = \Theta(t - t_{ejec}) \times I_\infty(1 - e^{-(t-t_{ejec})/\tau_i}), \tag{4.5}$$

where τ_i is the characteristic time constant of the ion yield increase, representing the gradual increase due to different ejection times for different starting locations of the measured ensemble. The inset in Fig. 4.24a shows the resulting ejection times t_{ejec} for various excitation wavelengths. There is no systematic correlation, indicating that the photoexcitation energy has no influence on the ejection dynamics. We mention that the time constants τ_e (Eq. 4.4) and τ_i (Eq. 4.5) are also not significantly influenced by the excitation wavelength (not shown).

Droplet size variation

Fig. 4.25a shows the PE energy transients of the short time scale dynamics for T_{nozzle} ranging from 12 to 20 K, covering a droplet size range $\bar{N}$ from 22000 to 2600. The transients suggest that there is no influence of the droplet size on the bubble expansion dynamics, as the curves are nearly parallel. This is supported by TDDFT simulations of the PE energy shift (Fig. 4.25b), which predict very similar PE peak transients for droplet sizes from $N = 1000$ to $N = 8000$, with the impurity placed in the droplet center. This independence of the droplet size shows that the bubble expansion is a purely local process that only depends on the fluid density in the direct vicinity of the impurity (solvation shell), which is constant within the droplet (Fig. 4.27) and independent of droplet size.
Fig. 4.26a shows the transient PE energy up to 200 ps for droplet sizes from $\bar{N} = 2600$ to 40000. Surprisingly, the overall form of the transients is very similar also for the long time scale dynamics. The curves are again fitted with Eq. 4.4, with a fit interval between 3 and 200 ps. The retrieved oscillation times t_{osc} are plotted in the inset of Fig. 4.26a. As can be seen, there is a 20% increase of t_{osc} from (28 ± 1) to (34 ± 2) ps, corresponding to an oscillation frequency decrease, for a decreasing nozzle temperature from 20 to 10 K. We note that the trend in t_{osc} might be biased because of slightly different ejection times, resulting in different helium densities at the moment of oscillation (see discussion section below). Closer inspection additionally reveals that the bubble oscillation amplitude increases for larger droplets. The similarity of the PE transients above 50 ps (Fig. 4.26) suggests that the ejection dynamic is only marginally influenced by the droplet size, a behaviour that is confirmed by the transient ion yields (Fig. 4.26b). The inset in Fig. 4.26a compares the fitted ejection times t_{ejec} (Eq. 4.5), showing a 60% rise of t_{ejec} from (32 ± 4) ps for the smallest, to (52 ± 1) ps for the largest droplets. This increase has to be contrasted to the much larger increase of the droplet radius by 150% from 30 Å ($\bar{N} = 2600$) to 75 Å ($\bar{N} = 40000$). One would expect that a second bubble oscillation becomes observable as the droplet

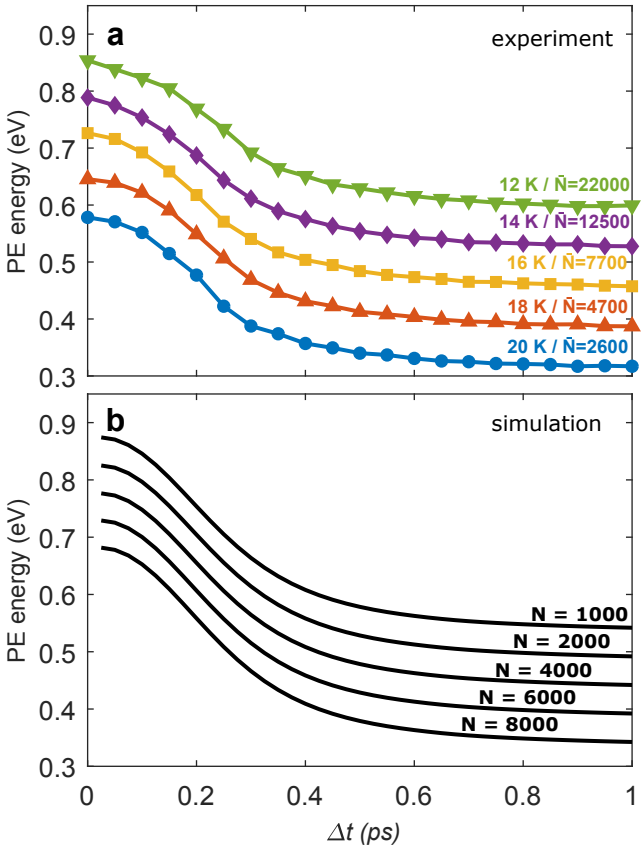

Figure 4.25: Droplet size dependence of the short time scale dynamics, obtained with 375 nm (3.31 eV) excitation wavelength. Panel (a) shows the measured PE transients as obtained by Gaussian fits, panel (b) shows simulated PE transients obtained with TDDFT, with the impurity placed in the center of the droplet. Note that the curves in all panels have been manually offset to each other.

radius is more than doubled, under the assumption that a significant fraction of In atoms are located in the center region of the droplet. To gain further insight into this question, we perform time-resolved simulations of the photoexcitation dynamics, which are presented in the following.

Trajectory analysis with TDDFT

We calculate dynamics of the In–He_N system for different dopant locations at the instant of photoexcitation, Fig. 4.27a shows the different trajectories of excited In atoms within a He_{4000} (36 Å radius). As can be seen, impurities placed closer than 16 Å to the droplet center show no ejection from the droplet within 100 ps. At longer time-delays, all impurities which are slightly displaced from the center will eventually be ejected, however the simulated time span is too short to observe this effect. The simulations indicate that the dopant velocity depends very non-linearly on the dopant position. This dependence seems to be a consequence of only small forces in the interior, with low radial He density differences, and an acceleration as the dopant reaches the surface region in which the He density decreases. We assume the atoms to be at rest before photoexcitation, which is justified by the following assumption: Possible velocities in the droplet center should be on the order of 10^{-2} Å/ps, assuming 0.4 K temperature and $(k_BT)/2$ kinetic energy in radial direction, which is too small to significantly influence the dynamics.
Figs. 4.27c and 4.27d show simulated PE energies for the different starting locations at short and long time

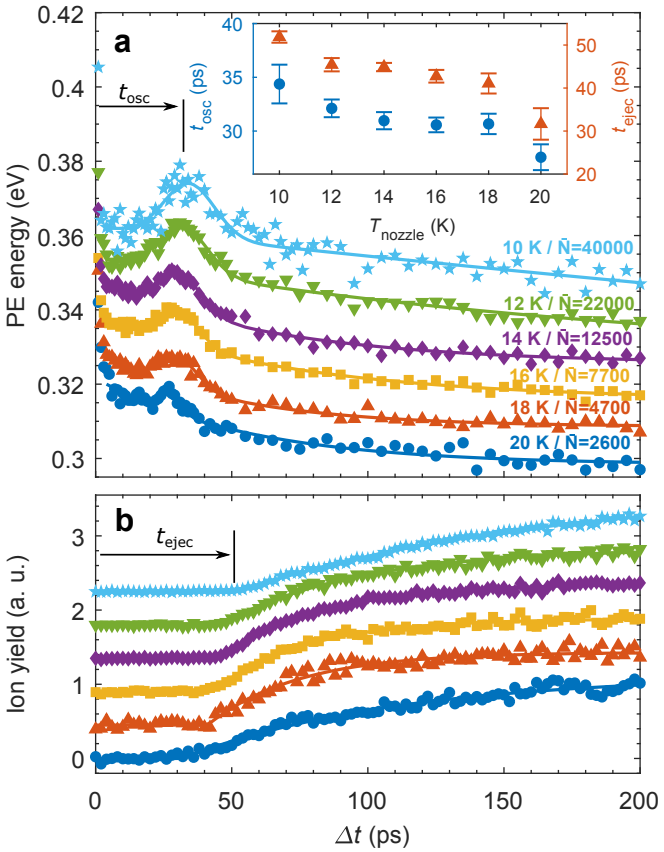

Figure 4.26: Droplet size dependence of the long time scale dynamics, obtained with 375 nm (3.31 eV) excitation wavelength. Panel (a) shows the PE energies and panel (b) shows the ion yields for different nozzle temperatures. The inset in panel (a) shows the fit constants for the oscillation time t_{osc} and the ejection time t_{ejec}. Note that the curves in all panels have been manually offset to each other.

scales, respectively. The bubble expansion (Fig. 4.27c) is independent of the starting location, which is in line with our previous assumption of a purely local process. The expansion dynamics are only influenced by the impurity's surrounding He density, which is similar for all chosen trajectories, as visualized by the inner plateau of the pure droplet density profile (grey shaded area in Fig. 4.27a). In contrast to the short time scale, the dynamics on longer time scales exhibit a significant dependency on the starting location (Fig. 4.27d). Whereas PE transients for trajectories starting around 20 Å show a PE energy decrease accompanied by a single temporary increase due to the bubble contraction, trajectories for impurities positioned closer than 16 Å to the center show no ejection and multiple, isolated bubble oscillations. Deviating oscillation periods between different trajectories can be explained with lower helium densities at the moment of contraction for impurities that leave the droplet. By analogy with the experimental oscillation period increase for bigger droplets (Fig. 4.26a), higher He densities lead to reduced oscillation frequencies, as well as increased amplitudes.

To compare the selected trajectories to the experimentally observed photoion transients (Fig. 4.26b), we analyze the potential energies E_{In^+}, which are obtained by integrating the In^+-He interaction over the He density for every time step, in analogy to Eq. 4.3. Fig. 4.27b shows E_{In^+} for different trajectories (dashed lines), the potentials are found to be extremely attractive in the droplet's vicinity due to the strong ionic attraction to He. Fig. 4.27b also shows transient negative kinetic energies $E_{kin,z}$ of selected trajectories

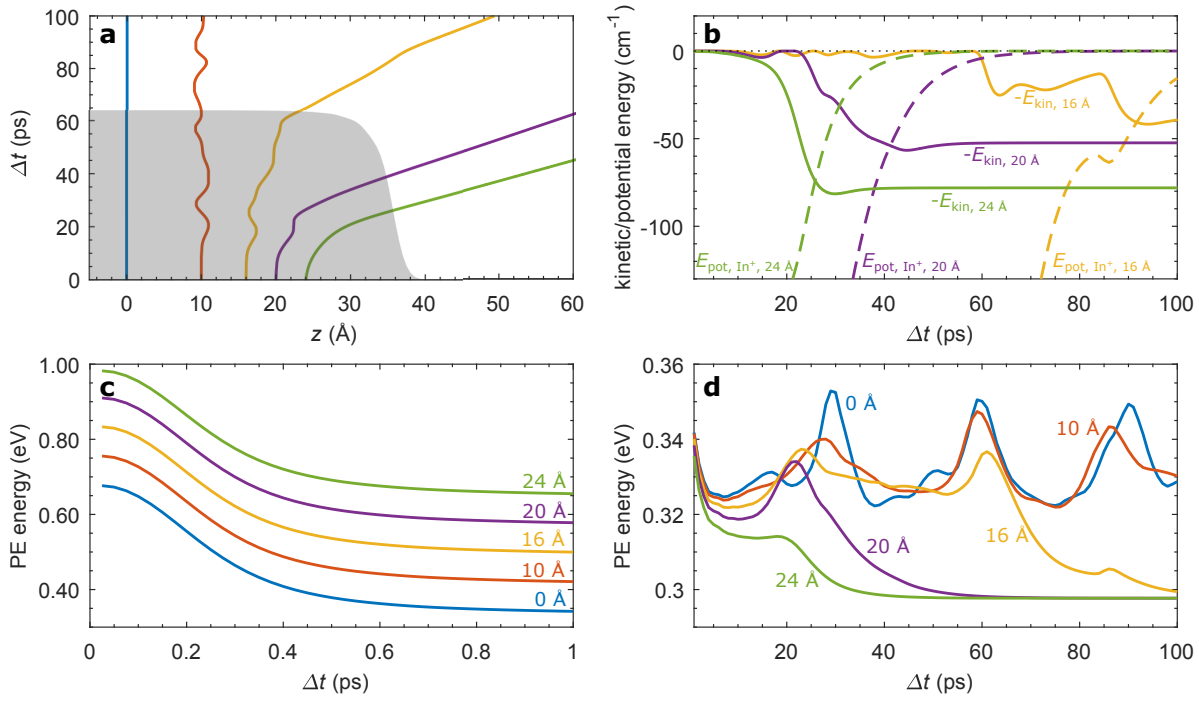

Figure 4.27: Trajectories and simulated transient PE energies, obtained with time-dependent He density functional theory for a droplet of 4000 atoms. Panel (a) shows simulated trajectories of an In atom started at different positions, the pure density profile of the droplet is indicated as grey shaded area. Panel (b) shows the kinetic energies of three selected trajectories, together with the transient In^+ potential energies. Panels (c) and (d) show simulated PE energies for short and long time scales, respectively, curves are labeled with the respective initial positions of the trajectories. Note that the curves in panel (c) have been manually offset to each other.

for the impurity still in the neutral, excited state. We define as condition for detection when the kinetic energy is sufficiently high to escape the attractive ionic potential, and therefore $-E_{\mathrm{kin}} < E_{\mathrm{In^+}}$ (which is at the intersection of the kinetic with the potential energy curve in Fig. 4.27). After this point in the trajectory, the impurity is able to escape the helium droplet potential, even after ionization. As $E_{\mathrm{In^+}}$ is strongly negative in the direct vicinity of the droplet, ion detection is hindered at short pump-probe delays, leading to the region of zero signal in the transient ion yield (Figs. 4.24b and 4.26b). For the trajectories started at 16, 20 and 24 Å, ion appearance times of 92, 41 and 26 ps are obtained, respectively. These times are, especially for the trajectory started at 20 Å, reasonably close to the fitted onset time value (t_{ejec}) of around 40 ps (Fig. 4.24). As the trajectory at 20 Å also exhibits a very similar transient PE energy (Fig. 4.27d) as in the experiment (Fig. 4.26), we assign it to be closest to the real situation for this droplet size.

Discussion

In combination, the experimental and theoretical results presented above provide unique insight into the spatial distribution of dopant atoms at the moment of photoexcitation, as well as the transfer of excess potential energy from the dopant to kinetic energy of the solvent, both of which are discussed in the following. The spatial probability distribution of ground state In atoms seems to be not significantly high in the region of the droplet center, but rather confined within a spherical shell beneath the droplet surface.

The strongest indication for this assumption comes from the surprisingly weak influence of the droplet size on the In-He_N ejection time scales (Fig. 4.26). An increase of the droplet radius by 150% only yields a 60% increase of the ejection time, which is defined as appearance time of the first ejected atoms. Moreover, we observe only a single bubble oscillation for all investigated droplet sizes ($\bar{N} = 2600 - 40000$), showing that after ~ 50 ps the vast majority of excited dopants has left the droplets. We note that transient photoion yields are affected by the recapture dynamics of ionized species, whereas PE transients directly resemble the dynamics of the neutral state, thereby giving more direct insights into the ejection process. The TDDFT trajectory simulations support our interpretation by predicting that only trajectories starting at $\lesssim 20$ Å beneath the surface will leave the droplet within 100 ps (Fig. 4.27a). Additionally, the simulated PE energy shift of the trajectory starting ~ 16 Å below the surface (Fig. 4.27d, 20 Å trajectory) yields the best agreement with the experiment (Fig. 4.26a), as it is the only trajectory with one complete bubble oscillation before ejection. Our interpretation of dopant location agrees with previously calculated dopant probability density profiles resulting from solvation-potentials of atoms [145, 190, 206, 207] and molecules [208, 209], where the probability maximum was mostly found between the center and the surface. For the In–He_N system in particular, where quantitative agreement with the radial probability density is found [98], we note however, that the solvation-potential and thus the probability distribution are subject to significant uncertainties.

Despite the insensitivity of the observed dynamics to the droplet size, we nevertheless observe weak influences, manifested as slight increase of the bubble oscillation period, as well as an increase of the corresponding PE energy amplitude with larger droplets (Fig. 4.26). These observations can be explained with slightly different interaction times of the In atom with the He solvent. As the bubble contraction takes place around times where dopants are about to leave the droplet (see Supplementary Movie 2 of Ref. [108]), longer ejection times for larger droplets increase the number of atoms that can accomplish a complete oscillation. On average, the He density that surrounds the In atom increases for larger droplets, causing first, a stronger reduction of the ionization potential due to more atom-He interactions, which increases the PE energy, and second, changes in surface tension and He oscillator mass, which affect the oscillation period.

We assign the fastest solvent response to impurity photoexcitation, namely the bubble expansion, to be a purely local process, independent of dopant location. Assuming an atom location in the ground state at least 10 Å below the surface explains the missing dependence of the expansion dynamics on the droplet size (Fig. 4.25a), as the helium density profile flattens after a few Å below the surface (Fig. 4.27a) and the relaxed bubble radius lies around 8 Å [108]. The local character of the expansion process is further evidenced by the identical form of simulated PE energies for different droplet sizes (Fig. 4.25b), as well as for various atom starting positions (Fig. 4.27c).

In contrast, the amount of excess energy shows a pronounced influence on the bubble dynamics: An increased excitation energy, indicated through the blue shift with respect to the bare-atom transition, leads, first, to faster energetic relaxations (Fig. 4.23) and, second, to slightly longer bubble oscillation periods (Fig. 4.24a). The faster bubble expansion with higher excitation energy is easily explained with an increasing steepness of the excited state potential (Fig. 4.22a). The oscillation period increase might be indicative of oscillation in an anharmonic potential, where an increase of the oscillation energy leads to an increase in oscillation periods: During the bubble expansion, energy is dissipated into kinetic energy of He density waves. After this process the system will end up with a certain amount of residual energy within a local minimum of the excited state potential (compare Fig. 4.22b). An increase of this remaining energy with the photoexcitation energy would explain the observed trend. Nearly all excess energy is however still converted into He kinetic energy, also leading to an independence of ejection duration on excitation energy: Both the PE energy decay (Fig. 4.24a) and the ejection times (Fig. 4.24b) are equal

for all excitation wavelengths. Our findings for fully solvated atoms thus contrast with results obtained for alkali-metal atoms on the droplet surface [25, 26]. For Rb atoms, photoinduced desorption times vary between 0.5 and 100 ps, depending on the excited state, its geometry and the excess energy within the excitation band [25]. This comparison clearly indicates that in the droplet interior the momentum of the dopant is not changed in consequence of the symmetric bubble expansion. In contrast, species located in a dimple on the droplet surface gain momentum due to a very asymmetric solvation layer expansion in response to photoexcitation, leading to the observed energy dependent ejection.

Conclusion

We performed a detailed study on photoinduced processes of single In atoms fully solvated inside He_N. By applying time-resolved photoelectron and photoion spectroscopy we investigated the influence of droplet size and excitation energy on the photoexcitation dynamics. In combination with TDDFT simulations, we could confirm and extend the mechanistic model, which groups the dynamic processes into the three steps of bubble expansion, bubble oscillation and dopant ejection: First, indium in its electronic ground state was found to reside close to the droplet surface, a geometry that only slightly changes with droplet size and therefore only slightly longer ejection times could be measured for larger droplets. Second, dynamics related to the solvation shell, like the bubble expansion, turned out to be purely local effects and are therefore not influenced by the system geometry. Third, the excess energy required for photoexcitation inside the droplet, corresponding to the blue-shifted excitation band, is fully converted into kinetic energy of the surrounding He within the first picosecond.
The presented measurements of time-resolved ejection dynamics in combination with TDDFT trajectory analysis provide insight into the spatial distribution of single, ground state dopant atoms or molecules in the interior of He_N. Such measurements could therefore also be a benchmark for theoretical predictions of solvation potentials for ground state dopants, enabling further insights into their kinetics and thermodynamics.
Our results also pave the way for investigations of more complex dynamics in larger systems, which can be readily synthesized inside He_N. Following photoexcitation, the droplet-induced processes will be superimposed to any intramolecular dynamics [168]. A detailed understanding of, for example, the system-droplet excess energy transfer rates, or the system location within the droplet, will be crucial in the interpretation of such studies.

4.5 Femtosecond electronic relaxation dynamics in helium nanodroplets

After the complete characterization of dynamics proceeding in the first excited state of In ($^2S_{1/2}$), experiments regarding higher excited states were started. The density of electronic states in atoms and molecules increases with energy. For the case of solvation inside He_N, the coupling of the chromophore to the solvent leads to the formation of In^*-He_n (with n=1,2,3...) potential energy surfaces (exciplexes) that should lead to relaxation channels through curve crossings. In static experiments, such relaxation processes have been described in several experiments on metal atoms in the droplet interior [59, 63, 65, 67, 69, 70, 72], and for the case of Al, even an upper temporal limit of 50 ps for the radiationless decay could be estimated [63].

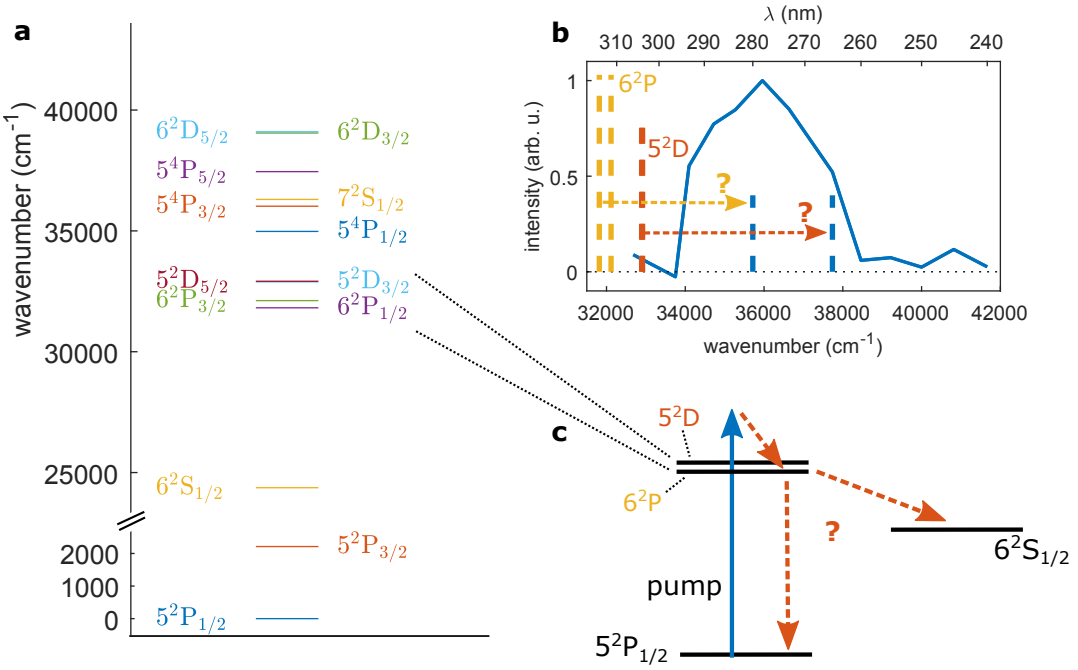

Figure 4.28: Overview of the energetic structure of In and expected relaxation pathways in He_N. Panel **a** shows the Jablonski diagram of In, panel **b** shows the measured excitation spectrum in the high energetic region. Possible candidates that might be excited within this spectrum are the 6^2P and the 5^2D manifold, which bare atom excitation energies are indicated, as well as probable blue-shifts to the applied excitation wavelengths of 280 and 265 nm. Panel **c** shows the possible relaxation pathways, either to the lower lying 6^2S state, on which experiments described in the previous sections have been conducted, or completely down to the electronic ground state.

Relaxation dynamics after In 6^2P / 5^2D excitation

The most important energy levels of In are shown in Fig. 4.28a. An excitation spectrum in the region of higher energies was recorded with the same technique like in the case of the $6^2S_{1/2}$ state (see Fig. 4.5): The In mass yield as function of excitation wavelength, tuned with the OPA, was monitored at long pump-probe delays. All described experiments in this section have been obtained by 405 nm probe (SHG) ionization. The result for the excitation spectrum is shown in Fig. 4.28b. As can be seen, a broad excitation band centred around 36,000 cm^{-1} (280 nm) is retrieved. As possible candidates only

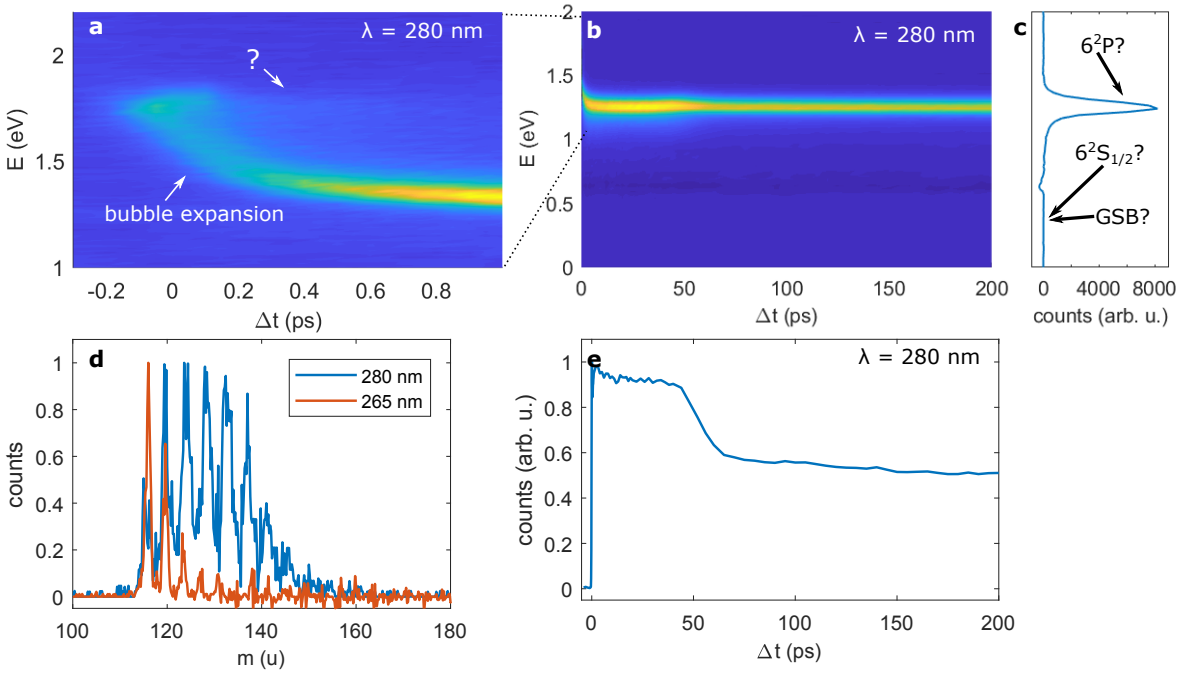

Figure 4.29: Transient PE spectra after excitation at the center of the excitation band at 36,000 cm^{-1} (280 nm). Panel **a** shows short time scale dynamics, with a similar bubble expansion behaviour as for the $6^2S_{1/2}$ state. An additional unknown signal around 1.75 eV, not undergoing any shifts, is indicated with a question mark. Panel **b** shows long time scale dynamics up to 200 ps, panel **e** the respective integrated PE yield and panel **c** the PE spectrum at 200 ps time delay. The PE energy where a $6^2S_{1/2}$ peak or also ground state bleach (GSB) should be visible is marked. Panel **d** depicts the mass spectra at long time delays, both for 280 nm and 265 nm excitation.

a few states could be responsible: the 5^2D states, with bare-atom energies around 33,000 cm^{-1} and high oscillator strengths, and the 6^2P states, with bare-atom energies around 32,000 cm^{-1}, and whose excitation is however forbidden in the bare phase. Because not resolvable with our laser bandwidths (approx. 450 cm^{-1}), we do not write out the J-components of the atomic states and mean always the complete spin-orbit manifold when terming a state e.g. 6^2P. Despite the 6p←5p transition being not allowed in the gas phase, population in He_N might still be present due to softened transition rules, or a 5^2D to 6^2P relaxation channel. The close separation (max. 0.1 eV) of all four 6^2P and 5^2D levels unfortunately hinders an easy excitation band assignment with femtosecond lasers. Precise photoelectron spectroscopy measurements at high time delays suggest that the low energy side of the band might be related to 6^2P ejection, and the high energy side to 5^2D ejection. Also the fact that excitation at 280 nm results in a great number of ejected $InHe_n$ exciplexes, while excitation at 265 nm produces mainly In atoms (Fig. 4.29d), suggests that two different states with different binding behaviour might be involved. We conclude that also if 6p←5p might be forbidden in He_N, a fast relaxation from 5^2D to 6^2P could take place, explaining the different results. Unfortunately, such a relaxation process is not resolvable in our TRPES measurements due to the low energy resolution at early times: Fig. 4.29a shows the short time scale bubble expansion for excitation at the center of the excitation band (280 nm). As can be seen, the bubble expansion proceeds on a similar time scale as for the $6^2S_{1/2}$ state, namely within about 600 fs, although the PE energy shift (500 meV) is considerably larger (compared to 300 meV). The increased shift can be explained with an increased repulsive interaction due to the larger spatial expansion of higher excited states and therefore stronger interaction with the helium surrounding. During the bubble

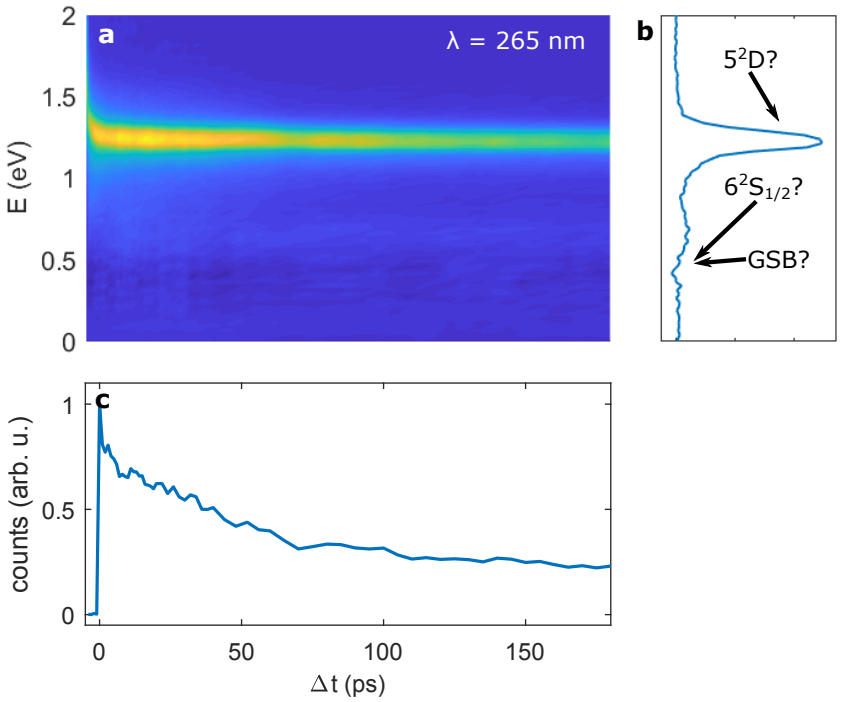

Figure 4.30: Transient PE spectra after excitation of at the high energy side of the excitation band at 38,000 cm^{-1} (265 nm). Panel **a** shows long time scale dynamics up to 185 ps, and panel **b** the PE spectrum at 185 ps time delay. The PE energy where a $^2S_{1/2}$ peak or also ground state bleach (GSB) should be visible is marked. Panel **c** shows the integrated PE yield up to 185 ps.

expansion, the intensity of the PE spectrum increases, in stark contrast to the expansion dynamics after $6^2S_{1/2}$ excitation, which starts with high intensity and then decreases (see Fig. 4.7). Also this transient intensity behaviour might be a hint at a relaxation channel from 5^2D to 6^2P, if an increased ionization probability from 6^2P should be present. In the short time scale measurement, an additional PE signal at around 1.75 eV (Fig. 4.29a) is present, with minor intensity, which does not undergo a bubble expansion. The origin of this band is not known and was not further investigated. Fig. 4.29b shows the long time scale PE spectra. As can be seen, intensity is mainly measured at the peak position of the 5^2D / 6^2P states, with no significant (gradual) decrease that might hint at relaxation, although the peak intensity rapidly drops after 60 ps (Fig. 4.29e), which might be related to a dopant ejection process: Assuming an excitation of only near-surface located atoms might result in a narrow distribution of ejection times, resulting in the pronounced PE intensity change due to different ionization probabilities of solvated and bare atom states. A near-surface location could also explain 6^2P excitation, as the anisotropy next to the surface breaks the symmetry of the system, similar to the case for alkali metal atoms [122]. At the PE energy, where a possible relaxed $6^2S_{1/2}$ state is expected (around 0.3 eV, Fig. 4.29c), no signal increase is measured, hinting at absent relaxation to the $6^2S_{1/2}$. As for all measurements the probe-only contribution is subtracted, a possible relaxation to the ground state might be visible through a vanishing bleach signal at high probe powers (2-photon probe background), which was however also not the case. We conclude that no droplet-induced relaxation at this excitation energy (280 nm) is present.

Contrastingly, after 265 nm excitation and therefore at the presumable 5^2D end of the spectrum, a signal decay could be measured (see Fig. 4.30c). The gradual intensity decrease proceeds up to approximately 60 ps, followed by constant signal, hinting at relaxation processes proceeding only during He_N interaction, which is limited due to dopant ejection. However also here, no $^2S_{1/2}$ signal increase was found (see

Fig. 4.30a&b) and no significant GSB could be detected (also with significantly increased probe power), which might explain the observed signal decrease.
Our efforts trying to observe high excited state relaxation of $InHe_N$ must therefore be described as not successful. Two important open questions however still remain to be answered: First, the temporal intensity behaviour during the bubble expansion after 280 nm (6^2P?) excitation is still unclear. Contrastingly to 6^2S excitation, the PE yield increases for larger bubbles, opening the question of how the excited state geometry in He_N might influence the PE yield. An alternative explanation might be a fast droplet induced 5^2D to 6^2P relaxation, with increased ionization probability in the 6^2P state. Second, the long time scale relaxation dynamics (signal decrease) upon 265 nm excitation remains unclear, especially to which state it proceeds. Detailed TRPES and TRPIS on short and long time scales with variable excitation energy and exact energetic calibration might shed some light on those questions. Because however no clear relaxation with corresponding time scales within He_N could be detected, no more experiments on high excited states of In were continued.

Relaxation dynamics after Al 3^2D excitation

For the case of Al 3^2D←3^2P excitation, previous time-correlated photon couting experiments have revealed that 3^2D population completely transfers non-radiatively within 50 ps down to the 4^2S state [63]. We therefore chose to switch to Al, as its electronic structure is very similar to In, and results should be easy to interpret.
The excitation spectrum of the 3^2D←3^2P transition is blue-shifted inside He_N with respect to the bare-atom line by around 1000 cm^{-1} [63] (see Fig. 4.31a). The possible decay pathways can be seen in Fig. 4.31c, which are identical to In. Fig. 4.31b shows the transient integrated PE yield, obtained for an excitation wavelength of 301 nm (OPA, indicated in Fig. 4.31a) and probe wavelength of 395 nm (SHG). As can be seen, the signal completely decays within about 20 ps, which contrasts to the expected relaxation to 4^2S, which should still be observable with the chosen probe wavelength (2.84 eV binding energy, compared to 3.14 eV probe energy). Fig. 4.31c shows PE spectra for selected time delays. The strong peak around 1.2 eV is assigned to 3^2D population, which decays within the observed 20 ps. If relaxation to 4^2S was present, the assigned signal would appear at 0.3 eV (Fig. 4.31d), which is clearly not the case. However, a clear ground state bleach (GSB) is measured at the very same energy, as the probe wavelength is nearly identical to the bare atom energy of the 4^2S (1+1 REMPI). The bleach clearly vanishes for higher time delays, indicating full relaxation not to the 4^2S, but rather the ground state. This observation contrasts with the results obtained in Ref. [63], where following 3^2D excitation, a clear fluorescence signal from the 4^2S state was observed. However, based on these experiments it is not retrievable, what fraction of initial 3^2D population undergoes relaxation to the 4^2S, which might be too low to be detectable for our case, especially with the overlying ground state bleach at the same PE energy. Additionally, differences in fluorescence and/or ionization probabilities might explain the deviating results. As interesting side effect, we observed a second prominent PE band, measured at around 2.4 eV. This band emerges within about 2 ps after photoexcitation and decreases within the next few ps, exhibiting therefore only a very short temporary appearance. An explanation might a transient population of an electronic state, which is populated and subsequently completely emptied during the relaxation process. The only possible state between 3^2D and the ground state, besides the 4^2S state, is the 3^4P state. A 3-photon ionization from this state might explain the observed PE band, assuming ionization to the $^3P^o$ ionic state (Fig. 4.31c&d). Slight deviation in energy could be caused by the He influence, which is known to shift both excited, and also ionic states [108]. The transient population of 3^4P has to involve not only a curve crossing, but also a spin flip due to the different multiplicity, as has

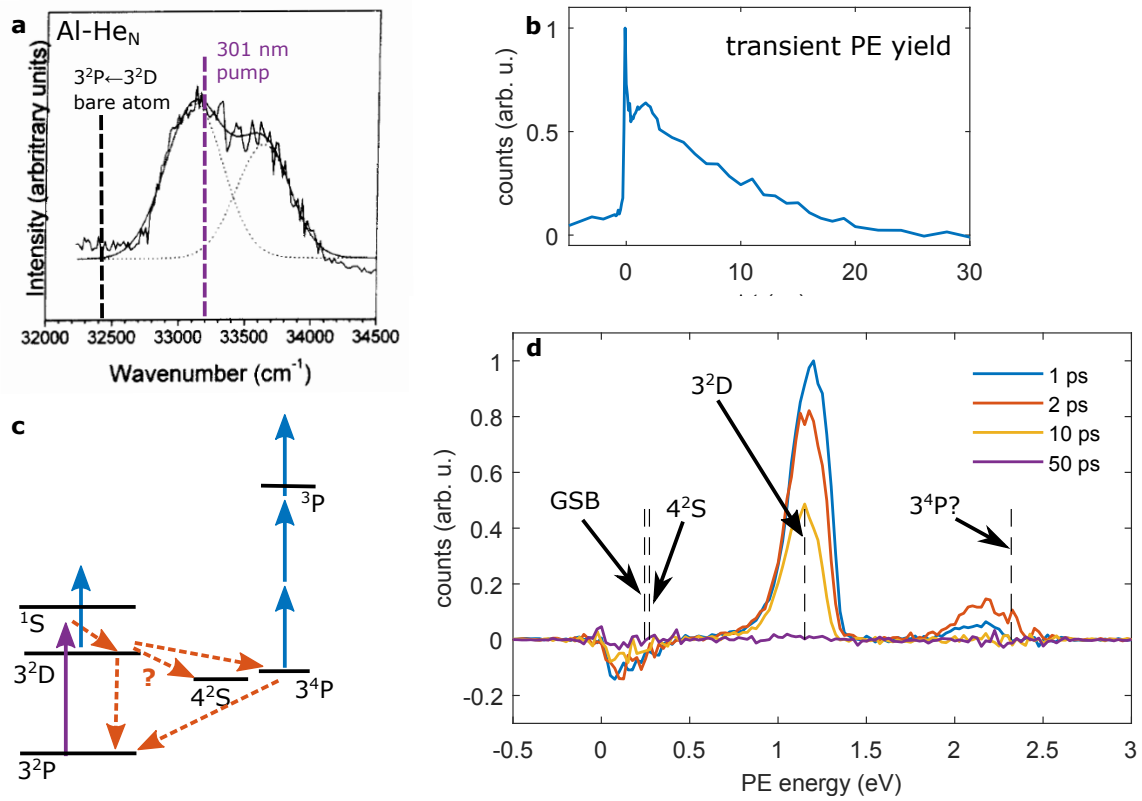

Figure 4.31: Measured dynamics after Al $3^2D \leftarrow 3^2P$ excitation at 301 nm. Panel **a** shows the in-droplet excitation spectrum, adapted from Ref. [63]. The bare atom transition as well as the pump wavelength used in this experiment are indicated. Panel **b** shows the integrated transient PE yield, a clear decaying signal is observed. Panel **c** shows possible relaxation pathways, mostly identical to the ones from In, part from a possible transient 3^4P population. Panel **d** shows selected PE spectra, possible state signals are indicated and bare atom transition energies are indicated with dashed lines.

been observed for the case of Cr excitation [65, 70, 72].

In conclusion, the experiments on high excited Al states gave a much more interesting relaxation behaviour than for In. However, more exact measurements are still necessary, to closely analyse the time constants related to 3^2D signal relaxation and compare it to the time constant of the vanishing ground state bleach as well as 3^4P signal. This bleach, as well as the presumable 3^4P signal at 2.4 eV should be identifiable with probe power scans, to verify the 2-photon and 3-photon contributions, respectively. Further tests could involve the excitation with different wavelengths, to test if the relaxation might change (e.g. in speed or populated state) with excitation energy. Changes in probe wavelength (THG) could further make it easier to disentangle GSB, 4^2S and possible 3^4P signals.

4.6 Femtosecond solvation dynamics of indium dimers inside superfluid helium nanodroplet

This section consists of the following published publication:

Femtosecond solvation dynamics of indium dimers inside superfluid helium nanodroplet

M. Meyer, B. Thaler, P. Heim, and M. Koch*

EPJ Web Conf. **205**, 06005, 2019
https://doi.org/10.1051/epjconf/201920506005

* corresponding author

contributions	
funding	M. Koch
experimental design	M. Koch
preparation / setup	P. Heim, B. Thaler, M. Koch
data acquisition	M. Meyer, B. Thaler
data analysis	M. Meyer, B. Thaler
interpretation	all authors
publication writing	M. Meyer, B. Thaler, M. Koch

Abstract

Indium dimers (In_2) solvated inside helium nanodroplets are studied with femtosecond photoelectron and photoion spectroscopy. The solvation dynamics triggered by photoexcitation of the In_2 include expansion of the solvation shell and dopant ejection from the droplet, which both proceed more slowly than for In atoms. Oscillation of the solvation shell, in contrast, is similar to the case of In atoms. These processes are observed in combination with intrinsic dynamics of the molecule and set the time-frame for the dopant interaction with the quantum fluid environment.

Introduction

Superfluid helium nanodroplets (He_N) represent a special approach for the synthesis of tailor-made or fragile molecules and clusters. In view of time-resolved spectroscopy, they provide access to novel classes of systems that have eluded ultrafast dynamical studies so far. Pure He_N [36] and surface-located alkali-metals [6] have been subject to femtosecond experiments. Concerning molecules immersed inside the He_N, the only attempt to observe ultrafast dynamics used the salt molecules sodium- and lithium iodide, which, however, was not successful [137].
Recently, we demonstrated that time-resolved photoelectron (PE) spectroscopy can be used to observe photoinduced dynamics of single atoms that are fully solvated inside the droplet [108]. The PE kinetic energy turned out to be a sensitive observable to follow the temporal evolution of the solvation shell around the photoexcited dopant. Supported by time-dependent density functional theory, we developed the following mechanistic picture: Photoexcitation of a single indium (In) atom inside a He_N leads to expansion of the solvation shell within 600 fs, followed by an oscillation of the bubble with a period of about 30 ps, and, finally, ejection of the In atom from the droplet after about 60 ps.
Here, we investigate the photoexcitation dynamics of the In_2-He_N system, for which we observe solvation dynamics similar to the monomer case, as well as intrinsic In_2 molecular dynamics. In the presented work we concentrate on the former and interpret the corresponding transient signals by comparison to the previous In-He_N results.

Method

As described in detail previously [98, 108], He_N with a mean number of N=8000 He atoms are generated in a supersonic expansion and doped inside a resistively heated pickup cell with two In atoms per droplet, which form an In_2 molecule. Dynamics of the In_2-He_N system are investigated with a femtosecond pump-probe photoionization experiment with variable time-delay, where the kinetic energy of photoelectrons (PEs) and charge-to-mass ratio of ions are measured with a time-of-flight spectrometer. Pump pulses are obtained from a commercial Ti:sapphire laser system and frequency upconverted by an optical parametric amplifier to a photon energy of 3.59 eV (345 nm) in order to excite the $B^3\Pi_g(II)\leftarrow X^3\Pi_g$ transition of In_2 inside He_N [98]. Probe pulses are frequency doubled to 3.05 eV (406 nm).

Results and Discussion

Fig. 4.32a shows the time evolution of the PE spectrum within the first two picoseconds after photoexcitation. The signal is modulated with a period of about 400 fs, which we ascribe to a nuclear wave packet oscillation of the In_2 molecule. The periodic signal maxima correspond to ionization from the excited

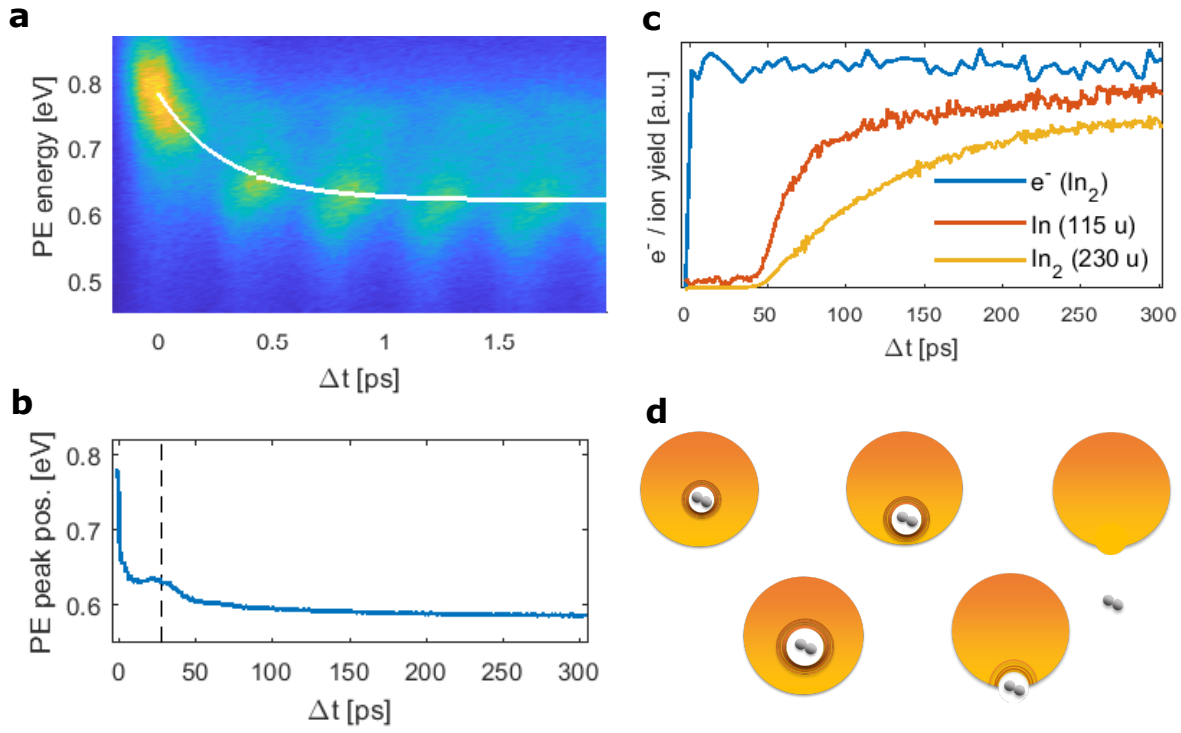

Figure 4.32: Time evolution of the In_2-He_N system after photoexcitation. (a) PE spectrum within the first 2 ps. The white line connects the signal maxima. (b) PE peak position up to 300 ps, as determined by Gaussian fits to the corresponding PE spectra. The dashed line at 28 ps indicates the maximum of the temporal increase in PE energy. (c) Ion yields recorded at the In monomer/dimer masses of 115/230 u for photoexcitation at the monomer/dimer band at 376/345 nm (red/yellow line) and total PE yield integrated over all kinetic energies for excitation at 345 nm (blue line). (d) Sketch of the In_2 ejection process.

$B^3\Pi_g$ state to the cationic ground state of In_2, at a certain nuclear distance of the two In atoms (Condon point) [79]. The In_2 wave packet dynamics will be further analysed in an upcoming publication.

The maxima are energetically shifted by 150 meV from 780 meV to 630 meV within the first picosecond, as indicated by a white line in Fig. 4.32a. This shift is related to the expansion of the He bubble as consequence of the enlargement of the valence electron orbital during photoexcitation [108]. Compared to the In-He_N system, where a shift of 290 meV is observed within 1 ps and 90% peak shift are completed within 500 fs, the shift of the In_2-He_N is smaller (150 meV) and takes longer (90% within 700 fs). Both indicate that the excited state interaction with the He solvation shell is less pronounced for the In dimer compared to the monomer.

The PE peak shift up to 300 ps is shown in Fig. 4.32b. After a steep, initial decrease, representing the bubble expansion, the peak position is shifted further towards lower energies with a temporal energetic increase around 28 ps (marked by the dashed line), before it slowly approaches a constant value of 590 meV. The impulsive expansion of the solvation shell triggers an oscillation of the He bubble, the first contraction of which leads to the temporal increase in energy. This contraction is observed at the same time as for the monomer [108]. The decrease after 1 ps of the PE energy represents the ejection process of In_2 from the droplet, as the ionization energy inside the He_N is reduced due to polarization effects [60], compared to that of bare In_2.

Ejection from the He_N is particularly well observed by the transient ion yield. In Fig. 4.32c the transient dimer ion yield for photoexcitation at the In_2 band (345 nm, yellow line) is compared to the monomer

yield for excitation at the monomer band (376 nm, red line) [98]. Additionally, the total electron yield over time for excitation at 345 nm (blue line) is shown. While the electron signal shows an immediate rise at time-zero and remains constant afterwards, the ion signals both exhibit a delayed onset at 50 ps followed by a faster rise of the monomer within 50 ps and a slower dimer rise within 200 ps. This shows that In_2 is ejected from the droplet, in consequence of a repulsive, heliophobic excited state, as it is also the case for the In monomer [108]. Due to the cylindrical symmetry of In_2 the repulsive force experienced by the molecule depends on its orientation inside the He_N, which is not the case for the spherically symmetric monomer. This would be a possible explanation for the similar onset time and slower rise of the dimer compared to the monomer.
In conclusion, the photoinduced solvation dynamics of the In_2-He_N system, as sketched in Fig. 4.32d, show all three signatures previously observed for In-He_N [108] – bubble expansion, bubble oscillation and dopant ejection. Bubble expansion and ejection proceed more slowly and are less pronounced for In_2 dopants, while the bubble oscillation is surprisingly similar to the atomic case.

4.7 Long-lived nuclear coherences inside helium nanodroplets

This section consists of the following publication:

Long-lived nuclear coherences inside helium nanodroplets
B. Thaler, M. Meyer, P. Heim, M. Koch*
submitted to Physical Review Letters, 2019

* corresponding author

contributions	
funding	M. Koch
experimental design	M. Koch
preparation / setup	P. Heim, B. Thaler, M. Koch
data acquisition	B. Thaler, M. Meyer
data analysis	B. Thaler, M. Meyer
interpretation	all authors
publication writing	B. Thaler, M. Koch

Abstract

Much of our knowledge about dynamics and functionality of molecular systems has been achieved with femtosecond time-resolved spectroscopy. Despite extensive technical developments over the past decades, some classes of systems have eluded dynamical studies so far. Here, we demonstrate that superfluid helium nanodroplets, acting as thermal bath of 0.4 K temperature to stabilize weakly bound or reactive systems, are well suited for time-resolved studies of single molecules solvated in the droplet interior. By observing vibrational wavepacket motion of indium dimers (In_2) for tens of picoseconds, we demonstrate that the perturbation imposed by this quantum liquid can be lower by a factor of 10-100 compared to any other solvent, which uniquely allows to study processes depending on long nuclear coherence in a dissipative environment. Furthermore, tailor-made microsolvation environments inside droplets will enable to investigate the solvent influence on intramolecular dynamics in a wide tuning range from molecular isolation to strong molecule-solvent coupling.

Main

A comprehensive understanding of mechanisms to convert solar energy into other energy forms is a prime objective for many research fields, with potential impact on light harvesting applications or the modelling of photoprotection in biomolecules. Insight into the functionality and dynamics of photoactive systems can be obtained in a unique way with time-resolved laser spectroscopy [2], revealing information about, for example, non-adiabatic coupling dynamics of electrons and nuclei [210], charge transfer [211], electron dynamics [195], or molecular chirality [212]. Recent experiments on technologically and biophysically relevant molecules suggest that nuclear motions and in particular their coherences have strong influence on the electronic evolution of the system [213]; examples include prototypical molecules for photosynthesis [214–216] and photovoltaics [217], or metal-halide perovskites [218, 219].

The evolution of a molecular system after photoexcitation strongly depends on its immediate environment, with significant differences between isolated systems, where photodynamics can be precisely studied [50, 196], and the system in its real-world environment in condensed phase. Isolated molecules can be produced in a seeded supersonic expansion [220], where investigations are, however, often prevented by fragmentation resulting from excess energy during photoexcitation, or simply by the fact that weakly bound systems cannot be produced. This harmful vibrational energy can be dissipated to a thermal bath by embedding molecules in a high-pressure buffer gas [221] or a cryogenic matrix [75]. As a disadvantage, influences of the environment on intrinsic dynamics can be severe and disentangling intra- and intermolecular dynamics is often impossible. Moreover, in such environments molecular dynamics cannot be probed with time-resolved photoelectron (PE) or -ion spectroscopy [50, 196], two very powerful methods that are independent of selection rules and dark states. Because of these drawbacks, many systems have eluded ultrafast studies.

Here we demonstrate that superfluid helium nanodroplets (He_N) are well suited to fill this gap. By tracing vibrational dynamics of fully solvated molecules for the first time, we show that superfliud He as a solvent can have very little influence on the coherence of nuclear dynamics, which comes as surprise based on existing knowledge (see below). Our results also demonstrate that time-resolved PE spectroscopy is a proper method to observe the dynamics of solvated molecules. The benefits of He_N for spectroscopy have been unveiled over the last three decades [5, 8]: these nanometer-sized quantum fluid containers have enabled researchers to produce, isolate and investigate, for example, fragile agglomerates [11, 54], tailor-made complexes [13, 55], highly reactive species [203], or molecules in a controlled microsolvation

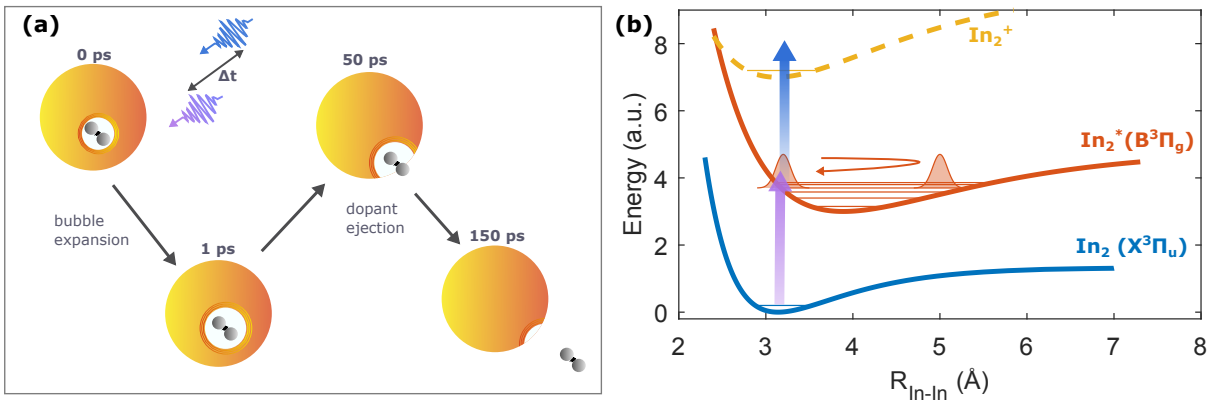

Figure 4.33: Schematic drawing of the photoinduced dynamics of the In_2–He_N system. (a) Solvent response: Expansion of the He solvation shell (bubble) during the first picosecond is followed by In_2 ejection within about 100 ps. (b) Intramolecular In_2 dynamics: A coherent superposition of vibrational states is generated by the spectrally broad pump pulse, leading to vibrational WP motion in the excited molecule. The WP is probed with a second pulse, resulting in a modulation of the photoelectron/ion yield due to an alternating ionization probability. Ground and excited state Morse potentials were taken from Ref. [165], the shape of the ionic potential is not known and therefore only schematically drawn.

environment [14]. Femtosecond time-resolved investigations of He_N, building on pioneering works in bulk superfluid He [130], have recently moved into the focus of researchers and various studies have been presented, including pure droplets [36], alkali-metal atoms and molecules located on the droplet surface [6, 25, 27], as well as alignment [44] and rotational studies [139]. However, for fully solvated molecules in the droplet interior, where the majority of species is located, the exceptionally low deterioration of nuclear coherences was not foreseeable from previous results: (1) The solvent-chromophore interaction upon photoexcitation is very strong in the droplet interior, typically two to three orders of magnitude larger than on the surface [8]. (2) Even though sharp vibrational lines were observed in special cases [55], indicating weak vibrational energy relaxation, no information is available about the destruction of coherence through dephasing, which is typically much stronger. (3) The influence on coherent molecular rotations by the He environment was found to be strong [139]. (4) Previous attempts to observe molecular dynamics in the droplet interior were unsuccessful [137], leading to the interpretation of strong solvent-induced relaxation. The pronounced signatures for nuclear coherence of the In_2–He_N system are thus remarkable and enable us to quantify the influence of the quantum fluid on vibrational WP motions. We disentangle these intramolecular dynamics from solvation dynamics by comparison to photoexcitation experiments of solvated atoms [108].

The setup is described in detail elsewhere [98, 108]. In short, He_N with a mean droplet size of about 9000 atoms are generated via continuous supersonic expansion of high purity helium gas through a cryogenic nozzle (5 μm nozzle diameter, 15 K nozzle temperature, 40 bar stagnation pressure) into vacuum. The droplets are loaded with, on average, two In atoms by a resistively heated indium-oven, resulting in In_2 molecules solvated in the droplet interior. We investigate the In_2–He_N system with femtosecond time-resolved photoelectron spectroscopy using pulses from a amplified Ti:sapphire laser system (Coherent Vitara Oscillator and Legend Elite Amplifier: 800 nm center wavelength, 25 fs duration, 4.2 mJ pulse energy, 3 kHz repetition rate). Pump pulses are frequency up-converted by combining optical parametric amplification (Light Conversion, OPerA Solo) and subsequent frequency quadrupling to 345 nm (3.60 eV, 70 meV FWHM), in order to excite In_2 at the maximum of the in-droplet $B^3\Pi_g \leftarrow X^3\Pi_u$ transition band (see Supplementary Note 1 [222]). Probe pulses are frequency doubled to 406 nm (3.05 eV, 40 meV

FWHM) in a 1 mm thick BBO crystal. Pump and probe powers are optimized in favor of the pump-probe signal contrast with respect to single pulse backgrounds, typical pulse energies lie in the range of a few μJ for both pulses. The cross correlation based on the In_2 overlap signal is estimated to be below 250 fs. Indium dimers are photoionized by the probe pulses and PE kinetic energies and ion charge-to-mass ratios are measured in a time-of-flight spectrometer. For photelectrons the spectrometer is operated in a magnetic bottle configuration and for photoions a strong positive repeller voltage of about 2 kV is applied.

Photoexcitation of the In_2–He_N system triggers two different types of dynamics: The response of the He solvation shell (Fig. 4.33a) and a vibrational WP in In_2 (Fig. 4.33b). Both dynamics are represented in the transient PE spectra with overlapping time scales (Fig. 4.34) and we identify the solvation shell response by comparison with the In atom transient, which is described in our previous work [108]. Ground state atoms and molecules inside He_N reside in cavities termed bubbles due to Pauli repulsion between the dopant's valence electrons and the closed shell He atoms. Photoexcitation and the correlated expansion of the valence electron orbital leads to an increase of the bubble size (Fig. 4.33a). For In_2, the connected transfer of potential energy to He kinetic energy is observed as shift of the PE peak from about 0.75 to 0.60 eV within the first picosecond (Fig. 4.34b). In the excited state, In_2 is ejected from the droplet, which can be deduced from the transient In_2^+ ion yield (red line in Fig. 4.34a). Following absent ion signals for the first 50 ps, the ion yield shows a slow rise within 200 ps because ionization of In_2 inside or in the vicinity of the droplet leads to trapping of the ion, preventing In_2^+ detection [6, 25].

We now turn to the intramolecular In_2 WP-dynamics. Photoexcitation with a spectrally broad femtosecond laser pulse leads to coherent superposition of the vibrational eigenfunctions and the periodic movement of the resulting WP is detected as modulation of the PE signal (Fig. 4.33b). This modulation with a periodicity of 0.42 ps is clearly seen in the time-resolved PE spectrum (Fig. 4.34b), as well as the integrated PE yield (Fig. 4.34e). Anharmonicity of the potential leads to dispersion of the eigenfunctions and a spreading of the WP, detected as decrease of the modulation contrast (Fig. 4.34e). The reversible character of dispersion leads to refocusing of the WP at characteristic revival times, restoring the signal contrast to some extent. Half and full revivals of the In_2 motion are indeed observed around 145 ps (Figs. 4.34c & f) and 290 ps (Figs. 4.34d & g), respectively; the assignment stems from a comparison to the theoretical revival time, which is based on the anharmonicity parameter of the Morse potential (see Supplementary Note 1 [222]). The reduced amplitude in the revival signal, compared to the initial oscillation, reflects decoherence (dephasing) of the WP due to molecule-He interaction. Note that the full revival around 290 ps is observed at times where all excited dimers have left their droplets, as indicated by the leveling off of the In_2^+ ion signal (Fig. 4.34a). As expected, the next revival (3/2) can be observed around 435 ps, exhibiting the same oscillation contrast and temporal amplitude characteristics (see Supplementary Note 4 [222]). The fact that fractional and full revivals are also observed in the In_2^+ yield (Fig. 4.34a), whereas they are absent during the initial oscillation, proves that the WP signals are associated to In_2 molecules that are originally solvated inside the droplet (see Supplementary Note 2 [222]).

Fourier transformation of the three datasets shown in Figs. 4.34b-d reveals always the same central frequency of (2.42 ± 0.05) THz, corresponding to an oscillation period of (0.42 ± 0.01) ps. To obtain insight into the transient changes of the oscillating signals, we apply sliding window Fourier analysis (see Supplementary Note 3 [222]). Figs. 4.35a-c show the three spectrograms corresponding to the initial WP oscillation, the half revival and the full revival, respectively. The transient amplitudes of the central frequency are shown in Figs. 4.35d-f, revealing that the signal amplitude of the initial WP oscillation (Fig. 4.35d) decreases faster than the amplitudes of the half and full revivals (Figs. 4.35e & f). The same frequency for In_2 inside and outside the He_N hints at a minor influence of the helium solvent on the shape

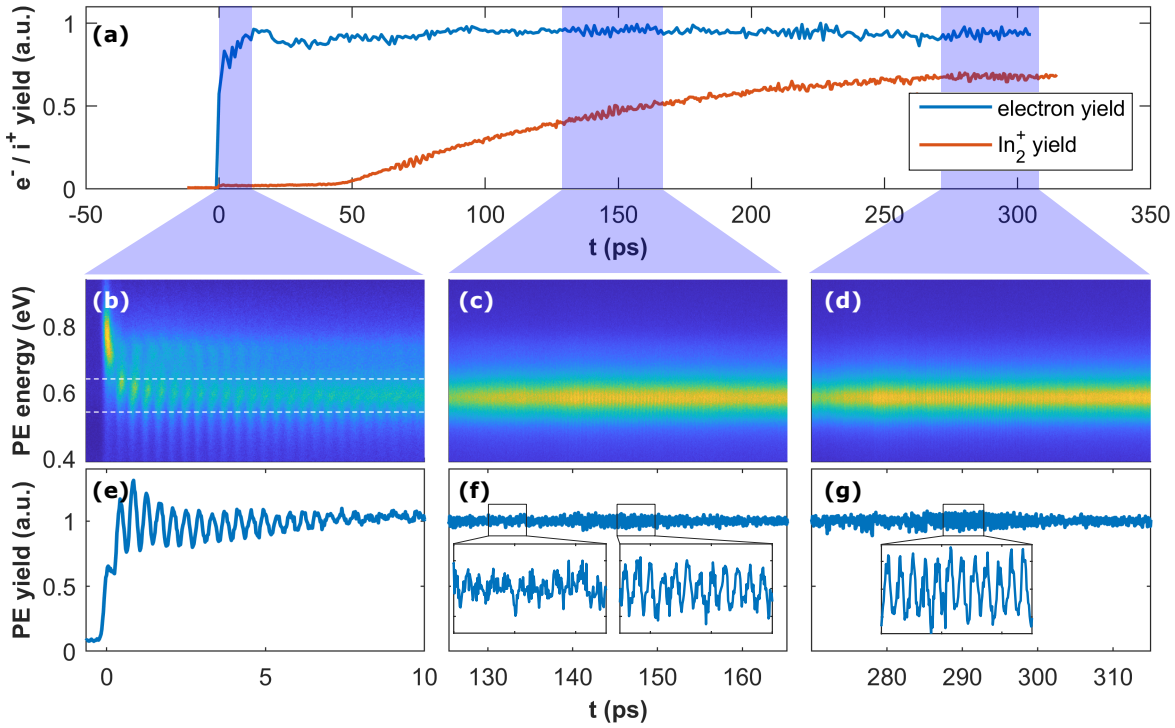

Figure 4.34: Photoelectron and -ion transients representing the dynamics of the In_2–He_N system. (a) Transient PE (blue) and In_2^+ (red) ion yields. (b) to (d) PE kinetic energy spectrum as function of pump-probe delay for temporal regions of the initial WP signal (b), as well as the first half (d) and full (d) revival, respectively; dashed lines mark the integration region. (e) to (g) Integrated PE signal for the energy region 0.54 to 0.64 eV, containing close ups of the half and full revival to better visualize the oscillating signals. Integrated curves are normalized to their sliding average (2.5 ps window), in order to compensate for long-term laser drifts.

of the excited state potential. Upward-bent potentials, as observed for halogens in rare gas matrices [75], might however still influence WP motion at higher vibrational energies.

We now further analyze the time- and frequency domain representations of the WP motion. The persistent strong oscillation signals within the first 10 ps (Figs. 4.34e & 4.35d), as well as the appearance of WP revivals (Figs. 4.34f & g and Figs. 4.35e & f) show that coherence is conserved to some degree inside He_N. Since the full revival occurs after the molecules are ejected from the droplet, comparison of the oscillation signal decay times for solvated and free molecules is possible and provides insight into the He-induced decoherence. Solvated In_2 experience both dispersion and He-induced decoherence of the WP, resulting in a 50% decrease of the oscillation amplitude within (4 ± 1) ps (Fig. 4.35d). Free In_2, in contrast, experience only dispersion, leading to a slower decrease of about (8 ± 1) ps (Fig. 4.35e & f). We thus estimate a decoherence half-life caused by He-interaction on the order of ~ 10 ps. From this decoherence time a lower limit for the duration of the In_2 ejection can be estimated. The oscillation contrast at the peak of the revivals is roughly 20% of its initial value after photoexcitation (Fig. 4.34e-g). Assuming an exponential-like decrease, we estimate that the In_2 molecule is surrounded by He for about 20 ps, corresponding to twice the decoherence time. This interpretation is in line with the absent ion yield within the first 50 ps (Fig. 4.34a), taking into account that the ejected In_2 has to move a certain distance from the droplet surface to avoid recapture by the droplet upon ionization [6, 25]. We note that the revivals could, in principle, also be related to In_2 molecules that are ejected earlier than 20 ps

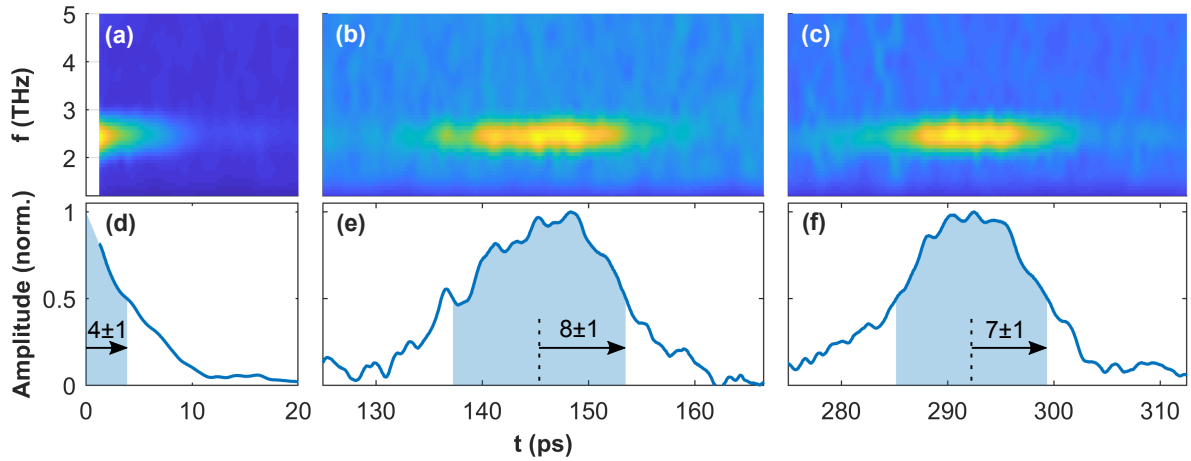

Figure 4.35: Sliding window fast Fourier analysis of the WP signals shown in Figs. 4.34b-d. A Hamming window function of 2.5 ps width was used (see Supplementary Note 3 [222]), resulting in a spectral width of 0.55 THz (FWHM). (a) to (c): spectrograms, for which the PE energy range between 0.49 and 0.64 eV was considered. (d) to (f): time-dependent amplitudes of the central frequency (2.42 THz). Arrows indicate the time after which the signal has decreased to 50% of its maximum value (for the extrapolation to 0 ps in panel (d), see Supplementary Note 3 [222]).

after excitation, which seems very unlikely in view of the ion yield onset at 50 ps. However, this scenario would not change the observation of coherent oscillations lasting for over 20 ps, which is purely based on the initial oscillation contrast decay. In general, the slow ion yield increase within 200 ps, reflecting the spatial distribution inside the droplet in combination with the droplet size distribution, suggests that the vast majority of In_2 undergoes much longer He interaction than 20 ps. This is in line with the previously measured PE transient, where the PE peak energy slowly decreases to the bare-molecule value within more than 100 ps in consequence of a lower ionization energy in the He environment and ejection from the droplet [167]. In this case, the decoherence time would be significantly shorter than the average In_2 ejection time, pointing towards a non-constant, time-dependent loss of phase information; the vibrational WP dephases more strongly within the first few picoseconds after photoexcitation.

Because the vibrational motion of In_2 is started at short internuclear distances (see Fig. 4.33b), one might expect a particularly strong energy transfer to the droplet during the first half oscillation perdiod of 0.21 ps, as the atoms hit the solvation shell boundary. However, the photoexcitation-induced expansion of this shell takes also place within the first few hundred femtoseconds; the He boundary layer moves therefore at a similar pace as the separating In atoms, relativizing this assumption. A possible explanation for stronger initial He-influence might be found in helium density waves, which are initiated by the bubble expansion and reflected by the droplet surface to interact with the molecule after a few ps [108]. Subsequent to this relatively strong initial interaction, decoherence during the molecule's propagation through the droplet seems to be much weaker. Even dopant ejection does not destroy the vibrational phase relations, despite possible recoil effects when the molecule ruptures the droplet boundary.

Coherence decay can be caused in two ways: (1) pure dephasing of the vibrational modes (elastic dephasing), or (2) vibrational relaxation within the In_2 excited electronic potential, resulting in energy transfer from the molecule to the droplet (inelastic dephasing). As phase-conserving vibrational relaxation would lead to a WP frequency increase [81], which is not observed in our case (Figs. 4.35a-c), we can conclude that for In_2 either solely elastic dephasing, or elastic dephasing in combination with non-coherent vibrational relaxation are present.

Viewing the In_2 and the He bubble as two quantum oscillators that are only weakly coupled because

of their different excitation energies further suggests a low influence of the He surrounding: In_2 has a much larger excitation energy of 80 cm^{-1} (0.42 ps oscillation period) compared to 1.1 cm^{-1} (30 ps) of the He bubble [108]. Apart from the bubble, the In_2 motion might also couple to the droplet's elementary excitations, which can be grouped in bulk excitations (phonons) and surface excitations (ripplons) [9]. Whereas ripplons should only weakly couple to the molecular vibration due to their small energies (below 1 cm^{-1}), phonons can have energies on the order of 10 cm^{-1}, which is closer to the energy spacing of In_2 vibrations. Experiments on molecules with very high vibrational energy spacing (HF, 2000 cm^{-1}) showed no relaxation within at least 0.5 ms [55], whereas simulations for I_2 excited to low vibrational states inside He_N predict timescales down to a few hundred picoseconds [138], for a vibrational energy spacing of around 200 cm^{-1}. Based on these results, we conclude that the In_2 spends insufficient time within the droplet in order to experience substantial vibrational relaxation.

The low perturbing character of superfluid He as a quantum solvent becomes especially clear when the observed long-lasting vibrational coherences of tens of ps are compared to other solvents, where coherence loss typically proceeds within some hundred femtoseconds up to a few picoseconds in special cases [80]. Even in cryogenic rare-gas matrices decoherence times are limited to few picoseconds [75]. For alkali metal dimers on He_N, which reside on the droplet's surface, a range of weak decoherence ($\sim$ 1.5 ns) [21, 23] to strong decoherence ($\sim$ 5 ps) [22] was observed. Given the pronounced blue-shift of the electronic transition that launches the WP in solvated In_2, the observation of low decoherence is remarkable.

The preservation of nuclear coherence inside He_N will be particularly important for systems with processes that are dominated by coherent nuclear motion [213], such as prototypical systems for photosynthesis [214–216] and photovoltaics [217]. Due to their confinement character, He_N are able to isolate single donor-acceptor pairs of light-harvesting complexes [223]. The generation of controlled microsolvation environments inside He_N will allow to follow the transition from dynamics of isolated molecules in He_N to the interaction-dominated behavior of solvated systems by successively adding solvent molecules [14].

In a general perspective, all dynamical studies in a dissipative environment face the problem that on the one side, coupling to a thermal bath is required to dissipate energy, while on the other side, transition states of chemical reactions are generally prone to increased solvent interaction as they are associated with large amplitude nuclear movements. Our results indicate that the strongly reduced influence of superfluid He might allow to follow transition state dynamics in many systems that were previously inaccessible. Coupling to the solvent depends on many aspects, such as the molecule's vibrational energy, the character of the vibrational mode, or the excited state electronic structure. More complex molecular systems are expected to couple more strongly to the He solvent, examples include molecules with permanent dipole moments, electronic states with ionic character, or low-frequency vibrational modes, all of which will be interesting to study in the future.

Supplements to: Long lived nuclear coherences inside helium nanodroplets

The following sections will accompany the publication as online supplementary material.

Supplementary Online Information

Supplementary Note 1: In_2-He_N excitation spectrum and transition assignment

Supplementary Fig. 4.36 shows excitation spectra of the indium monomer (In) and dimer (In_2) inside helium nanodroplets (He_N). The broad monomer excitation band around 27000 cm^{-1} has been assigned to the atomic $6^2S_{1/2} \leftarrow 5^2P_{1/2}$ transition and is 2600 cm^{-1} blue-shifted inside the droplets compared to the free atom [98]. For In_2, we find two strong excitation bands in the investigated region. For the experiments shown within this work, excitation of the strong band around 29000 cm^{-1} is applied, which we assign to an in-droplet $B^3\Pi_g(II) \leftarrow X^3\Pi_u$ transition. A band for this transition, assigned by ab-initio calculations [165], has been measured in absorption around 27700 cm^{-1} in cryogenic matrices [224], as well as in emission in a hot In gas [225]. We conclude that the band exhibits a blue-shift of approximately 1300 cm^{-1} (160 meV) inside the droplets, which is consistent with the measured transient photoelectron (PE) peak shift after photoexcitation (solvation bubble expansion within the first picosecond, see Fig. 2b in the main manuscript).

The second prominent In_2 band centered around 27500 cm^{-1} cannot be ascribed as easily. Its origin remains a speculation and might be due to the formation of a different dimer ground state inside the droplet [165] or to photoinduced dimerization of separated indium atoms after monomer excitation, similar to the behavior that has been described for magnesium [64, 145].

For the assigned $B^3\Pi_g(II)$ excited state we now compare the measured wave packet (WP) parameters (oscillation period, dispersion time and revival time) to theoretical values derived from the fitted Morse-

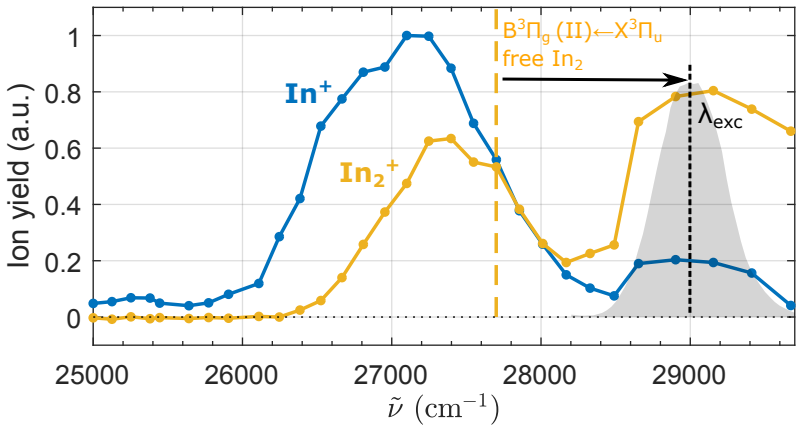

Figure 4.36: Excitation spectra of In and In_2 in helium nanodroplets. The spectra are measured with pump-probe photoionization with ion detection, by using a fixed time-delay of 200 ps and scanning the wavelength of the pump pulse. The assigned transition of the free molecule is marked with the dashed yellow line. The black arrow indicates the blue-shift resulting from solvation inside the He_N together with the excitation photon energy used for the experiments in this publication. The measured spectrum of the pump pulse is indicated as shaded area.

parameters of the ab-initio potential from Ref. [165]. We start with the general form of the Morse potential:

$$V(R) = D_e(1 - e^{-a(R-R_e)})^2, \tag{4.6}$$

where D_e is the dissociation energy, a the range parameter of the Morse potential and R_e the equilibrium bond distance. The fundamental frequency ω and the corresponding energy ω_e are defined by

$$\omega_e = \hbar\omega = \hbar a\sqrt{2D_e/\mu}, \tag{4.7}$$

where μ is the reduced mass of the In_2 oscillator. The theoretical full revival time [226], meaning the time at which the vibrational eigenfunctions of the WP are again fully in phase, can be obtained with

$$T_{rev} = h/(\omega_e x_e), \tag{4.8}$$

where $\omega_e x_e = \omega^2\hbar^2/(4D_e)$ is termed the anharmonicity of the potential. As the degree of anharmonicity affects the initial dispersion of the wave packet, we can calculate the characteristic dispersion time T_{disp} (meaning the time after which the wave-packet has completely dispersed; for a derivation see Ref. [227]) for a given central frequency ν and the energetic spreading (FWHM) of the wave packet ΔE, by

$$T_{disp} = h^2\nu(E)/(2\omega_e x_e \Delta E). \tag{4.9}$$

Table 4.2 compares the experimental time constants to the theoretical ones, which are calculated with the measured central frequency $\nu = 2.42$ THz (81 cm^{-1}) of the WP, the energetic bandwidth ΔE of the pump pulse (6.5 nm at 345 nm; corresponding to 550 cm^{-1}) and the Morse parameters of Ref. [165]: $D_e = 1.14$ eV and $\omega_e = 70$ cm^{-1}.

Table 4.2: Comparison of theoretical and experimental values of the revival time (T_{rev}, Equ. 4.8) and the 50% value of the dispersion time ($T_{disp}/2$, Equ. 4.9). The experimental value for $T_{disp}/2$ is obtained as average of the half and full revival (see Fig. 3 in main manuscript).

	T_{rev} (ps)	$T_{disp}/2$ (ps)
theory	250	9
experiment	290 ± 5	8 ± 1

We describe the difference between theory and experiment for T_{rev} to a deviation of the Morse model from the actual $B^3\Pi_g(II)$ potential. Nevertheless, the values are sufficiently similar for an assignment of the revivals: Based on the theoretical value of 250 ps, we assign the measured revivals at 145 ps and 290 ps to the half and full revival, respectively. Deviation of the Morse model is also reflected by the exceedance of the measured oscillation frequency of $\nu = 2.42$ THz (80.7 cm^{-1}) with respect to the predicted maximum value of $\nu = 2.1$ THz (70 cm^{-1}). The values for $T_{disp}/2$ (Tab. 4.2) are in agreement within the experimental uncertainty.

Supplementary Note 2: Exclusion of a free dimer background

The conclusions drawn from analysis of the In_2 wave packet (WP) are based on the assumption that all dimers are initially solvated inside He droplets and that no bare dimers are present in the droplet beam. These bare dimers would corrupt our results because they do not undergo He interaction after photoexcitation and are thus not subject to dephasing. Bare In_2 molecules could, in principle, originate from the pickup source, or be generated inside a He_N and set free due to complete He evaporation in consequence of the cooling process. The most important argument that bare dimers do not contribute

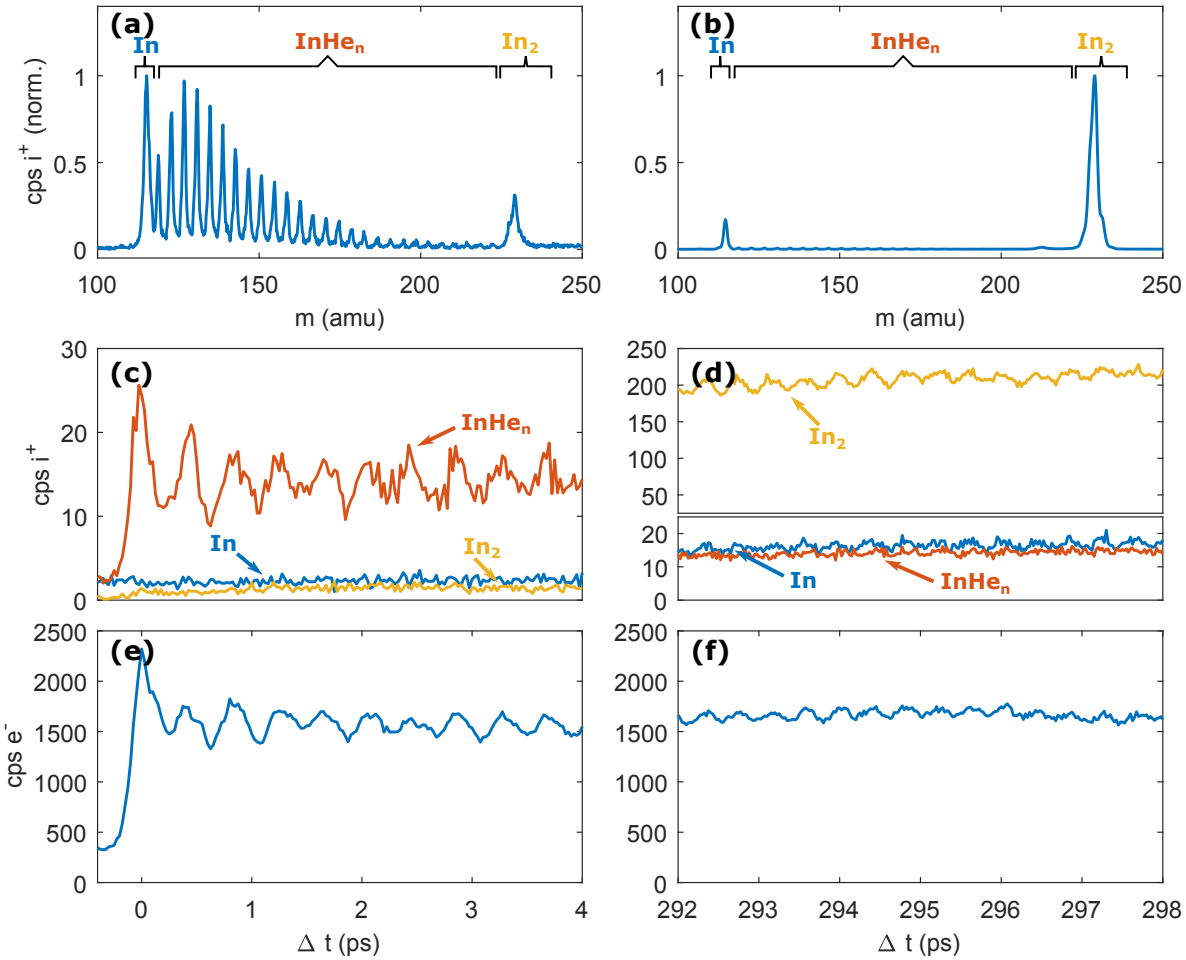

Figure 4.37: Comparison of photoion and photoelectron signals for the initial WP oscillation and for the full revival. Panels (a) and (b) show mass spectra integrated within the time windows shown in (c) and (d), respectively. Panels (c) and (d) show the transient ion yields for mass intervals as indicated in (a) and (b). Panels (e) and (f) show corresponding time-resolved integrated electron yields.

to the presented signals is that they cannot be photoexcited with the applied pump wavelength because the in-droplet excitation band is significantly blue shifted with respect to the bare In_2 excitation (see Supplementary Note 1). However, in the following we additionally present experimental verification of this assumption.

Bare dimers originating directly from the pickup cell can be excluded because, first, the In vapor pressure inside the pickup source is far too low for molecule formation ($< 10^{-3}$ mbar) and second, the PE signal vanishes when the valve between the He_N source and the pickup region is closed.
Free dimer production can be mediated by He_N, as both the double In pickup and In_2 formation dissipate significant amounts of energy into the droplet, potentially leading to complete He evaporation. This production mechanism can be analyzed by photoion yields at short time delays, as photoions produced inside He_N cannot escape the strong trapping potential of the droplet, unless they have large kinetic energies. Supplementary Figs. 4.37a & 4.37b show photoion mass spectra for the initial WP oscillations and the full revival, respectively, and Supplementary Figs. 4.37c and 4.37d show transients of selected species. The In_2 mass signal at early times is very low and exhibits no oscillations, whereas at later times

it dominates the mass spectrum with a pronounced oscillatory behavior. This strong signal increase confirms that the full revival oscillations are correlated to In_2 ejection from the droplet and that the contribution of initially bare In_2 is negligible.
Surprisingly however, we find that the early ion spectrum is dominated by $InHe_n^+$ ($n = 0, ..., \sim 30$) clusters. We explain this ion signal with a fragmentation channel in the ionic state caused by the probe pulse. Ionization of the dimer partly proceeds to a dissociative state and substantial kinetic energy is released in the subsequent fragmentation process. At these early times ionization takes place inside the droplet and the produced In^+ can escape from the droplet due to their kinetic energy, while the attractive In^+-He interaction leads to the formation of $InHe_n^+$ clusters. As the fragmentation is probe-pulse induced, the $InHe_n^+$ yield is modulated with the neutral In_2 oscillation period. The very similar forms of the $InHe_n^+$ (Supplementary Fig. 4.37c) and the total photoelectron transients (Supplementary Fig. 4.37e) support this interpretation. The ionic fragmentation channel is also active for the free In_2 at long time delays, leading to oscillation signals in the In^+ yield, whereas $InHe_n^+$ complex formation is less likely (Supplementary Fig. 4.37d). The overall ion yield at short delays is much smaller compared to that of the full revival, while the photoelectron signal is approximately the same, showing that only a fraction of the ion fragments leave the droplets.
Interpretations in the main manuscript are based on transient photoelectron spectra and are thus not influenced by this fragmentation process, which follows the probe-ionization.

Supplementary Note 3: Sliding window Fourier analysis

The measured energy resolved photoelectron transients $S(t, E)$ (c.f., Fig. 2b-d) exhibit small oscillations on a big constant background. To increase the signal quality in the sliding Fourier analysis, we apply two adjustments to the transients: First, we analyse the spectrum only at time delays > 0 ps, as the steep edge around $t = 0$ ps makes it nearly impossible to detect small frequency components in Fourier space. Second, we apply a spectral filter at low frequencies in order to exclude problems arising from a strong peak at $f = 0$ THz, which stems from the constant offset in the PE transients and would blur the spectrum after convolution with the window function. Fourier transformation $\mathcal{F}\{S(t, E)\}$ of the whole measurement shows two distinct peaks, one at $f = 0$ THz, as mentioned, and another at $f = 2.42$ THz, which we assign to the WP motion. The transient PE spectrum is spectrally filtered with the function F to obtain a filtered signal S':

$$S'(t, E) = \mathcal{F}^{-1}\{\mathcal{F}\{S(t, E)\}F(f)\} \tag{4.10}$$

The filter function is defined with two Heaviside step functions Θ:

$$F(f) = \Theta(|f| - 1.4 \text{ THz}) - \Theta(|f| - 10 \text{ THz}) \tag{4.11}$$

The sliding window Fourier analysis is now performed by Fourier transformation of the filtered signal S'(t,E) multiplied with a window function $W(t, t')$, resulting in an energy resolved spectrogram $\tilde{S}'(f, E, t')$:

$$\tilde{S}'(f, E, t') = \mathcal{F}\{S'(t, E)W(t, t')\} \tag{4.12}$$

A Hamming window function with a total width of Δt is used to reduce spectral leakage:

$$W(t, t') = \left[\Theta\left(t - t' + \frac{\Delta t}{2}\right) - \Theta\left(t - t' - \frac{\Delta t}{2}\right)\right]\left[\frac{25}{46} + \frac{21}{46}\cos\left(\frac{2\pi(t - t')}{\Delta t}\right)\right] \tag{4.13}$$

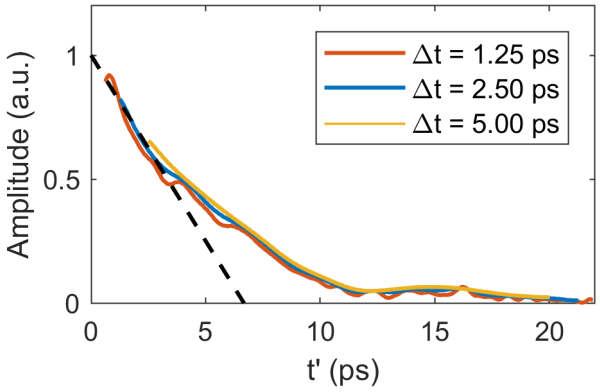

Figure 4.38: Integrated Fourier amplitude of the f = 2.42 THz frequency with different Hamming window sizes Δt for the first wavepacket signals after photoexcitation. At short time delays the transient amplitude is linearly extrapolated.

Because the phase of the WP oscillation depends on the PE energy, we integrate only the amplitude of $\tilde{S}'(f, E, t')$ within the energy window between 0.49 and 0.64 eV to prevent interferences and finally obtain the desired spectrogram:

$$\tilde{S}'(f, t') = \int_{0.49\ \text{eV}}^{0.64\ \text{eV}} |\tilde{S}'(f, E, t')| dE \tag{4.14}$$

In the main manuscript, we extract the 50% decay time of the first WP signal by evaluation of the central frequency's (2.42 THz) transient amplitude. Because the abscissa resembles the center of the Hamming window, we linearly extrapolate the missing data points to 0 ps. Supplementary Fig. 4.38 shows transient frequency amplitudes for different Hamming window sizes. The curve with $\Delta t = 2.50$ ps is fitted with a linear function from 1.25 to 3.2 ps, the resulting straight line extrapolates to 0 ps. Testing this approach for different window sizes and extrapolation regions results in the stated uncertainty (1 ps) of the 50% decay time, as is shown in Fig. 3 in the main manuscript. We note that in the main manuscript, the variable t' of this derivation is termed t for the sake of comparability.

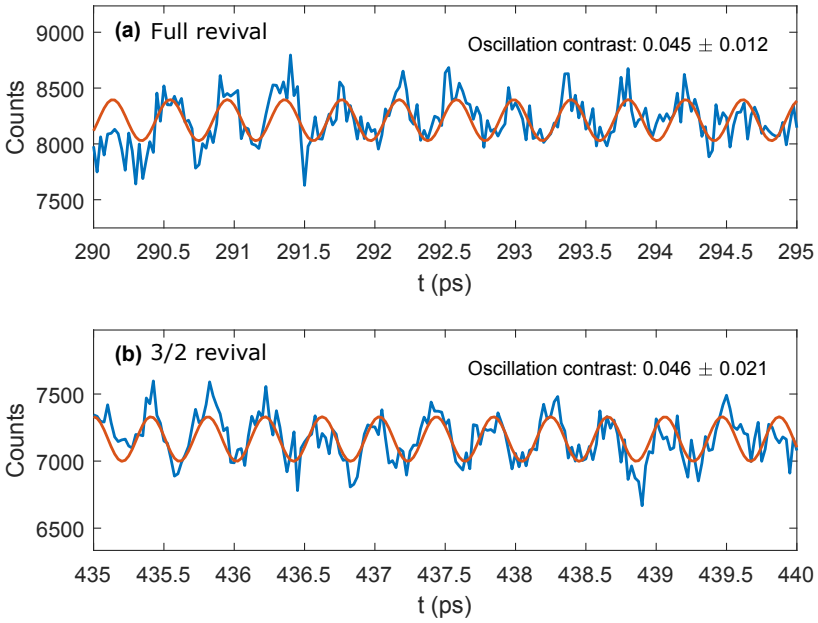

Figure 4.39: Comparison of the full WP revival (panel a) with the 3/2 revival (panel b). The oscillation contrast is indicated, defined as the amplitude of a fitted sine function divided by its average value (offset).

Supplementary Note 4: 3/2 revival

Figure 4.39 shows the oscillation signal of the total PE yield for the full revival around 290 ps, as well as the 3/2 revival around 435 ps. As expected, a same oscillation contrast is retrieved for both of them.

4.8 Photoinduced fragmentation dynamcis of indium dimers in helium nanodroplets

Many biological molecules in nature are usually present in a deprotonated or protonated form (e.g during acid-base reactions) and their background free, high resolved, spectroscopic investigation is of great interest. He_N offer to serve as environment for a controlled and high resolved investigation of such molecular ions. However, spectroscopy on ionized species in He_N is usually hard to achieve due to the experimental challenge to load He_N with ions, and due to the limited observation possibility, as the ion usually stays strongly bound to the droplet [149]. Recently it has been demonstrated that resonant IR excitation of ions inside He_N can lead to the complete evaporation of the droplet, enabling background free detection [228]. This technique enables the recording of high resolution IR spectra of ionized species in a cold environment [103], opening the possibility to study a wide variety of ions, including large biological molecules, inside the quantum solvent [57, 229–231].
Here we show that dissociation of molecular ions could provide a way to directly monitor translational dynamics of ionic species inside He_N, and directly compare it to dynamics of neutral species. While performing investigations of WP dynamics on In_2 molecules (Sec. 4.7), we found strong photoion signals on $InHe_n^+$ mass channels. As no atomic transitions should be resonant in the excited energy region, as possible source only a fragmentation behaviour of the ionized dimer molecule could be envisaged. As will be shown within this section, fragmentation is found to proceed in the In_2^+ molecule after a subsequent excitation of a probe photon to a repulsive ionic state. The energy release during dissociation provides the ion fragment with sufficient kinetic energy to leave the droplet, enabling detection. As already shortly discussed in the supporting information in Sec. 4.7, the question arose, if the ion signals could however also be related to non-solvated, free molecules. The main results of low In_2 WP decoherence in He_N (Sec. 4.7, and Ref. [168]) depend on the assumption that nearly all signals stem from fully solvated species. Before we discuss the proposed ion dissociation channel, we therefore closely check if the photoion signals could also stem from isolated molecules, which are not solvated in He_N.

Introduction:
Regarding the formation of isolated In_2, three possible formation channels can be envisaged, which then could be responsible for the observed low degree of WP decoherence:

1. In_2 might form already in the pickup cell through a three body collision. This process is however extremely unlikely due to the low vapour pressure inside the cell ($<1{\cdot}10^{-3}$ mbar). Such molecules then would further have to be present also without the droplet beam, which was tested by closing the valve between source and pickup chamber. Furthermore, the blue-shifted excitation band as well as the measured bubble expansion clearly show a pronounced He_N influence.

2. During pickup as well as molecule formation, the kinetic energy of the two dopant atoms as well as the In_2 binding energy are dissipated to the helium environment. The droplet releases this excess energy through the evaporation of He atoms, which could lead to the full evaporation of the droplet. The average binding energy per He atom is about 5 cm^{-1} (7.20 K) [5]. Assuming approximately 900 K pickup temperature results in an average kinetic energy ($3k_BT/2$) of 1350 K, corresponding to in total 375 He atoms (for pickup of two In atoms). The In_2 ground state binding energy of about 0.72 eV [165] additionally results in the evaporation of 1200 atoms. Considering a mean droplet size of 9000 atoms, these overall evaporated 1575 atoms should have no major influence. The large amounts of energy coupled into the droplet leads to a system strongly out of equilibrium, and

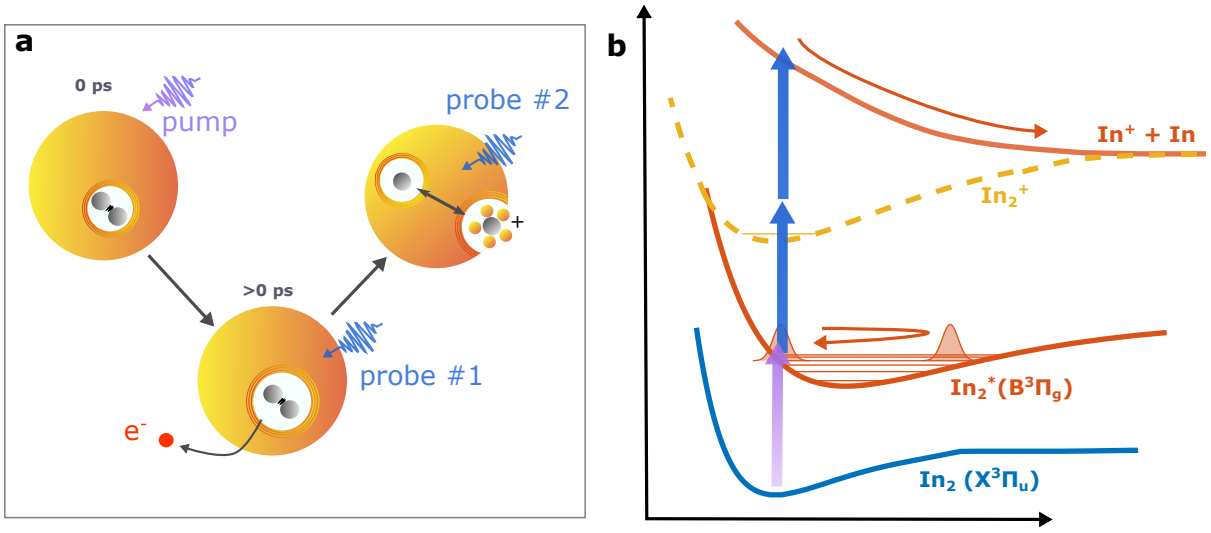

Figure 4.40: Schematic of the proposed fragmentation channel. Panel **a** shows the two-step probe interaction with first, ionization and second, subsequent excitation, resulting in fragmentation. Panel **b** shows the corresponding potential energy surface picture. It is noted that the ionic state curves have not been calculated, ground and excited state are taken from Ref. [165].

strong local evaporation might still cause the liberation of some near surface occupants. However besides this rough estimation based on He-He binding energies, also the aforementioned blue-shift and measured bubble expansion rule out this mechanism of creating free dimers.

3. As last remaining source, the through the bubble expansion incoupled excess energy could very well also lead to a generation of free dimers through the same evaporation effects. Assuming approximately 200 meV excess energy however still evaporates only another 300 atoms, which is still a too small number of He.

Apart from these theoretical considerations, also an experimental observable can be used to exclude a free dimer background, namely the observation of photoions. As fully immersed species should preclude photoion detection, no coherent wave packet motion should be measured in the ion yield at short time delays prior to In_2 ejection. However, as can be seen in Fig. 4.37 (see previous section), significant amounts of photoions are measured at short delays. The mass spectrum (Fig. 4.37a) shows pronounced abundances of $InHe_n^+$ complexes, and only little amounts of In_2^+. The complexes exhibit a strong oscillatory signal (Fig. 4.37c), exactly in phase with the measured photoelectrons (Fig. 4.37e). At higher time delays (Fig. 4.37b), mainly In_2^+ molecules are measured in the mass spectrum, with significantly larger abundance than $InHe_n^+$ at short delays. Those In_2^+ therefore must have been previously solvated, and their oscillating yield proves that coherence is conserved during the ejection process. Additionally at high delays, increased amounts of In^+ are measured, clearly exhibiting oscillations in phase with the transient In_2^+ signals.
As open question, the origin of the measured $InHe_n^+$ and their coherent signals must be resolved. It will be shown in the following, that they can be explained with a probe pulse induced fragmentation channel in the In_2^+ molecule. Dissociation then provides the fragmented products with sufficient kinetic energy to escape the droplet. In^+ atoms bind some He atoms due to the strong attractive forces, eventually resulting in the measured $InHe_n^+$ signals. At larger time delays, mainly bare In_2 molecules are ionized, resulting in more bare In^+ fragmentation products, stemming from the same dissociation channel. Fig. 4.40 schematically shows the proposed process. After pump excitation, the WP propagates within the excited state potential, periodically reaching regions of enhanced ionization probability (Condon window). At the

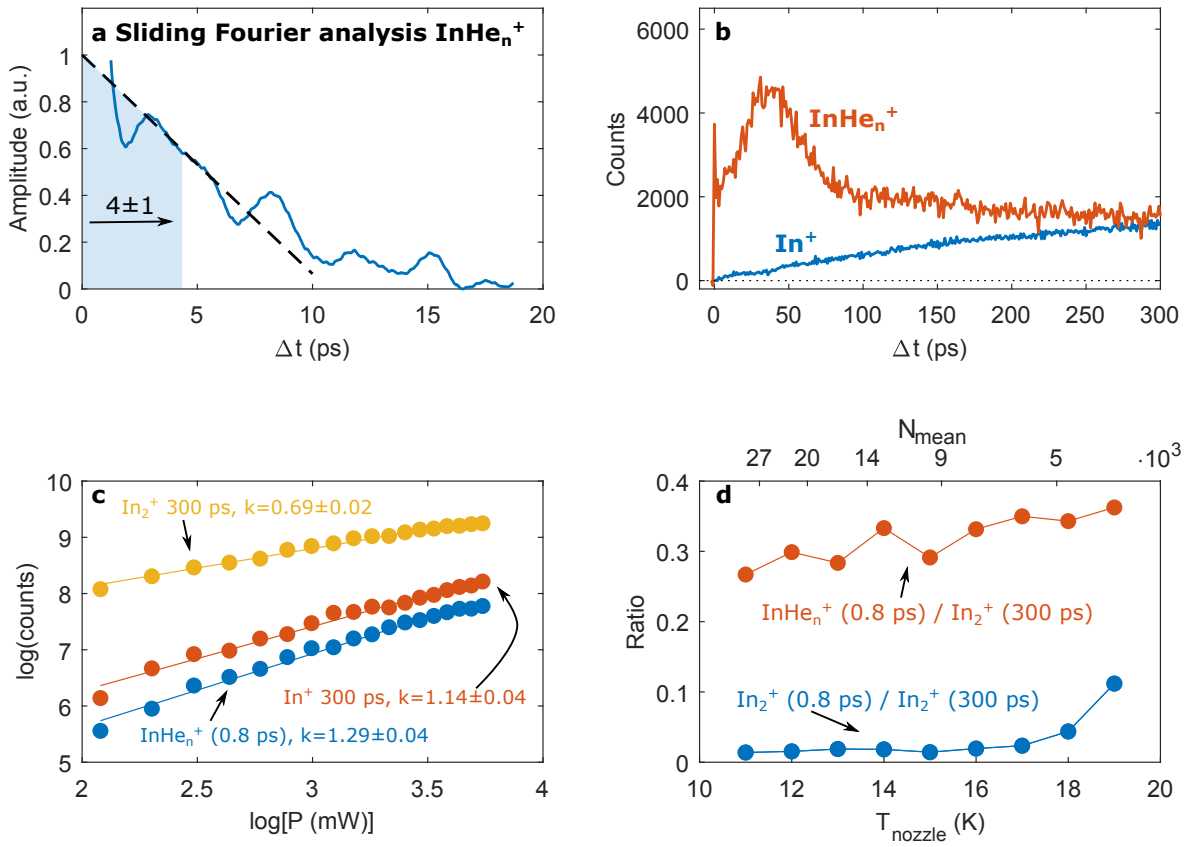

Figure 4.41: Characterization measurements of the $InHe_n^+$ signals at short time delays. Panel **a** shows an oscillation amplitude obtained from a sliding Fourier analysis of the coherent motion, the time until which half of the Fourier amplitude is reached is indicated. Panel **b** shows the integrated ion yields over the full temporal range for the $InHe_n^+$ and the In^+ signals. Panel **c** shows the yields of the mass signals as function of laser power, and panel d shows the ratio of the $InHe_n^+$ and In_2^+ yields at short delays to the In_2 yield at high delays as function of the nozzle temperature (mean droplet size).

turning point of WP motion, a first probe photon ionizes the molecule, and the resulting electron quickly escapes from the droplet. However, a second probe photon may be absorbed subsequently, populating a repulsive ionic state, which leads to dissociation. To substantiate that indeed such a mechanism is happening, further characterization measurements were performed.

Results:

First, a sliding Fourier analysis of the oscillation photoion yields is performed, in analogy to the obtained spectrograms for the PE yield (see previous section). Fig. 4.41a shows the transient amplitude of the 2.42 THz signal obtained from the $InHe_n^+$ transients shown in Fig. 4.37c. As can be seen, for photoions a 50% decrease time of about 4 ps is obtained, which is the same value as the one deduced from the transient photoelectrons stemming from the neutral In_2 (see Fig. 4.35). This observation proves that for both observables the underlying coherence has the same origin, namely the WP dynamics in the neutral excited state.

Next, the probe power dependence of the different mass channels is analysed. Fig. 4.41c shows ion yields as function of probe power in a double-logarithmic plot. The fitted slope of the signal increase provides an indication of the number of involved photons, non-integer slopes originate from saturation effects and

have to be rounded up. For In_2^+ at 300 ps, a value of 0.69±0.02 is obtained, indicating that only one photon is involved in the ionization process. In contrast, for $InHe_n^+$ at 0.8 ps and In^+ at 300 ps, slopes of 1.29±0.04 and 1.14±0.04 are obtained, respectively, hinting at two involved photons, which is in line with the proposed fragmentation channel. We note that the power dependencies slightly saturate at large powers (Fig. 4.41c), for which reason fits have also been performed including only half of the data (lower powers). The then obtained slopes are slightly larger, but the qualitative identifications of 1- and 2-photon contributions stay the same.
Next, we analyse the transient ion yields over the full temporal range. Fig. 4.41b shows the $InHe_n^+$ and In^+ yields up to 300 ps. Whereas for In^+, a similar rise as for In_2^+ (Fig. 4.34) is obtained, the transient form of the $InHe_n^+$ yield is more puzzling. Following a sharp cross correlation, the yield slowly rises up to a maximum at around 45 ps, and then again decreases, reaching a nearly constant signal after 100 ps. This temporal behaviour could be explained with several superimposing effects: $InHe_n^+$ measured at short delays stem from the proposed fragmentation process in the ionic state. However at short time delays, not all fragments are able to escape the droplet, and are recaptured, which hinders their detection. As the excited In_2 molecule is however ejected and reaches the outer droplet volume, the distance to the droplet edge gets shorter and fragmented In^+ are able to escape more easily, explaining the signal rise up to 45 ps. Within about 100 ps, a great part of the In_2 ensemble gets fully ejected, and subsequent probe excitation of In_2^+ solely leads to In^+ without any He atoms attached to it, explaining the $InHe_n^+$ yield decrease. The $InHe_n^+$ trend can therefore be also seen as direct visualization of the ejection process. Surprisingly, complexes are also measured at high time delays (>200 ps), where they should not originate from In_2^+ fragmentation. These complexes must be connected to neutral In_2 fragmentation. The proposed mechanism involves the ejection of In_2He_n complexes, followed by full fragmentation into In and $InHe_n^+$ upon ionization, as no $In_2He_n^+$ are present in the mass spectrum. The binding of He atoms to In_2 seems to enhance the fragmentation probability, as is indicated by the absence of $In_2He_n^+$ signals, as well as the non-constant overall fragmentation yield over the full time delay (sum of In^+ and $InHe_n^+$).
As last measurement, the droplet size dependence of different mass channels is analysed. Fig. 4.41d shows different mass ratios as function of He source temperature, higher temperatures thereby correspond to smaller droplet sizes. As can be seen, the ratio of $InHe_n^+$ at 0.8 ps to In_2^+ at 300 ps rises for increasing temperature (decreasing droplet size). This result is in line with the assumption that early fragmentation products are less likely to escape the droplet: For smaller droplets, the escape pathways become shorter, and the In^+ kinetic energy cannot be dissipated away completely, leading to ejection and an increase in $InHe_n^+$ yield. Fig. 4.41d also shows that the ratio of In_2^+ at short to In_2^+ at high time delays increases at the smallest droplet sizes (largest temperatures). This increase should be related to the in the beginning of this section discussed effect that released energies during pickup, dimer formation and bubble expansion might vaporize the surrounding He droplet. As estimated above, the thereby released energy corresponds to the binding energy of about 1900 He atoms. Considering a mean droplet size of about 3700 atoms at 19 K, the described effect could very likely lead to a destruction of the observed 10% of doped droplets. This result also again clearly demonstrates that free In_2 resulting from droplet evaporation are fully negligible at 15 K, which was the temperature used for the measurements in Sec. 4.7.

Discussion and Conclusion:
To rationalize the described process, it would be favourable to know the In_2^+ potential energy surfaces. Unfortunately, there exist no calculated potentials for the In_2^+ molecule, so their forms can only be guessed. However, calculated potentials exist for the Al_2^+ molecule, which electronic structure might be comparable, as In and Al have very simliar electronic structures as they are part of the same main group in the periodic table. Also the neutral In_2 and Al_2 $^3\Pi_u$ ground state Morse parameters are comparable

($r_e = 3.14$ Å, $D_e = 0.83$ eV for In_2 [165] and $r_e = 2.71$ Å, $D_e = 1.36$ eV for Al_2 [232]). For Al_2^+, ionic states with very similar forms like the ones schematically drawn for In_2^+ in Fig. 4.40b have been retrieved [233]. The vertical excitation energy to the excited ionic state was found to be approximately 3 eV, which is exactly in the range of our probe photon energy. After subtraction of the ionic ground state binding energy, still 1.61 eV potential energy might be available for the conversion to kinetic energy. Assuming an equal energy distribution between In and In^+, initial velocities of approximately 820 m/s would be reached.

These values can be compared with velocity measurements following dissociation experiments on neutral alkyl iodides in He_N [113, 114]. In these experiments, the dissociation reaction of different X-I molecules with different X:I mass ratios was investigated. The authors of those studies discussed two possible escape mechanisms for the fragments: First, a direct escape, and second, a thermal escape via a full thermalization of the kinetic energy release to the droplet, causing its full evaporation. By analysing the kinetic energy and anisotropy parameter distributions, the direct escape mechanism could be clearly identified. The investigated molecule closest to the mass ratio of In_2 was CF_3I, with a X:I mass ratio of approximately 1:2 (CF_3: 69u , I: 127u). For the largest droplet size it was found, that CF_3 loses approximately 90% of its kinetic energy, when propagating through the droplet (corresponding to a deceleration from about 1000 to 300 m/s mean velocity). For the iodine fragment, about 75% of initial energy was found to be dissipated (corresponding to a deceleration from 600 to 300 m/s). Moreover also for I, the fragment was found to escape with several He atoms attached to it. Comparing those value to an assumed initial In^+ velocity of 820 m/s it is reasonable, to also account the direct escape mechanism to be the primary source of the $InHe_n$ complexes. Assuming a however stronger deceleration of In^+ compared to the neutral I could explain the absent $InHe_n^+$ yield during the first ten ps.

In conclusion, a fragmentation channel in the In_2^+ molecule could be identified. The fact that fragmentation is induced by the probe pulse after resonant pump excitation, in combination with In_2 ejection, allows to investigate the fragmentation behaviour on the full ejection coordinate, starting from full immersion to the bare molecule. Analysing the total yields of In^+, $InHe_n^+$, In_2^+ and absent $In_2He_n^+$ suggests a strong dependence of the fragmentation probability on the presence of He. For example, the increase and decrease of $InHe_n^+$ during the first 100 ps could indicate that nearly all In_2^+ might dissociate during the first few ps, but are however not detected as they are captured inside the droplets. The fragmentation ratio at 300 ps is considerably lower, and only small amounts of In^+ are measured, compared to In_2^+.

As open points, the data in Fig. 4.41d could be fitted with an appropriate model that describes all the mentioned effects. Unfortunately, the described process takes place in the ionized molecule, for which reason no easy pump-probe experiment based on photoionization is conceivable, which could directly resolve the fragmentation in a time-resolved experiment. A possible experiment involves photoionization of the neutral In atom, the here up to now not discussed by-product of the fragmentation, with a third laser pulse. Both the photoelectrons as well as the photoions (similar to a Coulomb Explosion experiment [234]) could be traced in a pump-probe-probe scheme. Experimentally, it would also be interesting to measure the transient fragment velocities with imaging techniques, which would allow to trace the dissipative effects of the He environment as a function of time delay and therefore In_2 location at the moment of ionization/dissociation. A comparison with for example neutral alkyl iodide dissociation dynamics, as well as a direct comparison of the In^+ and neutral In speeds after ejection, would then allow to compare the dissipative effects on neutral and ionized fragments.

CHAPTER 5

Summary, discussion and outlook

Within this chapter the key research questions formulated in Ch. 1 are recalled and, where possible, appropriate concluding answers are given. Remaining open questions are discussed and a possible outlook for further studies is given.

(1) Are photoelectrons good observables for the study of ultrafast processes of dopants inside He_N?
Our TRPES experiments on In and In_2 photoexcitation clearly give a positive answer to this question. We were not only able to identify photoelectron peaks from the corresponding solvated species, but also to follow dynamical shifts (bubble expansion/oscillation/dopant ejection) with femtosecond resolution. While for In and In_2, these shifts are quite pronounced due to the strong repulsive interaction, they might be not as intense for more complex molecular structures (especially for excitation of non-Rydberg states). PE spectra were found to be only slightly disturbed for ionization inside He_N. Especially after the bubble expansion, only a small tail extending to the low energy side of the spectrum was found, best resolved for spectra at time delays > 0.5 ps (Fig. 4.21b), resulting from inelastic collisions of the electrons with He, in agreement with Ref. [60]. During the bubble expansion, the fast PE energy change resulted in significant broadening of the peaks (see Fig. 4.12), however the shifts could still be resolved. These results might not hold for every other species, as we could show that In does not reside completely in the droplet center, but is rather found in a region close to the droplet surface, though still fully solvated (see Sec. 4.4). Within this thesis, only two other species were investigated with TRPES, namely In_2 and Al, with equally low PE spectra perturbations. Due to the similar electronic structures to In, also similar equilibrium locations may be assumed for both dopants. Therefore, only near surface locations of the dopants might favour undisturbed PE propagation, if the electrons only move the shortest way to the droplet edge. In future, it will be interesting to compare TRPES spectra for different dopants that are solvated more deeply inside the droplet, and check for He_N size dependencies.

(2) What is the response of the droplet solvent on chromophore photoexcitation?
Fully solvated atoms in He_N exhibit significantly blue-shifted excitation bands. Photoexcitation therefore results in an excess energy, which is redistributed within the chromophore-droplet system. For the case

of Rydberg state excitation of atoms (and likely similar excitation conditions for the case of diatomic molecules), the most pronounced response was found to be the expansion of the solvation bubble (see Secs. 4.3 and 4.4). For the case of In, this expansion manifests itself in fast dynamical PE energy shifts of 270 meV within 600 fs, as the system relaxes to larger bubble radii. Following the expansion, the extended bubble starts a breathing oscillation at a much slower period of around 30 ps, and slowly moves to the droplet edge, ultimately leading to dopant ejection. We found that nearly all excess energy resulting from the blue-shifted excitation band is transferred to the He environment in the form of He density waves that ultimately lead to evaporation of He atoms at the droplet surface. Based on the large blue shift of In, it can be assumed that the bubble expansion will not be as pronounced for other dopants. For the case of inner valence transitions or excitation of large molecules the expansion might be completely absent, as such molecules were found to exhibit hardly any blue shifts or even slight red shifts inside He_N [5]. It will therefore be interesting to compare the dynamical solvent response following chromophore excitation for different molecular species.

(3) What is the available time scale for studies inside the droplet?
Due to remaining repulsive interactions of dopants with He after the bubble expansion, photoexcitation can result also in energy transfer to the dopant via an ejection process. In the case of In or In_2, we found that dopants were ejected from the droplet within a few ten ps. Assuming such ejection times also for other molecules, this time window should be clearly sufficient to enable femtosecond studies on nearly all systems. For In we found that the ejection time does not depend on excitation energy (Fig. 4.24), as nearly all excess energy from the blue-shifted excitation is consumed during the bubble expansion. For other dopants, the branching ratio of the excess energy, either coupled into the bubble expansion or transferred to the dopant through ejection, might be different. We nevertheless imagine the In system to be representative for most solvated species, considering that the bubble expansion should always be a symmetric process and ejection velocities are limited through the Landau criterion of frictionless movement [71]. In contrast, for the case of atom excitation on the droplet's surface, a significant fraction of excess energy is transferred to dopant kinetic energy, leading to very fast desorption times [25].
Based on these results, the limiting factor for femtochemistry experiments in He_N will most likely not be the dwell time of the dopant after photoexcitation, but rather the decoherence time of the excited vibronic states (see question 5).

(4) What are the time scales of intrinsic electronic dopant relaxation?
For In excited to it's first excited state (6^2S) no droplet induced relaxation could be identified (Sec. 4.3). Unfortunately also in experiments on higher excited states no clear results on electronic relaxations could be obtained (Sec. 4.5): A broad excitation spectrum in the range around 280 nm could be measured, which was assigned to stem most likely from 5^2D state excitation, and probably also from an either directly, or via fast relaxation populated 6^2P state. Whereas some interesting dynamics like a transient intensity change not only during bubble expansion (Fig. 4.29), but also on a longer time scale of several 10 ps (Fig. 4.30), could be measured, no clear relaxation dynamics, for example down to the 6^2S state or to the ground state, could be observed.
For the case of Al, on the other hand, a clear signal decay after in-droplet 3^2D excitation could be measured, with a time constant of approximately 10 ps (Fig. 4.31). However, also here no lower lying populated state (4^2S) could be identified, and a transient bleach signal rather suggested relaxation down to the electronic ground state, in contrast to literature [63]. In addition, a temporary PE signal at high kinetic energies was measured, presumably from a shortly populated intermediate state, which has to be identified more clearly, calling for additional measurements. If electronic relaxation for Al can be as-

signed, it will be interesting to compare the observed time scales for different droplet sizes and excitation energies, and probably also change the solvation conditions by co-doping with different species to achieve a microsolvation environment.

(5) What is the droplet's influence on intrinsic molecular dynamics?
Closely related to the above mentioned processes of electronic relaxation and vibrational cooling is the question of the He_N's general influence on molecular excited states dynamics, especially on coherent properties, which also determine the observability with TRPES. For In_2 excited at the $B^3\Pi_g(II) \leftarrow X^3\Pi_u$ transition, coherent WP signals were found that lasted several ps, and the observation of WP revivals indicated partly conversed coherence for at least around 20 ps (Fig. 4.34). This low degree of decoherence exceeds coherence times obtained in comparable solutions [75, 221], opening the possibility to be able to study femtosecond dynamics also in more complex, e.g. biologically relevant, systems.
As open question, it is still not completely clear which property of the superfluid droplet is responsible for the low degree of decoherence. Vibrational relaxation in He_N is believed to depend on the mismatch between adjacent vibrational energies to the He droplet modes. However, for alkali metal dimers on the droplet's surface, similar vibrational energies gave significantly different decoherence times [22, 23] (see Sec. 2.4). It remains to be answered if the low degree of decoherence is related to other chromophore-droplet interactions, e.g. the formation and propagation dynamics of the solvation bubble, which could act as a protecting layer and minimize decoherent collisions. Other properties that might play a role include the vibrational energy, amplitude or molecular mass. Future experiments should closely analyse those influences, for example by investigating the In_2 WP dynamics for different excitation energies. Additionally, molecules with similar electronic structure but different mass could be investigated, like Al_2 or Ga_2. The influence of states with weaker repulsive interactions could be studied by creating WP in the electronic ground state by resonant impulsive stimulated Raman scattering.
The introdution of In_2 inside He_N to a microsolvation environment might allow to probe the coherence of vibrational motion in an intermediate regime between the isolated and condensed phase. This experiment is motivated by the fact that electronic relaxation in general is closely related to the coupling of a chromophore to its bath, a widely studied topic in the femtochemistry community: Strong couplings between solvent and chromophore are thought to play a crucial role for the vibrational cooling of excited electronic states in nucleobases, leading to the photostability of DNA [235, 236]. He_N might allow to study the transition from isolated to fully solvated molecules and thereby closely monitor the complex interplay of non-adiabatic relaxation (e.g. through conical intersections) and vibrational cooling that is responsible for processes like the photoprotection mechanism.
The molecular bond in In_2 has covalent character, performing a stretch vibrational motion. Investigations should also include the question, how modes with different binding character or vibrational (e.g. 3-atomic) motion might be influenced by the He surrounding. Such influences were not investigated within this thesis, but are briefly mentioned in the next question.

(6) How strong does the coupling of the droplet's internal modes with the molecule depend on the excited mode?
The low decoherence observed for In_2 might not be representative for all molecular systems. For example, large ampliutde motion, or also modes in more complex molecules, like bending, twisting or out-of-plane motion, might couple much stronger to the He solvent. Also, the strength of the mode might play a crucial role, interesting cases include molecules exhibiting dipole moments, or in the extreme case bonds with ionic character. For the latter case, attempts to temporally resolve the WP motion of LiI in He_N, excited to the ionic Li^+-I^- potential, were not successful [137]. The increased dipole-He interaction of

such a molecule might cause significant changes in the electronic potential curves, as observed for diatomic halogen molecules in cryogenic matrices [237], leading to fast relaxations through curve crossings.

CHAPTER 6

Appendix

6.1 Appendix A: Derivation of the wave-packet dispersion time $\tau_{\mathbf{disp}}$

The ansatz and the idea for the following derivation was taken from Ref. [227]. Although outlined there, a more detailed and complete derivation is presented here for the sake of consistency.

We start with a wave-packet (WP) in a Morse oscillator. An ultrashort laser pulse of bandwidth $\Delta E(= 2\delta E)$ coherently excites energy levels between

$$E_2 = E + \delta E \tag{6.1}$$

$$E_1 = E - \delta E. \tag{6.2}$$

We now think of two two-level beats directly at the edges of the excitation profile, namely stemming from an oscillation between the levels E_1 and E_2 and their direct neighbours. We define the WP to be completely dispersed when the time-dependent beat signals around E_2 and E_1 show a phase shift of 2π, as then every beat between all adjacent levels within ΔE will have some counterpart with phase-shift π, leading to destructive interference. This condition is fulfilled when

$$T_{\mathrm{disp}} = nT_2 \tag{6.3}$$

$$T_{\mathrm{disp}} = (n-1)T_1 \tag{6.4}$$

is true, meaning that the the two beats with periods T_i are exactly one oscillation period out of phase. Equs. 6.4 then lead to a condition for T_{disp}:

$$T_{\mathrm{disp}} = \frac{T_1 T_2}{T_1 - T_2} = \frac{T_1 T_2}{T_1 T_2 (T_2^{-1} - T_1^{-1})} = \frac{T_2^{-1} + T_1^{-1}}{T_2^{-2} - T_1^{-2}}. \tag{6.5}$$

The last expression for T_{disp} will be practical for its final derivation. The main parameters of the Morse potential are the characteristic angular frequency ω (with energy $\omega_e = \hbar\omega$) and the depth of the potential

D_e, which is connected to the unitless anharmonicity constant x_e constant via

$$D_e = \frac{\hbar\omega}{4x_e}. \tag{6.6}$$

Frequency beats in a Morse oscillator follow the form

$$\nu(E) = \frac{\omega}{2\pi}\left(1 - \frac{E}{D_e}\right)^{\frac{1}{2}} = \frac{1}{2\pi}(\omega^2 - c\omega E)^{\frac{1}{2}} \tag{6.7}$$

with the here defined constant factor $c = 4x_e/\hbar$. This equation stems from the assumption of classical motion inside the Morse potential [238]; the classical oscillation period is thereby directly related to the energy distance of the beat via the correspondence principle. Transforming Eq. 6.7 yields the period T

$$T(E) = \frac{1}{\nu(E)} = 2\pi\left(\omega^2 - c\omega E\right)^{-\frac{1}{2}}. \tag{6.8}$$

Substituting this expression into eq. 6.5 yields

$$T_{\text{disp}} = \frac{2\pi}{2c\omega\delta E}\left[(\omega^2 - c\omega E_2)^{\frac{1}{2}} + (\omega^2 - c\omega E_1)^{\frac{1}{2}}\right]. \tag{6.9}$$

The remaining two terms in the bracket are approximated with a Taylor expansion of the form

$$(a \pm x)^{\frac{1}{2}} \approx a^{\frac{1}{2}} \pm \frac{1}{2}a^{-\frac{1}{2}}x, \tag{6.10}$$

with the argument $x = E_i = E \pm \delta E$ taken around the central energy E, yielding:

$$[\omega^2 - c\omega \overbrace{(E + \delta E)}^{E_2}]^{\frac{1}{2}} \approx (\omega^2 - c\omega E)^{\frac{1}{2}} - \frac{1}{2}(\omega^2 - c\omega E)^{-\frac{1}{2}}\ c\omega\delta E \tag{6.11}$$

$$[\omega^2 - c\omega \overbrace{(E - \delta E)}^{E_1}]^{\frac{1}{2}} \approx (\omega^2 - c\omega E)^{\frac{1}{2}} + \frac{1}{2}(\omega^2 - c\omega E)^{-\frac{1}{2}}\ c\omega\delta E. \tag{6.12}$$

Putting everything back together in equation 6.9 and using the above definitions of ΔE and c, as well as expression 6.7 finally yields:

$$T_{\text{disp}} = \frac{2\pi}{2c\omega\delta E}\ 2\ \underbrace{(\omega^2 - c\omega E)^{\frac{1}{2}}}_{2\pi\nu(E)} = \frac{4\pi\ 2\pi\nu(E)\hbar}{c\omega\Delta E x_e} = \frac{h^2\nu(E)}{\Delta E\omega_e x_e}. \tag{6.13}$$

Note that the term ω_e represents the energy of the characteristic (angular) frequency ω of the Morse potential; in our terminology ω_e has therefore unity of energy, whereas in literature ω and ω_e are sometimes used interchangeably, with diverse units.

6.2 Appendix B: Motorization of source chamber valve

An encountered problem during the experiments with gas phase molecules pickup (see Sec. 3.2.3) was the very high effusive background, caused by the high molecular vapour pressure at room temperature. Such a background has never caused problems with heated metals like In or Al, as the necessary very hot temperatures needed caused the atoms to immediately condensate again at colder spots after evaporation, leading to high pressures only within the small volume of the pickup cells. However for any high vapour-pressure molecule, the vapour may extend throughout the whole pickup vacuum chamber, leading to a strong effusive beam into the measurement chamber, although the differential pumping section (DPS) in between. To get closer to the situation of the hot metal evaporation, a stronger cooling system of the gas pickup cell with liquid nitrogen will be implemented (see Sec. 3.2.3). As however every background should be subtracted for each pump-probe delay, we constructed a "low-cost" motorization unit for the UHV-valve (VAT 01032-CE01) between the source chamber and the pickup chamber.

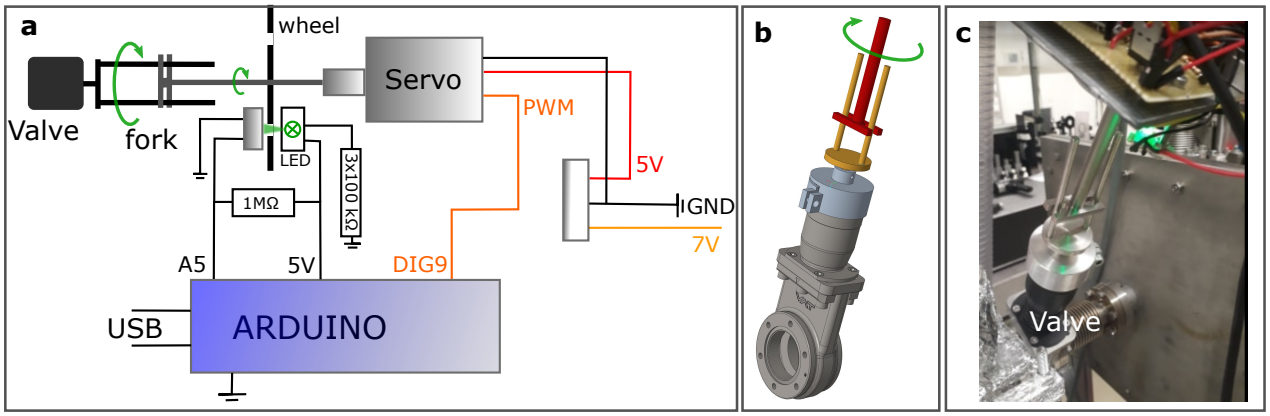

Figure 6.1: Motorized valve rotator. Panel **a** shows the schematic wiring of the servomotor with the transducer, as well as the wheel with illumination unit in order to measure absolute positions. Pins connected to the Arduino are indicated, the translation unit from 7 V to 5 V is marked. Panel **b** shows a technical sketch of the transducing unit. Panel **c** shows an image of the mechanical part of the motorized rotator, with the characteristic H-shaped transducer.

A strong enough continuous rotation servomotor (Feetech FS5113R) was chosen, which turns the (rotatable) valve via a translation gear. For the design of this gear, several configurations were tried, in order to get the rotation unit to work without blocking; those attempts included a flexible shaft to translate the force, as well as a direct axis-to-axis connection ("stick into a hole"). As final solution, a setup consisting of a mounted fork on the valve, which is rotated by a H-formed transducer was chosen (see Fig. 6.1), which turned out to work sufficiently.

As electronic control, an Arduino was chosen, which provides the pulse width modulation for the servomotor, and reads out a light sensing diode to measure the turning position of the motor: A wheel with 15 concentric holes was mounted axially symmetric to the rod that connects the H-formed transducer with the servomotor (c.f. Fig. 6.1c). The software on the Arduino counts the number of light pulses, stemming from a LED, mounted on the opposite side of the sensor, with the wheel in between. While the motor is turning, consecutive holes cause the diode to measures a square wave signal; the number of oscillation cycles is directly linked to the wheel position. The parameters defined in the software that are connected to the real valve positions are listed in table 6.1.

The circuit drawing with all chosen connection and parts is shown in Fig. 6.1a. Addressing is performed via Serial Communication, for example with Matlab. In the current version, single characters have to be

Table 6.1: Parameters defining the positioning system for the valve motor

possible total number of valve turns	5.3
total number of holes	79.5
defined open position	hole No. 10
defined close position	hole No. 70

sent to the Arduino in order to set the motor in rotation, the positions for "closed" and "open", are defined in the Arduino source code; in a following version, better control might be reached by sending the desired positions directly to the Arduino. The source code for the valve should be self explainable, the basic flow of the program roughly goes as this: The program runs in an infinite loop, executing three consecutive steps; first, the photodiode sensor is read out, checking if a new hole is reached. If this condition is fulfilled, and a new count is allowed (the hole actually is a new one), the internal counter counts up or down by one unit, depending on the current turning direction. Higher count values correspond to more open positions (see table 6.1). Second, the serial input buffer is read and possible incoming commands are interpreted and translated (e.g. the desired position is set to "open" or "closed"). Third, the servomotor is triggered, depending on the required position, which might already or not have been reached. These three steps are iterated permanently, independent on the current state of servomotor motion. As long as voltage is supplied, the current wheel position is saved within the program. An additional command allows to calibrate the valve control, by letting the rotation proceed to the two turning points and thereby setting the positioning scale (number of holes). dr

6.3 Appendix C: Implementation and application of the BCN-TLS HeDFT package

The basic application and first tutorial simulations with the open source BCN-TLS-4HeDFT simulation package (see Ref. [105]) are described in the manual, which is available online, see Ref. [239]. Here, the files and structures that were set up in order to implement the codes for time resolved PE spectroscopy simulations are shortly summarized in order to make it easier for future users to handle the simulation package.

In order to be able to use the more intuitive and common shell commands in Linux, a virtual PC was set up with the program "Oracle VM VirtualBox manager", which was then used to run the HeDFT codes on the TU Graz high performance computing system dCluster. The necessary pre- and postprocessing with custom-made python scripts was performed on the virtual machine. However, also working with windows should be no problem, as long as the codes and example commands are run on a Linux-based cluster system (e.g. dCluster, TUGraz). All codes, commands and example files necessary to perform calculations are included in the folder 'home', which will be backed up at the institute's network hard drive.

The HeDFT fortran code files are found in the directory 'home/HeDFT/code'. The files in general have to be compiled and installed on the cluster resource using the command 'make' with the according steps also explained in the manual. For HeDFT calculations involving impurities (like In), the corresponding He-impurity interaction potentials have to be included in the fortran code files (both for the static and the dynamic codes) prior compilation. The file to be changed is called 'V_impur.f90' and is found both in the directory '4hedft' (static simulation code) and in '4hetddft-(an)isotropic' (dynamic simulation code). In the file 'V_impur.f90', a great variety of different pair interaction potentials are already included, however for In and Sr new potentials were calculated by the theory group at the institute. As no easy parametrization / fitting was possible, the potentials were directly splined (with cubic spline, Matlab), and the resulting spline parameters were directly coded into the fortran file, with splines in 0.1 Å steps and an steadily continuing exponential rise to 0 for the largest radii (approx. >30 Å). The matlab programs that generate the spline and the fortran syntax are found under the name 'spline_pairpotential_groundstate/excitedstate/ion', for the case of In.

In the dCluster 'home' directory, a hidden file termed '.profile' exists, in which the intel fft library (included in the math kernel library 'mkl') had to be linked in order to get the codes running. The corresponding lines in the file starting with 'export ....' have to be set correctly. In the file, the folder 'scripts' is also linked to the bash program. In this folder, commands for calling the HeDFT codes are defined via a two-file protocol: A submission file calls a corresponding starter file, both files exist for the static ('starter_he'; 'sub_he') and for the isotropic dynamic calculation ('starter_he_td_isotropic', 'sub_he_td_isotropic'). Those files implement the necessary syntax of the queuing system TORQUE [240], which is used on the dCluster, to execute the compiled HeDFT codes.

Once everything is set up, the HeDFT codes are ready to be used to perform the simulations. The 'home' folder contains both a 'HeDFT/static', as well as 'HeDFT/dynamic' directory, for the two simulations. Most simulation steps include multiple HeDFT calculations (for example for various impurity locations), for which reasons python scripts are used to automatically generate the necessary input files and start the calculations.

6.3.1 Static calculation for a pure droplet

The first step in each calculation is the calculation of a pure droplet density, which is the starting point for calculations with impurities. An example for such a calculation might is found in the folder 'static/pure_diff_droplet_sizes/ pure-4he4000', for a droplet consisting of 4000 He atoms. The only necessary file for such a calculation from scratch (mode=1) is the input file (which is here called 'pure-4he1000.input'), the structure and parameters of which are explained in the dft-manual [239]. The necessary command to start a calculation is then simply:

sub_he *cores* pure-4he1000.input *time*,

where *cores* is the number of CPU-cores that shall be used (attention: this number has to match the value of 'nthreads' in the input file!), and *time* is the expected time of the simulation (in hours). The command sub_he calls the previously mentioned submission script that provides the queuing commands. The calculation will then run until convergence is reached or the specified time is over. The produced '.res' file then contains all necessary data, the 'den.out' file contains the three-dimensional density data of the chosen box, and the 'den-x.dat' files provide density profile cuts along the respective symmetry axis (here x). A 2D cut through the 3D profile can be evaluated with the script 'save_density_xz_static.py', and a 1D cut is retrieved with 'bubble_density_z_scan', both scripts are found in the folder 'static evaluation'.

6.3.2 Static calculation for a droplet with an impurity

The pure droplet density is then the starting point for a static calculation with an impurity placed at a certain position inside the droplet. An example calculation is found in the folder 'HeDFT/static/IndiumHelium/PES_ground_state_diff_droplet_sizes/InHe_gs_4000'. The python script 'InHe_z_scan.py' automatically generates subfolders, input files and links the respective starting density for various positions of the impurity along the z axis. The input parameters can be adjusted to the desired computation (note that the grid parameters have to equal those of the pure droplet calculation), the desired pair potential (along with the correct cutoff data, see Ref. [239]) and the number of cores as well as the expected computation time have to be given. The command 'python InHe_z_scan.py', while being in the respective folder executes the script, generates all necessary files and starts the computation. The output files are the same as for the pure droplet calculation, and can be analysed with the same python scripts. As can be specified in the input file, at specific iteration steps (e.g. each 1000 steps), intermediate results of the density file can be saved. As such files might be unnecessary when the calculation has ended and a converged density might be at hand, the script 'delete_files.py' can be executed to remove the intermediate density files.

6.3.3 Dynamic calculation for a droplet with an impurity in an isotropic state

To perform a dynamic calculation (in this thesis performed only for isotropic states), a density file from a static calculation like the result from the previous section has to be linked. An example calculation for a simulation of time resolved PE spectra is found in
'HeDFT/dynamic/ Dynamic_Indium/InHe_dynamic_diff_droplet_size/InHe4000_dynamics' in the subfolder '/Bubble_expansion/InHe_dyn_z_=20.0_ionic_energies'. As first step, a TD-HeDFT calculation is started for specific starting positions with the script 'start_dyncamical_various.py'. It again generates the necessary folders and input files, with the defined excited state pair potential ('In_6s') and specified time steps. In the script also the respective links to the densities of the static calculations are set

and the submission shell command is given ('sub_he_td_td_isotropic'). During the calculation, every $pcurr \cdot deltatps$ times a density file is saved, which can then be later used for the calculation of the ionic energy, or for animations of time resolved processes.
The dynamic calculation runs again for the specified time span, generating the density files as well as trajectory files ('rimp.out.0', 'vimp.out.0', 'aim.out.0'). With the script 'generate_ionic_trajectories.py', short dynamic calculations with the impurity-He interaction switched to the ionic state ('In_plus_gs') are performed. These calculations might have to run only a few seconds, if the desired output is only the ionic energy, or longer, if one is interested in the ionic dynamics.
With the python script 'save_density_profile_dynamics.py', a 2D density cut is generated, and the corresponding data is saved in a smaller (2D) file ('densprof_xz_plane_...'), which can then be printed with 'save_He_density.py'. PE spectra can be obtained by retrieving the total system's energies at various time steps both for the excited state ('.res' file of the dynamic calculation) and for the ionic state ('.res' file for each ionic calculation, first energy). An example how the data can then be extracted via python is the script 'bubble_expansion_peakshift.py'.

Bibliography

1. Rohatgi-Mukherjee, K. *Fundamentals of photochemistry* (New Age International, 1978).
2. Zewail, A. H. Femtochemistry: Atomic-scale dynamics of the chemical bond. *J. Phys. Chem. A* **104,** 5660–5694 (2000).
3. Scoles, G., Bassi, D., Buck, U. & Laine, D. *Atomic and molecular beam methods* (Oxford university press New York, 1988).
4. Andrews, L. & Moskovits, M. *Chemistry and physics of matrix isolated species* (North-Holland, 1989).
5. Toennies, J. P. & Vilesov, A. F. Superfluid helium droplets: A uniquely cold nanomatrix for molecules and molecular complexes. *Angew. Chem. Int. Ed.* **43,** 2622–2648 (2004).
6. Mudrich, M. & Stienkemeier, F. Photoionisaton of pure and doped helium nanodroplets. *Int. Rev. Phys. Chem.* **33,** 301–339. http://dx.doi.org/10.1080/0144235X.2014.937188 (2014).
7. Choi, M. Y. *et al.* Infrared spectroscopy of helium nanodroplets: novel methods for physics and chemistry. *Int. Rev. Phys. Chem.* **25,** 15–75. https://doi.org/10.1080/01442350600625092 (2006).
8. Callegari, C. & Ernst, W. E. in *Handbook of High Resolution Spectroscopy* (eds Merkt, F. & Quack, M.) (John Wiley & Sons, Chichester, 2011).
9. Stienkemeier, F. & Lehmann, K. K. Spectroscopy and dynamics in helium nanodroplets. *J. Phys. B: Atomic, Molecular and Optical Physics* **39,** R127. http://stacks.iop.org/0953-4075/39/i=8/a=R01 (2006).
10. Nauta, K. & Miller, R. E. Nonequilibrium self-assembly of long chains of polar molecules in superfluid helium. *Science* **283,** 1895–1897 (1999).
11. Higgins, J. *et al.* Photoinduced chemical dynamics of high-spin alkali trimers. *Science* **273,** 629–631 (1996).
12. Küpper, J., Merritt, J. M. & Miller, R. E. Free radicals in superfluid liquid helium nanodroplets: A pyrolysis source for the production of propargyl radical. *J. Chem. Phys.* **117,** 647–652. https://doi.org/10.1063/1.1484104 (2002).
13. Haberfehlner, G., Thaler, P., Knez, D., Volk, A., Hofer, F., Ernst, W. E. & Kothleitner, G. Formation of bimetallic clusters in superfluid helium nanodroplets analysed by atomic resolution electron tomography. *Nat. Comm.* **6,** 8779 (2015).
14. Gutberlet, A. *et al.* Aggregation-induced dissociation of $HCl(H_2O)_4$ below 1 K: the smallest droplet of acid. *Science* **324,** 1545–1548 (2009).

15. Mani, D. *et al.* Acid solvation versus dissociation at "stardust conditions": Reaction sequence matters. *Science advances* **5,** eaav8179 (2019).

16. Stienkemeier, F, Meier, F, Hägele, A, Lutz, H., Schreiber, E, Schulz, C. & Hertel, I. Coherence and relaxation in potassium-doped helium droplets studied by femtosecond pump-probe spectroscopy. *Phys. Rev. Lett.* **83,** 2320 (1999).

17. Schulz, C., Claas, P & Stienkemeier, F. Formation of K* He exciplexes on the surface of helium nanodroplets studied in real time. *Phys. Rev. Lett.* **87,** 153401 (2001).

18. Droppelmann, G, Bünermann, O, Schulz, C. & Stienkemeier, F. Formation times of RbHe exciplexes on the surface of superfluid versus normal fluid helium nanodroplets. *Phys. Rev. Lett.* **93,** 023402 (2004).

19. Claas, P, Droppelmann, G, Schulz, C. P., Mudrich, M & Stienkemeier, F. Wave packet dynamics of K_2 attached to helium nanodroplets. *J. Phys. B: Atomic, Molecular and Optical Physics* **39,** S1151. http://stacks.iop.org/0953-4075/39/i=19/a=S23 (2006).

20. Claas, P., Droppelmann, G., Schulz, C. P., Mudrich, M. & Stienkemeier, F. Wave Packet Dynamics in Triplet States of Na_2 Attached to Helium Nanodroplets. *J. Phys. Chem. A* **111,** 7537–7541. https://doi.org/10.1021/jp070893i (2007).

21. Mudrich, M., Heister, P., Hippler, T., Giese, C., Dulieu, O. & Stienkemeier, F. Spectroscopy of triplet states of Rb_2 by femtosecond pump-probe photoionization of doped helium nanodroplets. *Phys. Rev. A* **80,** 042512. https://link.aps.org/doi/10.1103/PhysRevA.80.042512 (2009).

22. Schlesinger, M., Mudrich, M., Stienkemeier, F. & Strunz, W. T. Dissipative vibrational wave packet dynamics of alkali dimers attached to helium nanodroplets. *Chem. Phys. Lett.* **490,** 245 –248. http://www.sciencedirect.com/science/article/pii/S0009261410004586 (2010).

23. Gruner, B., Schlesinger, M., Heister, P., Strunz, W. T., Stienkemeier, F. & Mudrich, M. Vibrational relaxation and dephasing of Rb_2 attached to helium nanodroplets. *Phys. Chem. Chem. Phys.* **13,** 6816–6826. http://dx.doi.org/10.1039/C0CP02355H (2011).

24. Von Vangerow, J *et al.* Desorption dynamics of heavy alkali metal atoms (Rb, Cs) off the surface of helium nanodroplets. *J. Phys. Chem. A* **118,** 6604–6614 (2014).

25. Von Vangerow, J. *et al.* Imaging Excited-State Dynamics of Doped He Nanodroplets in Real-Time. *J. Phys. Chem. Lett.* **8,** 307–312. http://dx.doi.org/10.1021/acs.jpclett.6b02598 (2017).

26. Dozmorov, N. V., Baklanov, A. V., von Vangerow, J., Stienkemeier, F., Fordyce, J. A. M. & Mudrich, M. Quantum dynamics of Rb atoms desorbing off the surface of He nanodroplets. *Phys. Rev. A* **98,** 043403. https://link.aps.org/doi/10.1103/PhysRevA.98.043403 (2018).

27. Bruder, L. *et al.* Coherent multidimensional spectroscopy of dilute gas-phase nanosystems. *Nat. Comm.* **9,** 4823 (2018).

28. Coppens, F., Von Vangerow, J., Barranco, M., Halberstadt, N., Stienkemeier, F., Pi, M. & Mudrich, M. Desorption dynamics of RbHe exciplexes off He nanodroplets induced by spin-relaxation. *Phys. Chem. Chem. Phys.* **20,** 9309–9320 (2018).

29. Mateo, D., Hernando, A., Barranco, M., Loginov, E., Drabbels, M. & Pi, M. Translational dynamics of photoexcited atoms in ^{4}He nanodroplets: the case of silver. *Phys. Chem. Chem. Phys.* **15,** 18388–18400. http://dx.doi.org/10.1039/C3CP52221K (2013).

30. Vilà, A., Gonzalez, M. & Mayol, R. Photodissociation dynamics of homonuclear diatomic molecules in helium nanodroplets. The case of $Cl_2@(^4He)_N$. *J. Chem. Theory Comput.* **11,** 899–906 (2015).

31. Vilà, A., González, M. & Mayol, R. Quantum dynamics of the pick up process of atoms by superfluid helium nanodroplets: the Ne+$(^4He)_{1000}$ system. *Phys. Chem. Chem. Phys.* **18,** 2006–2014 (2016).

32. Kornilov, O. *et al.* Ultrafast dynamics in helium nanodroplets probed by femtosecond time-resolved EUV photoelectron imaging. *J. Phys. Chem. A* **114,** 1437–1445 (2009).

33. Kornilov, O., Bünermann, O., Haxton, D. J., Leone, S. R., Neumark, D. M. & Gessner, O. Femtosecond photoelectron imaging of transient electronic states and Rydberg atom emission from electronically excited He droplets. *J. Phys. Chem. A* **115,** 7891–7900 (2011).

34. Bünermann, O., Kornilov, O., Leone, S. R., Neumark, D. M. & Gessner, O. Femtosecond extreme ultraviolet ion imaging of ultrafast dynamics in electronically excited helium nanodroplets. *IEEE J. Sel. Top. Quantum Electron.* **18,** 308–317 (2011).

35. Bünermann, O., Kornilov, O., Haxton, D. J., Leone, S. R., Neumark, D. M. & Gessner, O. Ultrafast probing of ejection dynamics of Rydberg atoms and molecular fragments from electronically excited helium nanodroplets. *J. Chem. Phys.* **137,** 214302 (2012).

36. Ziemkiewicz, M. P., Neumark, D. M. & Gessner, O. Ultrafast electronic dynamics in helium nanodroplets. *Int. Rev. Phys. Chem.* **34,** 239–267. http://dx.doi.org/10.1080/0144235X.2015.1051353 (2015).

37. Mudrich, M *et al.* Ultrafast relaxation of photoexcited superfluid He nanodroplets. *arXiv preprint arXiv:1905.04489* (2019).

38. Pentlehner, D., Nielsen, J. H., Slenczka, A., Mølmer, K. & Stapelfeldt, H. Impulsive laser induced alignment of molecules dissolved in helium nanodroplets. *Phys. Rev. Lett.* **110,** 093002 (2013).

39. Pentlehner, D., Nielsen, J. H., Christiansen, L., Slenczka, A. & Stapelfeldt, H. Laser-induced adiabatic alignment of molecules dissolved in helium nanodroplets. *Phys. Rev. A* **87,** 063401 (2013).

40. Shepperson, B., Chatterley, A. S., Søndergaard, A. A., Christiansen, L., Lemeshko, M. & Stapelfeldt, H. Strongly aligned molecules inside helium droplets in the near-adiabatic regime. *J. Chem. Phys.* **147,** 013946 (2017).

41. Shepperson, B., Søndergaard, A. A., Christiansen, L., Kaczmarczyk, J., Zillich, R. E., Lemeshko, M. & Stapelfeldt, H. Laser-induced rotation of iodine molecules in helium nanodroplets: revivals and breaking free. *Phys. Rev. Lett.* **118,** 203203. https://link.aps.org/doi/10.1103/PhysRevLett.118.203203 (2017).

42. Chatterley, A. S., Shepperson, B. & Stapelfeldt, H. Three-dimensional molecular alignment inside helium nanodroplets. *Phys. Rev. Lett.* **119,** 073202. https://link.aps.org/doi/10.1103/PhysRevLett.119.073202 (2017).

43. Shepperson, B., Chatterley, A. S., Christiansen, L., Søndergaard, A. A. & Stapelfeldt, H. Observation of rotational revivals for iodine molecules in helium droplets using a near-adiabatic laser pulse. *Phys. Rev. A* **97,** 013427 (2018).

44. Chatterley, A. S., Schouder, C., Christiansen, L., Shepperson, B., Rasmussen, M. H. & Stapelfeldt, H. Long-lasting field-free alignment of large molecules inside helium nanodroplets. *Nat. Comm.* **10,** 133 (2019).

45. Döppner, T., Fennel, T., Diederich, T., Tiggesbäumker, J & Meiwes-Broer, K. Controlling the Coulomb explosion of silver clusters by femtosecond dual-pulse laser excitation. *Phys. Rev. Lett.* **94,** 013401 (2005).

46. Göde, S, Irsig, R, Tiggesbäumker, J & Meiwes-Broer, K.-H. Time-resolved studies on the collapse of magnesium atom foam in helium nanodroplets. *New J. Phys.* **15,** 015026. http://stacks.iop.org/1367-2630/15/i=1/a=015026 (2013).

47. Krishnan, S. R. *et al.* Evolution of dopant-induced helium nanoplasmas. *New J. Phys.* **14,** 075016 (2012).

48. Kelbg, M., Heidenreich, A., Kazak, L., Zabel, M., Krebs, B., Meiwes-Broer, K.-H. & Tiggesbäumker, J. Comparison of Electron and Ion Emission from Xenon Cluster-Induced Ignition of Helium Nanodroplets. *J. Phys. Chem. A* **122,** 8107–8113 (2018).

49. Dantus, M, Janssen, M. & Zewail, A. Femtosecond probing of molecular dynamics by mass-spectrometry in a molecular beam. *Chem. Phys. Lett.* **181,** 281–287 (1991).

50. Stolow, A., Bragg, A. E. & Neumark, D. M. Femtosecond time-resolved photoelectron spectroscopy. *Chem. Rev.* **104,** 1719–1757 (2004).

51. Eppink, A. T. & Parker, D. H. Velocity map imaging of ions and electrons using electrostatic lenses: Application in photoelectron and photofragment ion imaging of molecular oxygen. *Rev. Sci. Instrum.* **68,** 3477–3484 (1997).

52. Reid, K. L. Photoelectron angular distributions. *Ann. Rev. Phys. Chem.* **54,** 397–424 (2003).

53. Stert, V, Radloff, W, Schulz, C. & Hertel, I. Ultrafast photoelectron spectroscopy: Femtosecond pump-probe coincidence detection of ammonia cluster ions and electrons. *Eur. Phys. J. D: Atomic, Molecular, Optical and Plasma Physics* **5,** 97–106 (1999).

54. Nauta, K. & Miller, R. E. Nonequilibrium self-assembly of long chains of polar molecules in superfluid helium. *Science* **283,** 1895–1897 (1999).

55. Nauta, K. & Miller, R. E. Formation of cyclic water hexamer in liquid helium: the smallest piece of ice. *Science* **287,** 293–295 (2000).

56. Thaler, P. *et al.* Formation of bimetallic core-shell nanowires along vortices in superfluid He nanodroplets. *Phys. Rev. B* **90,** 155442 (2014).

57. Bierau, F., Kupser, P., Meijer, G. & von Helden, G. Catching proteins in liquid helium droplets. *Phys. Rev. Lett.* **105,** 133402 (2010).

58. Denifl, S. *et al.* Ion–molecule reactions in helium nanodroplets doped with C_{60} and water clusters. *Ang. Chen. Int. Ed.* **48,** 8940–8943 (2009).

59. Radcliffe, P., Przystawik, A., Diederich, T., Döppner, T., Tiggesbäumker, J. & Meiwes-Broer, K.-H. Excited-state relaxation of Ag_8 clusters embedded in helium droplets. *Phys. Rev. Lett.* **92,** 173403 (2004).

60. Loginov, E., Rossi, D. & Drabbels, M. Photoelectron spectroscopy of doped helium nanodroplets. *Phys. Rev. Lett.* **95,** 163401. https://link.aps.org/doi/10.1103/PhysRevLett.95.163401 (2005).

61. Kazak, L., Göde, S., Meiwes-Broer, K.-H. & Tiggesbäumker, J. Photoelectron Spectroscopy on Magnesium Ensembles in Helium Nanodroplets. *J. Phys. Chem. A* **123,** 5951–5956. https://doi.org/10.1021/acs.jpca.9b02880 (2019).

62. Peterka, D. S., Lindinger, A., Poisson, L., Ahmed, M. & Neumark, D. M. Photoelectron imaging of helium droplets. *Phys. Rev. Lett.* **91,** 043401 (2003).

63. Reho, J. H., Merker, U., Radcliff, M. R., Lehmann, K. K. & Scoles, G. Spectroscopy and dynamics of Al atoms solvated in superfluid helium nanodroplets. *J. Phys. Chem. A* **104,** 3620–3626 (2000).

64. Przystawik, A., Göde, S., Döppner, T., Tiggesbäumker, J. & Meiwes-Broer, K.-H. Light-induced collapse of metastable magnesium complexes formed in helium nanodroplets. *Phys. Rev. A* **78,** 021202. https://link.aps.org/doi/10.1103/PhysRevA.78.021202 (2008).

65. Kautsch, A., Koch, M. & Ernst, W. E. Electronic relaxation after resonant laser excitation of Cr in superfluid helium nanodroplets. *J. Phys. Chem. A* **117,** 9621–9625 (2013).

66. Lindebner, F., Kautsch, A., Koch, M. & Ernst, W. E. Laser ionization and spectroscopy of Cu in superfluid helium nanodroplets. *Int. J. Mass Spectrom.* **365,** 255–259 (2014).

67. Messner, R., Schiffmann, A., Pototschnig, J. V., Lasserus, M., Schnedlitz, M., Lackner, F. & Ernst, W. E. Spectroscopy of gold atoms and gold oligomers in helium nanodroplets. *J. Chem. Phys.* **149,** 024305. https://doi.org/10.1063/1.5026480 (2018).

68. Federmann, F, Hoffmann, K, Quaas, N & Close, J. Rydberg states of silver: excitation dynamics of doped helium droplets. *Phys. Rev. Lett.* **83,** 2548 (1999).

69. Loginov, E. & Drabbels, M. Excited state dynamics of Ag atoms in helium nanodroplets. *J. Phys. Chem. A* **111,** 7504–7515. https://doi.org/10.1021/jp0716278 (2007).

70. Kautsch, A., Hasewend, M., Koch, M. & Ernst, W. E. Fano resonances in chromium photoionization spectra after photoinduced ejection from a superfluid helium nanodroplet. *Phys. Rev. A* **86,** 033428. http://dx.doi.org/10.1103/PhysRevA.86.033428 (2012).

71. Brauer, N. B. *et al.* Critical Landau velocity in helium nanodroplets. *Phys. Rev. Lett.* **111,** 153002. https://link.aps.org/doi/10.1103/PhysRevLett.111.153002 (2013).

72. Koch, M., Kautsch, A., Lackner, F. & Ernst, W. E. One-and Two-Color Resonant Photoionization Spectroscopy of Chromium-Doped Helium Nanodroplets. *J. Phys. Chem. A* **118,** 8373–8379 (2014).

73. Brühl, F. R., Trasca, R. A. & Ernst, W. E. Rb-He exciplex formation on helium nanodroplets. *J. Chem. Phys.* **115,** 10220–10224. https://aip.scitation.org/doi/abs/10.1063/1.1410118 (2001).

74. Zadoyan, R, Li, Z, Ashjian, P, Martens, C. & Apkarian, V. Femtosecond dynamics of coherent photodissociation—recombination of I2 isolated in matrix Ar. *Chem. Phys. Lett.* **218,** 504–514 (1994).

75. Guhr, M., Bargheer, M., Fushitani, M., Kiljunen, T. & Schwentner, N. Ultrafast dynamics of halogens in rare gas solids. *Phys. Chem. Chem. Phys.* **9,** 779–801. http://dx.doi.org/10.1039/B609058N (2007).

76. Wu, G., Hockett, P. & Stolow, A. Time-resolved photoelectron spectroscopy: from wavepackets to observables. *Phys. Chem. Chem. Phys.* **13,** 18447–18467 (2011).

77. Schoenlein, R., Peteanu, L., Mathies, R. & Shank, C. The first step in vision: femtosecond isomerization of rhodopsin. *Science* **254,** 412–415 (1991).

78. Hammarström, L. & Styring, S. Coupled electron transfers in artificial photosynthesis. *Philosophical Transactions of the Royal Society B: Biological Sciences* **363,** 1283–1291 (2007).

79. Fischer, I., Vrakking, M. J., Villeneuve, D. & Stolow, A. Femtosecond time-resolved zero kinetic energy photoelectron and photoionization spectroscopy studies of I_2 wavepacket dynamics. *Chem. Phys.* **207,** 331–354 (1996).

80. Monni, R., Auböck, G., Kinschel, D., Aziz-Lange, K. M., Gray, H. B., Vlček, A. & Chergui, M. Conservation of vibrational coherence in ultrafast electronic relaxation: The case of diplatinum complexes in solution. *Chem. Phys. Lett.* **683.** Ahmed Zewail (1946-2016) Commemoration Issue of Chem. Phys. Lett., 112 –120. http://www.sciencedirect.com/science/article/pii/S0009261417301872 (2017).

81. Bargheer, M., Gühr, M. & Schwentner, N. Collisions transfer coherence. *Israel journal of chemistry* **44,** 9–17 (2004).

82. Jahnke, T *et al.* Multicoincidence studies of photo and Auger electrons from fixed-in-space molecules using the COLTRIMS technique. *Journal of Electron Spectroscopy and Related Phenomena* **141,** 229–238 (2004).

83. Boguslavskiy, A. E. *et al.* The Multielectron Ionization Dynamics Underlying Attosecond Strong-Field Spectroscopies. *Science* **335,** 1336–1340. http://science.sciencemag.org/content/335/6074/1336 (2012).

84. Wilkinson, I. *et al.* Excited state dynamics in SO_2. I. Bound state relaxation studied by time-resolved photoelectron-photoion coincidence spectroscopy. *J. Chem. Phys.* **140,** 204301 (2014).

85. Maierhofer, P., Bainschab, M., Thaler, B., Heim, P., Ernst, W. E. & Koch, M. Disentangling Multichannel Photodissociation Dynamics in Acetone by Time-Resolved Photoelectron–Photoion Coincidence Spectroscopy. *J. Phys. Chem. A* **120,** 6418–6423. http://dx.doi.org/10.1021/acs.jpca.6b07238 (2016).

86. Koch, M., Heim, P., Thaler, B., Kitzler, M. & Ernst, W. E. Direct observation of a photochemical activation energy: a case study of acetone photodissociation. *J. Phys. B: Atomic, Molecular and Optical Physics* **50,** 125102. http://stacks.iop.org/0953-4075/50/i=12/a=125102 (2017).

87. Callegari, C., Lehmann, K. K., Schmied, R. & Scoles, G. Helium nanodroplet isolation rovibrational spectroscopy: Methods and recent results. *J. Chem. Phys.* **115,** 10090–10110 (2001).

88. Auboeck, G. *Spectroscopy of Alkali-Metal Atoms and their High-Spin Oligomers on Helium Nanodroplets in External Magnetic Fields* PhD Thesis (Institute of Experimental physics, Graz University of Technology, 2008).

89. Koch, M. *Magnetic Resonance Spectroscopy of Single Alkali-Metal Atoms Isolated in Superfluid Helium Nanodroplets* PhD Thesis (Institute of Experimental physics, Graz University of Technology, 2009).

90. Theisen, M. *Aggregation of Rb and Cs atoms on helium nanodroplets and laser ionization of cold clusters* PhD Thesis (Institute of Experimental physics, Graz University of Technology, 2011).

91. Lackner, F. *Rydberg States of Alkali-Metal Atoms on Superfluid Helium Nanodroplets* PhD Thesis (Institute of Experimental physics, Graz University of Technology, 2012).

92. Kautsch, A. *Photoinduced Dynamics of Transition Metal Atoms and Clusters in Helium Nanodroplets* PhD Thesis (Institute of Experimental physics, Graz University of Technology, 2014).

93. Barranco, M., Guardiola, R., Hernández, S., Mayol, R., Navarro, J. & Pi, M. Helium Nanodroplets: An Overview. *J. Low Temp. Phys.* **142,** 1. https://doi.org/10.1007/s10909-005-9267-0 (2006).

94. Harms, J., Toennies, J. P. & Dalfovo, F. Density of superfluid helium droplets. *Phys. Rev. B* **58,** 3341–3350. https://link.aps.org/doi/10.1103/PhysRevB.58.3341 (1998).

95. Lehmann, K. K. & Callegari, C. Quantum hydrodynamic model for the enhanced moments of inertia of molecules in helium nanodroplets: Application to SF_6. *J. Chem. Phys.* **117,** 1595–1603 (2002).

96. Nauta, K & Miller, R. Vibrational relaxation of Ne, Ar, Kr–HF (v= 1) binary complexes in helium nanodroplets. *J. Chem. Phys.* **115,** 4508–4514 (2001).

97. Koch, M., Auböck, G., Callegari, C. & Ernst, W. E. Coherent spin manipulation and ESR on superfluid helium nanodroplets. *Phys. Rev. Lett.* **103,** 035302. http://link.aps.org/abstract/PRL/v103/e035302 (2009).

98. Thaler, B. *et al.* Conservation of Hot Thermal Spin–Orbit Population of ^{2}P Atoms in a Cold Quantum Fluid Environment. *J. Phys. Chem. A* **123,** 3977–3984. https://doi.org/10.1021/acs.jpca.9b02920 (2019).

99. Ancilotto, F., Lerner, P. B. & Cole, M. W. Physics of solvation. *J. Low Temp. Phys.* **101,** 1123–1146 (1995).

100. Goyal, S, Schutt, D. & Scoles, G. Vibrational spectroscopy of sulfur hexafluoride attached to helium clusters. *Phys. Rev. Lett.* **69,** 933 (1992).

101. Hartmann, M, Miller, R., Toennies, J. & Vilesov, A. Rotationally Resolved Spectroscopy of SF_6 in Liquid Helium Clusters: A Molecular Probe of Cluster Temperature. *Phys. Rev. Lett.* **75,** 1566 (1995).

102. Grebenev, S., Toennies, J. P. & Vilesov, A. F. Superfluidity within a small helium-4 cluster: The microscopic Andronikashvili experiment. *Science* **279,** 2083–2086 (1998).

103. Verma, D., Tanyag, R. M. P., O'Connell, S. M. & Vilesov, A. F. Infrared spectroscopy in superfluid helium droplets. *Advances in Physics: X* **4,** 1553569 (2019).

104. Ben Ltaief, L. *et al.* Charge-exchange dominates long-range interatomic Coulombic decay of excited metal-doped He nanodroplets. *J. Phys. Chem. Lett.* (2019).

105. Pi, M. *et al.* *^{4}He-DFT BCN-TLS: a computer package for simulating structural properties and dynamics of doped liquid helium-4 systems. https://github.com/bcntls2016/ (2016)*

106. Ancilotto, F. *et al.* Density functional theory of doped superfluid liquid helium and nanodroplets. *Int. Rev. Phys. Chem.* **36,** 621–707. https://doi.org/10.1080/0144235X.2017.1351672 (2017).

107. Dalfovo, F., Lastri, A., Pricaupenko, L., Stringari, S. & Treiner, J. Structural and dynamical properties of superfluid helium: a density-functional approach. *Phys. Rev. B* **52,** 1193–1209 (1995).

108. Thaler, B. *et al.* Femtosecond photoexcitation dynamics inside a quantum solvent. *Nat. Comm.* **9,** 4006. https://doi.org/10.1038/s41467-018-06413-9 (2018).

109. Landau, L. Theory of the Superfluidity of Helium II. *Phys. Rev.* **60,** 356 (1941).

110. Ancilotto, F., Barranco, M., Eloranta, J. & Pi, M. Onset of nanoscale dissipation in superfluid He 4 at zero temperature: Role of vortex shedding and cavitation. *Phys. Rev. B* **96,** 064503 (2017).

111. Leal, A., Mateo, D., Hernando, A., Pi, M. & Barranco, M. Capture of heliophobic atoms by ^{4}He nanodroplets: the case of cesium. *Phys. Chem. Chem. Phys.* **16,** 23206–23213. http://dx.doi.org/10.1039/C4CP03297G (2014).

112. Coppens, F., Ancilotto, F., Barranco, M., Halberstadt, N. & Pi, M. Capture of Xe and Ar atoms by quantized vortices in ^{4}He nanodroplets. *Phys. Chem. Chem. Phys.* **19,** 24805–24818. http://dx.doi.org/10.1039/C7CP03307A (2017).

113. Braun, A. & Drabbels, M. Imaging the Translational Dynamics of CF_3 in Liquid Helium Droplets. *Phys. Rev. Lett.* **93,** 253401. https://link.aps.org/doi/10.1103/PhysRevLett.93.253401 (2004).

114. Braun, A. & Drabbels, M. Photodissociation of alkyl iodides in helium nanodroplets. I. Kinetic energy transfer. *J. Chem. Phys.* **127,** 114303 (2007).

115. Braun, A. & Drabbels, M. Photodissociation of alkyl iodides in helium nanodroplets. II. Solvation dynamics. *J. Chem. Phys.* **127,** 114304. https://doi.org/10.1063/1.2767262 (2007).

116. Braun, A. & Drabbels, M. Photodissociation of alkyl iodides in helium nanodroplets. III. Recombination. *J. Chem. Phys.* **127,** 114305 (2007).

117. Vilá, A., González, M. & Mayol, R. Quantum interferences in the photodissociation of Cl_2 (B) in superfluid helium nanodroplets (^4He_N. *Physical Chemistry Chemical Physics* **17,** 32241–32250 (2015).

118. Vilà, A. & González, M. Mass effects in the photodissociation of homonuclear diatomic molecules in helium nanodroplets: inelastic collision and viscous flow energy exchange regimes. *Phys. Chem. Chem. Phys.* **18,** 27630–27638 (2016).

119. Kautsch, A., Koch, M. & Ernst, W. E. Photoinduced molecular dissociation and photoinduced recombination mediated by superfluid helium nanodroplets. *Phys. Chem. Chem. Phys.* **17,** 12310–12316. http://dx.doi.org/10.1039/C5CP01009H (2015).

120. Von Vangerow, J. *et al.* Imaging excited-state dynamics of doped He nanodroplets in real-time. *J. Phys. Chem. Lett.* **8,** 307–312. http://dx.doi.org/10.1021/acs.jpclett.6b02598 (2017).

121. Reho, J, Higgins, J, Lehmann, K. & Scoles, G. Alkali–helium exciplex formation on the surface of helium nanodroplets. II. A time-resolved study. *J. Chem. Phys.* **113,** 9694–9701 (2000).

122. Loginov, E., Callegari, C., Ancilotto, F. & Drabbels, M. Spectroscopy on Rydberg states of sodium atoms on the surface of helium nanodroplets. *J. Phys. Chem. A* **115,** 6779–6788 (2011).

123. Fechner, L., Grüner, B, Sieg, A, Callegari, C, Ancilotto, F, Stienkemeier, F & Mudrich, M. Photoionization and imaging spectroscopy of rubidium atoms attached to helium nanodroplets. *Phys. Chem. Chem. Phys.* **14,** 3843–3851 (2012).

124. Hernando, A., Barranco, M., Pi, M., Loginov, E., Langlet, M. & Drabbels, M. Desorption of alkali atoms from ^4He nanodroplets. *Phys. Chem. Chem. Phys.* **14,** 3996–4010 (2012).

125. Loginov, E. & Drabbels, M. Dynamics of excited sodium atoms attached to helium nanodroplets. *J. Phys. Chem. A* **118,** 2738–2748 (2014).

126. Ziemkiewicz, M. P., Bacellar, C., Siefermann, K. R., Leone, S. R., Neumark, D. M. & Gessner, O. Femtosecond time-resolved XUV+ UV photoelectron imaging of pure helium nanodroplets. *J. Chem. Phys.* **141,** 174306 (2014).

127. Moroshkin, P., Hofer, A. & Weis, A. Atomic and molecular defects in solid ^4He. *Phys. Rep.* **469,** 1–57 (2008).

128. Hernandez, J. P. & Silver, M. Dynamics of electron-bubble formation in helium. *Phys. Rev. A* **2,** 1949 (1970).

129. Rosenblit, M. & Jortner, J. Dynamics of the formation of an electron bubble in liquid helium. *Phys. Rev. Lett.* **75,** 4079 (1995).

130. Benderskii, A., Eloranta, J, Zadoyan, R & Apkarian, V. A direct interrogation of superfluidity on molecular scales. *J. Chem. Phys.* **117,** 1201–1213 (2002).

131. Von Haeften, K., Laarmann, T., Wabnitz, H. & Möller, T. Bubble Formation and Decay in ^{3}He and ^{4}He Clusters. *Phys. Rev. Lett.* **88,** 233401 (2002).

132. Jeffs, J. *et al.* Metastable aluminum atoms floating on the surface of helium nanodroplets. *Phys. Rev. Lett.* **114,** 233401 (2015).

133. Lindsay, C., Douberly, G. & Miller, R. Rotational and vibrational dynamics of H_2O and HDO in helium nanodroplets. *Journal of molecular structure* **786,** 96–104 (2006).

134. Giese, C, Mullins, T, Grüner, B, Weidemüller, M, Stienkemeier, F & Mudrich, M. Formation and relaxation of RbHe exciplexes on He nanodroplets studied by femtosecond pump and picosecond probe spectroscopy. *J. Chem. Phys.* **137,** 024316 (2012).

135. Mudrich, M., Stienkemeier, F., Droppelmann, G., Claas, P. & Schulz, C. P. Quantum Interference Spectroscopy of Rubidium-Helium Exciplexes Formed on Helium Nanodroplets. *Phys. Rev. Lett.* **100,** 023401. https://link.aps.org/doi/10.1103/PhysRevLett.100.023401 (2008).

136. Giese, C., Stienkemeier, F., Mudrich, M., Hauser, A. W. & Ernst, W. E. Homo-and heteronuclear alkali metal trimers formed on helium nanodroplets. Part II. Femtosecond spectroscopy and spectra assignments. *Phys. Chem. Chem. Phys.* **13,** 18769–18780 (2011).

137. Schmidt, H. *et al.* Predissociation dynamics of lithium iodide. *J. Chem. Phys.* **142,** 044303. https://doi.org/10.1063/1.4906512 (2015).

138. Vilà, A., Paniagua, M. & Gonzàlez, M. Vibrational energy relaxation dynamics of diatomic molecules inside superfluid helium nanodroplets. The case of the I_2 molecule. *Phys. Chem. Chem. Phys.* **20,** 118–130. http://dx.doi.org/10.1039/C7CP05694J (2018).

139. Shepperson, B., Søndergaard, A. A., Christiansen, L., Kaczmarczyk, J., Zillich, R. E., Lemeshko, M. & Stapelfeldt, H. Laser-induced rotation of iodine molecules in helium nanodroplets: revivals and breaking free. *Phys. Rev. Lett.* **118,** 203203 (2017).

140. Pickering, J. D., Shepperson, B., Christiansen, L. & Stapelfeldt, H. Femtosecond laser induced Coulomb explosion imaging of aligned OCS oligomers inside helium nanodroplets. *J. Chem. Phys.* **149,** 154306 (2018).

141. Pickering, J. D., Shepperson, B., Christiansen, L. & Stapelfeldt, H. Alignment of the CS 2 dimer embedded in helium droplets induced by a circularly polarized laser pulse. *Phys. Rev. A* **99,** 043403 (2019).

142. Schouder, C., Chatterley, A. S., Calvo, F., Christiansen, L. & Stapelfeldt, H. Structure determination of the tetracene dimer in helium nanodroplets using femtosecond strong-field ionization. *Structural Dynamics* **6,** 044301 (2019).

143. Blancafort-Jorquera, M., Vilà, A. & González, M. Rotational energy relaxation quantum dynamics of a diatomic molecule in a superfluid helium nanodroplet and study of the hydrogen isotopes case. *Phys. Chem. Chem. Phys.* **21,** 21007–21021 (2019).

144. Reho, J., Callegari, C., Higgins, J., Ernst, W. E., Lehmann, K. K. & Scoles, G. Spin–orbit effects in the formation of the Na–He excimer on the surface of He clusters. *Faraday Discussions* **108,** 161–174 (1997).

145. Hernando, A., Barranco, M., Mayol, R., Pi, M. & Ancilotto, F. Density functional theory of the structure of magnesium-doped helium nanodroplets. *Phys. Rev. B* **78,** 184515. http://link.aps.org/doi/10.1103/PhysRevB.78.184515 (2008).

146. Higgins, J., Callegari, C., Reho, J., Stienkemeier, F, Ernst, W., Gutowski, M & Scoles, G. Helium cluster isolation spectroscopy of alkali dimers in the triplet manifold. *J. Phys. Chem. A* **102,** 4952–4965 (1998).

147. Lackner, F. & Ernst, W. E. Photoinduced molecule formation of spatially separated atoms on helium nanodroplets. *J. Phys. Chem. Lett.* **9,** 3561–3566. https://doi.org/10.1021/acs.jpclett.8b01530 (2018).

148. Döppner, T., Diederich, T., Göde, S., Przystawik, A., Tiggesbäumker, J. & Meiwes-Broer, K.-H. Ion induced snowballs as a diagnostic tool to investigate the caging of metal clusters in large helium droplets. *J. Chem. Phys.* **126,** 244513 (2007).

149. Theisen, M., Lackner, F. & Ernst, W. E. Forming Rb^+ snowballs in the center of He nanodroplets. *Phys. Chem. Chem. Phys.* **12,** 14861–14863. http://dx.doi.org/10.1039/C0CP01283A (2010).

150. Müller, S, Mudrich, M & Stienkemeier, F. Alkali-helium snowball complexes formed on helium nanodroplets. *J. Chem. Phys.* **131,** 044319 (2009).

151. Krishnan, S. *et al.* Dopant-induced ignition of helium nanodroplets in intense few-cycle laser pulses. *Phys. Rev. Lett.* **107,** 173402 (2011).

152. Kelbg, M, Zabel, M, Krebs, B, Kazak, L, Meiwes-Broer, K.-H. & Tiggesbäumker, J. Auger emission from the Coulomb explosion of helium nanoplasmas. *J. Chem. Phys.* **150,** 204302 (2019).

153. Wang, C. C., Kornilov, O., Gessner, O., Kim, J. H., Peterka, D. S. & Neumark, D. M. Photoelectron imaging of helium droplets doped with Xe and Kr atoms. *J. Phys. Chem. A* **112,** 9356–9365 (2008).

154. Buchta, D. *et al.* Charge transfer and penning ionization of dopants in or on helium nanodroplets exposed to EUV radiation. *J. Phys. Chem. A* **117,** 4394–4403 (2013).

155. Shcherbinin, M. *et al.* Interatomic Coulombic decay in helium nanodroplets. *Phys. Rev. A* **96,** 013407 (2017).

156. LaForge, A., Shcherbinin, M., Stienkemeier, F., Richter, R., Moshammer, R., Pfeifer, T. & Mudrich, M. Highly efficient double ionization of mixed alkali dimers by intermolecular Coulombic decay. *Nature Physics* **15,** 247–250 (2019).

157. LaForge, A. *et al.* Collective autoionization in multiply-excited systems: a novel ionization process observed in helium nanodroplets. *Scientific reports* **4,** 3621 (2014).

158. Ovcharenko, Y *et al.* Novel collective autoionization process observed in electron spectra of He clusters. *Phys. Rev. Lett.* **112,** 073401 (2014).

159. Fennel, T., Meiwes-Broer, K.-H., Tiggesbäumker, J, Reinhard, P.-G., Dinh, P. M. & Suraud, E. Laser-driven nonlinear cluster dynamics. *Rev. Mod. Phys.* **82,** 1793 (2010).

160. Bainschab, M. *Multiphoton Ionization Channels in Molecules Investigated by Photoelectron-Photoion-Coincidence Spectroscopy* Master Thesis (Institute of Experimental physics, Graz University of Technology, 2016).

161. Ranftl, S. *Ultrafast Photoinduced Ejection Dynamics of Indium Atoms inside Superfluid Helium Nanodroplets* Master Thesis (Institute of Experimental physics, Graz University of Technology, 2017).

162. Cesnik, S. *The Role of Molecular Symmetries in Non-adiabatic Relaxation Dynamics* Master Thesis (Institute of Experimental physics, Graz University of Technology, 2018).

163. Kramida, A., Ralchenko, Y., Reader, J. & and NIST ASD Team. NIST Atomic Spectra Database (ver. 5.6.1), https://physics.nist.gov/asd [Tue Apr 09 2019]. National Institute of Standards and Technology, Gaithersburg, MD. 2018.

164. Thaler, B., Heim, P., Treiber, L. & Koch, M. Ultrafast photoinduced dynamics of single atoms solvated inside helium nanodroplets. *submitted to J. Chem. Phys.* (2019).

165. Balasubramanian, K & Li, J. Spectroscopic properties and potential energy surfaces of In2. *J. Chem. Phys.* **88,** 4979–4986 (1988).

166. Meyer, M. *Nuclear Wave Packet Dynamics of Indium Dimers inside Superfluid Helium Nanodroplets* Master Thesis (Institute of Experimental physics, Graz University of Technology, 2018).

167. Meyer, M., Thaler, B., Heim, P. & Koch, M. Femtosecond solvation dynamics of indium dimers inside superfluid helium nanodroplets. *EPJ Web Conf.* **205,** 06005. https:/articles/epjconf/abs/2019/10/epjconf_up2019_06005/epjconf_up2019_06005.html (2019).

168. Thaler, B., Meyer, M., Heim, P. & Koch, M. Long-lived nuclear coherences inside helium nanodroplets. *arXiv preprint arXiv:1907.04157* (2019).

169. Auböck, G., Nagl, J., Callegari, C. & Ernst, W. E. Electron spin pumping of Rb atoms on He nanodroplets via nondestructive optical excitation. *Phys. Rev. Lett.* **101,** 035301 (2008).

170. Buchenau, H., Knuth, E. L., Northby, J., Toennies, J. P. & Winkler, C. Mass spectra and time-of-flight distributions of helium cluster beams. *J. Chem. Phys.* **92,** 6875–6889. http://link.aip.org/link/?JCP/92/6875/1 (1990).

171. McCarty, R. D. Thermodynamic properties of helium 4 from 2 to 1500 K at pressures to 10^8 Pa. *J. Phys. Chem. Ref. Data* **2,** 923–1042 (1973).

172. Krems, R. V. Cold controlled chemistry. *Phys. Chem. Chem. Phys.* **10,** 4079–4092 (2008).

173. Douberly, G. E., Merritt, J. M. & Miller, R. E. IR–IR double resonance spectroscopy in helium nanodroplets: Photo-induced isomerization. *Phys. Chem. Chem. Phys.* **7,** 463–468 (2005).

174. Braun, A. & Drabbels, M. Photodissociation of alkyl iodides in helium nanodroplets. I. Kinetic energy transfer. *J. Chem. Phys.* **127,** 114303. https://doi.org/10.1063/1.2767261 (2007).

175. Braun, A. & Drabbels, M. Photodissociation of alkyl iodides in helium nanodroplets. III. Recombination. *J. Chem. Phys.* **127,** 114305 (2007).

176. Woon, D. E. & Dunning-Jr., T. H. Gaussian basis sets for use in correlated molecular calculations. IV. Calculation of static electrical response properties. *J. Chem. Phys.* **100,** 2975–2988. https://doi.org/10.1063/1.466439 (1994).

177. Metz, B., Stoll, H. & Dolg, M. Small-core multiconfiguration-Dirac–Hartree–Fock-adjusted pseudopotentials for post-d main group elements: Application to PbH and PbO. *J. Chem. Phys.* **113,** 2563–2569. http://dx.doi.org/10.1063/1.1305880 (2000).

178. Werner, H.-J. *et al. MOLPRO, version 2012.1, a package of ab initio programs* see http://www.molpro.net. 2012.

179. Knowles, P. J. & Werner, H.-J. An efficient second order MCSCF method for long configuration expansions. *Chem. Phys. Lett.* **115,** 259–267. http://dx.doi.org/10.1016/0009-2614(85)80025-7 (1985).

180. Werner, H.-J. & Knowles, P. J. A second order multiconfiguration SCF procedure with optimum convergence. *J. Chem. Phys.* **82,** 5053–5063. https://doi.org/10.1063/1.448627 (1985).

181. Knowles, P. J. & Werner, H.-J. Internally contracted multiconfiguration reference configuration interaction calculations for excited states. *Theor. Chem. Acc.* **84,** 95–103 (1992).

182. Werner, H.-J. & Knowles, P. J. An efficient internally contracted multiconfiguration reference CI method. *J. Chem. Phys.* **89,** 5803–5814. http://dx.doi.org/10.1063/1.455556 (1988).

183. Tao, F. The use of midbond functions for ab initio calculations of the asymmetric potentials of He-Ne and He-Ar. *J. Chem. Phys.* **98,** 3049–3059. https://doi.org/10.1063/1.464131 (1993).

184. Baranowska, A., Capelo, S. B. & Fernández, B. New basis sets for the evaluation of interaction energies: an ab initio study of the He-He, Ne-Ne, Ar-Ar, He-Ne, He-Ar and Ne-Ar van der Waals complex internuclear potentials and ro-vibrational spectra. *Phys. Chem. Chem. Phys.* **12,** 13586–13596. http://dx.doi.org/10.1039/C0CP00535E (2010).

185. Shaw, R. A. & Hill, J. G. Midbond basis functions for weakly bound complexes. *Mol. Phys.* **116,** 1460–1470. https://doi.org/10.1080/00268976.2018.1440018 (2018).

186. Boys, S. F. & Bernardi, F. The calculation of small molecular interactions by the differences of separate total energies. Some procedures with reduced errors. *Mol. Phys.* **19,** 553–566 (1970).

187. Feller, D. Application of systematic sequences of wave functions to the water dimer. *J. Chem. Phys.* **96,** 6104–6114. https://doi.org/10.1063/1.462652 (1992).

188. Wilson, A. K. & Thom H. Dunning, J. Benchmark calculations with correlated molecular wave functions. X. Comparison with "exact" MP2 calculations on Ne, HF, H_2O, and N_2. *J. Chem. Phys.* **106,** 8718–8726. https://doi.org/10.1063/1.473932 (1997).

189. Gdanitz, R. J. Accurately solving the electronic Schrödinger equation of atoms and molecules by extrapolating to the basis set limit. I. The helium dimer (He_2). *J. Chem. Phys.* **113,** 5145. http://dx.doi.org/10.1063/1.1290001 (2000).

190. Mella, M., Calderoni, G. & Cargnoni, F. Predicting atomic dopant solvation in helium clusters: The $MgHe_n$ case. *J. Chem. Phys.* **123,** 054328. https://doi.org/10.1063/1.1982787 (2005).

191. Hernando, A., Mayol, R., Pi, M., Barranco, M., Ancilotto, F., Bünermann, O. & Stienkemeier, F. The structure and energetics of ^{3}He and ^{4}He nanodroplets doped with alkaline earth atoms. *J. Phys. Chem. A* **111,** 7303–7308 (2007).

192. Zewail, A., De Schryver, F., De Feyter, S. & Schweitzer, G. *Femtochemistry: With the Nobel Lecture of A. Zewail* (Wiley, 2001).

193. Townsend, D. *et al.* The roaming atom: straying from the reaction path in formaldehyde decomposition. *Science* **306,** 1158–1161 (2004).

194. Blanchet, V., Zgierski, M. Z., Seideman, T. & Stolow, A. Discerning vibronic molecular dynamics using time-resolved photoelectron spectroscopy. *Nature* **401,** 52–54 (1999).

195. Calegari, F. *et al.* Ultrafast electron dynamics in phenylalanine initiated by attosecond pulses. *Science* **346,** 336–339. http://www.sciencemag.org/content/346/6207/336.abstract (2014).

196. Hertel, I. V. & Radloff, W. Ultrafast dynamics in isolated molecules and molecular clusters. *Rep. Prog. Phys.* **69,** 1897–2003. http://iopscience.iop.org/0034-4885/69/6/R06 (2006).

197. Von Haeften, K., Laarmann, T., Wabnitz, H. & Möller, T. Bubble formation and decay in ^{3}He and ^{4}He clusters. *Phys. Rev. Lett.* **88,** 233401. http://link.aps.org/abstract/PRL/v88/e233401 (2002).

198. Kruit, P & Read, F. H. Magnetic field paralleliser for 2π electron-spectrometer and electron-image magnifier. *J. Phys. E: Sci. Instrum.* **16,** 313–324 (1983).

199. Kramida, A., Yu. Ralchenko, Reader, J. & and NIST ASD Team. NIST Atomic Spectra Database (version 5.5.2), [Online]. Available: https://physics.nist.gov/asd [Fri Jan 19 2018]. National Institute of Standards and Technology, Gaithersburg, MD. 2018.

200. Ancilotto, F., Barranco, M., Caupin, F., Mayol, R. & Pi, M. Freezing of ^{4}He and its liquid-solid interface from density functional theory. *Phys. Rev. B* **72,** 214522. https://link.aps.org/doi/10.1103/PhysRevB.72.214522 (2005).

201. Peterson, K. A., Figgen, D., Goll, E., Stoll, H. & Dolg, M. Systematically convergent basis sets with relativistic pseudopotentials. II. Small-core pseudopotentials and correlation consistent basis sets for the post-d group 16–18 elements. *J. Chem. Phys.* **119,** 11113–11123. https://doi.org/10.1063/1.1622924 (2003).

202. Nagl, J., Auböck, G., Hauser, A. W., Allard, O., Callegari, C. & Ernst, W. E. Heteronuclear and homonuclear high-spin alkali trimers on helium nanodroplets. *Phys. Rev. Lett.* **100,** 063001 (2008).

203. Küpper, J. & Merritt, J. M. Spectroscopy of free radicals and radical containing entrance-channel complexes in superfluid helium nanodroplets. *Int. Rev. Phys. Chem.* **26,** 249–287 (2007).

204. Nauta, K & Miller, R. Infrared spectroscopy and structures of Ar_n–HF in liquid helium nanodroplets. *J. Chem. Phys.* **115,** 10138–10145 (2001).

205. Göde, S, Irsig, R, Tiggesbäumker, J & Meiwes-Broer, K. Time-resolved studies on the collapse of magnesium atom foam in helium nanodroplets. *New J. Phys.* **15,** 015026 (2013).

206. Cargnoni, F. & Mella, M. Solubility of metal atoms in helium droplets: Exploring the effect of the well depth using the coinage metals Cu and Ag. *J. Phys. Chem. A* **115,** 7141–7152 (2011).

207. Ratschek, M., Pototschnig, J. V., Hauser, A. W. & Ernst, W. E. Solvation and Spectral Line Shifts of Chromium Atoms in Helium Droplets Based on a Density Functional Theory Approach. *J. Phys. Chem. A* **118,** 6622–6631 (2014).

208. Lehmann, K. K. Potential of a neutral impurity in a large ^{4}He cluster. *Mol. Phys.* **97,** 645–666. https://doi.org/10.1080/002689799163497 (1999).

209. Zillich, R. E. & Whaley, K. B. Solvation structure and rotational dynamics of LiH in ^{4}He clusters. *J. Phys. Chem. A* **111,** 7489–7498 (2007).

210. Kobayashi, Y., Chang, K. F., Zeng, T., Neumark, D. M. & Leone, S. R. Direct mapping of curve-crossing dynamics in IBr by attosecond transient absorption spectroscopy. *Science* **365,** 79–83. ISSN: 0036-8075, 1095-9203. https://science.sciencemag.org/content/365/6448/79 (July 2019).

211. Consani, C., Auböck, G., van Mourik, F. & Chergui, M. Ultrafast Tryptophan-to-Heme Electron Transfer in Myoglobins Revealed by UV 2D Spectroscopy. *Science* **339,** 1586–1589. http://dx.doi.org/10.1126/science.1230758 (2013).

212. Beaulieu, S. *et al.* Photoexcitation circular dichroism in chiral molecules. *Nat. Phys.* **14,** 484–489. https://www.nature.com/articles/s41567-017-0038-z (2018).

213. Scholes, G. D. *et al.* Using coherence to enhance function in chemical and biophysical systems. *Nature* **543,** 647–656. https://www.nature.com/articles/nature21425 (2017).

214. Lee, H., Cheng, Y.-C. & Fleming, G. R. Coherence Dynamics in Photosynthesis: Protein Protection of Excitonic Coherence. *Science* **316,** 1462–1465. http://science.sciencemag.org/content/316/5830/1462 (2007).

215. Collini, E., Wong, C. Y., Wilk, K. E., Curmi, P. M. G., Brumer, P. & Scholes, G. D. Coherently wired light-harvesting in photosynthetic marine algae at ambient temperature. *Nature* **463,** 644–647. https://www.nature.com/articles/nature08811 (2010).

216. Fuller, F. D. *et al.* Vibronic coherence in oxygenic photosynthesis. *Nat. Chem.* **6,** 706–711. https://www.nature.com/articles/nchem.2005 (2014).

217. Falke, S. M. *et al.* Coherent ultrafast charge transfer in an organic photovoltaic blend. *Science* **344,** 1001–1005. http://science.sciencemag.org/content/344/6187/1001 (2014).

218. Park, M. *et al.* Excited-state vibrational dynamics toward the polaron in methylammonium lead iodide perovskite. *Nat. Comm.* **9,** 1–9. ISSN: 2041-1723. https://www.nature.com/articles/s41467-018-04946-7 (June 2018).

219. Batignani, G. *et al.* Probing femtosecond lattice displacement upon photo-carrier generation in lead halide perovskite. *Nat. Comm.* **9,** 1–5. ISSN: 2041-1723. https://www.nature.com/articles/s41467-018-04367-6 (May 2018).

220. Bondbey, V. E. Laser-induced fluorescence and bonding of metal dimers. *Science* **227,** 125–131 (1985).

221. Liu, Q., Wan, C. & Zewail, A. H. Solvation Ultrafast Dynamics of Reactions. 13. Theoretical and Experimental Studies of Wave Packet Reaction Coherence and Its Density Dependence. *J. Phys. Chem.* **100,** 18666–18682. https://doi.org/10.1021/jp962432v (1996).

222. See Supplementary Material for the assignment of the In_2 $B^3\Pi_g \leftarrow X^3\Pi_u$ band, measurements excluding a free dimer background, details on the sliding window Fourier analysis, and the 3/2 revival.

223. Renzler, M. *et al.* Communication: Dopant-induced solvation of alkalis in liquid helium nanodroplets. *J. Chem. Phys.* **145,** 181101. https://aip.scitation.org/doi/abs/10.1063/1.4967405 (2016).

224. Douglas, M., Hauge, R. & Margrave, J. Electronic adsorption spectra of the Group 3A metal dimers isolated in cryogenic matrixes. *J. Chem. Phys.* **87,** 2945–2947 (1983).

225. Bicchi, P, Marinelli, C & Bernheim, R. Electronic spectral transitions in In_2. *J. Chem. Phys.* **97,** 8809–8810 (1992).

226. Vrakking, M. J. J., Villeneuve, D. M. & Stolow, A. Observation of fractional revivals of a molecular wave packet. *Phys. Rev. A* **54,** R37–R40. https://link.aps.org/doi/10.1103/PhysRevA.54.R37 (1996).

227. Gühr, M. *Coherent dynamics of small molecules in rare gas crystals* (Cuvillier Verlag, 2005).

228. Smolarek, S., Brauer, N. B., Buma, W. J. & Drabbels, M. IR spectroscopy of molecular ions by nonthermal ion ejection from helium nanodroplets. *J. Am. Chem. Soc.* **132,** 14086–14091 (2010).

229. Zhang, X., Brauer, N. B., Berden, G., Rijs, A. M. & Drabbels, M. Mid-infrared spectroscopy of molecular ions in helium nanodroplets. *J. Chem. Phys.* **136,** 044305 (2012).

230. Filsinger, F., Ahn, D.-S., Meijer, G. & von Helden, G. Photoexcitation of mass/charge selected hemin+, caught in helium nanodroplets. *Phys. Chem. Chem. Phys.* **14,** 13370–13377 (2012).

231. Flórez, A. I. G., Ahn, D.-S., Gewinner, S., Schöllkopf, W. & von Helden, G. IR spectroscopy of protonated leu-enkephalin and its 18-crown-6 complex embedded in helium droplets. *Phys. Chem. Chem. Phys.* **17,** 21902–21911 (2015).

232. Greeff, C., Lester Jr, W. & Hammond, B. Electronic states of Al and Al_2 using quantum Monte Carlo with an effective core potential. *J. Chem. Phys.* **104,** 1973–1978 (1996).

233. Johnston, M. D., Lockwood, S. P. & Metz, R. B. Photofragment imaging and electronic spectroscopy of Al_2^+. *J. Chem. Phys.* **148,** 214308. https://doi.org/10.1063/1.5034353 (2018).

234. Stapelfeldt, H., Constant, E., Sakai, H. & Corkum, P. B. Time-resolved Coulomb explosion imaging: A method to measure structure and dynamics of molecular nuclear wave packets. *Phys. Rev. A* **58,** 426 (1998).

235. Pecourt, J.-M. L., Peon, J. & Kohler, B. DNA excited-state dynamics: Ultrafast internal conversion and vibrational cooling in a series of nucleosides. *J. Am. Chem. Soc.* **123,** 10370–10378 (2001).

236. Crespo-Hernández, C. E., Cohen, B., Hare, P. M. & Kohler, B. Ultrafast excited-state dynamics in nucleic acids. *Chem. Rev.* **104,** 1977–2020 (2004).

237. Gühr, M & Schwentner, N. Effective chromophore potential, dissipative trajectories, and vibrational energy relaxation: Br_2 in Ar matrix. *J. Chem. Phys.* **123,** 244506 (2005).

238. Slater, N. Classical motion under a Morse potential. *Nature* **180,** 1352 (1957).

239. Coppens, F. *^{4}He-DFT BCN-TLS manual* 2016. https://github.com/bcntls2016/.

240. Staples, G. *TORQUE Resource Manager* in *Proceedings of the 2006 ACM/IEEE Conference on Supercomputing* (Association for Computing Machinery, Tampa, Florida, 2006), 8–es. https://doi.org/10.1145/1188455.1188464.

Danksagung

Nach nun insgesamt vier Jahren am Institut für Experimentalphysik an der TU Graz, unzähligen Stunden im Labor, dem dauerhaften Entwerfen, Verfassen und Korrigieren von Papers und dem Lesen wohl hunderter Publikationen, gilt es nun Resümee zu ziehen und einigen Personen besonderen Dank auszusprechen. Das größte Dankeschön geht an meinen Betreuer, Assoc. Prof. Markus Koch, der wohl versucht hat, mir seine gesamte und umfassende Expertise über Experimentalphysik und Spektroskopie beizubringen. Durch seine besonnene und kompetente Herangehensweise an physikalische Probleme laufen die unzähligen, oft langwierigen Diskussionen und Besprechungen innerhalb der Forschungsgruppe immer auf Augenhöhe und mit einer ruhigen Sachlichkeit, die ideal ist für ein entspanntes und produktives Forschungsumfeld. Mit seinen immer frischen und nicht-endenden Ideen und seinem akademischen Enthusiasmus bleibt die Begeisterung für das wissenschaftliche Arbeiten stets ungebrochen. Nicht zu unterschätzen ist auch seine Kunstfertigkeit mit der Espresso-Maschine (inklusive passender Mühle), mit welcher der Start in die Woche im Zuge der allwöchentlichen Montags-Besprechung optimal gelingt. Ich bedanke mich auch für die vielen Anregungen und Korrektur-Vorschläge für diese Dissertation.
Die Person, von der ich nach Markus wohl am meisten lernen durfte, ist mein langjähriger Schreibtisch-Nachbar und mittlerweile guter Freund Pascal Heim. Seine zu mir oft komplementäre Herangehensweise an physikalische Fragestellungen, sowie seine umfassenden Skills im Programmieren und mathematischen Lösen von Problemen haben dieser Dissertation mit Sicherheit zu deutlich mehr Qualität verholfen - vielen Dank dafür. Auch seine mittlerweile berüchtigte Korrekturfähigkeit und genaue Kritik bei Publikationen, Abstracts und anderen Texten sorgt stets für den nötigen Feinschliff.
Ein großer Dank geht auch an Leonhard Treiber, für sein umfassendes Wissen, seine konstruktive Unterstützung und immer währende Motivation bei unzähligen Problemen und für seine Fähigkeit, immer die richtigen und spannendsten Fragen zu stellen (und damit ist nicht "Darf ich dich kurz nerven?" gemeint). Sowohl Leo und Pascal sind hauptverantwortlich für die unglaublich entspannte und lockere Atmosphäre in unserem Büro, welche dem sonst oft stressigen Arbeitsalltag die nötige Ruhe einhaucht. Im Zuge der letzten vier Jahre durfte ich auch die Gesellschaft von vielen weiteren fantastischen Kolleg*innen im Büro und Labor genießen: Ich bedanke mich bei Stefan Cesnik, Sascha Ranftl, Miriam Meyer, Werner Kleinsasser und Michael Stadlhofer für die immer freundliche und konstruktive Zusammenarbeit. Bei Paul Maierhofer und Markus Beinschab, unseren Vorgängern, bedanke ich mich für die reibungslose Einschulung.
Das gesamte Institut für Experimentalphysik und die respektvolle und umgängliche Art der Mitarbeiter*innen untereinander sind wohl ebenso beispiellos. Bei Univ. Prof. Wolfgang E. Ernst bedanke ich mich für die vielen Ratschläge und Anregungen, ich wünsche ihm nach seiner Emeritierung noch viele spannende Jahre in der Wissenschaft und eine wohlverdiente, ruhige Zeit.
Besonderer Dank gebührt meinen mittlerweile auch schon langjährigen Instituts-Gefährten Roman Mess-

ner, Martin Schnedlitz, Max Lasserus, Adrian Ruckhofer und Ralf Meyer, die beinahe zeitgleich mit mir Diplomarbeit und Dissertation durchlaufen haben. Ihnen und auch allen anderen wissenschaftlichen Mitarbeiter*innen am Institut möchte ich danken, für experimentelle Ratschläge, für unzählige lustige Stunden und spannende Unterhaltungen beim wöchentlichen Barilla-, Toast- oder Volta-Genuss.
Fachlicher Dank gebührt unserer Theorie-Gruppe um Andreas Hauser, Johann V. Pototschnig, und insbesondere Ralf Meyer, dessen Support bei der Berechnung, Implementierung und Durchführung der Simulationen in dieser Arbeit unglaublich hilfreich war.
Für eine reibungslose und entschleunigte Organisation des Arbeitsalltags möchte ich den Damen im Sekretariat danken, die immer hilfsbereit mit Rat und Tat zur Seite stehen. Den Mitarbeitern der mechanischen und elektronischen Werkstatt möchte ich für ihre kompetente und professionelle Hilfe bei technischen Aufgabenstellungen und Problemen danken, genauso wie für ihre Geduld mit uns "Technikern".
Dank gebührt auch den Entwicklern des im Zuge dieser Dissertation verwendeten HeDFT Simulationspakets, insbesondere Manuel Barranco und Marti Pi aus Barcelona. Ihr Support und Rat besonders zu Beginn meiner Dissertation waren sehr hilfreich und haben mir wichtige Inputs zur fehlerfreien Benutzung der Programmpakete gegeben.

Neben diesen vielen tollen Menschen aus dem wissenschaftlichen Umfeld möchte ich auch noch einige Personen aus meinem privaten Kreis erwähnen, die mich stets motivieren und mir die nötige Energie geben. Danke an meine vielen langjährigen Studienkollegen, insbesondere Andreas, Stefan, Sascha, Pascal, Lukas und Michael, für die spaßige Zeit bei zusammen gerechneten Übungszetteln, Programmier-Stunden, dem Schreiben von Protokollen und Lernen für Prüfungen. Danke an meine langjährigen Freunde aus Hartberg, insbesondere Jakob, Joachim, Rainer, David, Matthias, Christopher, Christian und Sebastian. Es freut mich, euch alle immer hinter mir zu wissen.
Ein großer Dank geht an meine fantastische, große Familie, angefangen bei der Schwieger-Family (Anna, Robert, David) aus Kroisbach, meinen Großeltern aus Gersdorf und Hartberg, meiner Schwester Elisabeth und Raffael, Martha und Robert, und zu guter Letzt meinen lieben Eltern, Birgit und Horst. Danke liebe Mama und danke lieber Papa für eure immerwährende Unterstützung und euren Rückhalt, den ich unglaublich schätze.

Ich widme diese Arbeit meiner größten Unterstützerin, meiner besten Freundin, und der Liebe meines Lebens, nämlich dir, lieber Barbara. Deine immer währende Geduld mit mir, deine ungebrochene Unterstützung und dein steter Rückhalt sorgen für den nötigen Rahmen den ich brauche, um voranzukommen und mich zu motivieren. Danke.

Graz, Jänner 2020